UTS UNIVERSITY OF TECHNOLOGY SYDNEY

Assessment of Soil Arching in a Pile-supported Railway Embankment under the Moving Train Load and Earthquake

by Naveen Kumar Meena

Thesis submitted in fulfilment of the requirements for the degree of

Doctor of Philosophy

under the supervision of Dr. Sanjay Nimbalkar and A/Prof. Behzad Fatahi

University of Technology Sydney
Faculty of Engineering and Information Technology (FEIT)

January 2022

CERTIFICATE OF ORIGINAL AUTHORSHIP

I, *Naveen Kumar Meena* declare that this thesis, is submitted in fulfilment of the requirements for the award of *Doctor of Philosophy*, in the *School of Civil and Environmental Engineering, Faculty of Engineering and Information Technology* at the University of Technology Sydney.

This thesis is wholly my own work unless otherwise referenced or acknowledged. In addition, I certify that all information sources and literature used are indicated in the thesis.

This document has not been submitted for qualifications at any other academic institution.

This research is supported by the Government of India under National Overseas Scholarship, No. 11016/16/2016 Education.

Signature: Production Note: Signature removed prior to publication.

(**NAVEEN KUMAR MEENA**)

Date: 03/January/2022

Dedicated

To my family and friends

Acknowledgment

PhD become the most memorable period in my life where I challenged and improved myself over these four years of journey. Successful completion of my PhD would not have been possible without the motivation of many people. Therefore, I am conveying my sincere thanks to all of them.

First and foremost, I would like to express my deep gratitude to my principal supervisor, Dr. Sanjay Nimbalkar, for his continuous support and guidance throughout this journey. Apart from academic expertise, his encouraging nature has been the key to success. His proficiency in understanding students' learning nature and guiding them is remarkable. I am profoundly indebted and blessed to have him as my principal supervisor. I would also like to thank my co-supervisor, Associate Professor Behzad Fatahi, for his supervision and willingness to help whenever possible. I am also very appreciative to my candidature committee for their support during my candidature assessments.

My sincere thank go to the Ministry of Tribal Affairs, Government of India, for providing me the financial support as National Overseas Scholarship, No. 11016/16/2016 Education. I am also very thankful to the Consulate General of India Sydney for lookout all matters regarding my scholarship during my full candidature.

Finally, I would like to thank all my family and friends for their encouragement and unconditional love when I needed it most.

LIST OF PUBLICATIONS

RELATED TO THE THESIS:

Journal articles

1. **Meena, N. K.** Nimbalkar, S. Fatahi, B. and Yang, G. (2020). "Effects of soil arching on behavior of pile-supported railway embankment: 2D FEM approach", *Computers and Geotechnics*, vol. 123, pp. 103601.
2. **Meena, N. K.** and Nimbalkar, S. "Two-Dimensional Analytical Solution of Soil Arching in a Pile-supported Geosynthetic-reinforced Railway Embankment", *Geosynthetics International*, (***Under review***)
3. **Meena, N. K.** Nimbalkar, S. and Fatahi, B. "Investigation of soil arching in a geosynthetic-reinforced pile-supported embankment under the earthquake". (***draft under preparation***)

Book chapter

1. Nimbalkar, S. and **Meena, N. K.** (2022). "Static and Seismic Assessment of Soil Arching in Piled Embankments" In: Kolathayar S., Pal I., Chian S.C., Mondal A. (eds) *Civil Engineering for Disaster Risk Reduction*. Springer Tracts in Civil Engineering. Springer, Singapore.

Peer-reviewed conference papers

1. **Meena, N. K.** Nimbalkar, S. and Fatahi, B. (2019). "Finite element modeling of soil arching in pile supported embankment: 2D approach", In *International Congress and Exhibition "Sustainable Civil Infrastructures"* (pp. 40-50). Springer, Cham.

2. **Meena, N. K.**, and Nimbalkar, S. (2019). “Seismic assessment of soil arching in piled embankment using finite element approach”, In *4th Australasian Conference on Computational Mechanics*, Hobart, Australia, p. 24.
3. **Meena, N. K.**, Nimbalkar, S., and Fatahi, B. (2021). “Finite Element Analysis of Soil Arching in Piled Embankment”, In *International Conference of the International Association for Computer Methods and Advances in Geomechanics* (pp. 817-824). Springer, Cham.
4. **Meena, N. K.**, Nimbalkar, S. (2021). “Soil Arching in Geosynthetic-Reinforced Pile-supported Railway Embankments under the Seismic Condition”, *Australian Earthquake Engineering Society (AEES) conference*.
5. **Meena, N. K.**, Nimbalkar, S., and Fatahi, B. (2022). “Finite element simulation of the soil arching in a pile-supported railway embankment considering train loading”, In *Proceedings of the 20th International Conference on Soil Mechanics and Geotechnical Engineering*, Sydney 2022.

OTHERS:

1. **Meena, N. K.,** and Nimbalkar, S. (2019). “Effect of water drawdown and dynamic loads on piled raft: two-dimensional finite element approach”, *Infrastructures*, 4(4), 75.
2. Rajeev, A., **Meena, N. K.**, and Pallav, K. (2019). “Comparative Study of Seismic Design and Performance of OMRF Building Using Indian, British, and European Codes”, *Infrastructures*, 4(4), 71.

TABLE OF CONTENTS

LIST OF FIGURES

FIGURE **Page**

LIST OF TABLES

LIST OF SYMBOLS

The following symbols and abbreviations are used in this thesis:

Notations

A	Effective surface area of a pile
A_{Emtop}	Area of embankment top
A_{ef}	Effective surface area of a single pile
A_{h}	Horizontal acceleration
A_{p}	Cross-sectional area of a pile
A_{s}	Area of clear pile spacing
A_{sb}	Area of subballast
A_{v}	Vertical acceleration
A_{wall}	Area of the pile wall
$A_{\sigma\mathrm{track}}$	Area of applied stress due to the track
$A_{\sigma\mathrm{train}}$	Area of applied stress due to the train loading
$A_{\sigma\mathrm{RT}}$	Area of applied stress on the soil arching crown
b'	Plate width
C_{c}	Soil arching coefficient
c'	Effective cohesion
D	Pile diameter
D_{act}	Active depth of subsoil
d	Width of the pile wall
E	Elastics modulus
E_{em}	Elastics modulus of embankment
E_{eq}	Equivalent elastic modulus of a pile

E_{geo}	Elastics modulus of geosynthetic layer
E_p	Elastic modulus of a pile
E_{sub}	Elastic modulus of subsoil
E_{set}	Settlement efficacy
E_{str}	Stress efficacy
E_o	One-dimensional modulus of the subsoil
g	Gravity load
F	Uniform force acting on the embankment lateral boundary
F_d	Design wheel load
F_s	Static wheel load
f_{eq}	Dominant frequency
h	Embankment height
h_{arch}	Soil arching height
h_{opt}	Optimum embankment height
h'	Embankment depth up to soil arching crown
I_{pile}	Second moment of the area of a pile
I_{sub}	Second moment of the area of subsoil
I_{wall}	Second moment of the area of a pile wall
J	Stiffness of geosynthetic layer
K	Lateral stress coefficient
K_o	Lateral stress coefficient at rest
K_a	Lateral stress coefficient at active stage
K_p	Lateral stress coefficient at passive stage
k_h	Coefficient of horizontal acceleration

k_s	Modulus of the subgrade reaction
k_{soil}	Soil stiffness parameter
k_v	Coefficient of vertical acceleration
N_{em}	Normalised embankment height
N_{vs}	Normalised vertical stress
l	Length of sleeper
l_d	diagonal spacing between pile
M_L	Earthquake magnitude
m	Mass of the embankment
P	Total force acting on the pile head
P_c	Vertical stress on the pile head
Q	Total force carried by the pile
q	Surcharge on the embankment top
r	Radial distance of soil arching
s	Pile spacing
s_x	Pile spacing in x-axis
s_y	Pile spacing in y-axis
T	Tension in geosynthetic layer
T_{max}	Maximum tension in a geosynthetic layer
t_{EQ}	Earthquake excitation time
t_{geo}	Thickness of geosynthetic layer
V	Train speed
W_{track}	Total weight of track
y	Maximum deflection of geosynthetic layer

a, b, and c	Elastic modulus coefficients relating to *SAR*
α and β	Damping coefficients
α' and β'	Mean value of impact factor
γ	Unit weight
γ'	Standard deviation of the impact factor
ε_{geo}	Axial strain in geosynthetic layer
Φ	Dynamic impact factor
λ	Interface factor
$\Delta_{lateral}$	Lateral displacement
μ	Interface frictional coefficient
δ	Soil settlement without piles
δ_{int}	Interface friction angle between pile and the surrounding subsoil
δ_{em}	Settlement of embankment
δ_{es}	Total settlement of subsoil
δ_{P}	Soil settlement with piles
δ_{sp}	Settlement of a plate
$\delta/(s\text{-}d)$	Normalised settlement of embankment
υ	Poisson's ratio
ρ	Material density
σ_{geo}	Vertical stress on the geosynthetic layer
σ_{h}	Horizontal stress
σ_{i}	Vertical stress, just below the inner boundary of the soil arching
σ_{max}	Maximum vertical stress

σ_n	Normal stress in the interface
σ_p	Vertical stress on the pile
σ_r	Radial stress in soil arching
σ_s	Vertical stress on the subsoil
σ_t	Train-induced vertical stress
σ_{track}	Self-weight of the rail track
σ_{train}	Self-weight of the moving train
σ_{RT}	Total vertical stress on the soil arching crown
σ_{up}	Upward vertical reaction stress on the bottom of the geosynthetic layer
σ_v	Vertical stress
σ_{vEQ}	Additional vertical stress due to a seismic excitation
σ_o	Radial stress at soil arching crown
σ_θ	Tangential stress in soil arching
τ	Shear stress along with the geosynthetic layer interface
τ_{bottom}	Shear stress along with the geosynthetic layer and subsoil
τ_{top}	Shear stress along with the geosynthetic layer and embankment
ϕ'	Effective friction angle of soil
ψ	Dilation angle of soil
ξ_o	Damping ratio

Abbreviations

2D	Two-dimensional
3D	Three-dimensional

ARE	American Railways Engineering Association
ARR	Area replacement ratio
CA	Concentric arch
CINPE4	Four-node plane strain linear infinite element
CPE4R	Four-node plane strain element with reduced integration
CPE8R	Eight-node, reduced-integration, two-dimensional, quadratic solid element
DAF	Dynamic amplification factor
DEM	Discrete element method
EA	Equivalent area
EEM	Equivalent elastic modulus
EFS	Equivalent flexural stiffness
FEM	Finite element method
FFT	Fast Fourier transform
FLAC	Fast lagrangian analysis of continua
GRC	Ground reaction curve
GRPS	Geosynthetic-reinforced pile-supported
MC	Mohr-Coulomb
MCC	Modified Cam Clay
ORE	Office of Research and Experiments
PFC	Particle flow code
PGA	Peak ground acceleration
SAR	Soil arching ratio
SCR	Stress concentration ratio

Abstract

The pile-supported embankments provide feasible solutions for railway infrastructure projects on the soft soil and allow rapid construction with less differential settlement. In the pile-supported embankments, the embankment load including surcharge is transferred to the pile heads through a load transfer mechanism known as soil arching. The pile-supported railway embankments often encounter dynamic loading due to the moving trains and earthquake. The dynamic loading may influence the soil arching phenomenon. Over the past decade, soil arching has been significantly studied under static conditions, and several analytical methods have been proposed to evaluate soil arching. However, the dynamic behaviour of soil arching under moving train-induced load and earthquake is yet to be investigated. Furthermore, the vertical stress on soil arching crown in the existing analytical methods is considered only due to self-weight of embankment and the stress distribution due to additional surcharge is neglected, resulting in inaccurate predictions.

In this thesis, finite element method (FEM)-based numerical analyses are performed to investigate the dynamic behaviour of soil arching. The physical visualisation of the soil arching phenomenon in the pile-supported embankments is very complex and usually requires a large setup. Therefore, numerical analysis is the unsurpassed approach to investigate soil arching. The two-dimensional (2D) unit cell model is analysed. A 2D idealisation method (i.e. equivalent area method) is used to convert a hypothetical three-dimensional (3D) problem into 2D to reduce the complexity and computational time.

This work begins with investigating the soil arching in a railway embankment under static condition. The equivalent dynamic load induced by a moving train is

chosen for train loading. The results confirm that the analysed numerical model can predict the soil arching phenomenon in a pile-supported railway embankment with reasonable accuracy. The key parameters of pile-supported embankments and their optimum value are identified. The inclusion of a geosynthetic layer is also investigated. The comparison of different analytical methods has also been reported to identify the variation in different methods. Subsequently, the accuracy of the existing analytical methods is improved by incorporating a realistic approximation of vertical stress on the soil arching crown. Results show that the failure of soil arching at the pile top is critical in the 3D condition, whereas the soil arching failure at the crown is more critical in the 2D condition.

Subsequently, the influence of earthquake-induced loading on soil arching phenomenon is investigated. The results show that soil arching is significantly affected under the seismic excitation. The parametric investigation reveals that friction angle of embankment fill should be higher for better performance of pile-supported embankment during an earthquake. The geosynthetic layer at the base of the embankment encourages stress transfer to the pile head through the membrane effect. Also, the amplitude of the earthquake significantly affects the mobilisation of soil arching.

Finally, the mobilisation of soil arching under moving train-induced dynamic loading is investigated. The results revealed that the dynamic loading significantly affects the soil arching phenomenon and should be considered during the design of a pile-supported railway embankment. The application of a geosynthetic layer enhances the load transfer from the subsoil to the pile head through the membrane effect.

Therefore, the findings of this thesis enhance the current knowledge of the dynamic behaviour of soil arching under the moving train load and earthquake. The

presented analytical methods can be used for accurate evaluation of vertical stress on the soil arching crown.

CHAPTER 1

INTRODUCTION

This chapter covers the general background of the soil arching phenomenon in a pile-supported embankment which helps readers to gain basic knowledge about this research project. It also includes the problem statement, research objectives, and outline of this thesis.

1.1 BACKGROUND

In the 2020-21 financial budget, the Australian government committed to invest billions of dollars in railway projects to strengthen the national economy. Most of these projects involve construction in coastal regions where the conditions are unfavourable for construction activities due to the compressible nature of the soil. These soils are vulnerable to potential failure due to excessive settlement which can adversely affect the stability of overlaid railway infrastructure projects. For the construction of embankments, many techniques such as the use of lightweight fill material (Puppala et al. 2019), temporary surcharge (López-Acosta et al. 2019), use of the geosynthetic layer at the embankment base (Bergado and Teerawattanasuk 2008), use of prefabricated vertical drains (Liu and Rowe 2015), and the inclusion of rigid columns such as piles (Liu et al. 2007), semi-rigid columns such as cement mix columns (Phutthananon et al. 2020) and flexible columns such as stone columns (Hosseinpour et al. 2019) are used to overcome these issues. Among these techniques, the

geosynthetic-reinforced pile-supported (GRPS) embankments provide feasible solutions for railway infrastructure projects on soft soil due to their rapid construction and less differential settlement. A typical schematic diagram of a GRPS railway embankment resting on the pile-improved area is shown in Figure 1.1. The type of rigid pile can be floating or end-bearing according to the subsoil stratum. Almeida et al. (2007) reviewed 16 case studies and found that the GRPS has been extensively used since 1995, and more than 80% of studies are related to railway or highway infrastructure. Therefore, this thesis deals with railway embankments supported by end-bearing rigid piles.

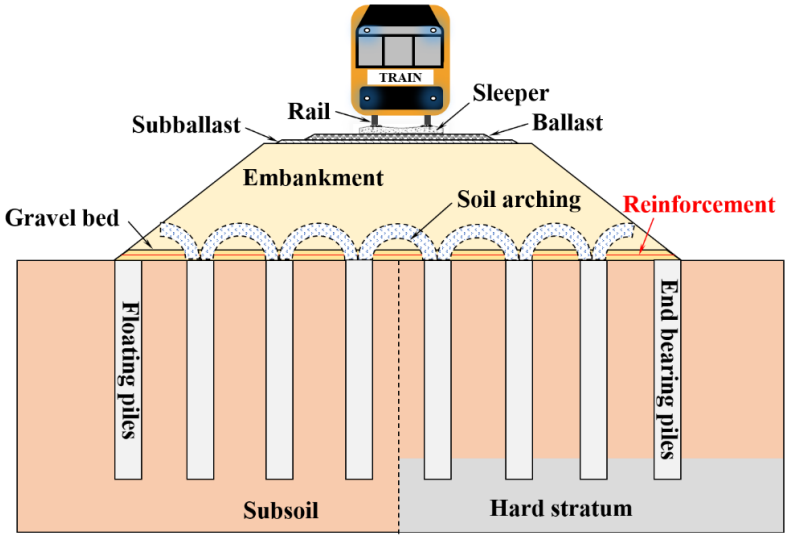

Figure 1.1: Schematic diagram of geosynthetic-reinforced pile-supported railway embankment and soil arching mechanism

In GRPS embankments, a granular material layer with a high friction angle is used to transfer embankment load, including surcharge to pile heads, resulting in reduced differential and total settlement at the embankment surface. Due to the stiffness difference in the rigid piles and the adjacent subsoil, shear stress is mobilised within the embankment fill. Consequently, the embankment load including surcharge

is transferred to the pile heads through a load transfer mechanism which is known as soil arching (Terzaghi 1943), as shown in Figure 1.1.

Many studies have investigated soil arching in GRPS embankments. These studies included, numerical studies (Han and Gabr 2002; Le Hello and Villard 2009; Zhuang et al. 2012; Rowe and Liu 2015; Pham and Dias 2019; Meena et al. 2020; George and Dasaka 2021), experimental studies (Liu et al. 2007; Chen et al. 2010; Van Eekelen et al. 2012a; 2012b; Han et al. 2015; Zhang et al. 2016; Hen et al. 2017; King et al. 2019; Rui et al. 2019; Wang and Chen 2019; Da Silva Burke and Elshafie 2020; Zhang et al. 2021) and theoretical analysis (Hewlett and Randolph 1988; Abusharar et al. 2009; Van Eekelen et al. 2013; Zhuang et al. 2014; Zhuang and Wang 2017; Rui et al. 2018; Pham 2020a; Lai et al. 2021). Most of the studies among the above listed are described further in this thesis.

GRPS railway embankments are subjected to cyclic loading due to moving trains which may affect the soil arching phenomenon (Han et al. 2015). Most of the past studies so far deal with the static behaviour of soil arching. In contrast, the dynamic behaviour of soil arching under moving train-induced load and earthquake is yet to be investigated. Furthermore, the surcharge on soil arching crown in reported analytical methods is considered either due to the self-weight of the embankment or similar to acting on the embankment top, resulting in vertical stress on the soil arching crown which is not accurate as in GRPS embankments, the magnitude of surcharge decreases with an increase in embankment depth. Therefore, this thesis aims to cover these aspects of soil arching.

1.2 PROBLEM STATEMENT AND RESEARCH OBJECTIVES

In the past, soil arching has been examined under the static loading condition, while a

few studies (Heitz et al. 2008; Han et al. 2015; Pham and Dias 2019; Tang et al. 2020) have reported the dynamic nature of soil arching. However, the effect of moving train-induced load and seismic excitation on soil arching has not been fully investigated yet. Further, there is no method for the accurate evaluation of vertical stress on the crown of soil arching in the existing literature. Thus, it is expected that this thesis will provide insight into the dynamic behaviour of soil arching, and the accurate evaluation of vertical stress on the crown of soil arching which can ensure the better performance of GRPS embankments, especially from a soil arching viewpoint. Figure 1.2 shows a flow chart of objectives with the outcome. There are three issues associated with the stability of GRPS embankments under dynamic loading:

- In GRPS embankments, soil arching is the primary load transfer mechanism and there is scant knowledge in the literature on the dynamic behaviour of soil arching under a moving train.
- The dynamic behaviour of soil is substantially different from static behaviour. This aspect needs to be carefully considered in GRPS embankment design.
- Lateral earthquake excitations are usually high in earthquake-prone areas depending on the ground motion characteristics of the site. An insight into soil arching under seismic excitation is required to properly design a GRPS embankment.

Consequently, the major objectives of this thesis are as follows:

- To examine soil arching mobilisation under the equivalent dynamic load induced by a moving train using the finite element method (FEM).
- To develop analytical methods in both 2D and 3D conditions considering accurate evaluation of vertical stress on the soil arching crown.
- To investigate the dynamic behaviour of soil arching under a moving train and

seismic excitation using FEM.

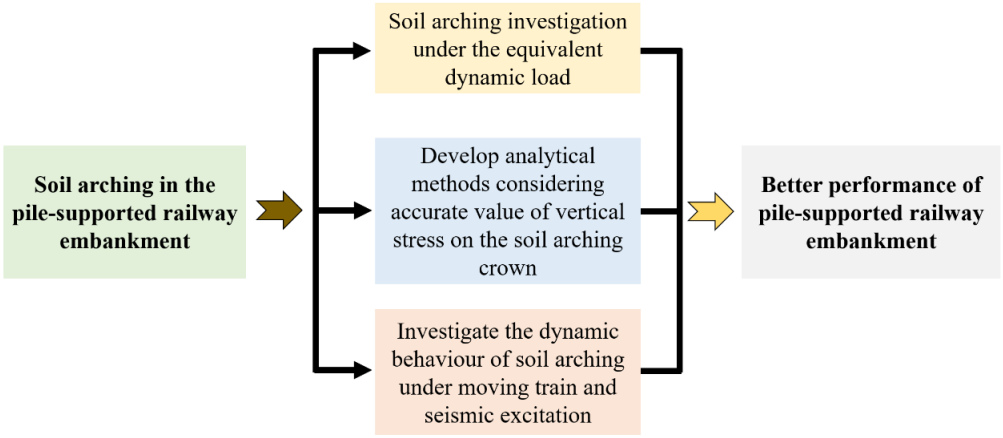

Figure 1.2: A flow chart of the research objectives and the outcome

Firstly, the equivalent dynamic load induced by a moving train is considered to achieve the first objective of this thesis. The equivalent dynamic load is equal to the weight of the train multiplied by an impact factor (i.e., dynamic amplification factor), which accounts for the dynamic effects due to the moving train (Doyle NF. 1980; Esveld, C. 2001).

An analytical approach is used to accomplish the second objective of this thesis. Based on Low et al.'s (1994) analytical model, a two-dimensional (2D) theoretical method of soil arching in a GRPS railway embankment is presented. Further, the 2D theoretical method is extended to a three-dimensional (3D) condition following Zhuang et al.'s (2014) method.

Subsequently, a moving train load is considered at the embankment top to assess the dynamic behaviour of soil arching under a moving train. In addition, seismic excitation is applied at the base of the numerical modelling to see the soil arching nature under an earthquake condition. These both accomplish the third objective of this thesis.

Overall, this thesis aims to identify critical parameters of the pile-supported railway embankment for soil arching mobilisation. Subsequently, the effect of moving train and seismic excitation on the soil arching is investigated which demonstrates the practical importance to this thesis.

1.3 LIMITATIONS OF THIS THESIS

The research work, presented in this thesis has the following limitations which can be incorporated in future work:

- In this thesis, a unit cell, situated in the centre of a pile-supported railway embankment, is considered to investigate the soil arching. In addition, a single rail track is taken on the embankment top.
- The subsoil profile is taken homogeneous thought-out the depth. However, in reality, the subsoil properties can be varied with respect to depth.
- In the 2D idealization of piles, only the elastic pile response could be captured, and this idealization works for vertical + static loading conditions. However, piles may be subjected to plastic deformation due to lateral loading for seismic loading conditions.
- Influence of the excess pore water pressure is neglected, which can affect the soil arching.
- Numerical simulation is conducted under the two-dimensional (2D) plane strain condition using some 3D to 2D conversion methods. Whereas, the pile-supported embankments are a three-dimensional (3D) problem.

1.4 THESIS OUTLINE

This thesis is organised into eight chapters. The current chapter presents a brief

introduction, the problem statement, and the objectives related to this research. It also includes the outline of this thesis.

Chapter 2 includes a comprehensive review of the existing literature regarding soil arching in GRPS embankments along with the possible research gaps. It starts with an introductory background of GRPS embankments and soil arching for the readers' convenience. Further, it consists of an in-depth review of the past studies and their outcomes followed by identifying the research gaps which will be addressed in this thesis.

In chapter 3, a series of numerical analyses in two-dimensional (2D) plane strain conditions are carried out to investigate soil arching in a railway embankment. Primarily, it is focused on the visualisation of soil arching in a pile-supported railway embankment. Subsequently, the key parameters of pile-supported embankments and their optimum value are identified which help the effective mobilisation of soil arching against the equivalent dynamic loading in both unreinforced and reinforced conditions. The equivalent dynamic load is equal to the weight of the train multiplied by a dynamic amplification factor (DAF), which accounts for the dynamic effects due to the moving train. The effect of a geosynthetic layer is found to be significant for reducing the load on the subsoil and improving the load transfer through the membrane effect. Different analytical methods compared to identify the variation in different methods.

Based on Low et al.'s (1994) analytical model, a 2D theoretical method of soil arching in a pile-supported railway embankment is presented in chapter 4. The proposed method is refined to consider the realistic approximation of vertical stress on the soil arching crown. The proposed method is validated by a field study and a full-scale model test and is found to be in good agreement with reasonable accuracy for both studies. In addition, it is also compared with other design methods such as Guido

el al. (1987), Low et al. (1994) and BS8006 (2010). The results show that the load on the pile top increases with an increase of embankment height and a decrease of pile spacing. The importance of the geosynthetic layer is also investigated. In addition, the effect of an earthquake is also incorporated in this chapter.

Chapter 5 presents a 3D theoretical method of soil arching following Zhuang et al.'s (2014) method. The surcharge on the embankment top is neglected in Zhuang et al. (2014) whereas, in this chapter, a train and track-induced appropriate surcharge value is incorporated. The results reveal that the failure of soil arching at the pile top is critical in the 3D condition, whereas the soil arching crown is normative in the 2D plane strain condition. The geosynthetic layer and compression modulus of subsoil significantly contribute to the load transfer mechanism, and the geosynthetic layer plays a crucial role in large pile spacing and very compressive subsoil.

Chapter 6 incorporates a series of 2D numerical analyses to investigate the effect of seismic excitation on soil arching. Different aspects of soil arching and the most sensitive parameters of the pile-supported embankment, which are identified in the numerical simulation of Chapter 3, are assessed under an earthquake condition. The computational results include the vertical stress and settlement on subsoil and pile top during the earthquake. Results show that the vertical stress on subsoil significantly reduces with an increase of friction angle resulting in the settlement also reduces and the load transfer mechanism being significantly improved. The effect of a geosynthetic layer resting at the base of the embankment is also investigated.

The Dynamic behaviour of soil arching under a moving train in the 2D plane strain condition is numerically investigated in chapter 7. The moving train load is validated against the existing literature which served as the basis of further analysis. Results revealed that moving train load significantly affected soil arching. The

dynamic nature of soil arching is different from the static condition.

The last chapter, Chapter 8, details the conclusions of this thesis and suggests future research directions.

CHAPTER 2

LITERATURE REVIEW

This chapter covers the existing literature and research gap associated with the current study. It primarily provides essential background regarding this research study. The chapter begins with a fundamental concept of pile-supported embankments. Subsequently, load transfer mechanisms including soil arching are reviewed in detail. Finally, the chapter concludes with a discussion of the research gaps which will be addressed in this research study.

2.1 PILE-SUPPORTED EMBANKMENTS

In the past few decades, the exponential growth in urbanisation has increased the global demand for transportation and transit systems such as highways, railways, and airports (Aqoub et al. 2020). To meet this huge demand for transportation infrastructures, construction activities have rapidly expanded. Consequently, the number of road vehicles, trains and aircraft have drastically increased, resulting in congestion and air pollution.

In contrast, rail transport is considered environment-friendly, dependable, and suitable for bulk freight and commuters. Therefore, railroad construction is undergoing a significant expansion across the world, such as in Asia (Wang and Chen 2019; Wu et al. 2018; Zhou et al. 2016; Zhuang and Cui 2016), Europe (Briançon and Simon

2017), and Australia (King et al. 2017). These railroads often encounter weak soil with poor engineering characteristics such as high compressibility and low bearing capacity. Subsequently, mud pumping, possible bearing failure, ballast pocket, excessive settlement and instability of the railroad are prime concerns (Wang et al. 2019).

Piles and embankment are increasingly used to enhance the strength of weak soil and elevate the ground level, respectively, for the construction of railroads on these soils. The piles may be floating or end-bearing, which is typically in a rectangular, square or triangular arrangement (as shown in Figure 1.1). Pile-supported embankments (i.e., typical arrangement of piles with an embankment) allow for rapid construction with an overall low cost and small settlement (including total and differential) of the railroad on weak soils (King et al. 2017). A pile-supported embankment is often reinforced with a number of geosynthetic layers at the base of the embankment which is commonly known as a geosynthetic-reinforced pile-supported (GRPS) embankment (Briançon and Simon 2017; Wang and Chen 2019).

2.2. SOIL ARCHING

In the non-geotechnical context, the soil arching phenomenon has been investigated for over a century. Early in the1800s, French military engineers found that a grain silo supported only a certain portion of the total weight of the grains (Feld 1948). Similarly, in the early 1900s, United States engineers observed that the load on top of a buried pipe is lower than the weight of the soil cover during a land drainage project (Marston 1930). As shown in Figure 2.1, Terzaghi (1936) established some empirical relations for tunnel support loading using the classical trapdoor test, which is still very useful for the analysis of soil arching in a pile-supported embankment.

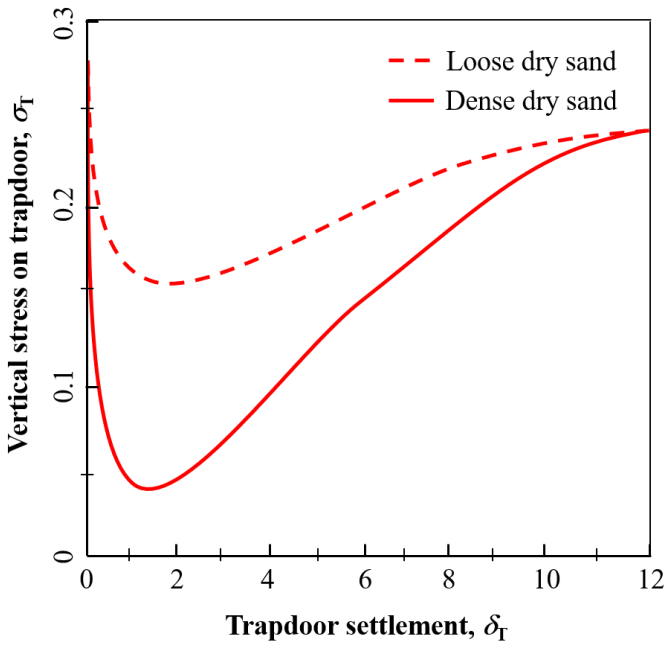

Figure 2.1: Vertical stress-settlement curve (modified from Terzaghi 1936)

Terzaghi (1943) categorised the ground condition into mobilised and stationary parts and defined soil arching based on the stress distribution on these parts. The stress transfer from the mobilised to stationary parts through the development of shear stress at the interface of both portions is defined as soil arching. Based on the relative movement of the mobilised portion, the nature of soil arching is categorised as positive or negative soil arching (Han et al. 2017). Figure 2.2 shows a schematic diagram of positive and negative soil arching. When the mobilised part moves downward relative to the stationary part, the shear stress is projected upward in the overburdened soil, resulting in a reduction of stress on the mobilised part and an increase of stress on the stationary part. This is referred to as positive soil arching. In contrast, the stress on the mobilised part increases and the stress on the stationary part decreases, which is referred to as negative soil arching.

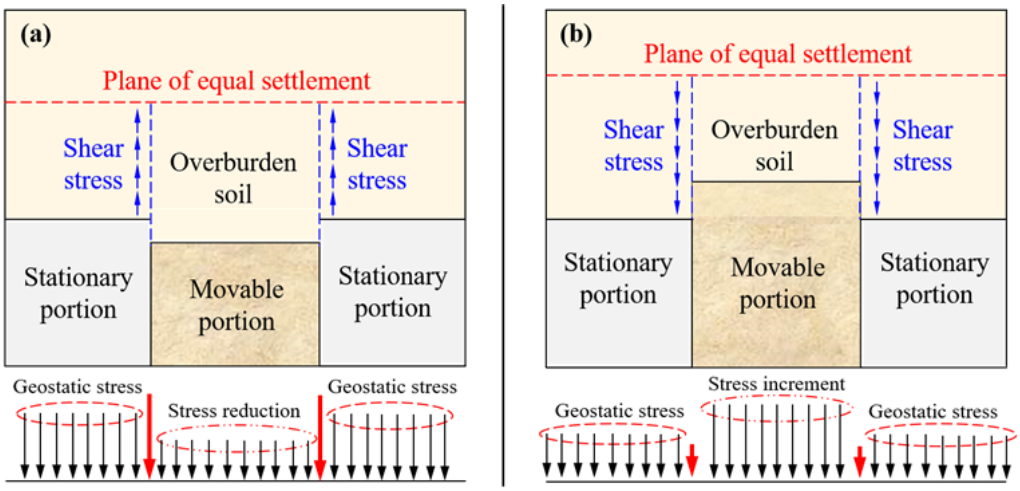

Figure 2.2: A typical schematic diagram of (a) positive soil arching, and (b) negative soil arching (modified from Han et al. 2017)

In pile-supported embankments, positive soil arching always occurs, where weak soil and piles indicate the mobilised and stationary parts, respectively. When embankment height is sufficient, an imaginary plane develops above the soil arching zone. Above this plane, the vertical stress in embankment fill follows overburdened stress. Consequently, uniform settlement occurs which is known as the plane of equal settlement. Soil arching is the principal load transfer mechanism in conventional pile-supported embankments. However, Han and Gabr (2002) reported that in GRPS embankments, the load transfer mechanism is classified into three mechanisms: the soil arching effect, the tensioned membrane effect in the geosynthetic layer and stress concentration due to the stiffness difference between the piles and the adjacent weak soil.

2.2.1 Soil arching terminologies

In the literature, the load transfer mechanism and settlement behaviour of the GRPS embankments are described using different terminologies which are briefly discussed here.

2.2.1.1 Stress concentration ratio (*SCR*):

The stress concentration ratio (*SCR*) evaluates the stress transfer to pile top through the soil arching. It is defined as the ratio of stress on pile (σ_p) to subsoil top (σ_s) in unreinforced pile-supported embankments, as shown in Equation 2.1, whereas in GRPS embankments, the stress on the subsoil (σ_s) is substituted by the stress on the top geosynthetic layer (σ_{geo}).

$$SCR = \frac{\sigma_p}{\sigma_s} \quad (2.1)$$

SCR = 1 implies no soil arching (i.e., load transfer effect does not occur in the embankment fill; $\sigma_p = \sigma_s$), whereas a higher *SCR* refers to the mobilisation of soil arching. Several researchers (Han and Gabr 2002; Yun-Min et al. 2008; Abusharar et al. 2009) used it to assess the soil arching in pile-supported embankments.

2.2.1.2 Soil arching ratio (*SAR*):

The degree of stress transfer is measured by the soil arching ratio (*SAR*). In an unreinforced case, it is defined as the ratio of stress on subsoil top (σ_s) to geostatic stress on the subsoil top including surcharge magnitude on the subsoil top ($\gamma h + q$) as shown in Equation 2.2, whereas in GRPS embankments, the stress on the subsoil (σ_s) is substituted by the stress on the top of geosynthetic layer (σ_{geo}).

$$SAR = \frac{\sigma_s}{(\gamma h + q)} \quad (2.2)$$

It varies from 0 to 1. *SAR* = 0 represents the full mobilisation of soil arching (i.e., the

entire embankment load is transferred to the pile top). In contrast, *SAR* = 1 denotes no soil arching, implying the stress applied to the subsoil or top of the geosynthetic layer is equal to the overburdened stress including surcharge. Several studies (Low et al. 1994; Liu et al. 2007; Nunez et al. 2013; Zhuang et al. 2014; Rowe and Liu 2015; Han et al. 2017; Rui et al. 2019; Sen et al. 2020; Zhang et al. 2021) reported this terminology to assess soil arching in pile-supported embankments.

2.2.1.3 Stress efficacy on the pile top (E_{str}):

The percentage of total embankment weight that is transferred to the pile top is known as stress efficacy (E_{str}).

$$E_{\mathrm{str}} = \frac{Q}{A(\gamma h)} \tag{2.3}$$

where Q is the total force carried by the pile and A is the effective surface area of a pile. Past studies (Hewlett and Randolph 1988; Jenck et al. 2009; Nunez et al. 2013; Van Eekelen et al. 2013; Lee et al. 2020; Brzeziński and Michalowski 2021) have reported this terminology to evaluate the load transfer in pile-supported embankments. In addition, Nunez et al. (2013) reported settlement efficacy (E_{set}) to assess the overall performance of the pile-supported embankment. Settlement efficacy (E_{set}) is defined as:

$$E_{\mathrm{set}} = 1 - \frac{\delta_p}{\delta} \tag{2.4}$$

where δ_p and δ are the soil settlement with and without piles, respectively.

2.2.2 Theoretical evaluation of soil arching in GRPS embankments

Although the word "*arching*" is used to define soil arching, any physical arch inside the embankment between the piles does not exist in reality. Over time, many theoretical models have been proposed to evaluate load transfer through soil arching and the membrane effect of reinforcement, resulting in a reduction of load on the subsoil.

These models are based on various assumptions and assume different failure planes. There are three families of soil arching models, frictional, limit equilibrium, and rigid arch models (Van Eekelen et al. 2013; Rui el al. 2018) which are described in Table 2.1. A schematic diagram of these models is shown in Figure 2.3.

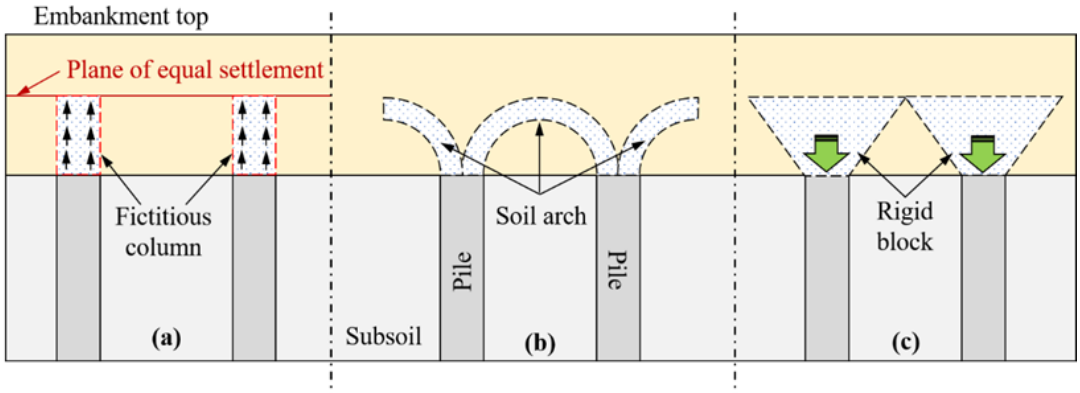

Figure 2.3: A typical schematic diagram of soil arching theoretical model families: (a) Frictional models; (b) Limit equilibrium models; (c) Rigid arch models (modified from Rui el al. 2018)

Table 2.1: Elementary model of soil arching

Model category	Description	Design guidelines that based on these model
Rigid arch models	The shape of failure plane is assumed triangular. Above this plane, the load including overburden and surcharge is directly transferred to the pile top. These models neglected the mechanical characteristics of embankment material.	Nordic Guidelines for Reinforced Soil and Fills (NGG 2005)
Limit equilibrium models	It is assumed that an arch of failure plane with a certain thickness develop between adjacent piles, where the major and minor principle stresses aligned in the tangential and radial direction, respectively. Hewlett and Randolph (1988) and Zaeske's (2001) models are widely adopted for design recommendation of GRPS embankments.	***i.*** Hewlett and Randolph (1988) model adopted in French ASIRI guideline (2012) and British Standards Institution (BSI) as BS8006 (BSI 2010). ***ii.*** Zaeske's (2001) model adopted in German standard EBGEO 2011) and the Dutch CUR226 (2016).
Frictional models	It is proposed by Terzaghi (1943) with plane of equal settlement and the failure plane is assumed based on the Mohr-Coulomb (MC) failure criterion. Russell and Pierpoint (1997) made a refinement incorporating the three-dimensional geometry of GRPS embankments in the Terzaghi (1943) model. Filz et al. (2012) further extended it by including the critical embankment height and reported that soil arching mobilises underneath this height.	-

2.2.3 Ground reaction curve (*GRC*)

Iglesia et al. (1999) proposed a novel method to evaluate the vertical loading on an underground structure in granular soils using trapdoor tests with some early soil arching theories. They found that soil arching depends on the trapdoor movement and it mobilised from an initial curved shape to a triangular shaper before reaching the ultimate state with two vertical shear planes. The curved shape is similar to Hewlett and Randolph's (1988) model (i.e., semi-circular arch model) whereas the triangular shape follows Guido et al.'s (1987) model, and the ultimate state is similar to Terzaghi (1943) model. Figure 2.4 illustrates the observations of Iglesia et al.'s (1999) novel method. The progressive mobilisation of soil arching is referred to as the ground reaction curve (GRC) and is classified into four stages. A generalised concept of GRC is shown in Figure 2.5.

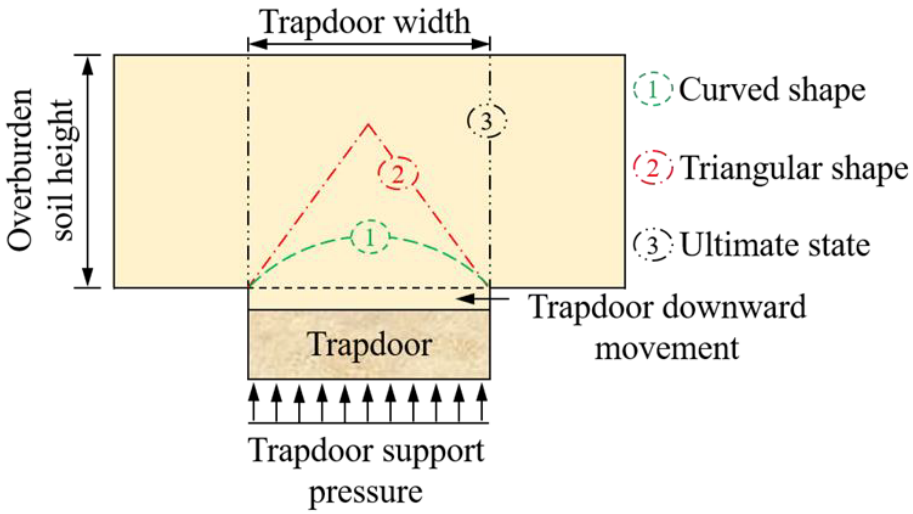

Figure 2.4: Soil arching evolution (modified from Iglesia et al. 1999)

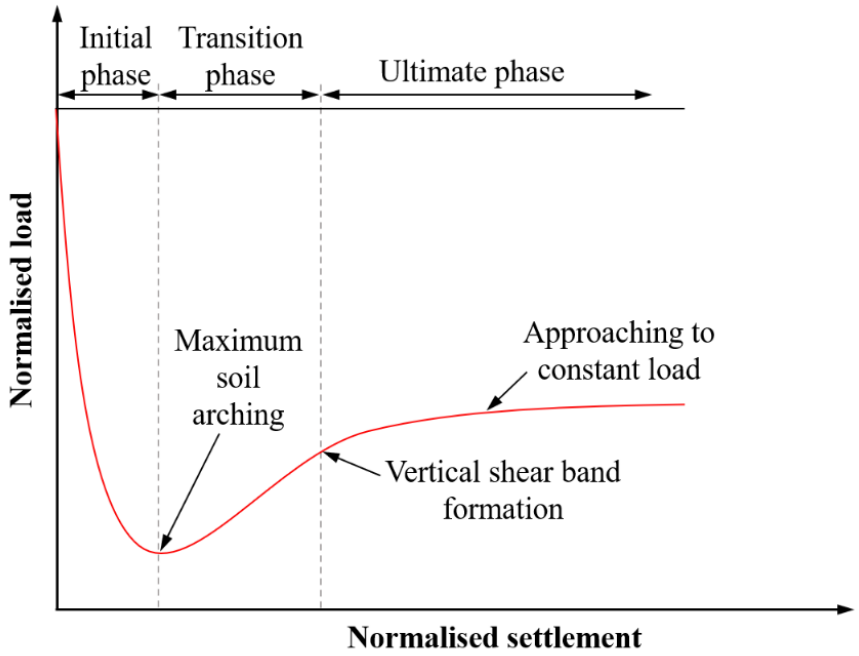

Figure 2.5: General concept of the ground reaction curve

2.2.4 Soil arching investigation in GRPS embankments

Over the past decades, a number of studies (i.e., experimental, numerical and theoretical) have been undertaken to investigate soil arching in GRPS embankments.

2.2.4.1 Experimental investigations

Table 2.2 lists several fields and laboratory-based studies which were performed to gain insight into soil arching in pile-supported embankments.

Table 2.2: Summery of the experimental studies of soil arching in the past years

Past studies	Location	Investigation type	Reinforcement	Observation
Liu et al. (2007)	Shanghai, China	Field study (highway embankment)	Yes	Due to soil arching, stress acting on the pile tops was 14 folds higher than stress acting on the subsoil top located between adjacent piles resulting in excess pore water pressure reduction.
Chen et al. (2010)	Southeast Zhejiang province, China	Field study (highway embankment)	No	***i.*** Three cases are used to investigate the soil arching. ***ii.*** The soil arching height is found to be 1.0-1.5 times of clear pile spacing, and the Y-shape pile significantly improved the load transfer mechanism.
Van Eekelen et al. (2012, part I and II)	Delft, Netherlands	Laboratory model test	Yes	***i.*** A series of twelve model tests are carried out to insight the soil arching. ***ii.*** The load transfer mechanism is categorised into three parts namely load transfer directly on pile top through the soil arching (A), load on pile through the tension in reinforcement (B), and load carried by the subsoil below the reinforcement (C). ***iii.*** From the experimental investigation, the stress on pile and subsoil top, differential settlement and strain in reinforcement are investigated.

Hong et al. (2014)	Western coast, Korea	Field study	No	***i.*** The beam foundation with end-bearing and floating piles is used to support the embankment on soft soil. ***ii.*** It is found that the mobilisation of soil arching is depends on the centre to centre distance between the beam foundation. ***iii.*** The load transfer in both types of pile is similar however the settlement behaviour of floating piles is different from the end-bearing piles which may due the interaction between pile and adjacent subsoil.
Zhang et al. (2016)	Guangxi province, China	Field study (railway embankment)	Yes	***i.*** The progressive load transfer phenomenon is observed during the embankment stage construction resulting in increased load on the pile top through soil arching and tension in the reinforcement layer. ***ii.*** The stress efficacy is found constant after an embankment height of 6 folds pile spacing, and it is affected by area replacement ratio and pile length. ***iii.*** Considering the triangular layout of piles, Hewlett and Randolph (1988) based, a new three-dimensional (3D) theoretical model of soil arching is proposed. The proposed model is in good agreement with the existing model in terms of stress efficacy and tensile force in the reinforcement layer.
Briançon and Simon (2017)	France, Europe	Field study (railway embankment)	Yes	***i.*** The stress efficacy is compared for both unreinforced and reinforced embankment cases and it is found that the reinforcement reduced settlement resulting in improve the load transfer to the pile heads.

Fagundes et al. (2017)	France, Europe	Laboratory test (centrifuge test)	Yes	***i.*** A series of centrifuge tests is performed to assess the load transfer and settlement behaviour of GRPS embankments. ***ii.*** Experimental results show that the load transfer to piles is fully attained through soil arching with membrane behaviour of geosynthetic. Also, stress efficacy in GRPS embankments is influenced by the pile spacing and embankment height, and the higher stiffness of geosynthetic does not affect much. ***iii.*** The differential settlement at the embankment top decreases with a decrease in pile spacing and increase in embankment height. ***iv.*** The observed maximum deflection of geosynthetic layer is in good agreement with BS8006 theoretical solution.
King et al. (2017)	Melbourne, Australia	Field study (railway embankment)	Yes	***i.*** An instrumented GRPS embankment is monitored over a period of two years and time-dependent load transfer phenomena and settlement of subsoil are observed. ***ii.*** At maximum arching condition, the soil arching ratio obtained from the experiment data yields better prediction with existing methods. ***iii.*** The ground reaction curve (GRC) method can be considered to predict the long-term performance of GRPS embankment in view of soil arching. Also, further investigation is required to see the effect of subsoil settlement on the long-term performance of soil arching.

Fonseca and Palmeira (2019)	Brazil, South America	Large-scale laboratory test	Yes	***i.*** The results show the significance of reinforcement on the performance of pile-supported embankments. the settlement of subsoil and strain decrease with an increase in reinforcement stiffness whereas the stress efficacy increases. ***ii.*** Results are in good agreement with the existing methods. The stress efficacy and subsoil settlement are well match with the concentric arches and BS8006 methods.
Rui et al. (2019)	Wuhan, China	Laboratory (two-dimensional multi-trapdoor) test	Yes	***i.*** In unreinforced analogical soil, the settlement contours are confirmed with Rui et al. (2016b) which used sand as fill material. Following patterns are identified: ***Normalised embankment height, $h/(s\text{-}d)$*** — ***Settlement patterns*** $h/(s\text{-}d) < 1.5$ — Triangular expanding pattern (TEP) $h/(s\text{-}d) \geq 1.5$ — Triangular arch (ESP-TA) with an equal settlement pattern $1.5 \leq h/(s\text{-}d) \leq 2.0$ and $(d/s\text{-}d) \leq 3.0$ — Tower-shaped pattern (TDP) ***ii.*** The ESP pattern is found to be more stable than the TEP and TDP patterns. ***iii.*** The settlement contours become concentric elliptical with the inclusion of a geosynthetic above the trapdoor which are similar to concentric arch model in two-dimensional condition.
Khansari and Vollmert (2020)	Hamburg, Germany	Field study (roadway embankment)	Yes	The vertical stress and deflection on the mid-span of geosynthetic reinforcement are overestimated by European design codes such as EBGEO, CUR226 and BS8006-1.

Van Eekelen et al. (2020)	Woerden, Netherlands	Field study (roadway embankment)	Yes	***i.*** The long-term performance of GRPS embankment is monitored. ***ii.*** Support from the subsoil is disappear after a few days however soil arching mobilised over the first three months and a yearly cycle in the load distribution evident. The mobilisation of soil arching becomes more pronounced relatively dry season.

2.2.4.2 Numerical investigations

The physical visualisation of the soil arching phenomenon in GRPS embankments is very complex and usually requires a large setup. In contrast, numerical investigations are able to solve complex problems with reasonable accuracy with less time and cost. Therefore, nowadays, numerical analyses are the unsurpassed approach to investigate soil arching in GRPS embankments.

Several numerical analyses have been undertaken using commercial computational programs, for example fast Lagrangian analysis of continua (FLAC), ABAQUS, PLAXIS, ANSYS, DIANA and particle flow code (PFC) which are based on different methods (i. e., finite element method (FEM), finite differential method (FDM), discrete element method (DEM)). The past numerical studies are briefly described in Table 2.3.

Table 2.3: Summery of the past studies based on numerical simulation

Past studies	Used computational method and software	Modelling type	Presence of reinforcement	Observation
Han and Gabr (2002)	FEM based software FLAC	2D	Yes	***i.*** The three parameters of piled embankment namely embankment height, tensile stiffness of a geosynthetic and elastic modulus of the pile are significantly affected soil arching and the settlement. ***ii.*** Stress concentration ratio (*SCR*) and maximum tension in geosynthetic which occurs near the inner edges of adjacent piles increase with an increase in the embankment height, tensile stiffness of a geosynthetic and elastic modulus of the pile. ***iii.*** Used design method neglected the effect of geosynthetic stiffness and pile modulus on soil arching ratio (*SAR*).
Huang and Han (2009)	FEM based software FLAC	3D	Yes	***i.*** The time-dependant behaviour of GRPS embankment is investigated. ***ii.*** In the GRPS embankment, excess pore water pressure drastically reduces due to the combination of efficient drainage and load transfer.
Zhuang et al. (2012)	FEM based software ABAQUS 3D	3D	No	***i.*** The vertical stress on subsoil is observed at maximum arching condition and found good comparison with Ellis an Aslam (2009a) experimental data. ***ii.*** The height of soil arching is found to be 2.0-2.5 folds clear pile spacing.
Nunez et al. (2013)	FEM based software FLAC	3D	Yes	***i.*** A full-scale experiment is numerically simulated. Results shows that the performance of pile-supported embankment is depends on the soil compressibility and shear resistance. ***ii.*** In the unreinforced case, interaction between subsoil and pile is correctly simulated. In contrast, it does not fit well with monitored

				data in reinforced case. Nevertheless, settlement efficacy is good in agreement.
Lai et al. (2014)	DEM based software PFC	2D	Yes	***i.*** Results show that the strong force network (SN) act as a load-carrying network while (WN) weak force network serves as a support system. ***ii.*** The mobilisation of soil arching occurs in three stages as surcharge increases; initially, the soil arching strengthened gradually. Subsequently, it attained full mobilisation and interact with the "*forming-failure-reforming*" zone with a further increase in surcharge. Further increase in surcharge, soil arching mobilisation jump into the third stage and no stable soil arching occurred in this stage. However, the third stage is not found in GRPS embankments due to the presence of reinforcement. It is also reported that the reinforcement does not change the mobilisation of soil arching from initial to failure stage, although it significantly improves the efficacy and stability of soil arching.

Rowe and Liu (2015)	FEM based software ABAQUS	3D	Yes	Full-scale embankments rested on the soft soil with different ground improvement methods are numerically investigated and the following conclusions are summarised: ***i.*** Settlement at subsoil top is reduced up to 52% by the inclusion of rigid piles compared to untreated section. ***ii.*** Further, the settlement reduces up to 31% by including a single layer reinforcement compared to the untreated section and differential settlement decreases up to 38% compared to piled improved section. ***iii.*** Adding two-layer reinforcement reduced the settlement up to 28% compared to untreated section. Also, it minimises the maximum lateral displacement below the embankment toe among all sections. ***iv.*** the settlement at embankment top is not reported in the filed data however it reduced up to 60%, 41%, and 38% for sections improved with rigid piles, single layer of reinforcement and two layers of reinforcement, respectively compared to untreated section.
Zhuang and Wang (2015)	FEM based software ABAQUS	3D	Yes	***i.*** Three types of elements (isotropic membrane, orthotropic membrane, and truss) are considered to investigate the behaviour of biaxial geogrid and a negligible effect has been found on the subsoil settlement and *SCR*. ***ii.*** Maximum tension in geogrid is reported up to 33% larger for isotropic membrane element compared to the other two elements. ***iii.*** The orthotropic membrane element is compared with four analytical methods of soil arching and it is found that tension in geogrid is overestimated in BS8006 (BSI 2010) and EBGEO (2011) methods whereas Zhuang et al. (2014) is in good agreement.

Yu et al. (2016)	FEM based software FLAC	2D	Yes	***i.*** The lateral displacement of embankment and subsoil is investigated using a modified unit cell with linear elastic springs at vertical boundaries of the unit cell. ***ii.*** A minor difference has been found in the maximum vertical stress and settlement in large and small strain cases for fully fixed vertical boundary condition. While in the case of lateral springs boundary, the lateral displacement of embankment and subsoil has increased the maximum vertical stress and settlement on the subsoil and reinforcement top.
Tran et al. (2019)	FDM based FLAC and DEM based PFC software	3D	No	***i.*** Two methods namely continuum and discrete-element method are used to investigate the shear-strength degradation of embankment fill material. For dense material, degradation of shear strength is obvious in the DEM method due to high friction angle and low porosity. While a cap-yield constitutive model improved with friction softening in continuum method. ***ii.*** For loose material, the soil arching does not visible in the continuum method because it is not able to capture the evolution of porosity.

Zhang et al. (2019)	FEM based software ABAQUS	2D and 3D	Yes	***i.*** The maximum deflection and strain in geosynthetic are overestimated in 2D compared to 3D condition corresponding to the modulus of subsoil reaction, the layout of pile arrangement and presence of gravel bed. ***ii.*** The maximum deflection and strain in geosynthetic decrease up to a constant value with an increase in modulus of subsoil reaction. A smooth pile top such as square shape with smooth corners or circular top, triangular pattern of pile layout compared to square pattern and inclusion of gravel bed significantly reduce the maximum strain in geosynthetic.
Lee et al. (2020)	FEM based software ABAQUS	3D	Yes	***i.*** The load distribution mechanism component, soil arching varies with modulus of subsoil (E_s), embankment height, pile spacing and applied surcharge on the embankment top. The maximum soil arching seen at E_s = 2000 kPa with embankment fill friction angle of 33°. The stress efficacy is in good agreement with concentric arch (CA) model at E_s < 2000 kPa. ***ii.*** The size and shape of soil arching reduce with an increase in E_s and the degree of stress efficacy differs with variation in the geometric configuration. The inclusion of a geosynthetic layer supports maximum efficacy and stable soil arching. ***iii.*** The load distribution mechanism component, combined with subsoil support and membrane effect in geosynthetic identifies differently from the CA model because it is assumed in the CA model that load transfer from these combined components is exerted on geosynthetic reinforcement only.

Ye et al. (2020)	FEM based software ABAQUS	3D	Yes	i. A 3D soil arching model is proposed considering the triangular arrangement of piles which consist of a lower and upper soil arch. The lower and upper soil arch appear a semi-circular shell and a semi-ellipsoid shape, respectively. The height of soil arching is found to be 1.4 times of clear pile spacing. ***ii.*** The inclusion of geosynthetic enhances the load transfer efficiency by increasing the load on the pile top. Also, the maximum strain in geosynthetic occurs at the edges of two adjacent pile top.
George and Dasaka (2021)	FEM based software PLAXIS	3D	No	***i.*** A trapdoor test is numerically simulated and found that the mobilisation of soil arching is more evident in Hardening Soil constitutive model compared to Mohr-Coulomb model. ***ii.*** The soil arching zone increases with an increase in normalised embankment height. Results reveals that the soil arching zone 1-1.5 folds of embankment height.

Of the available commercial software, the FEM-based ABAQUS is capable of simulating a wide range of simple linear to complicated nonlinear problems. Also, several types of elements are included in the ABAQUS library to ensure it can model any geometry. Different material constitutive models are available, which permits to easy behaviour of materials. It can solve a problem in two-dimensional (2D), axisymmetric, and three-dimensional (3D) conditions. In the nonlinear analysis, appropriate load increments and convergence tolerances can automatically be chosen. This thesis proposes a complex model of a GRPS railway embankment which will be struck by a moving train-induced load and earthquake. The ABAQUS is capable of simulating this kind of complexity with reasonable accuracy. Thus, this software package is more appropriate for this research study.

Two-dimensional (2D) idealisation

Typically, pile-supported embankments are a three-dimensional (3D) problem. However, 3D modelling is complex, time-consuming and needs advanced computing facilities. Therefore, two-dimensional (2D) plane strain modelling is used with reasonable accuracy in practice to overcome these problems (Zhang et al. 2014; Wu et al. 2019). Various approaches such as equivalent area (EA), area replacement ratio (ARR), equivalent flexural stiffness (EFS) and equivalent elastic modulus (EEM) of piles are used to transform a 3D problem to a 2D problem. In these methods, the pile arrangement is assumed to be in a square pattern (i.e., s_x and $s_y = s$).

In the EA method, the area replacement ratio of the pile to surrounding soil is kept the same in both 3D and 2D conditions. The area replacement ratio is defined as the ratio of the cross-sectional area to effective surface area of a single pile as shown in Equation 2.4, whereas in the other methods, the pile wall thickness is kept the same

with equivalent elastic modulus considering the normal and flexural stiffness of pile. Different methods have different formulas to evaluate the equivalent elastic modulus of the pile (Equations 2.5 to 2.7). The principle of the EA method to convert a pile diameter into the equivalent wall is illustrated in Figure 2.6.

$$\frac{A_{\mathrm{p}}}{A_{\mathrm{ef}}} = d\left(\frac{1}{s_{\mathrm{x}}}\right) \tag{2.4}$$

Equivalent elastic modulus (EEM) method:

$$E_{\mathrm{eq}} = E_{\mathrm{pile}}\left(\frac{A_{\mathrm{p}}}{A_{\mathrm{ef}}}\right) + E_{\mathrm{sub}}\left(1 - \frac{A_{\mathrm{p}}}{A_{\mathrm{ef}}}\right) \tag{2.5}$$

Equivalent flexural stiffness (EFS) method:

$$E_{\mathrm{eq}}\, A_{\mathrm{wall}} = E_{\mathrm{pile}} A_{\mathrm{pile}} + E_{\mathrm{sub}}\left(A_{\mathrm{wall}} - A_{\mathrm{pile}}\right) \tag{2.6}$$

Area replacement ratio (ARR) method:

$$E_{\mathrm{eq}}\, I_{\mathrm{wall}} = E_{\mathrm{pile}} I_{\mathrm{pile}} + E_{\mathrm{sub}} I_{\mathrm{sub}} \tag{2.7}$$

where, A_{p}, A_{ef}, A_{wall} are the cross-sectional area of a pile, the effective surface area of a single pile, and the area of the pile wall, respectively; E_{eq}, E_{p}, E_{sub} are the equivalent elastic modulus of a pile, the elastic modulus of a pile and subsoil, respectively; d is the width of the pile wall; s_{x} is the pile spacing in x-axis; I_{wall}, I_{pile}, I_{sub} are the second moment of the area of a pile wall, pile and subsoil, respectively.

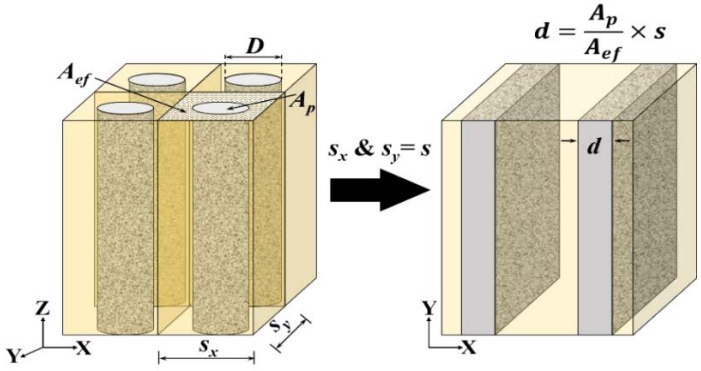

Figure 2.6: Illustration of the principle of the EA method (modified from Zhang et al. 2014)

2.2.4.3 Theoretical investigations

Based on the existing theoretical models of soil arching, many analytical investigations have been conducted. Chen et al. (2008) reported a theoretical solution for unreinforced pile-supported embankments based on the one-dimensional compression of subsoil. The stress concentration on the pile top, the settlement of the embankment and axial load and skin friction along the piles are investigated and compared with FEM results. It is found that the prediction of the proposed method is in good agreement with the FEM results. Abusharar et al. (2009) improved Low et al. (1994) analytical method including the surcharge on the embankment top. However, the magnitude of the surcharge is always taken constant on the soil arching crown. It is found that the inclusion of the geosynthetic layer increases the load transfer capacity to the pile top through the membrane effect. Also, a comparison of the existing methods shows that Low et al.'s (1994) method is in good agreement. However, vertical stress on the geosynthetic layer is found to be lower compared to BS8006 (1995) and Guido et al. (1987). Van Eekelen et al. (2013) proposed a new analytical model named "*concentric arch*" which is based on the limit-state equilibrium model category. It is found that the proposed model can predict the monitored soil arching

better than the other existing methods, especially for a relatively low embankment height. The contribution of a geosynthetic layer is also identified and the inclusion of the geosynthetic layer significantly improved the load transfer mechanism. Based on Hewlett and Randolph's (1988) method, Zhuang et al. (2014) presented a simplified 3D method for granular material. The failure mechanism of soil arching is considered at the crown and pile top. It is found that subsoil and reinforcement play a crucial role in the load transfer mechanism. However, the surcharge on the embankment top is not considered which can lead to further research.

2.2.5 GRPS embankment characteristics affecting soil arching

Over the past few decades, several parameters of pile-supported embankment have been assessed to see their influence on soil arching. Some common parameters of GRPS embankments such as embankment height, pile spacing embankment and pile modulus and the geosynthetic layer are reviewed here. In addition, the nature of the surcharge which is imposed on the embankment top is also reviewed.

2.2.5.1 GRPS embankment geometry and material parameters

Han and Gabr (2002) reported that the stress concentration ratio (*SCR*) increases with an increase of up to a certain embankment height. Also, a higher *SCR* is found in the reinforced case compared to the unreinforced. A similar observation is reported elsewhere in the literature. Jenck et al. (2009) investigated soil arching in a granular embankment under the static loading condition using numerical analysis. They found that stress efficacy increases with an increase in embankment height. However, after a certain embankment height (i.e., 3 m to 5 m), it remains constant (Rowe and Liu 2015). The same observation is reported elsewhere in the literature (Chen et al. 2010; van

Eekelen et al. 2012; Nunez et al. 2013). This implies that the tendency of stress transfer and soil arching increases with an increase of embankment height by up to a specific height which can be the optimum embankment height (i.e., 1.4 to 2.5 times of clear pile spacing (*s*-*d*)), for soil arching (Lu and Miao 2015; Yang et al. 2019). Bhasi and Rajagopal (2013) investigated various parameters such as the embankment fill properties, the stiffness of the geosynthetic layer and the modulus of the pile on the time-dependent behaviour of GRPS embankments. They found that stress efficacy increases with an increase in the friction angle, pile modulus and stiffness of the geosynthetic layer. Zhuang and Wang (2015) numerically studied the 3D behaviour of the biaxial geogrid in a GRPS embankment and reported that tension in the geogrid layer increases with an increase in the embankment height and pile spacing, the tensile stiffness of the geogrid and the compression modulus of the subsoil. Zhou et al. (2016) reported that earth pressure on the pile top increases with an increase of embankment height. Zhang et al. (2019) reported that maximum strain and deflection in the geosynthetic layer decreases by up to a constant value with an increase of the modulus of the subsoil reaction. This implies that the subsoil plays a crucial role in the load transfer mechanism. Lee et al. (2020) performed a series of 3D numerical simulations of a GRPS embankment using a unit cell. The results show that soil arching varies with the material parameters (e.g., friction angle, elastic modulus of embankment fill, which represents the frictional strength and stiffness of the embankment), subsoil stiffness and surcharge imposed on the embankment top. Furthermore, the stain of the geosynthetic layer is concentrated near the pile edges for low stiffness of subsoil. The different patterns of the pile layout are investigated by Ye et al. (2020). The results show that a triangular pattern of pile layout achieves a better performance in terms of soil arching. Also, a geosynthetic layer enhances the efficacy of load transfer on the

pile top through the membrane effect.

2.2.5.2 Nature of the imposed surcharge

Most of the aforementioned studies are conducted under static loading or self-weight of embankment fill, whereas a railway embankment usually interacts with the dynamic nature of loading induced by a moving train. Consequently, the assessment of soil arching in the railway embankment may be different from the static condition. The findings and observations of recent experimental and numerical studies regarding the dynamic behaviour of soil arching are reviewed here.

Heitz et al. (2008) performed a small-scale (1:3) model test to investigate the stress transfer phenomenon in a piled embankment induced by cyclic loading. It is observed that the number of cycles, frequency, amplitude, embankment height to pile spacing ratio (h/s) and geosynthetic layer parameters influence the arching effect. Han and Bhandari (2009) conducted a DEM-based numerical study to investigate soil arching, and geosynthetic layer tension in GRPS embankments under cyclic loading. Han et al. (2014) carried out a model test to investigate soil arching under dynamic loading. The model test results are validated by numerical analysis using ADINA 8.5. The results showed that dynamic loading significantly influenced soil arching in a low-height embankment. The dynamic behaviour of soil arching is classified into two types: soil arching is not mobilised in a dynamic load if the embankment height to diameter of the opening hole ratio (h/D) is less than 3. In contrast, if this ratio is greater than 3, soil arching is mobilised. Zhuang and Li (2015) investigated the dynamic behaviour of soil arching using FEM-based ABAQUS software. A sine wave is applied at the embankment top to replicate dynamic loading and they found that the embankment settlement and vertical stress on the subsoil increases with an increase in

the dynamic loading. The dynamic loading increased the maximum passive earth pressure for the embankment by up to 30% compared to static loading. The simple constitutive model Mohr-Coulomb (MC) is used for embankment fill which cannot capture the dynamic behaviour of soil. Lehn et al. (2016) simulated a GRPS embankment under quasi-static cyclic loading using PLAXIS 3D and compared the outcome with the existing design methods. They found that the shape of soil arching changes under cyclic loading. However, it can be stable. The concentric arches model gives more realistic results in both static and cyclic loading. Zhuang and Wang (2018) modelled a 3D unit cell and simulated soil arching in a pile-supported highway embankment subjected to moving vehicle loads. The results showed that the settlement increases by up to 68% with an increase in pile spacing from 2 to 3 m. Also, the maximum settlement and vertical stress increase by up to 23% and 19%, respectively compared to the static loading condition. Pham and Dias (2019) conducted a 3D FE simulation using ABAQUS to investigate the cyclic behaviour of the load transfer mechanism. An advanced hypoplastic constitutive model is considered for embankment fill which is able to capture the dynamic behaviour of soil. The numerical results show that the hypoplastic model is better than the linear elastic-perfectly plastic model to deal with the decrease in soil arching and cumulative settlements under cyclic loading. Bao et al. (2021) performed a DEM- based numerical 2D trapdoor model test. The results reveal that soil arching tends to degrade during cyclic loading, particularly for a low embankment height.

2.3 EFFECT OF SEISMIC ACTIVITIES ON SOIL ARCHING

In the past, the dynamic behaviour of soil arching has been analysed for the cyclic loading condition representing a train- or vehicular-induced load. Seismic activity also

induced dynamic loading on a pile-supported embankment, and the response of soil arching under the seismic condition may be different from static or traffic-induced dynamic behaviour. Son et al. (2010) analysed the stability of a GRPS embankment under the seismic condition, adopting the classical "*pseudo-static*" approach. However, the behaviour of the load transfer mechanism, including soil arching, has not been investigated. Further, the dynamic behaviour of a pile-supported embankment under the earthquake condition is reported by Zhang et al. (2012). The results were in terms of relative displacement and acceleration of embankment. Thus, there is no study which has investigated the effect of earthquake on soil arching which can significantly affect the performance of pile-supported embankments, especially from a soil arching point of view. Therefore, it is crucial to investigate the dynamic behaviour of soil arching under seismic excitation.

2.4 SUMMARY AND RESEARCH GAPS

This chapter commenced with the background of pile-supported embankments. Subsequently, a comprehensive literature review associated with soil arching in pile-supported embankments including the effect of seismic excitation was presented. Most of the studies are primarily concerned either with *i*) the influence of pile-supported embankment parameters on the load transfer mechanism; or *ii*) the height of soil arching, which is considered static load in the traffic scenario with the pile arrangement in a square pattern, whereas in railway embankments, imposed loading is dynamic in nature, induced by a moving train. Consequently, the assessment of soil arching in railway embankments may be different from the static condition. Several recent experimental and numerical studies (Zhuang and Wang 2018; Wang and Chen 2019; Bi and Huang 2020) focused on the traffic-induced dynamic nature of soil arching. On

the other hand, earthquake severely affects the performance of embankments. Although a few researchers investigated the seismic assessment of embankments, the studies related to soil arching during an earthquake are scarce. Therefore, an in-depth understanding of the traffic and seismic-excitation-induced dynamic nature of soil arching in a pile-supported embankment is crucial. Further, the vertical stress on the soil arching crown in the existing analytical methods is considered only due to the self-weight of the embankment. Moreover, the stress distribution due to additional surcharge is neglected which results in inaccurate predictions. Therefore, the aim of this research is to explore the possible effects of dynamic loading induced by seismic excitation on soil arching in pile-supported railway embankments. The current study also considers the variation of surcharge with depth, which is an improvement over existing methods that disregard this distribution in the analysis.

CHAPTER 3

SOIL ARCHING IN A PILE-SUPPORTED RAILWAY EMBANKMENT: 2D FEM APPROACH

This chapter covers the numerical simulation of a pile-supported railway embankment to investigate the soil arching in details. Primarily, it is focused on the parameters of pile-supported embankment to identify their influence on the size and shape of soil arching and find the most critical parameters with optimum value for effective load transfer against the train induced loading for unreinforced and reinforced case. The comparison of different analytical methods has also been reported to identify the variation and selection of an appropriate method.

3.1 INTRODUCTION

The pile-supported embankments are increasingly being used to support the railway tracks in areas where soft ground is encountered. Numerous numerical studies have investigated the soil arching mechanism in a pile-supported railway embankment (Fagundes et al. 2015). However, these studies have neglected the effect of train speed and associated loading. It is widely acknowledged that the increase in train speed would impose higher stresses on track foundations (Sun et al. 2014; Nimbalkar and Indraratna 2016). In addition, the past studies have considered the arrangement of piles in a square pattern (Han and Gabr 2002; Jenck et al. 2009; Bhasi and Rajagopal 2013).

However, a triangular pattern can be useful for railway embankments (Zhang et al. 2016). Therefore, the effect of train loading and pile arrangement on the performance of pile-supported railway embankment in terms of soil arching are addressed in this Chapter.

In view of these, the finite element (FE) method is used to provide an insight into the behaviour of the railway embankment supported by piles that are arranged in a triangular pattern with particular emphasis on the soil arching mechanism. The present chapter comprises of (*i*) calibration of the numerical model with existing experimental data, (*ii*) comparison of the soil arching mobilisation in embankment supported by piles that are arranged in two different patterns (i.e., square and triangular), (*iii*) comprehensive study focusing on the size and shape of soil arching to investigate the most critical parameters for unreinforced and reinforced cases, and (*iv*) a comparison with the available design methods.

3.1.1 Two-dimensional (2D) idealisation

Typically, pile-supported railway embankment is a 3D problem, and 3D modelling is complex, time-consuming and needs advanced computing facility. Various approaches such as equivalent area (EA), area replacement ratio (ARR), equivalent flexural stiffness (EFS) and equivalent elastic modulus (EEM) of piles are used to convert a 3D problem to 2D. These approaches are earlier explained in chapter 2. As shown in Figure 3.l, the highlighted region of a pile-supported embankment is adopted for 2D approximation. The soil arching is investigated in terms of vertical stress, settlement and lateral stress coefficient above the centre of the subsoil (point A) and piles (point B) top. Point B and B′ represent the same results, thus only point B is used for referring to the soil arching on the pile head in further investigation.

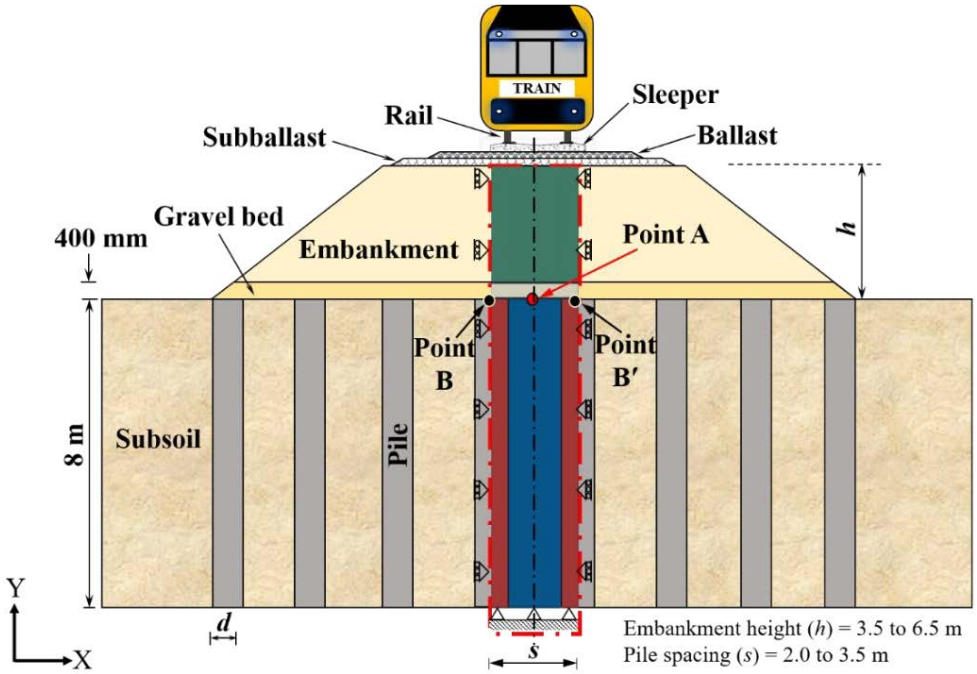

Figure 3.1: Typical pile-supported railway embankment with modelled unit cell

3.2 NUMERICAL MODELLING

3.2.1 Geometric description

The finite element method (FEM) based software, ABAQUS-version 2013 (Abaqus online documentation) is used to simulate a pile-supported railway embankment in a plane strain 2D condition. The modelled unit cell of a pile-supported embankment is highlighted in Figure 3.l. The vertical sides represent the lines which pass through the centre to centre pile spacing (s) and above the embankment fill, including the gravel bed. The 1383 eight-node, reduced-integration, two-dimensional, quadratic (second-order) solid elements (CPE8R) are used in this analysis. The reduced integration uses a lesser number of Gaussian co-ordinates when solving the integral and reduces computational time. Further, second order reduced-integration elements provide more accurate results than the corresponding integrated elements.

Roller supports were used on the vertical boundaries, restricting horizontal movement. The fixed support condition is used for the horizontal bottom boundary to completely restrict displacement. No boundary conditions are considered at the top of the embankment. The bottom boundary represents the base of the piles and subsoil, which is underlain by half-pile wall (width, $d/2$) on both sides and subsoil [width, (s-d)] at the middle of the piles. The pile diameter (D) is fixed at 1.0 m, and the centre to centre pile spacing (s) is 2.0, 2.5 or 3.5 m (i.e., pile width (d) is changing according to the pile spacing). The embankment height (h) varies from 2.5 to 6.5 m, including a 400 mm thick gravel bed at the embankment bottom. The geosynthetic layer is sandwiched in between two layers of the gravel bed. First, a 200 mm thick gravel layer is placed on the pile head and then a layer of geosynthetic layer with 2 mm thickness is laying without any physical damage. Another 200 mm thick gravel layer is placed on the geosynthetic layer top in order to the achieve required thickness of gravel bed (i.e., 400 mm). The depth of the subsoil and length of the pile are the same, both being 8 m. The mesh size of 0.01 m is taken for this study. The effect of boundary conditions and mesh size are not analysed in static loading condition.

The Finite Element Analysis (FEA) is carried out in three steps. First, initial stress and predefined void ratio are established in the subsoil using geostatic step. The rigid pile is activated in the next step, then the embankment including the gravel bed is constructed in the stages. After achieving full embankment height, an equivalent dynamic load of railway track including the moving train load is applied on the embankment top. The implicit iterative procedure with static general analysis is adopted in this chapter.

3.2.2 Material properties

The embankment fill, gravel bed and subsoil are considered as sand fill, well-graded gravel, and silty sand, respectively. A linear elastic perfectly plastic model with Mohr-Coulomb failure criterion is used for the embankment fill and subsoil material. The geosynthetic layer and piles were modelled as linear elastic materials. The stiffness of geosynthetic layer (J) is calculated as:

$$J = E_{geo}.t_{geo} \quad \textbf{(3.1)}$$

where, E_{geo} is elastic modulus and t_{geo} is thickness of geosynthetic layer, in this study J = 1 kN/m is taken for standard case.

In the research studies available in literature, the performance of embankments and subsoil were successfully simulated by the linear elastic-perfectly plastic model with Mohr-Coulomb failure criterion, and reasonable predictions of soil arching were obtained (Huang and Han 2010; Esmaeili and Arbabi 2015; Ye et al. 2020). The unsaturated soil and the corresponding constitutive model were not considered. The soil was assumed to remain in the dry state with facilitation of the fully drained conditions owing to the coarse-grained nature of materials used as the embankment fill and gravel bed. All the parameters used in the analyses are summarised in Table 3.1.

Table 3.1: Material parameters for pile-supported embankment

Material	Unit weight, γ (kN/m^3)	Young's modulus, E (MPa)	Poisson's ratio, v	Cohesion c'(kPa)	Friction angle, ϕ'(degree)	Dilation angle, ψ(degree)
Pile	24	**20 × 10^3** (15 × 10^3 - 30 × 10^3)	0.15	-	-	-
Embankment fill	20	**20** (15 - 30)	0.25	0.1	**30** (30 - 45)	**0** (0 - 15)
Gravel bed	21	25	0.25	0.1	35	5
Subsoil	18.4	10	0.3	8	22	0

Geosynthetic layer (2 % tensile strain)	-	500	0.3

Note: The bold values are for standard case (h = 3.5 m and s = 2.5 m)

3.2.3 Interface

In this study, basic Coulomb friction model was used to simulate the interaction of pile with the surrounding soil (Ye et al. 2020). This model allows the contacting surfaces (i.e., the surface of pile and subsoil) to carry shear stresses before sliding. The surface to surface contact is provided between pile and surrounding soil. The normal contact is considered as "*hard contact*" as it is able to transfer normal stress under compression. The tangential contact is provided as penalty contact with a frictional coefficient at interface between the pile and surrounding soil. The interface frictional coefficient is given by:

$$\mu = \tan \delta_{int} \tag{3.2}$$

where, δ_{int} is the interface friction angle between pile and the surrounding subsoil, and it can be determined as (Potyondy J.G. 1961; Yu et al. 2016; Pham and Dias 2019):

$$\tan \delta_{int} = 0.7 \tan \phi' \tag{3.3}$$

where, ϕ' is the friction angle of the soil. In this study, the ratio of the interface friction coefficient (tan δ_{int}) and the soil friction coefficient (tan ϕ') is assumed to be 0.7 for pile-subsoil interface. Interface friction is considered between the gravel bed and the geosynthetic layer during the analysis, and the interface friction angle is assumed to be the same as the friction angle of gravel (Zhang el al. 2019; Lee et al. 2021). It is reported that coefficient of interface friction typically varies from 0.6 to 1.0. With a value of 0.7 interface friction coefficient, the interface friction angle is the same as the friction angle if gravel.

3.2.4 Model validation

The model validation is performed against the experimental result (settlement above and amid the pile) for pile arrangements in a square pattern with dense sand sample reported by King et al. (2019) to ensure the accuracy of the numerical modelling (refer Figure 3.2). Material properties of the embankment are taken as reported by King et al. (2019), whereas appropriate properties of subsoil have been assumed. For reader understanding, the X-axis represents the settlement of embankment fill which is normalised for general applicability, and embankment height is considered in Y-axis. King et al. (2019) obtained the settlement results for the different increment of normalised settlement plate displacement (δ_{sp}/b'). However, in this study only δ_{sp}/b'= 2.8-4.0% has been considered for validation. Four different idealisation methods as discussed in the chapter 2 are used to convert 3D into 2D plane strain. It is found that the EA method shows an acceptable agreement between numerical modelling and experimental result, which serves the basis of further analysis for this study.

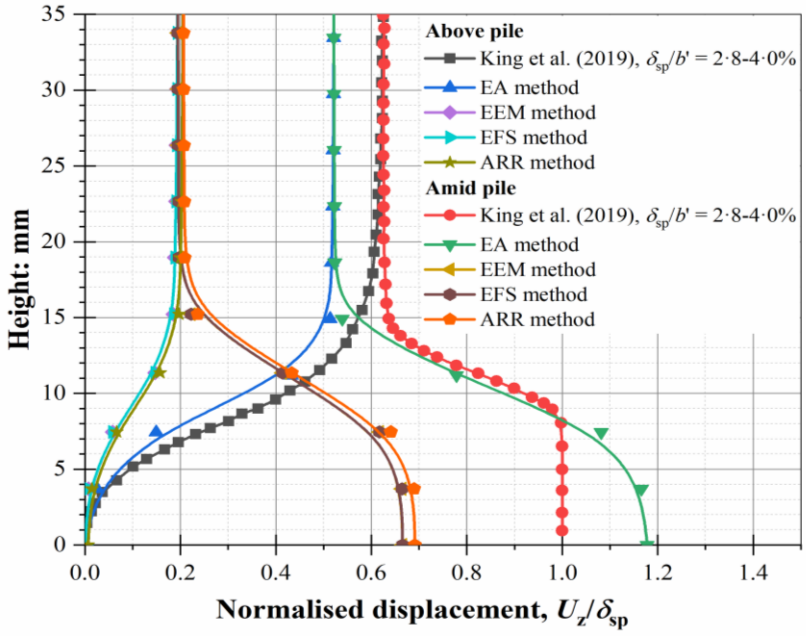

Figure 3.2: Model validation with experimental data reported by King et al. (2019)

3.2.5 Stress determination on the pile-supported embankment

A typical railway track is considered above the pile-supported embankment (as shown in Figure 3.1). In this study, the true dynamic nature of traffic loading and the dynamic response of the soil is not considered. The applied vertical load is equivalent dynamic load. The magnitude of the equivalent dynamic load is equal to the weight of the train multiplied by an impact factor (i.e., dynamic amplification factor), which accounts for the dynamic effects due to the moving train as (Doyle N.F. 1980; Esveld C. 2001; Nimbalkar and Indraratna 2016):

$$F_{\mathrm{d}} = \Phi\, F_{\mathrm{s}} \tag{3.3}$$

where, F_{d} is design wheel load (kN) incorporating dynamic effect, F_{s} is static wheel load (kN), and Φ is dimensionless dynamic impact factor. Various empirical methods such as Eisenmann, American Railways Engineering Association (AREA), and Office of Research and Experiments (ORE) are widely used to calculate dynamic amplification factor (DAF) catering for the effect of train speed. In this study, ORE method is adopted to determine dynamic impact factor as this method is most relevant to Australian conditions. In this method, the DAF is defined in terms of dimensionless speed coefficients as given by following equation:

$$\Phi = 1 + \alpha' + \beta' + \gamma' \tag{3.4}$$

where, α' and β' are associated with mean value of impact factor, and γ' is related to the standard deviation of the impact factor. Details on the calculations of DAF using various methods are provided in Table 3.2.

Table 3.2: Dynamic Amplification Factor (DAF) calculation with different methods

Method	Equation	Train speed, V (km/h)	DAF	Remarks
AREA[1]	$\Phi = 1 + \frac{0.00521 \cdot V}{D_w}$ where, $D_w = 0.97$	40 60 80 100 120 140 160	1.21 1.32 1.43 1.54 1.64 1.75 1.86	D_w is the diameter of wheel (m)
Eisenmann	$\Phi = 1 + \delta\eta t$ where, δ =0.2 (for good track condition); t =1; $\eta = 1$; for V< 60 km/h $\eta = \left(1 + \frac{V-60}{140}\right)$; for $60 \leq V \leq 200$ km/h	40 60 80 100 120 140 160	1.20 1.20 1.23 1.26 1.29 1.31 1.34	δ is a factor that depends on the track condition; t is a factor that depends on the upper confidence limit; η is factor that depends on the speed of the vehicle
ORE[2]	$\Phi = 1 + \alpha' + \beta' + \gamma'$ where, $\alpha' = 0.04\left(\frac{V}{100}\right)^3$; $\beta' = \frac{V^2(2h+h_s)}{127 R_c l_g} - \frac{2h_s h}{l_g^2}$; $\gamma' = \gamma_o \cdot a_o \cdot b_o$; $\gamma_o = 0.1 + 0.017\left(\frac{V}{100}\right)^3$	40 60 80 100 120 140 160	1.30 1.30 1.31 1.33 1.36 1.40 1.45	α' is a coefficient that depends on the track irregularities, train suspension, and speed; β' is a coefficient that accounts for the movement of train along a curve, γ' is a coefficient that depends on the train speed and configuration, and track condition; h_d is the cant/super-elevation deficiency (m), l_g is the gauge width (m), h is the vertical distance from rail top to centre of gravity of train (m), h_s is the super-elevation (m), R_c is the radius of curvature (m), a_o and b_o are the locomotive and track maintenance factors.
Japanese Standard	$\Phi = \left(1 + 0.3 \cdot \frac{V}{100}\right)(1 + C)$ where, $C \approx 0.3$	40 60 80 100 120 140	1.46 1.53 1.61 1.70 1.77 1.84	C is a coefficient

Table 3.2: Cont.

		160	1.92	
British Railways	$\Phi = 1 + \frac{8.784(\theta_1 + \theta_2)V}{P_0}\left(\frac{K_j W_u}{g}\right)^{0.5}$ where, $(\theta_1 + \theta_2) = 0.005$; $K_j = 55$; $W_u = 2.11 \times 9.81$; $g = 9.81$	40 60 80 100 120 140 160	1.20 1.29 1.38 1.48 1.58 1.67 1.77	$(\theta_1 + \theta_2)$ is the total dip angle of the rail joint (radians); K_j is the track stiffness at joint (kN/mm); W_u is the unsprung weight at one wheel (kN); g is the acceleration due to gravity (m/s^2).
Indian Railways	$\Phi = 1 + \frac{V}{58.14(k)^{0.5}}$ where, $k = 60$	40 60 80 100 120 140 160	1.08 1.13 1.18 1.22 1.27 1.31 1.36	k is the track modulus (MPa)
South African formula	$\Phi = 1 + \frac{4.92 \cdot V}{D_{w1}}$ where, $D_{w1} = 970$	40 60 80 100 120 140 160	1.20 1.30 1.40 1.50 1.60 1.71 1.81	D_{w1} is the diameter of wheel (mm)
WMATA[3]	$\Phi = (1 + 0.0001{V_o}^2)^{0.67}$ where, $V_o = V \times 0.621371$	40 60 80 100 120 140 160	1.04 1.09 1.16 1.24 1.34 1.46 1.58	V_o is the speed of train (miles/h)
Chinese Standard (MORPRC, 2009)	$\Phi = 1 + \alpha V$ where, $\alpha = 0.003$	40 60 80 100	1.12 1.18 1.24 1.30	-

Table 3.2: Cont.

		120	1.36	
		140	1.42	
		160	1.48	
German formula	(i) $\Phi = 1 + \frac{V^2}{3\times10^4}$; for $V \leq 100$ km/h	40	1.06	-
		60	1.13	
		80	1.21	
	(ii) $\Phi = 1 + \frac{4.5\,V^2}{10^5} - \frac{1.5\,V^3}{10^7}$; for $V > 100$ km/h	100	1.30	
		120	1.39	
		140	1.47	
		160	1.54	
Australian Standard (AS1085.14, 2012)	$\Phi = 2.5$	-	2.5	This value of Φ may be taken when the data from field investigations is unavailable.

[1]American Railway Engineering Association; [2]Office for Research and Experiments; [3]Washington Metropolitan Area Transit Authority

Various alternatives such as Odemark, Zimmermann, Trapezoidal approximation (2:1), and AREMA exist to calculate the maximum vertical stress on a subgrade (Doyle N.F. 1980). In this study, the maximum vertical stress is calculated by Trapezoidal approximation (2:1) method due to their simplicity. A train speed varying from 40 to 160 km/h is considered. Train-induced vertical stresses (σ_t) corresponding to 40-160 km/h speeds are determined as 105-118 kPa which is applied the top of the modelled unit cell. More details on train-induced vertical stresses are provided in Table 3.3.

Table 3.3: Induced vertical stress on embankment top obtained by Trapezoidal method

Stress calculation method	Impact factor calculation method	Train speed, V (km/h)	Vertical stress on subgrade, σ_t (kPa)
Trapezoidal approximation (2:1 method)	ORE method	40	105
		60	106
		80	107
		100	108
$[\boldsymbol{\sigma_{z\,max}} = \frac{\boldsymbol{Q}}{(\boldsymbol{b}+\hat{h})(\frac{\boldsymbol{l}}{\boldsymbol{3}}+\hat{h})}]$	$[\Phi = 1+\alpha'+\beta'+\gamma']$	120	110
		140	114
		160	118

where, $Q = \sigma_{max}$ (A_{sb}), l is sleeper length (m), α' and β' are related to the mean value of impact factor while γ' is related to the standard deviation of the impact factor.

3.2.6 Effect of pile arrangement on soil arching

Figure 3.3 demonstrates the effect of pile arrangement on the degree of soil arching. The pile arrangement is considered in a square and triangular pattern. Influence of an individual pile is assumed square and hexagonal soil block, when pile arranged in a square and triangular pattern, respectively. As earlier discussed that EA method serves the basis of further analysis, the square block (i.e., piles arranged in a square pattern) is easy to convert into plane strain wall using Equation 2.4. However, the hexagonal block (i.e., pile arranged in a triangular pattern) first converted into a square-shaped block of equivalent area. The width of the equivalent square block is considered as the

pile spacing (s) and converted into plane strain wall. It is evident that pile arranged in a triangular pattern can demonstrate more efficient load transfer mechanism compared to square pattern. Therefore, the pile arrangement in triangular pattern is used for further analysis.

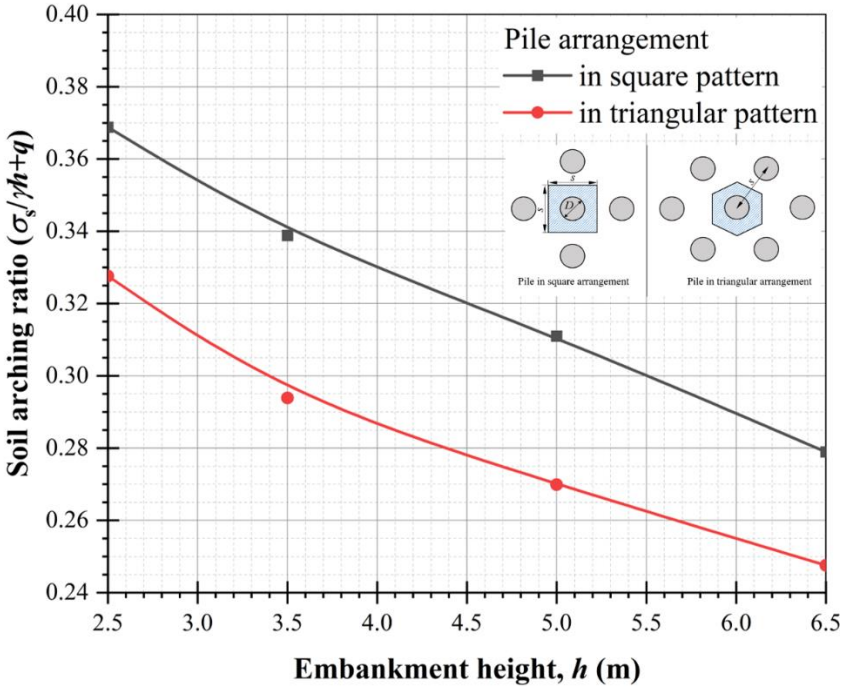

Figure 3.3: Comparison of two different pile arrangements

3.3 RESULTS AND DISCUSSION

This section investigates the soil arching using the same material parameters listed in Table 3.1 for the standard case. However, pile spacing (s) and embankment height (h) vary from 2.0 m to 3.5 m and 2.5 m to 6.5 m, respectively.

3.3.1 Vertical stress

The vertical stress profile in the embankment fill (including the gravel layer) can be used to assess the soil arching phenomenon. Figure 3.4 shows the vertical stress

contours for different embankment heights and pile spacing above point A and point B. Whereas, the effect of geosynthetic layer on vertical stress is shown in Figure 3.5. For the sake of general applicability, the vertical stress (σ_v) is normalised by $\gamma(s\text{-}d)$, whereas the varying embankment height (h) is normalised by clear spacing (s-d).

Figure 3.4(a) shows the vertical stress contours for three embankment height (i.e., 2.5 m, 3.5 m, and 5.0 m) fixed at pile spacing (s) 2.5 m. It is observed that the variation of vertical stress along the normalised embankment height increases on the point B for all considered embankment height and demonstrate the soil arching phenomena. For a specified embankment height (h), the vertical stress initially increases with a gradient equal to overburden stress extending from the embankment fill top to the outer boundary of the soil arch. The stress profile then disturbed (decreases on point A and increase on point B). At this level, the majority of the embankment load is transferred onto the pile. It is worth mentioning that in this study the full soil arching developed with 1.3(s-d) (outer boundary) and 0.25(s-d) (inner boundary) after embankment height (h) = 5 m, which is quite similar to the studies in the past (refer Table 3.4).

Table 3.4: Soil arching height verified by various studies

	Terzaghi (1943)	Bhasi and Rajagopal (2013)	Zhuang et al. ((2010)	Potts and Zdravkovic (2008)	Present study
Normalised length	Void width	(s-d)	(s-d)	Void width	(s-d)
Soil arching height in Plane strain	2-3	2.9	3	3	2.25

Note: All values in meter

Figure 3.4(b) shows the vertical stress contours for a fixed embankment height (h = 3.5 m) varied with three pile spacing (s) (i.e., 2.0 m, 2.5 m, and 3.5 m). For pile

spacing (s) = 2 m, the arching height increases more compared to pile spacing (s) = 2.5 m and 3.5 m, whereas the inner boundary remains the same (i.e., independent of spacing variation). It shows that pile spacing (s) variation affects soil arching (i.e., the arching zone can be increased by reducing s). The arching zone is referred to as the thickness of the soil arch. Due to the expansion of this zone, more load is transferred to the pile.

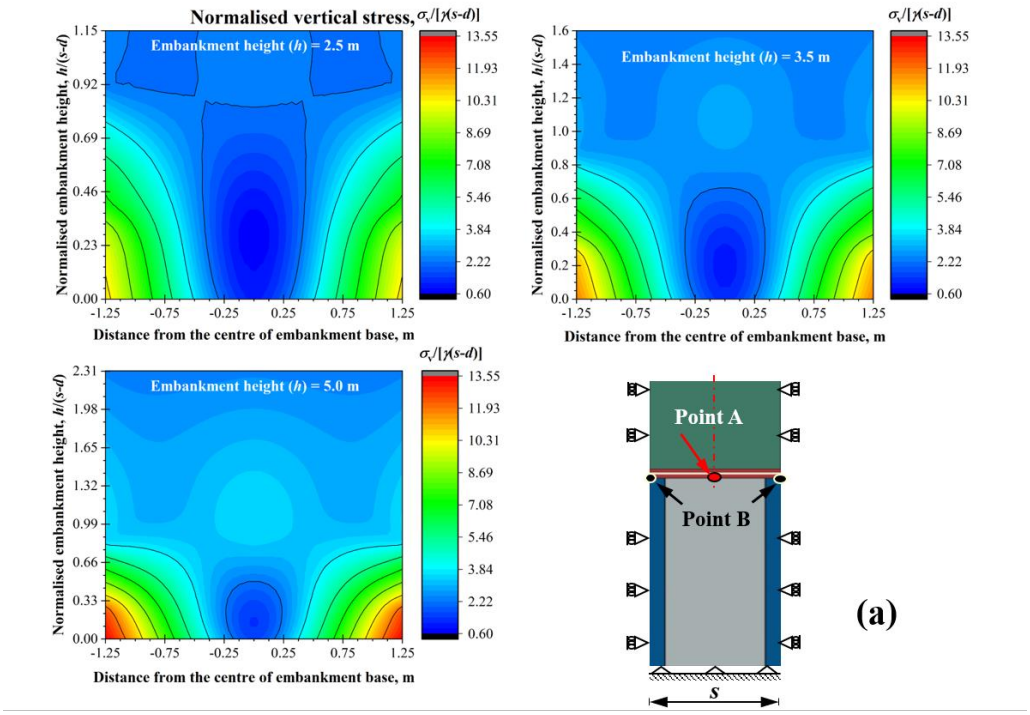

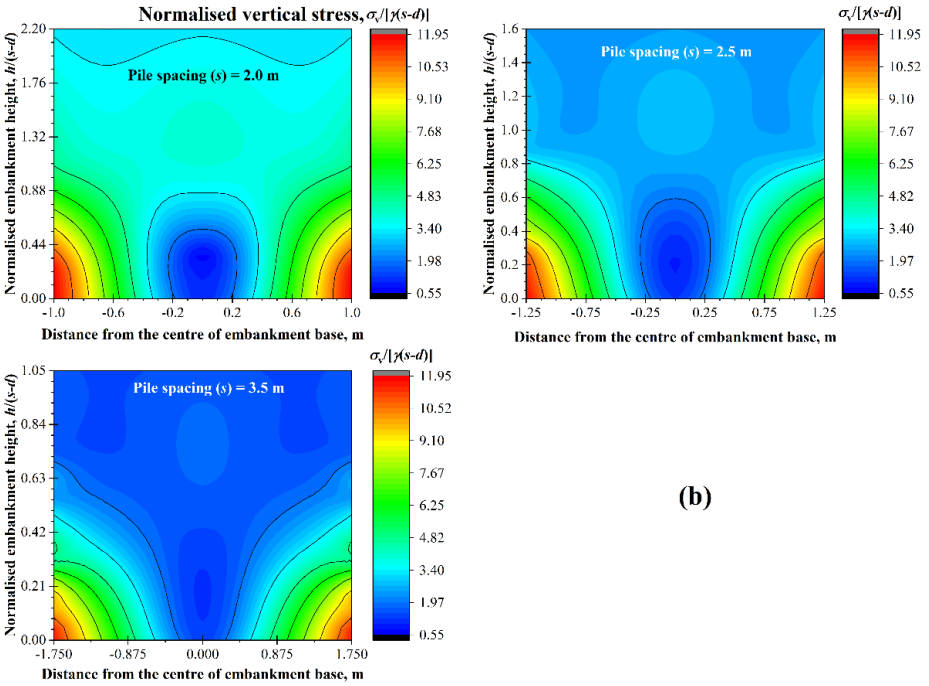

Figure 3.4: Normalised vertical stress contour for varied; (a) embankment height, and (b) pile spacing

Figure 3.5 illustrates the effect of geosynthetic layer on vertical stress for a fixed embankment height (h) and pile spacing (s) of 3.5 m and 2.5 m, respectively above point A (i.e., amid pile) and point B (i.e., above pile). It is evident that normalised vertical stress (N_{vs}) follows the depth-wise linearly increasing trend of geostatic stress from the embankment top to the depth attaining 0.7-fold normalised embankment height (N_{em}) for both (unreinforced and reinforced) cases above point A and point B. This embankment height represents the outer boundary of soil arching. Below this outer boundary above point A, the N_{vs} shows decrease up to the 0.2-fold N_{em} for both unreinforced and reinforced cases, which is represented as the inner boundary of soil arching. The N_{vs} is observed less up to 10% at the base of embankment in reinforced case compared to unreinforced. In contrast, the N_{vs} shows increase below the outer boundary of soil arching above point B. A higher N_{vs} up to 19% is observed at the base of embankment in reinforced case compared to unreinforced. Thus, it

implies that geosynthetic layer can enhance the load transfer on the pile head through the membrane action.

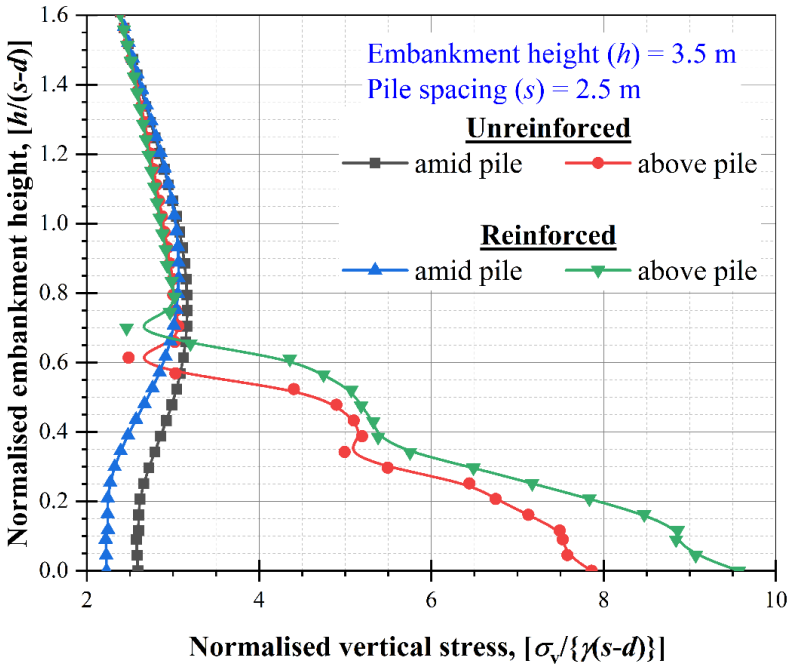

Figure 3.5: Effect of geosynthetic layer on vertical stress in embankment fill

3.3.2 Comparison with Hewlett and Randolph (1988) predictive method

Fagundes et al. (2015) and Zhuang et al. (2010) proposed three failure modes at the maximum arching to compare the observed behaviour with the Hewlett and Randolph method (1988). Figure 3.6 shows the ultimate subsoil stress (σ_s), illustrating the variation in normalised embankment height (h/s). The ultimate subsoil stress is normalised by γs. These three failure mechanisms (i.e., no arching, failure at the crown, and failure at pile head) are shown in Figure 3.6 by dotted (for no arching, and failure at pile head) and solid lines (failure at the crown). The different coloured solid lines show the FE results for different pile spacing (s).

The first mechanism is stipulated for the 'no arching' condition (i.e., $\sigma_s = \gamma h$). In the second mechanism, the failure is based on the limiting conditions at the crown

of the soil arch (failure at the crown). This mechanism indicates vertical stress (σ_s) = 0.5γs which corresponds to the nominal weight beneath the crown of the hemisphere. The third mechanism is related to failure at the pile head or punching the pile head into the base of the embankment. Additional, failure at the crown of the arch in the plane strain condition, as proposed by Low et al. (1994) is shown by the dotted centreline. The results plotted in Figure 3.6 show similar trends with other studies (Fagundes et al. 2015; Zhuang et al. 2010).

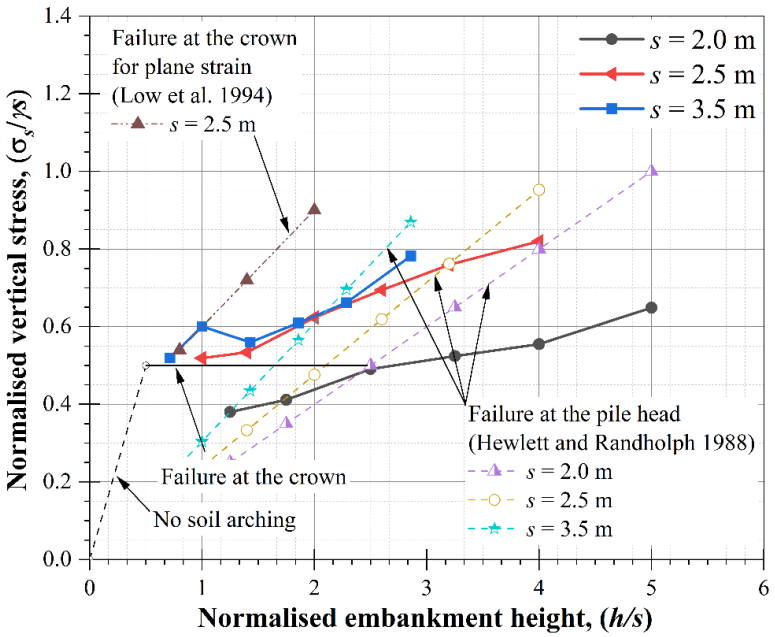

Figure 3.6: Comparison of FE results with Hewlett and Randolph (1988) method: normalised stress on point A (σ_s/ γs) vs. normalised embankment height (h/s)

It is evident that the vertical stress the subsoil (σ_s) is less than 0.5γs (approximately representing the weight of the material below the top of the semicircular arch) up to a critical value of (h/s). At a higher (h/s) value, conditions at the pile head are more critical as also reported by Hewlett and Randolph (1988). However, for plane strain conditions, Hewlett and Randolph (1988) predict that

conditions at the crown of the arch are always critical. Figure 3.6 demonstrates the FE results for failure occurring at the pile cap in terms of a simplified plane strain equation and resembling a three-dimensional failure state for the pile cap, as proposed by Hewlett and Randolph (1988). At the higher embankment height, it shows quite a similar trend of failure. However, the values from the plane strain failure appear to be overestimated for all pile spacing, especially as pile spacing (s) reduces.

3.3.3 Settlement

The settlement of embankment, especially when located on soft soils, is the crucial factor governing the embankment design and construction stages. Soil arching minimises the settlement of the subsoil by load transfer onto the piles.

Figures 3.7 shows the normalised settlement contours for the embankment on the vertical side through point A and point B (refer Figure 3.1). Figures 3.7(a) and 3.7(b) show the settlement contour for varied embankment height (h) and pile spacing (s), respectively. The embankment height (h) and settlement were normalised by the clear spacing between the adjacent pile head (s-d).

The differential settlement of the fill material above the pile head generates shear stresses that extend upward into the fill material. When the embankment is sufficiently high, it is assumed that the shearing force terminates at some horizontal plane: this plane is termed the plane of equal settlement. Above this plane, no differential settlement occurs, indicating that the vertical stress above this plane is not disturbed. However, below this plane, the embankment settlement over point A increases to a maximum value, while it reduces to almost zero over point B. It implies that the soil arching exists below the plane of equal settlement due to the differential settlement of the embankment fill over point A and point B.

As shown in Figure 3.7(a), after a certain embankment height (5 m for this study) there is no differential settlement (i.e., the existence of plane of equal settlement). It is observed that the plane of equal settlement is located at the normalised embankment height of 1.75 (i.e., h = 3.78 m) and soil arching develops under this height. It is worth noting that the settlement on point A increases with an increase in embankment height (h). In addition, Figure 3.7(b) shows that the settlement contour for different pile spacing. It is observed that settlement increases with an increase in pile spacing (s). For pile spacing (s) = 2 and 2.5 m, the plane of equal settlement occurs corresponding to the normalised height of 1.34 and 1.6, respectively. However, no plane exists for pile spacing (s) = 3.5 m owing to the non-formation of soil arching.

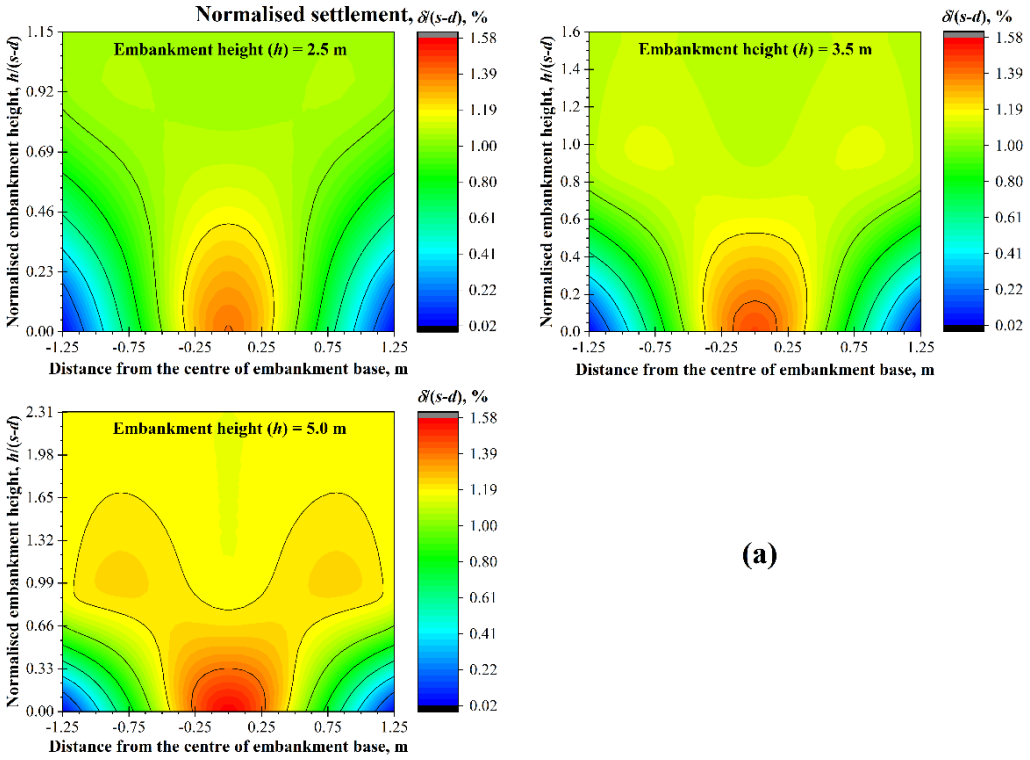

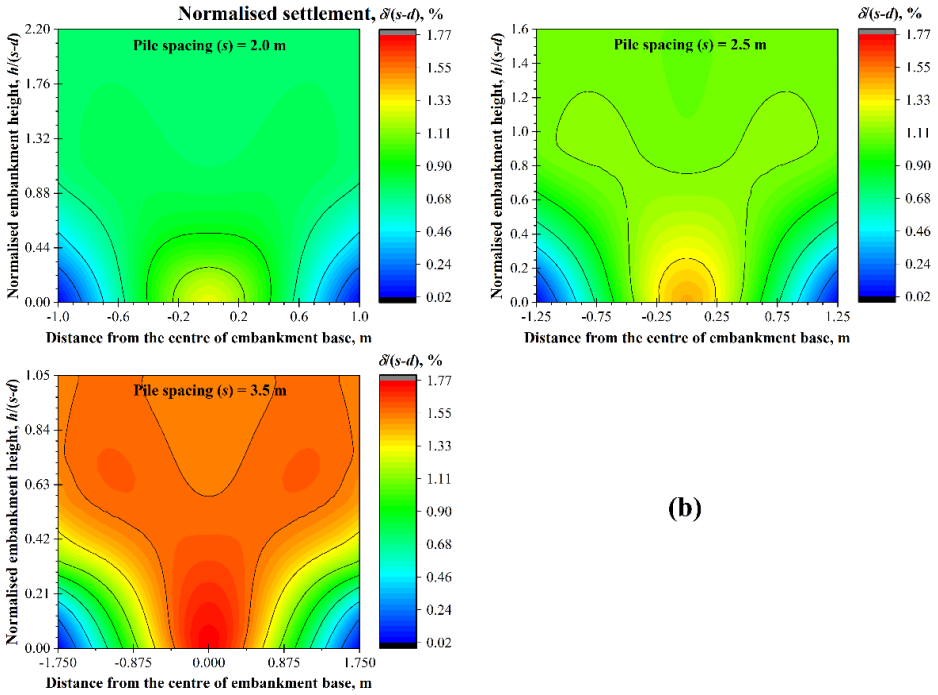

Figure 3.7: Normalised settlement contour for varied (a) embankment height, and (b) pile spacing

3.3.3.1 Total settlement

The total settlement refers to settlement of embankment on point A, and it is a prime concern for a pile-supported embankment and it should be predefined to minimise the risk of potential failure.

Figure 3.8 shows normalised total settlement on point A (amid piles) with the embankment height varies from 2.5 m to 6.5 m. The pile spacing is fixed at 2.5 m. It is evident that normalised total settlement increases up to 40% with an increase in embankment height from 2.5 to 6.5 m. It also shows that the presence of geosynthetic layer decreases the total settlement. The total settlement reduces up to 10% with incorporating the geosynthetic layer at embankment base. Thus, it implies that reinforcement can enhance the performance of embankment by reducing the settlement.

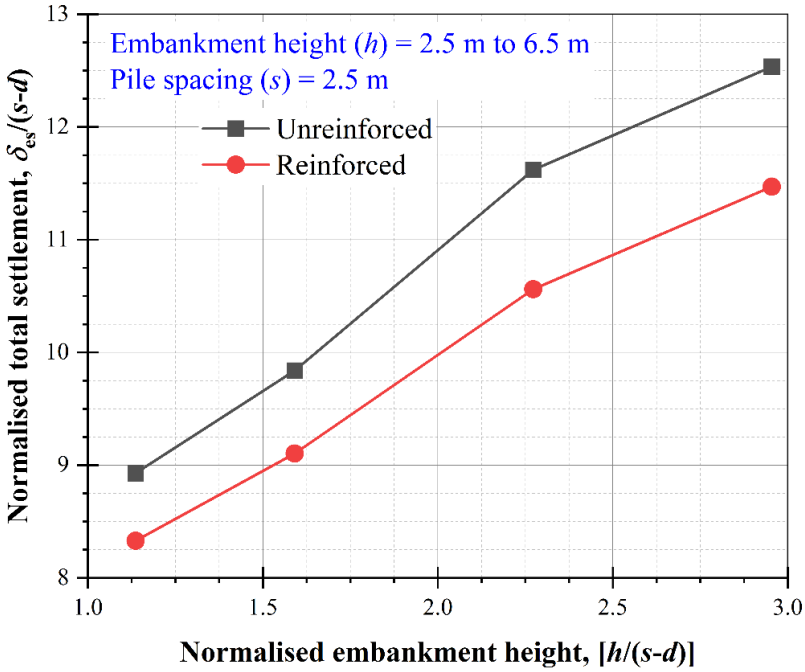

Figure 3.8: Effect of embankment height on total settlement

3.3.3.2 Differential settlement

Differential settlement (i.e., δ_{em}-δ_p) at the embankment top is defined as difference between maximum settlement at the top surface of embankment above point A and B (refer Figure 3.1). However, the settlement ratio (δ_{em}/δ_p) can be employed to represent the differential settlement. As evident, the settlement ratio (δ_{em}/δ_p) at the surface of the embankment is practically significant, in view of the embankment stability.

Figure 3.9(a) shows the settlement ratio variation with normalised embankment height (h/s) for unreinforced case. For normalised embankment height (h/s) > 1.7, settlement ratio (δ_{em}/δ_p) becomes one, implying uniform settlement. As embankment height decreases, settlement ratio increases, while showing a steep increase for (h/s) < 1. Figure 3.9(b) demonstrates the increase in settlement ratio at point A (δ_{em}/δ_s), with an increase in normalised embankment height (h/s) for the entire range of pile spacing (s) considered in this study. For pile spacing (s) = 3.5 m and low

embankment height ($h \leq 3.5$ m), settlement ratio at point A (δ_{em}/δ_s) decreases as the soil arching is not fully developed. However, for higher embankment ($h > 3.5$ m), soil arching is fully developed as indicated by the increase in δ_{em}/δ_s. In addition,

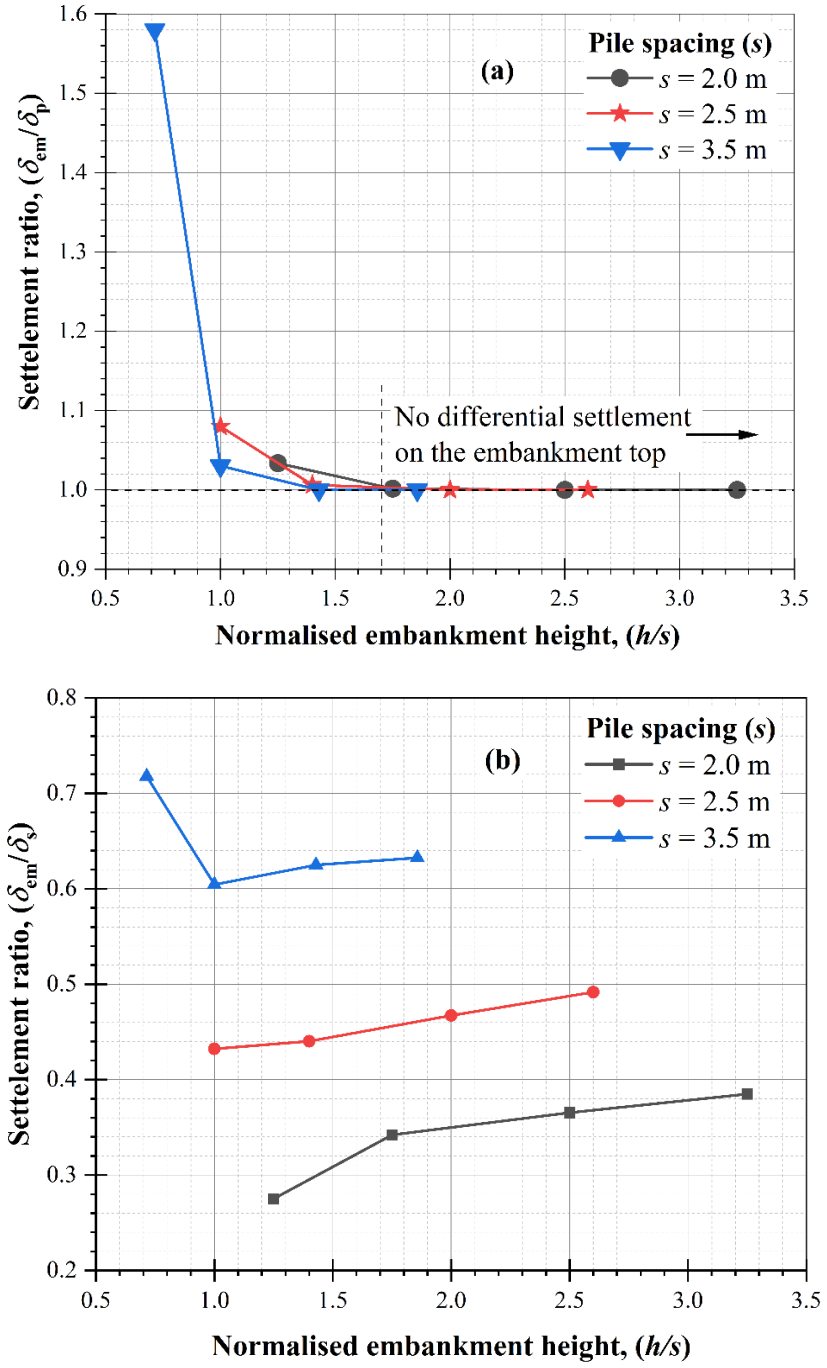

Figure 3.9: Settlement ratio at (a) the embankment top, (b) point A

It is noted that pile diameter is an importance parameter. However, the soil arching depends on the clear pile spacing, and is not mobilized by increasing the pile diameter (Liang and Zeng 2002). In addition, increase in pile diameter will increase the cost of the project.

3.3.4 Lateral stress coefficient (*K*)

The lateral stress coefficient (*K*) is plotted on a vertical profile at point A and point B, further demonstrating soil arching. The lateral stress coefficient is the ratio of horizontal stress (σ_h) to vertical stress (σ_v) as:

$$K = \frac{\sigma_h}{\sigma_v} \quad (3.4)$$

Figures 3.10 and 3.11 show the lateral stress coefficient (*K*) profiles for a range of embankment height (*h*) and pile spacing (*s*) respectively, plotted with vertical distance upwards from the base of the embankment (*h*) normalised by (*s*-*d*) in unreinforced case. The results do not extend to the top of the embankment for higher embankments. Only the values of 0.25(*s*-*d*), 0.5*s* and 1.5(*s*-*d*) are highlighted on the Y-axis; and lateral stress coefficient (*K*) = at active stage (i.e., K_a = 0.33); at rest (i.e., K_o = 0.5) and at passive stage (i.e., K_p = 3.0, considering the standard Rankine passive value and ignoring the small value of cohesion) on the X-axis. Figures 3.10(a) and (b) represent the *K* profile for varied embankment height (*h*) with fixed pile spacing (*s*) = 2.5 m at point A and point B respectively, whereas Figures 3.11(a) and (b) show the equivalent plot for embankment height (*h*) = 3.5 m at different pile spacing (*s*).

Referring to Figure 3.10(a) for normalised embankment height (*h*/(*s*-*d*)) > 1.5, lateral stress coefficient (*K*) is deduced to K_o and is not influenced by soil arching. For the embankment height (*h*) > 2.5, lateral stress coefficient (*K*) increases with depth for *h*/(*s*-*d*) < 1.5, approaching at passive stage (K_p) when embankment height (*h*) = 0.25(*s*-

d). Subsequently, the lateral stress coefficient (*K*) decreases until the embankment base for all considered embankment height which attribute the inner arch of soil arching where the horizontal stress is rapidly decreases. Although there is no direct evidence shown for the outer arch, Hewlett and Randolph (1988) considered it half of the pile spacing (*s*). For embankment height (*h*) = 2.5, lateral stress coefficient tends to approach the rest stage (K_o), however, the complete K_o stage is not achieved due to lower embankment height (*h*) resulting in undeveloped soil arching. The lower embankments (i.e., $h < 2.4$) show that stress along the entire height of the embankment is under the passive stage. Figure 3.10(b) shows lateral stress coefficient (*K*) at point B, an active stage observed for higher embankments when $h/(s\text{-}d) < 1.0$. It is evident that the vertical stress gets disturbed and soil arching mobilised below this height. Referring to Figure 3.10(a), it can be seen the outer arch suggested by Hewlett and Randolph (1988) is lies under this height. The lateral stress coefficient (*K*) returns to rest (K_o) at a similar height to Figure 3.10(a) tends to remain the same with a decrease in the embankment depth. However, it rapidly decreases and then increases at the $0.25(s\text{-}d)$ embankment height which represents the inner arch of soil arching similar to Figure 3.10(a). A comparison of soil arching height with various studies is listed in Table 3.4.

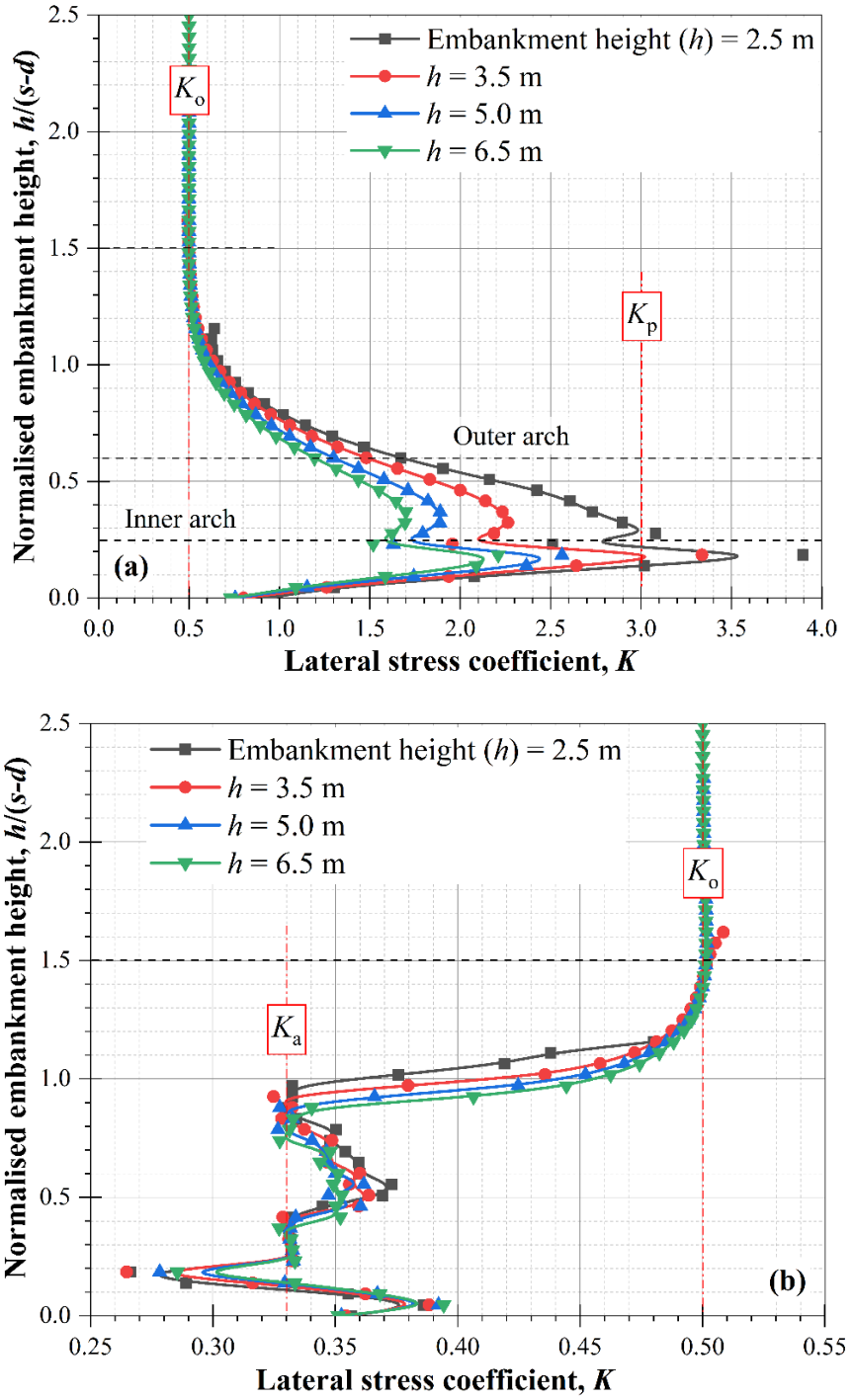

Figure 3.10: Lateral stress coefficient (K) for varied embankment height at (a) point A, (b) point B

As discussed earlier, Figure 3.11(a) shows lateral stress coefficient (K) at point A for embankment height (h) = 3.5 m at different pile spacing (s), resulting in the outer boundary of arch being dependent on pile spacing. The inner boundary remains the

same for different pile spacing (s), also referred to in Figure 3.4(b). Moreover, Figure 3.11(b) shows the equivalent plot at point B for different pile spacing. The lateral stress coefficient (K) returns to at rest (K_o) after the active stage for pile spacing (s) = 2 m, and 2.5 m. Further increments in pile spacing (s) will not result in the lateral stress coefficient (K) returning to K_o owing to the non-formation of soil arching.

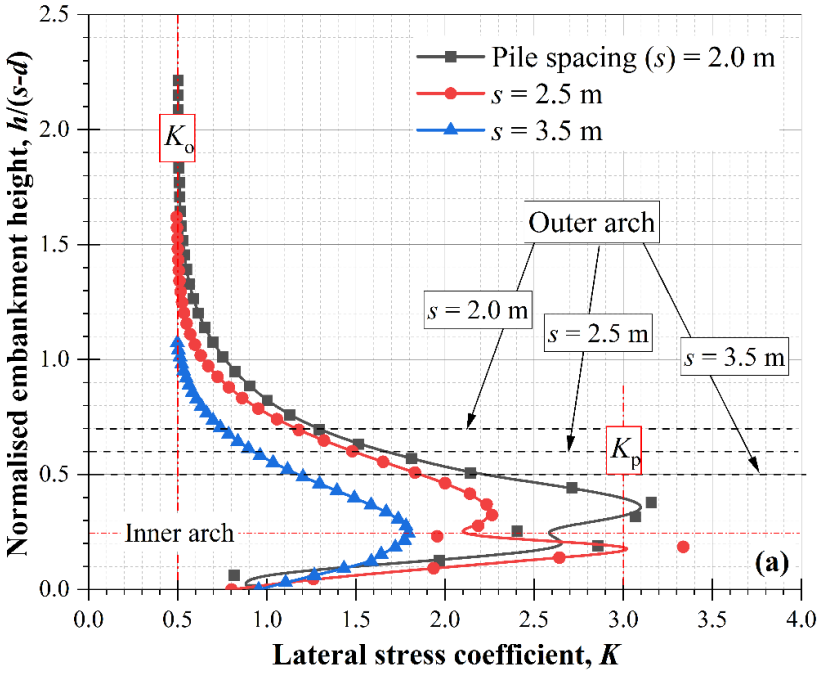

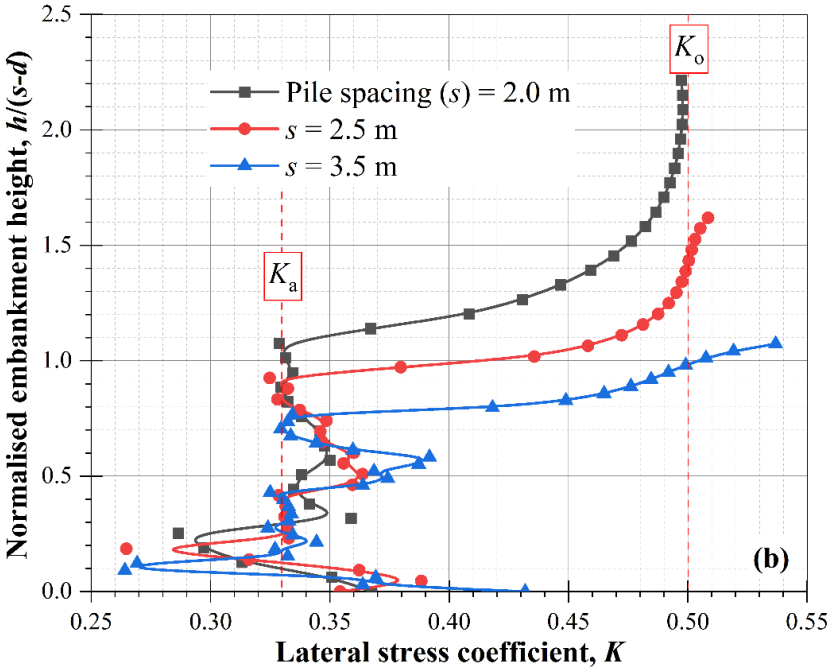

Figure 3.11: Lateral stress coefficient (K) for varied pile spacing at (a) point A, (b) point B

The results observed in Figures 3.10 and 3.11 are consistent with the three-dimensional arch theory proposed by Hewlett and Randolph (1988) in that the terms of active and passive conditions are perceived above point B and at the crown of the arch (at least near the inner boundary), respectively. These conditions are associated with the punching of the pile into the base of the embankment (for the active condition) and failure of the arch at the mid-span (for the passive condition), respectively. It may be observed that the effect on the stress state throughout the embankment fill is more widespread (higher) than the proposed discrete hemispherical boundaries since there is a gradual (rather than instantaneous) transition to K_o as embankment height (h) increases.

3.3.5 Tension in geosynthetic layer (*T*)

The tension in geosynthetic layer is captured as a function of distance from outer edges of two adjacent piles in the modelled unit cell. It is not uniform throughout the geosynthetic layer. As shown in Figure 3.12, it is evident that tension is maximum at near the inner edges of adjacent pile heads. This maximum tension is crucial to investigate for safe design of pile-supported embankment (Zhuang and Wang 2015). By knowing the maximum tension in geosynthetic we can predict the potential failure that occurred in the geosynthetic (if any happen). The tension in geosynthetic layer is increased up to its maximum value (dependent on the geosynthetic layer properties) from the outer to the inner edge of piles. further, it decreases to zero up to mid-distance of the geosynthetic layer.

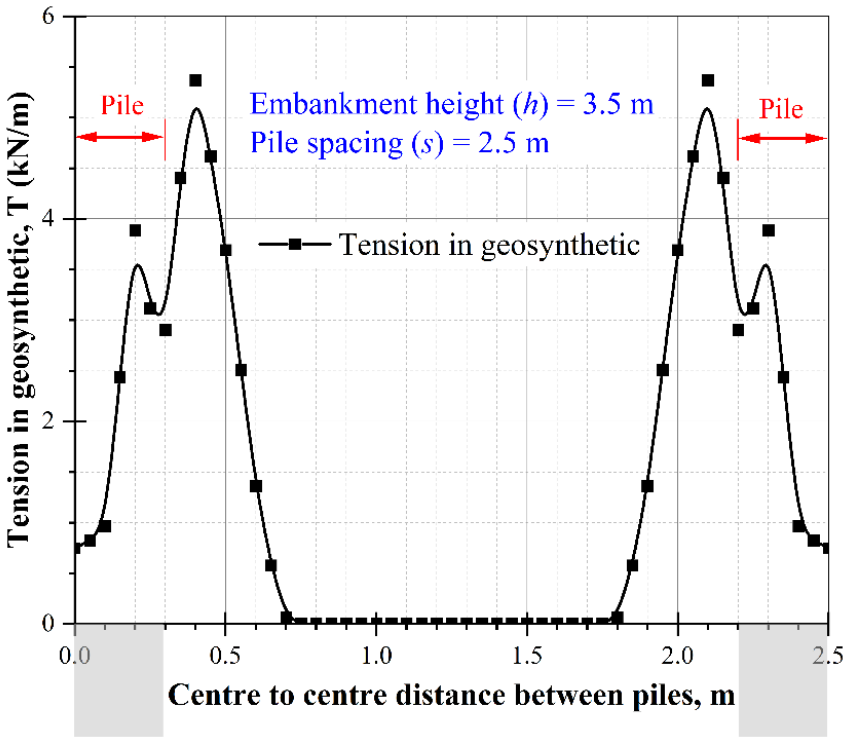

Figure 3.12: Tension distribution in a geosynthetic layer

3.4 PARAMETRIC STUDY

A parametric study is incorporated to see the effect of different material parameters on the size and shape of soil arching. Once the basic plane strain model is verified by the results available from past studies, the analysis is further extended for the effect of a range of input parameters on soil arching. It will help to understand the effect of different input parameters on soil arching. Only one parameter is changed at a time, while the others are kept at standard case values. The pile and embankment modulus are varying from 15 GPa to 30 GPa and 15 MPa to 30 MPa, respectively. In addition, the friction and dilation angle are varying from 30° to 45° and 0° to 15°, respectively. The details of these parameters were given in Table 3.1.

3.4.1 Total settlement

Figure 3.13(a) shows the combined effect of pile and embankment moduli on total settlement (δ_{es}). Whereas, the combined effect of friction and dilation angle is shown in Figure 3.13(b). For both Figures 3.13(a and b), the pile spacing (s) and embankment height (h) are considered as 2.5 m and 3.5 m, respectively. The settlement decreases with an increase in pile modulus (E_p) and embankment modulus (E_{em}). After a specific value of pile modulus (i.e., 15 GPa for this study), the total settlement keep constant which is in good agreement with Han and Gabr (2002). The embankment modulus (E_{em}) is a much sensitive parameter compared to the pile modulus (E_p). At a certain pile modulus, an increase in the embankment modulus leads to a decrease up to 6.5% in the total settlement.

Furthermore, the total settlement decreases up to 7.5% with an increase in friction angle from 30° to 45° and it decreases up to 2.0% with an increase in dilation angle from 0° to 15°. Thus, friction angle is a more prominent parameter compared to

dilation angle and it should be high enough to reduce the total settlement.

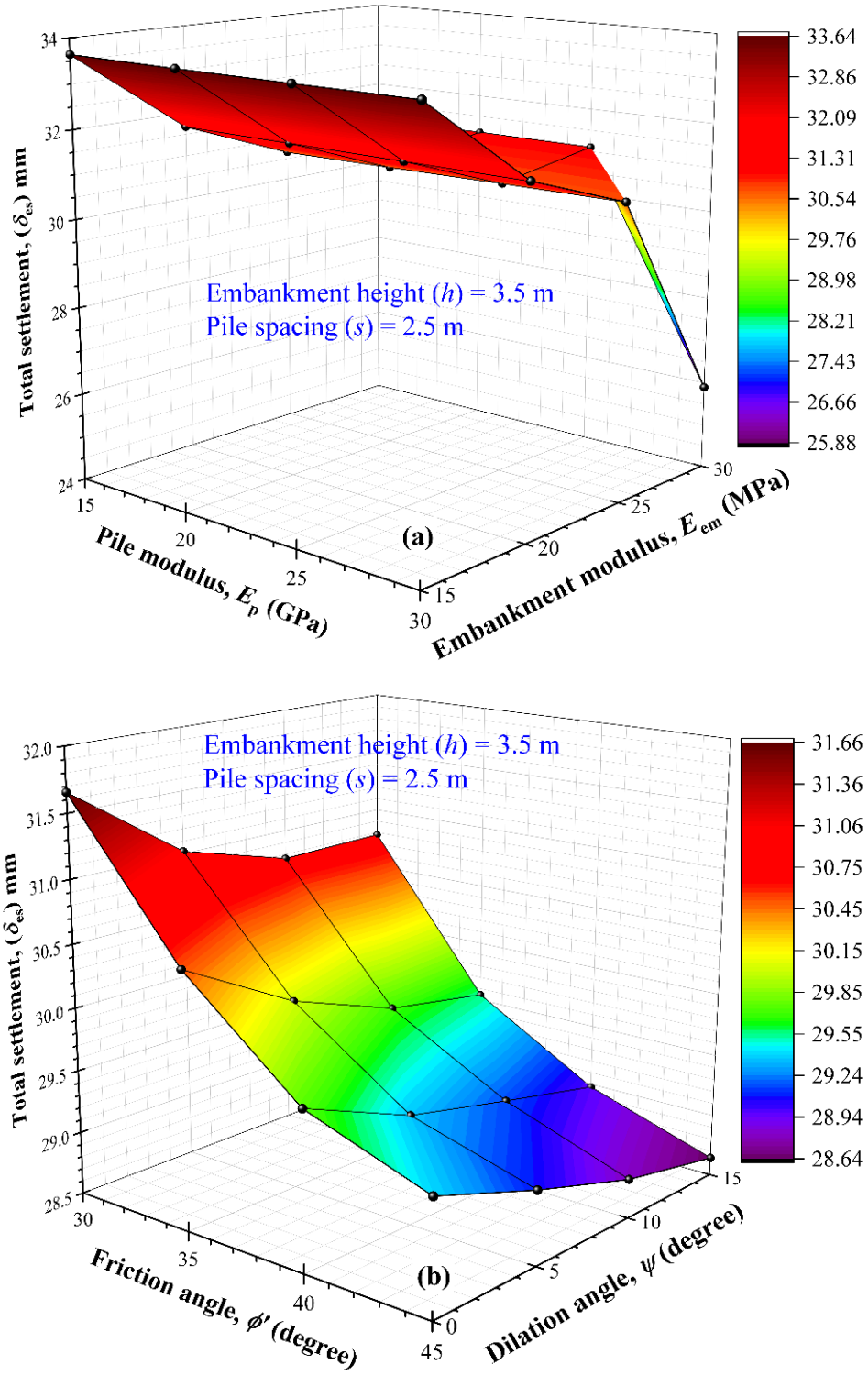

Figure 3.13: Influence on total settlement due to (a) pile modulus and embankment modulus (b) friction angle, and dilation angle

3.4.2 Differential settlement

For settlement ratio, embankment height is taken as 3.5 m (h is fixed) whereas pile spacing is varied (s = 2.0, 2.5 and 3.0 m). The effect of pile modulus (E_p) and embankment modulus (E_{em}) on the ratio (δ_{em}/δ_p) for pile spacing 2.5 m is demonstrated in Figure 3.14(a). It shows a trend which is depending on the embankment modulus (i.e., the settlement ratio increases 2% with an increase in pile modulus (E_p) when the embankment modulus (E_{em}) has a minimum value, while the settlement ratio decreases by 3% with an increase in pile modulus (E_p) when the embankment modulus (E_{em}) has maximum value). It implies that the pile modulus (E_p) should be enough with maximum embankment modulus (E_{em}) to reduce the differential settlement at embankment surface. A similar trend has been found for pile spacing (s) = 2 and 3.5 m.

Figure 3.14(b) indicates the effect of friction angle (ϕ') and dilation angle (ψ) for pile spacing (s) = 2.5 m. It can be seen that the settlement ratio increases by 17% with an increase in friction angle. The dilation angle does not affect much the settlement ratio. However, for higher friction angle with lower dilation angle, it shows a higher value of the settlement ratio. An increase in pile spacing (s) leads to an increase in the settlement ratio (δ_{em}/δ_p).

Thus, the settlement ratio (i.e., differential settlement) is substantially affected by the input parameters; the pile and embankment modulii, embankment height (refer Figure 3.9a) and pile spacing. A pile spacing (s) = 2 m and 2.5 m follows the serviceability condition, which means there is no differential settlement on the embankment surface. However, settlement of pile top and embankment is almost same due to the less embankment height. If the embankment height is increased, the settlement of the embankment increases.

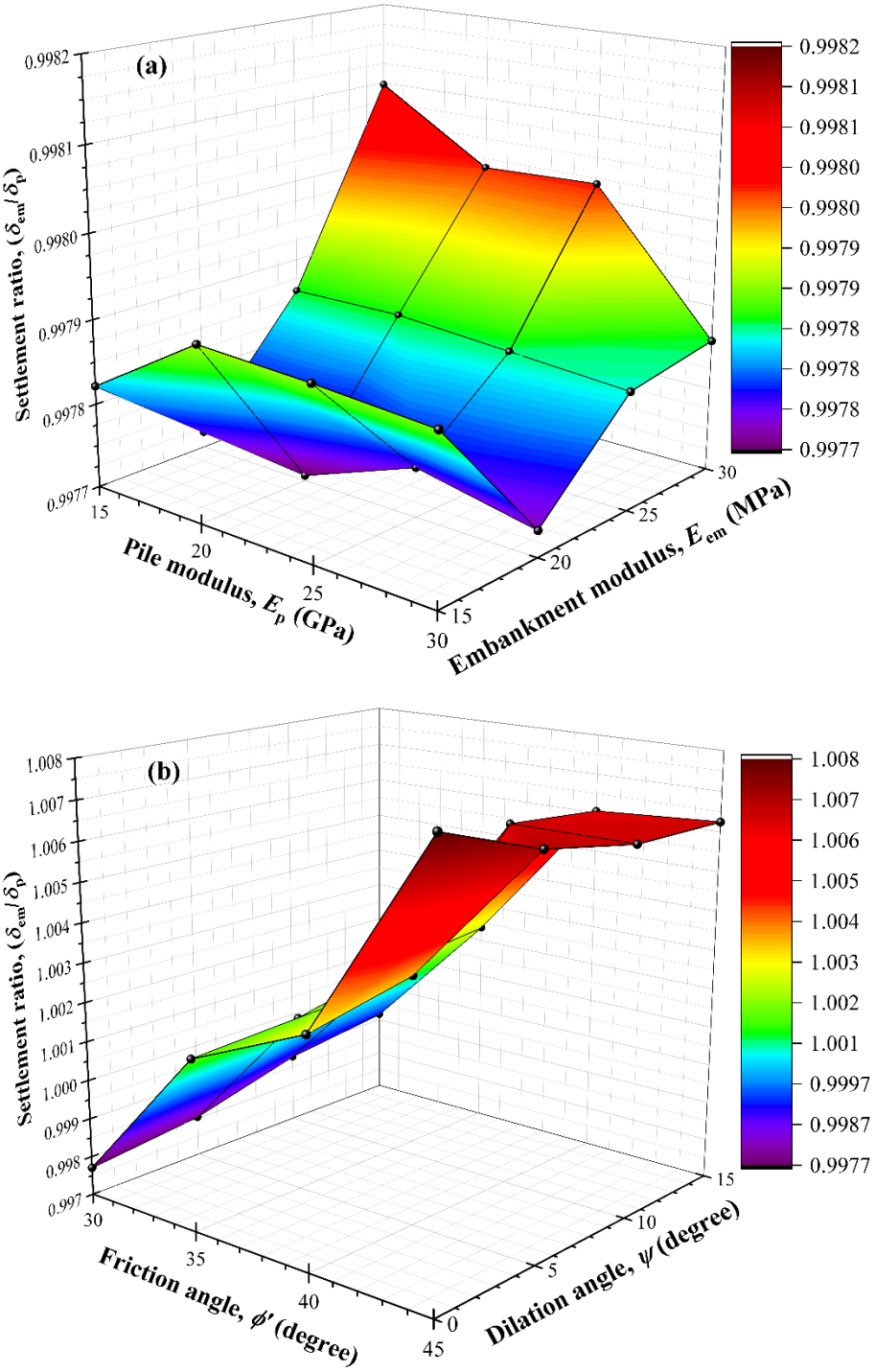

Figure 3.14: Influence on settlement ratio (δ_{em}/δ_p) due to (a) pile modulus and embankment modulus (b) friction angle, and dilation angle

3.4.3 Soil arching ratio (*SAR*)

The effect of pile modulus (E_p) and embankment modulus (E_{em}) on soil arching ratio

is shown in Figure 3.15(a). The soil arching ratio negligible effects with an increase in E_p. Further, soil arching ratio decreases (i.e., the tenancy of stress transfer to pile increase) by up to 61% with an increase in embankment modulus (E_{em}) from 15 to 30 MPa, which implies that a specific value of embankment modulus (E_{em}) is required for maximum stress transfer to pile. The effect of friction angle (ϕ') and dilation angle (ψ) is demonstrated in Figure 3.15(b). It shows that *SAR* decreases up to 30% with an increase in friction angle from 30° to 45° and the effect of dilation angle is found to be negligible. However, soil arching ratio increases up to 7% with an increase in dilation angle, at the lower friction angle. Which means that soil arching increases with an increase in friction angle (ϕ').

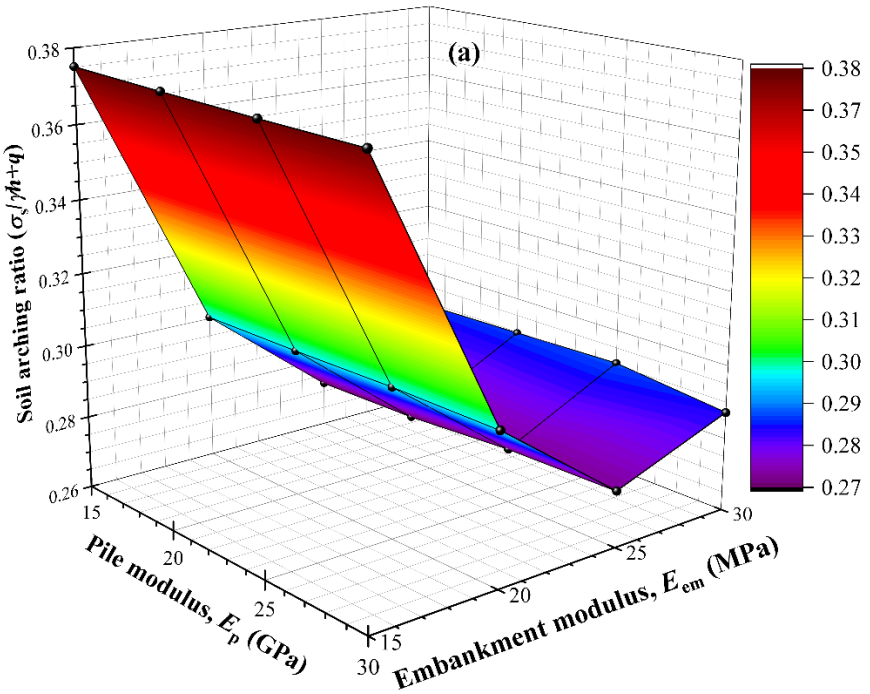

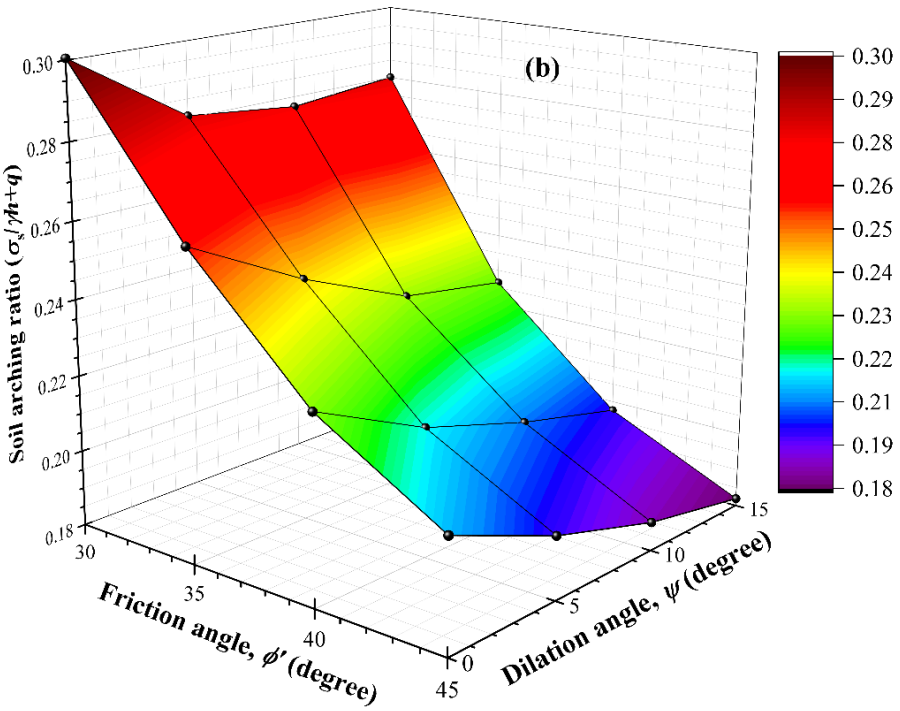

Figure 3.15: Influence on soil arching ratio (*SAR*) due to (a) pile modulus and embankment modulus (b) friction angle, and dilation angle

3.4.4 Stress concentration ratio (*SCR*)

The stress concentration ratio (*SCR*) signifies stress distribution on the pile head and adjacent subsoil. The pile and embankment moduli are considered 20 GPa and 20 MPa, respectively (refer to Table 3.1). Figure 3.16 represent the effect of embankment height (h) and pile spacing (s) on the stress concentration ratio. The *SCR* increases up to 83% with an increase in embankment height from 2.5 to 6.5. for a specific pile spacing (s). It implies that stress on the piles significantly increases resulting in the soil arching effect mobilised. However, the *SCR* decreases up to 54% with an increase in pile spacing. Although, large reduction in *SCR* can be observed at higher embankment height. Thus, pile spacing should be minimum to get full stress transfer to the pile head. This argument is in good agreement with Han and Gabr (2002) findings.

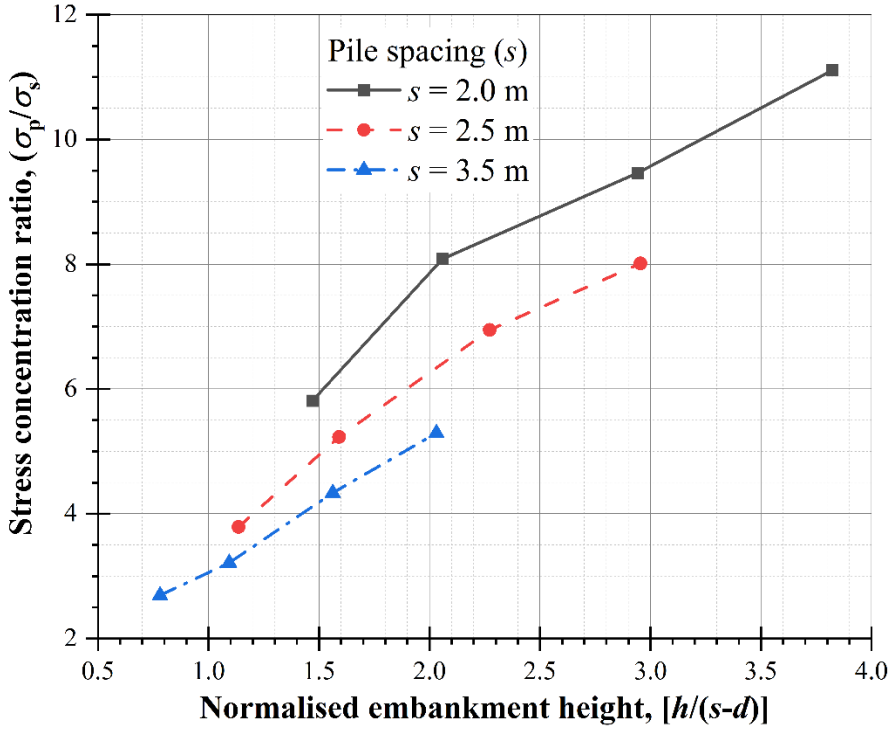

Figure 3.16: Effect of embankment height (*h*) and pile spacing (*s*) on stress concentration ratio (*SCR*)

The combined effect of pile and embankment moduli on the *SCR* is shown in Figure 3.17(a). Whereas, the combined effect of friction and dilation angle is shown in Figure 3.17(b). The pile modulus has negligible effect on the *SCR*. However, the *SCR* increases up to 44% with an increase in embankment modulus from 15 to 30 MPa. Furthermore, the *SCR* significantly affects by friction angle. It increases up to 90% with an increase in friction angle from 30° to 45°. The effect of dilation angle is found to be negligible (i.e., slightly increases up to 7% with an increase dilation angle from 0° to 15°) which implies that soil arching affects with an increase in friction angle.

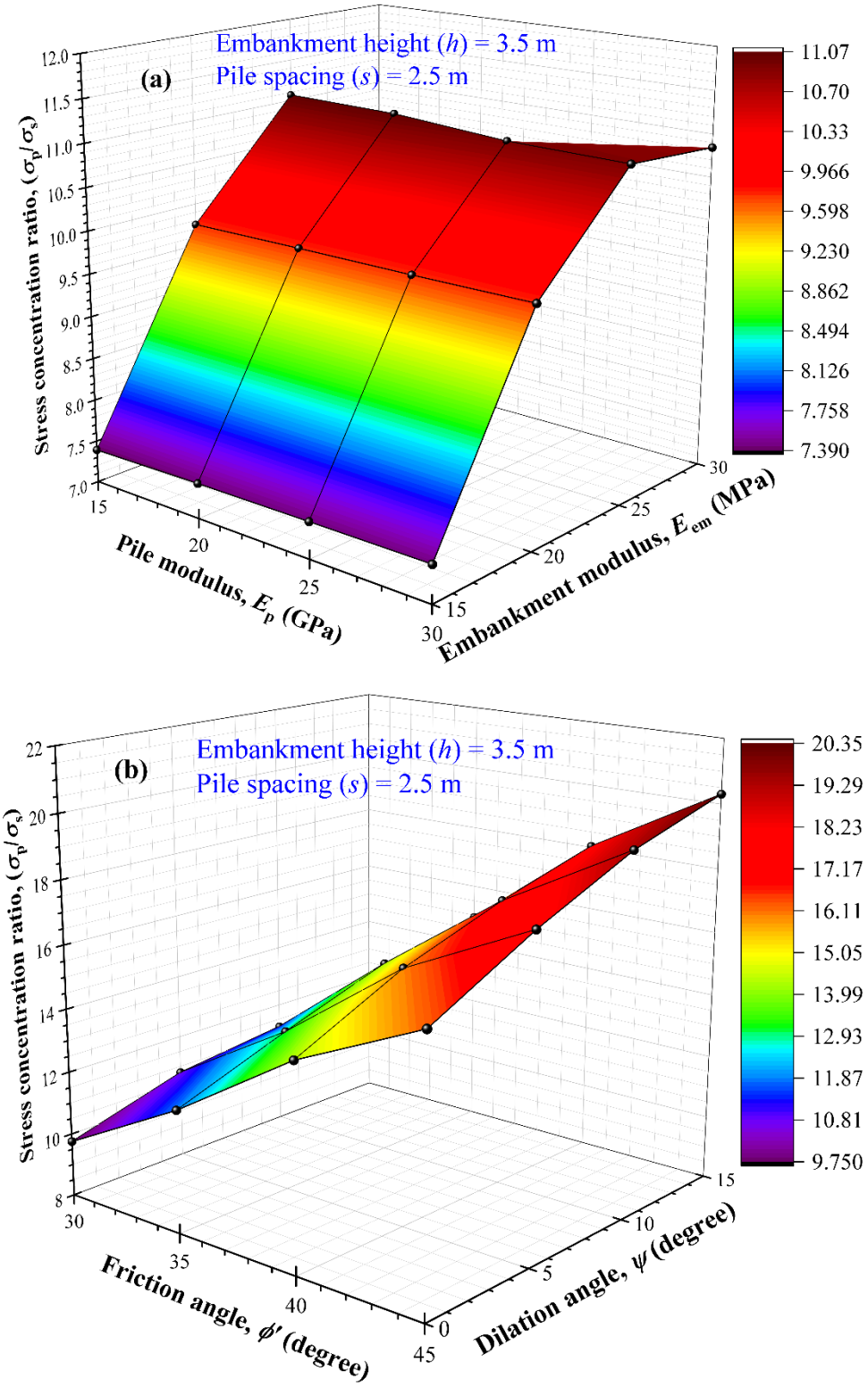

Figure 3.17: Influence on stress concentration ratio (*SCR*) due to (a) pile modulus and embankment modulus (b) friction angle, and dilation angle

Figure 3.18 shows that the stress concentration ratio increases up to 110% with

an increase in the embankment height (h) from 2.5 to 6.5m. The *SCR* value increases up to 21% in reinforced case compared to unreinforced. Thus, the stress transfer from the subsoil to the pile head is enhanced by the inclusion of geosynthetic layer. This argument is in good agreement with Han and Gabr (2002) findings. The geosynthetic layer increased the stiffness of the embankment base and take transfers additional vertical stress by the tension action in the geosynthetic layer.

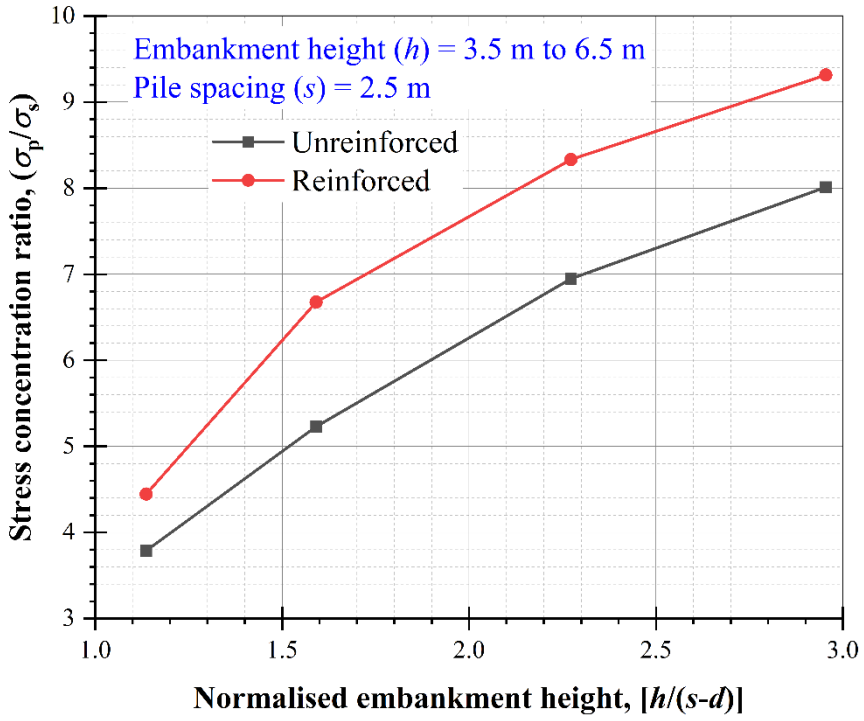

Figure 3.18: Effect of reinforcement on stress concentration ratio (*SCR*)

3.4.5 Stress efficacy (E_{str})

The effect of pile modulus (E_p) and embankment modulus (E_{em}) on efficacy is shown in Figure 3.19(a). The effect of pile modulus on efficacy is found to be negligible, and efficacy increases up to 87% with an increase in embankment modulus. It implies that efficacy is dependent on embankment modulus (E_{em}), and it should be up to a specific value (25 MPa for this study) for maximum efficacy. Figure 3.19(b) shows the effect

of friction angle (ϕ') and dilation angle (ψ) on efficacy. It shows that efficacy increases up to 20% with an increase in friction angle from 30° to 45° and the effect of dilation is found to be negligible. Thus, the effect of friction angle is more pronounced as soil arching increases with an increase of friction angle (ϕ').

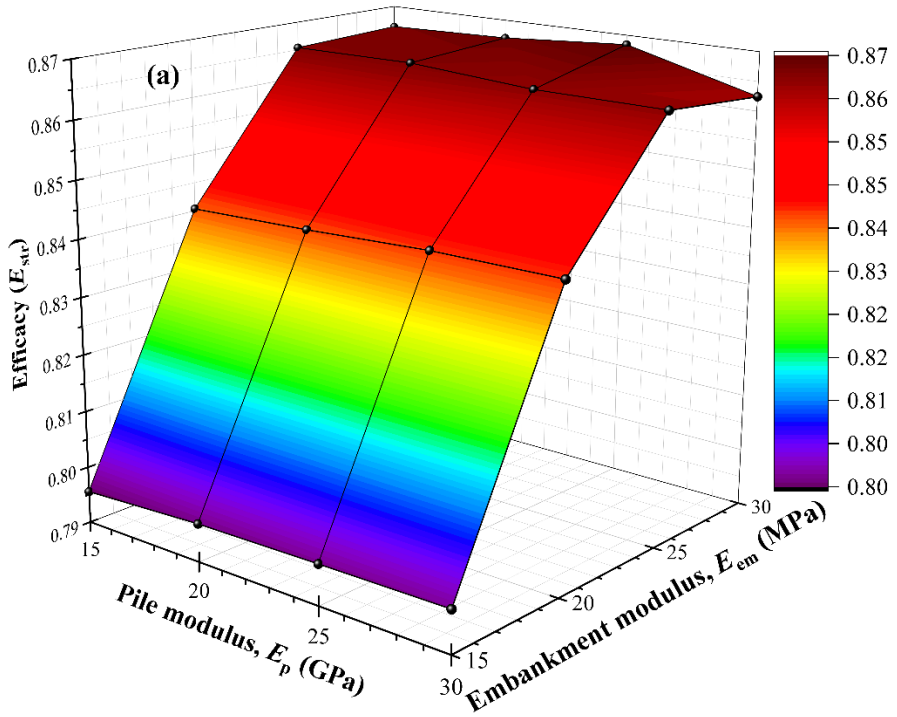

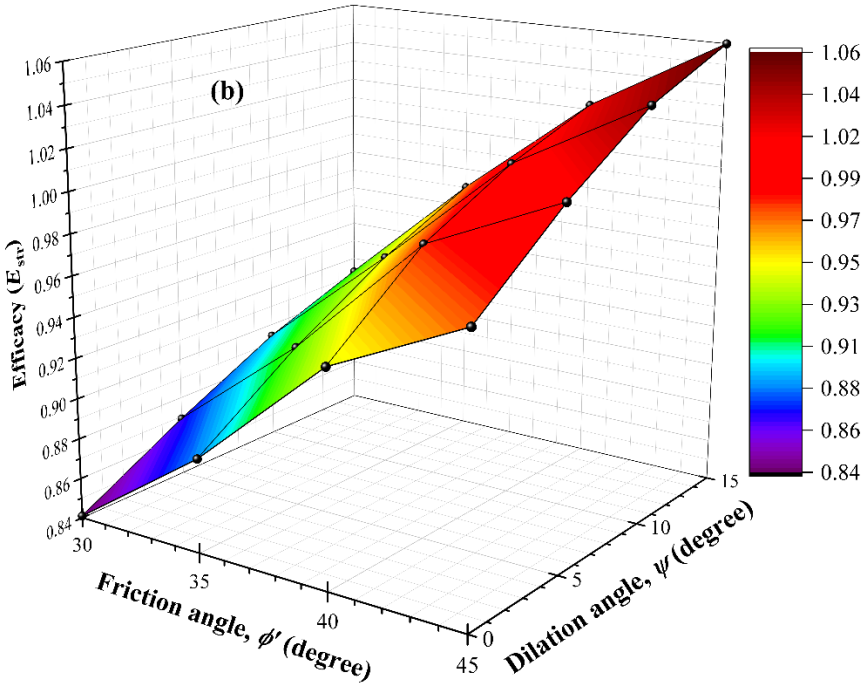

Figure 3.19: Influence on stress efficacy (E_{str}) due to (a) pile modulus and embankment modulus (b) friction angle, and dilation angle

3.4.6 Tension in geosynthetic layer (*T*)

The effect of pile modulus (E_p), embankment modulus (E_{em}), friction angle (ϕ') and dilation angle (ψ) on tension in geosynthetic layer are shown in Figure 3.20(a-d). The x-axis represented to centre-to-centre distance between two adjacent piles, and Tension in geosynthetic, T (kN/m) is plotted in y-axis. The effect of pile modulus on tension is found to be negligible as sufficient pile modulus is considered in this study. The pile modulus varies from 5 to 30 GPa to see the effect of pile modulus on the tension in the geosynthetic layer. Whereas, maximum tension decreases up to 35% with an increase in embankment modulus from 5 MPa to 30 MPa. Further, the maximum tension decreases up to 54% with an increase in friction angle from 25° to 45°, and the effect of dilation is found to be negligible. The maximum tension decreases up to 7% with an increase in dilation angle from 0° to 15°. It implies that the function of geosynthetic layer is not fully utilised, if the embankment modulus and

friction angle are high enough. Thus, the embankment modulus and friction angle should be optimum in the reinforced case.

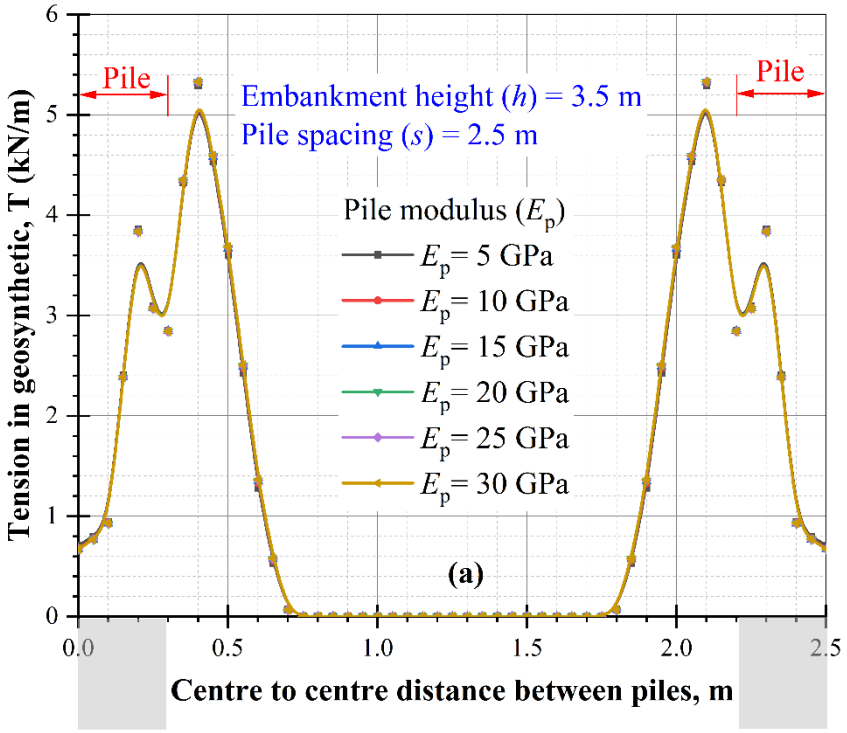

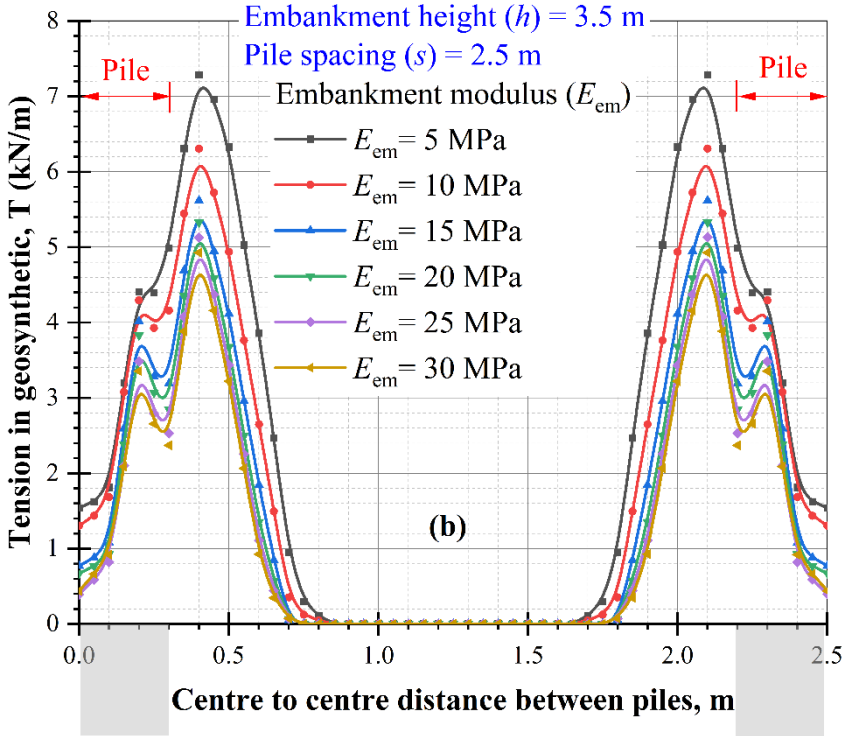

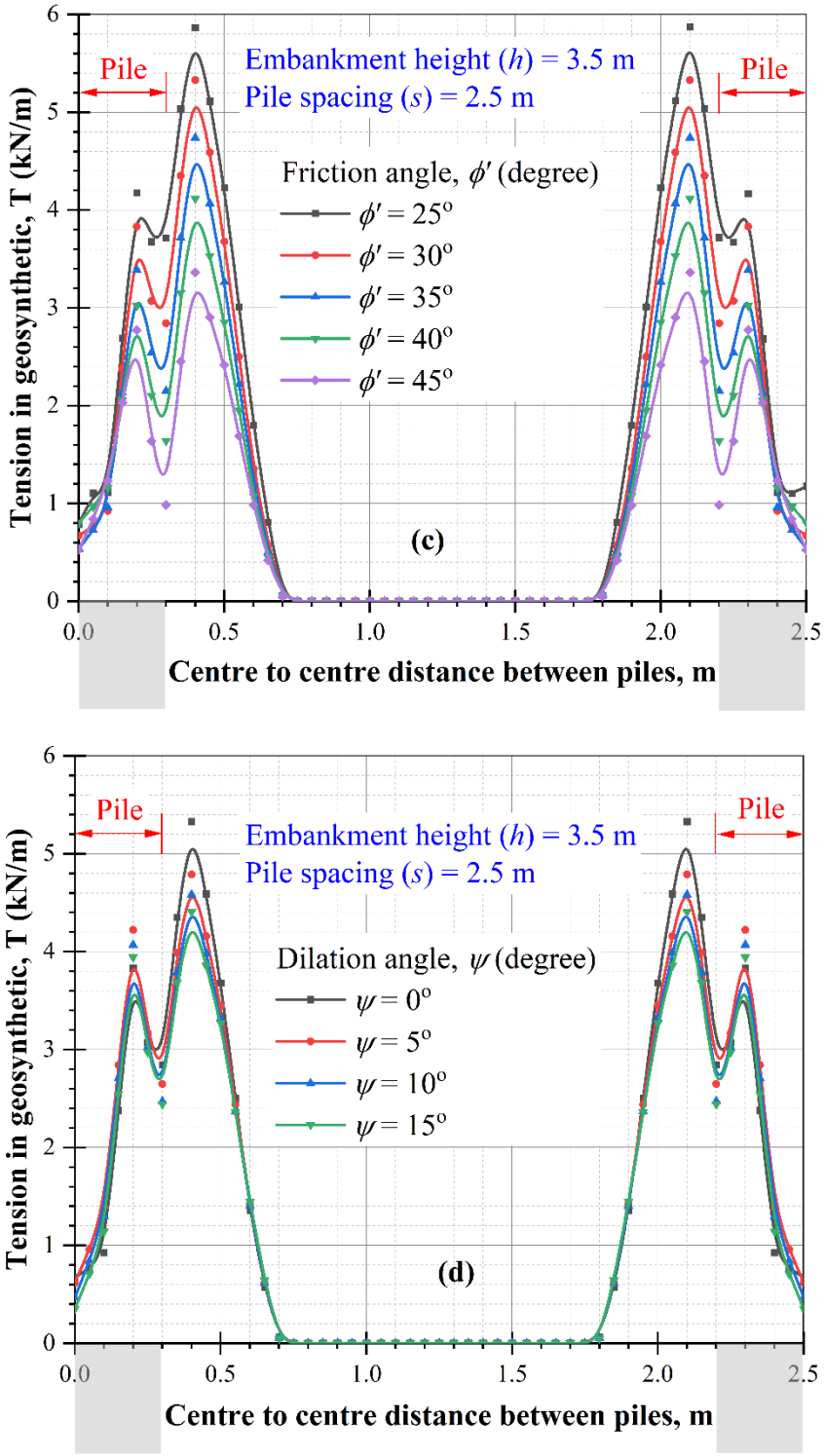

Figure 3.20: Influence on tension in geosynthetic layer (T) of (a) pile modulus, (b) embankment modulus, (c) friction angle, and (d) dilation angle

Figure 3.21 shows the effect of stiffness of geosynthetic layer on stress concentration ratio. The stress concentration ratio increases with an increase in the

stiffness of geosynthetic layer and after a certain value of stiffness (2500 kN/m for this study), it remains constant. It implies that geosynthetic layer improve the stiffness at the embankment base and encourage stress transfer to the pile head.

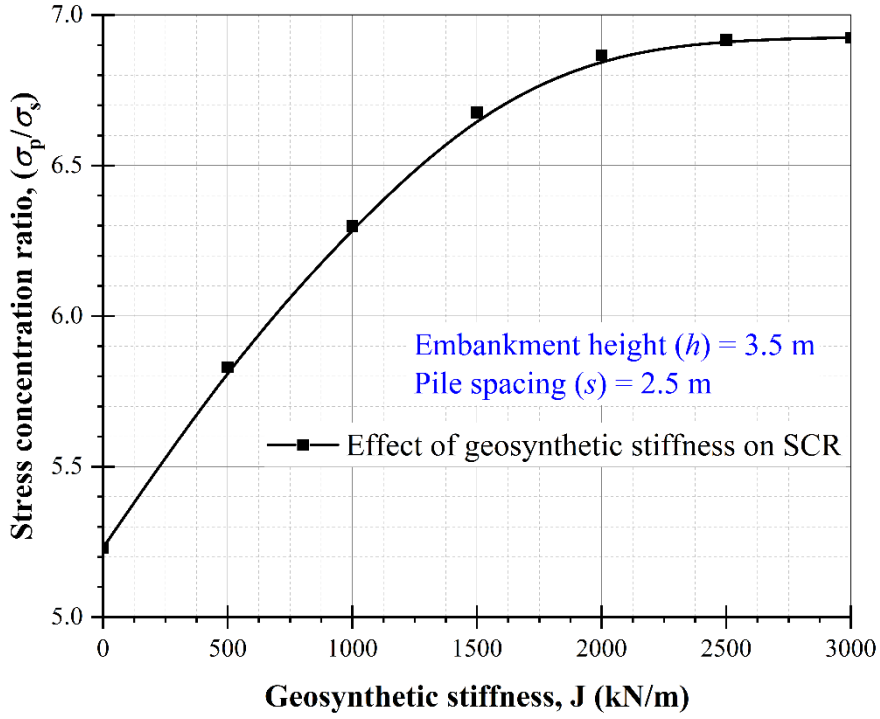

Figure 3.21: Influence of tension in geosynthetic layer (T) on stress concentration ratio (SCR)

3.4.7 Effect on arching height (h_{arch})

The soil arching height is defined as the minimum height required for the development of full soil arching. According to BS8006-1 (2010), soil arching will occur when the embankment height is equal to 1.4(s-d), whereas EBGEO (2011) suggested 0.7l_d. where s is the centre to centre pile spacing, d is the pile width, and l_d is the diagonal length.

The influence of the embankment height (h) on the height of the soil arch for different pile spacing (s) is presented in Figure 3.22(a), which shows that the height of the soil arch (h_{arch}) is closely related to embankment height (h). For a specific pile

spacing (s), it increases with an increase in embankment height up to a certain height (5·0 m in this study) and then remains constant beyond this critical embankment height. It can be verified by Figures 3.4(a), 3.7(a), and 3.10(a) for pile spacing (s) = 2.5 m.

The influence of the clear spacing between the piles (s-d) on the height of the soil arch for different embankment height (h) is observed in Figure 3.22(b). It is evident that clear pile spacing (s-d) has a significant effect on the height of the soil arch. For a specific embankment height, height of soil arching (h_{arch}) has been found to increase with an increase in (s-d) within the range from 1.5 to 3.5 m. It also shows that plot (h_{arch}) versus (s-d) are almost the same trend when embankment height is higher than its critical height (5m for this study).

The results of the (h_{arch}) plotted against the internal friction angle (ϕ') of the embankment fill are given in Figure 3.22(c). It can be seen that (h_{arch}) increases with an increase in the friction angle. When pile spacing (s) = 2 m, the h_{arch} is dramatically increased after 40° friction angle. The effect of embankment height (h) and clear pile spacing (s-d) on the arching height are consistent with Yang et al. (2019).

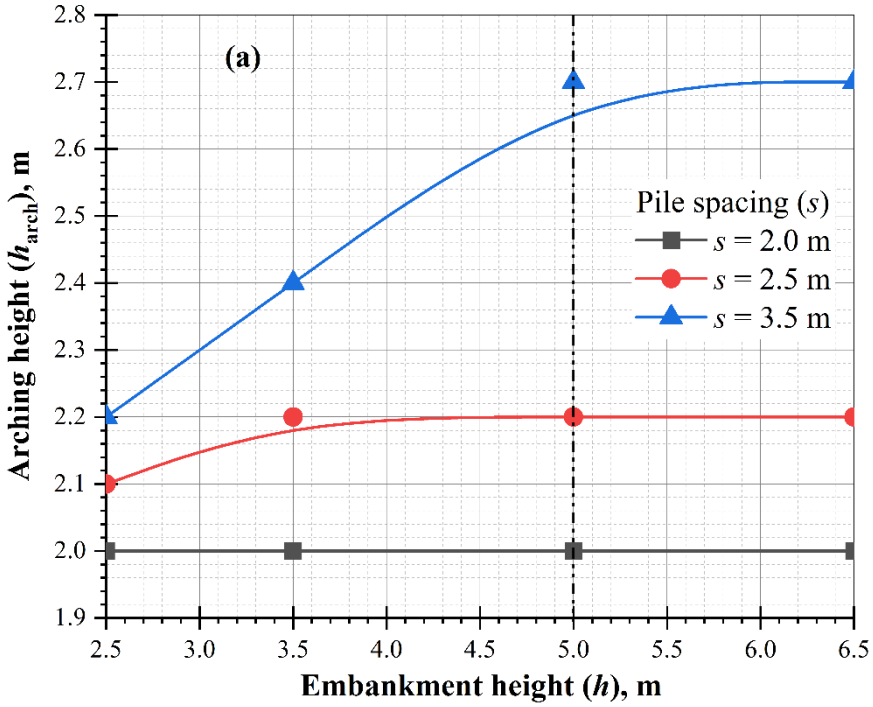
(a)
Pile spacing (s)
s = 2.0 m
s = 2.5 m
s = 3.5 m
Arching height (h_arch), m
Embankment height (h), m
2.8
2.7
2.6
2.5
2.4
2.3
2.2
2.1
2.0
1.9
2.5
3.0
3.5
4.0
4.5
5.0
5.5
6.0
6.5

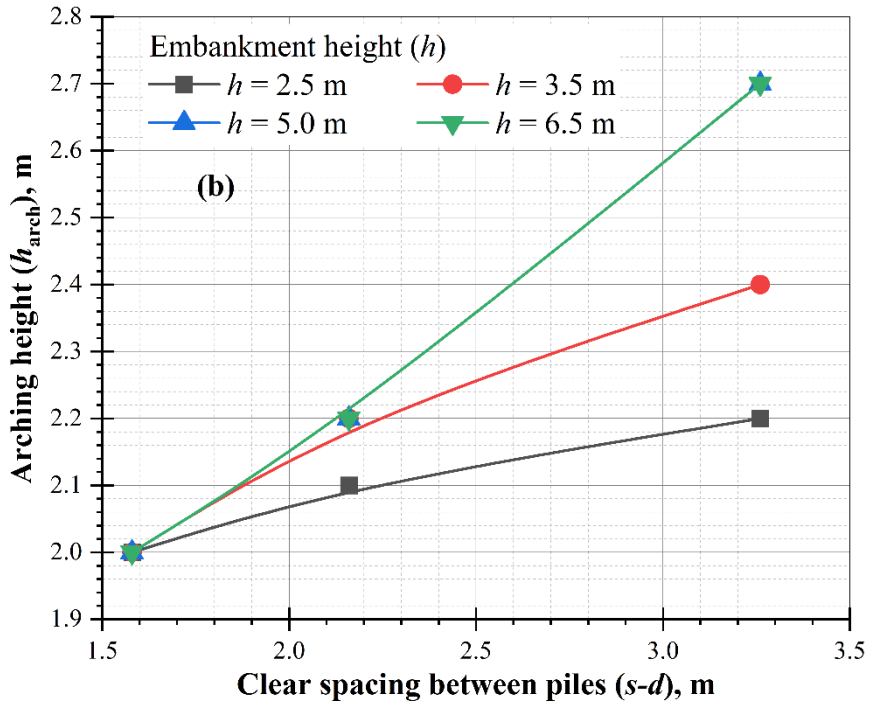
Embankment height (h)
h = 2.5 m
h = 3.5 m
h = 5.0 m
h = 6.5 m
(b)
Arching height (h_arch), m
Clear spacing between piles (s-d), m
2.8
2.7
2.6
2.5
2.4
2.3
2.2
2.1
2.0
1.9
1.5
2.0
2.5
3.0
3.5

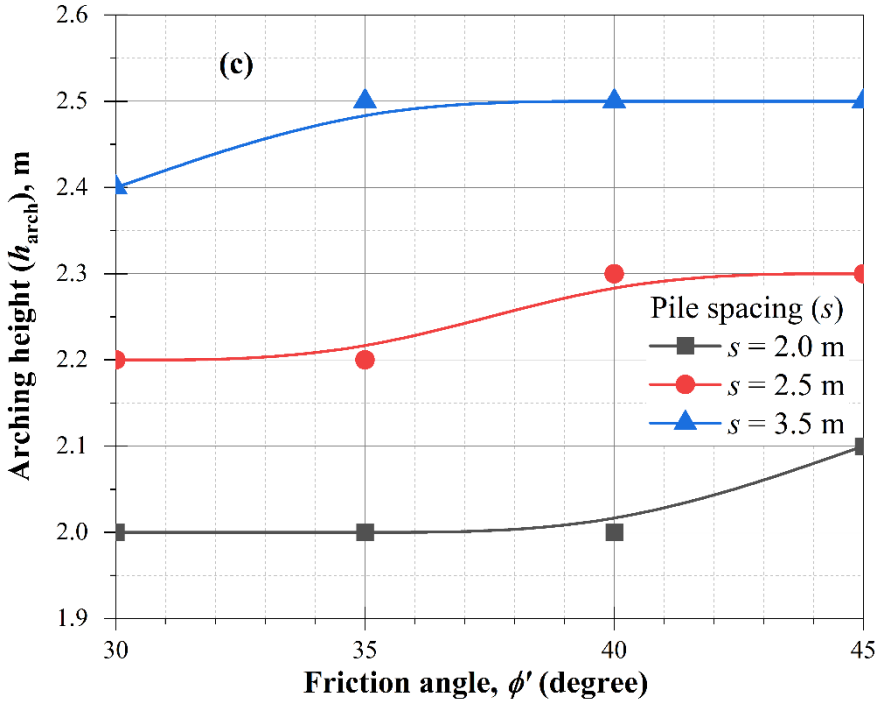

Figure 3.22: Influence on soil arching height (h_{arch}) due to (a) embankment height, (b) clear pile spacing (s-d), and (c) friction angle

3.4.8 Effect of equivalent dynamic load induced by different train speed

Figure 3.23 refers to the effect of vertical stress (σ_t) induced by a range of train speeds (V) on the settlement ratio (differential settlement) and soil arching ratio (SAR). Figure 3.23(a) shows that the settlement ratio (δ_{em}/δ_p) increases with an increase in $h/(s\text{-}d)$ (due to reduction in s). However, a mix trend settlement ratio is observed with an increase the equivalent dynamic load induced by different train speed (V) for a given value of $h/(s\text{-}d)$. At the lower $h/(s\text{-}d)$, it slightly less with increases the equivalent dynamic load. While for higher $h/(s\text{-}d)$, the settlement ratio increases with an increase in the equivalent dynamic load. As Table 3.3 indicates, the increased train speed implies increased σ_t on the top of the railway embankment. The effect of different train speed is evident in Figure 3.23(b). It implies that for smaller pile spacing, soil arching ratio (SAR) decreases with an increase in train speed (i.e., the tenancy of stress transfer

to pile increase). However, the effect on soil arching ratio (*SAR*) found to be negligible for larger pile spacing.

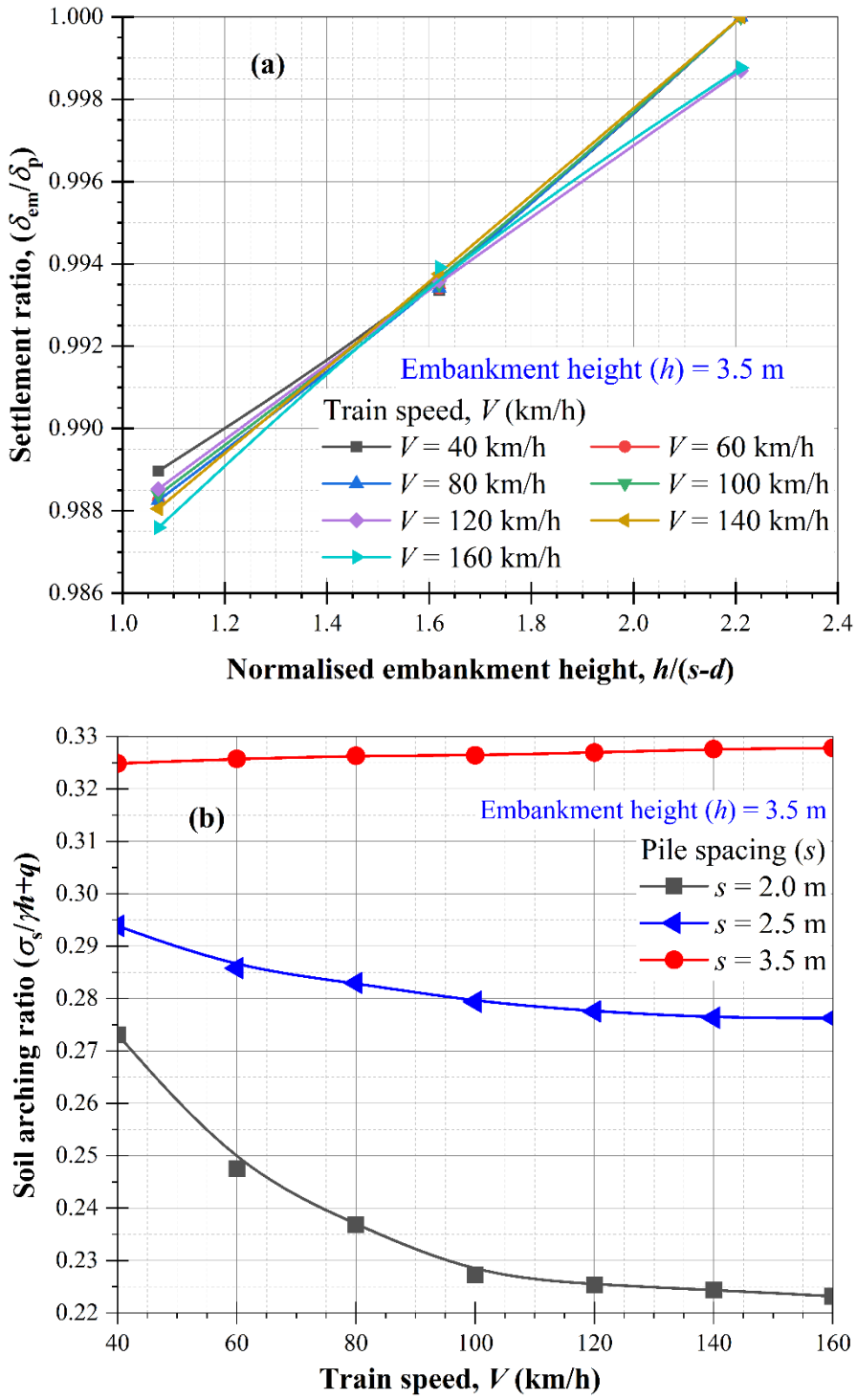

Figure 3.23: Influence of train speed on (a) settlement ratio, (b) soil arching ratio (*SAR*)

3.4.9 Shape of soil arching

A precisely defined soil arch shape is the essential requirement to perceive the soil arching effect accurately. In the literature, some assumed arch shapes are used to develop the analytical models of the soil arching effect. These models are summarised by Van Eekelen et al. (2015) as (a) *rigid arch models*: shape of the soil arch is assumed to be 2D or 3D triangular. Additionally, it is assumed that the entire load above the soil arch is directly transferred to the pile head, and the subsoil and reinforcements carry the weight of the soil below to the soil arch. (b) *Limit state equilibrium models*: these models are based on the failure condition either at the crown or the pile head of the soil arch. Commonly two limit-state equilibrium models are used in piled embankment design. One is explained by Hewlett and Randolph (1988) as the shape of soil arch semicircular in 2D and a hemispherical dome in 3D which was adopted in the French ASIRI guidelines and in the suggested BS8006-1 (2010) and was recently extended by Zhang et al. (2016) by considering the triangular arrangement of the piles. The other is the multi-shell arching theory models proposed by Kempfert et al. (2004), in which a set of multi-shell domes represent the soil arch. The multi-shell arching theory was adopted in the German guidelines EBGEO (2014) and Dutch guidelines. (c) *Frictional models* (Terzaghi K. 1943; McKelvey JA. 1994): the soil arching had no definite shape and is considered the plane of equal settlement. Thus, the existing analytical models of soil arching give a variation in the results for the same condition. One of the primary reasons for this may be related to the assumed shape of the soil arch. Therefore, the shape of the soil arch needs to be further evaluated.

The effect of the input parameters on the shape of the soil arch is illustrated in Figure 3.24. The vertical stress profile along different vertical planes in the clear pile spacing (*s*-*d*) is used to demonstrate the shape of arch inside the embankment fill. The

height of the maximum vertical stress from the embankment base for individual planes is considered to be the height of the outer boundary of the soil arch, whereas the height of the minimum vertical stress represents the inner boundary of the soil arch.

The vertical stress profile decreases at the height of 1.3 m [$h/(s\text{-}d) = 0.6$] above the base of the embankment and then again starts to increase at the height of 0.54 m [$h/(s\text{-}d) = 0.25$] above the embankment base. It means the thickness of the arch is about 0.76 m at the crown of the arch. However, Hewlett and Randolph (1988) and BS8006-1 (2010) assumed that the shape of the arch is semicircular with a uniform thickness which is equal to half of the pile head width. However, it evident that the shape of the arch is very similar to the multi-shell arching theory proposed by Kempfert et al. (2004).

The effect of the pile modulus (E_p) on the arching shape is shown in Figure 3.24(a). The shape of the arch negligible influenced at point A by increasing pile modulus. The effect of the embankment modulus (E_{em}) on the shape of the arch is shown in Figure 3.24(b). It is observed that the shape of the arch increases by increasing embankment modulus. It may be concluded that embankment modulus (E_{em}) should be sufficient to develop soil arching. The friction angle (ϕ') effect on the shape of the soil arch is evident in Figure 3.24(c). It implies that a more stable arch can be formed by increasing friction angle which is capable of transferring the maximum load onto the pile. The effect of dilation angle (ψ) on the shape of the soil arch is illustrated in Figure 3.24(d). It can be inferred that the thickness of the arch increases by increasing ψ. It may have practical importance as the thickness of the soil arch increases.

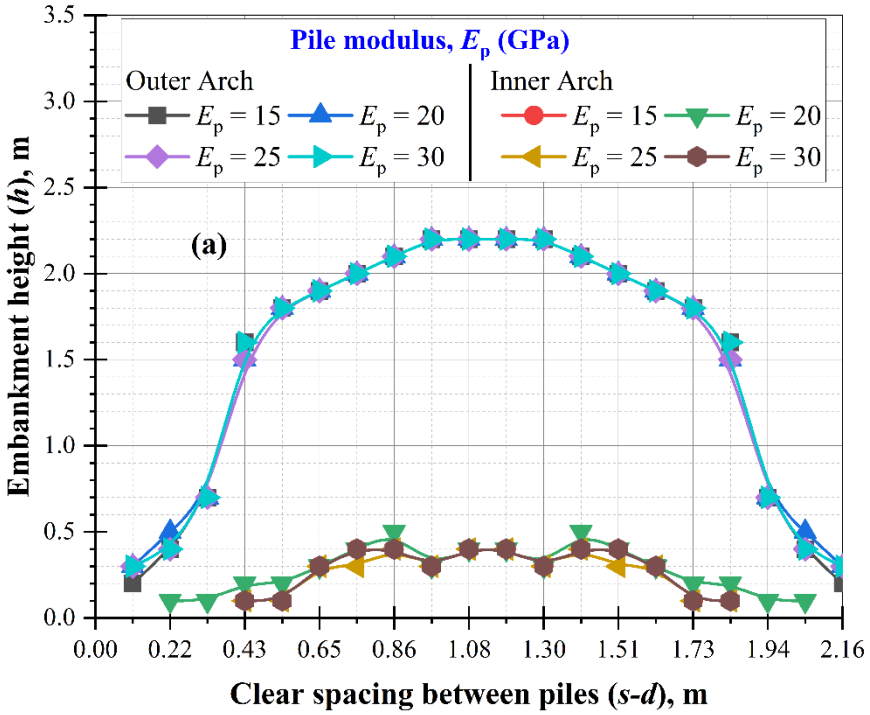
Pile modulus, E_p (GPa)
Outer Arch
E_p = 15
E_p = 20
E_p = 25
E_p = 30
Inner Arch
E_p = 15
E_p = 20
E_p = 25
E_p = 30
(a)
Embankment height (h), m
Clear spacing between piles (s-d), m
0.0
0.5
1.0
1.5
2.0
2.5
3.0
3.5
0.00
0.22
0.43
0.65
0.86
1.08
1.30
1.51
1.73
1.94
2.16

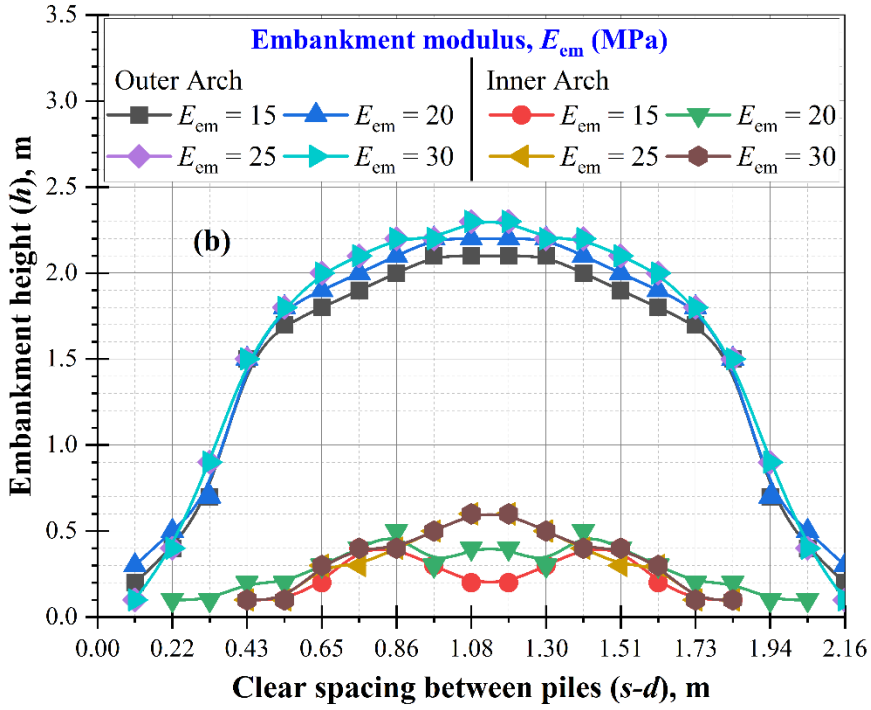
Embankment modulus, E_{em} (MPa)
Outer Arch
E_{em} = 15
E_{em} = 20
E_{em} = 25
E_{em} = 30
Inner Arch
E_{em} = 15
E_{em} = 20
E_{em} = 25
E_{em} = 30
(b)
Embankment height (h), m
Clear spacing between piles (s-d), m
0.0
0.5
1.0
1.5
2.0
2.5
3.0
3.5
0.00
0.22
0.43
0.65
0.86
1.08
1.30
1.51
1.73
1.94
2.16

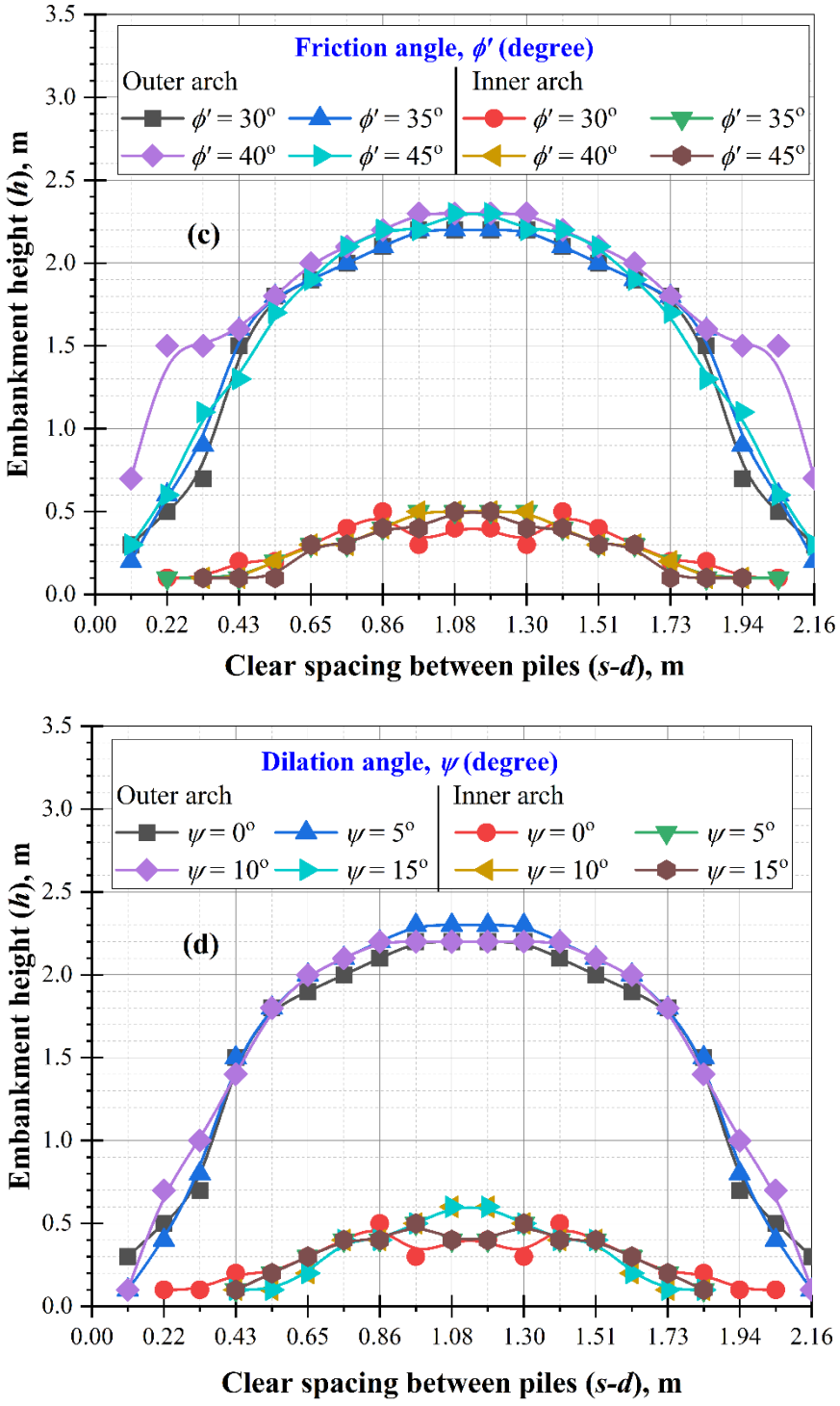

Figure 3.24: Influence on arching shape due to (a) pile modulus, (b) embankment modulus, (c) friction angle, and (d) dilation angle

3.4.10 Review of available design approaches

Various empirical approaches (Terzaghi K. 1943; Guido et al. 1987; Hewlett and Randolph 1988; BS8006 2010; EBGEO 2011) are available for piled embankment

design. Table 3.5 summarises the different equations used in various design methods to calculate soil arching ratio (SAR) and efficacy (E_{str}). However, these design methods show variations in the soil arching results due to the use of different analytical models. In this study, the soil arching ratio (SAR) and efficacy (E_{str}) are compared using different empirical design approaches for a range of normalised embankment heights (h/s). The pile spacing (s) is fixed (2.5 m) whereas the embankment height varies.

TABLE 3.5: Equations for calculating soil arching ratio (*SAR*) and stress efficacy (E_{str}) by different design methods

Design method	Soil arching ratio (*SAR*)	Stress efficacy (E_{str})
Terzaghi (1943)	$SAR = \frac{(s^2 - d^2)}{4hdK \tan\phi'}\left(1 - e^{(-4hdK\ tan\phi')/(s^2-d^2)}\right)$ where, $K = (1\text{-}sin\phi')$	
Hewlett and Randolph (1988)	**At the crown:** $SAR = \left(1 - \frac{d}{s}\right)^{(2K_p-1)}\left(1 - \frac{2s(K_p-1)}{\sqrt{2}h(2K_p-3)}\right) + \left(\frac{2(s-d)(K_p-1)}{\sqrt{2}h(2K_p-3)}\right)$ **At the pile top:** $SAR = \left(\frac{1}{\left(\frac{2K_p}{K_p+1}\right)\left[\left(1-\frac{d}{s}\right)^{(1-K_p)} - \left(1-\frac{d}{s}\right)\left(1+\frac{d}{s}K_p\right)\right] + (1-\frac{d^2}{s^2})}\right)$ where, $K_p = \frac{(1+sin\phi')}{(1-sin\phi')}$	$E_{str} = 1 - \left(\frac{(SAR)(s^2-d^2)}{s^2}\right)$
BS8006 (2010)	**For partial Arching:** $SAR = \frac{2s}{(s+d)(s^2-d^2)}\left[s^2 - d^2\left(\frac{P_c}{\gamma h}\right)\right]$	$E_{str} = 1 - \frac{1}{s^2}\left[s^2 - d^2\left(\frac{P_c}{\gamma h}\right)\right]$
	For full arching: $SAR = \frac{2.8s}{(s+d)^2 h}\left[s^2 - d^2\left(\frac{P_c}{\gamma h}\right)\right]$ where, $\left(\frac{P_c}{\gamma h}\right) = \left[\frac{C_c d}{h}\right]^2$	$E_{str} = 1 - \frac{1.4(s-d)}{s^2 h}\left[s^2 - d^2\left(\frac{P_c}{\gamma h}\right)\right]$
Guido (1987)	$SAR = \frac{(s-d)}{3\sqrt{2}\,h}$	-

where, s is pile spacing, d is pile width, h is the embankment height, and K is the lateral stress coefficient at rest (K_o), K_p is the passive lateral stress coefficient, ϕ' is friction angle of embankment fill, C_c is the arching coefficient, P_c is vertical stress on the pile head and γ is the unit weight of embankment fill.

Figure 3.25(a) shows the variation in soil arching ratio (*SAR*) using these approaches. It is observed that the Guido method (1987) is under-predicated. The Terzaghi (1943) and BS8006 methods (2010) are over-predicated. However, the Hewlett and Randolph method (1988) shows nearly the same trend for higher embankment height. Figure 3.25(b) compares efficacy (E_{str}), showing that Terzaghi method (1943) is very conservative. However, Hewlett and Randolph (1988), and BS8006 (2010) methods are shown closer prediction for higher embankment height. It also can be seen that for efficacy, Guido (1987) shows the slightly higher result with all embankment height.

Thus, it is confirmed that all available approaches for piled embankment design, yield inconsistent results. The possible reason for this inconsistency in the results is assumed shape of the soil arch in these approaches. The shape of soil arch is not convinced in frictional models and the frictional forces follow up vertically along with the pile edges. The rigid models are adopted as a triangular shape of soil arching in 2D and pyramid in 3D. Further, the failure condition is either on the crown of soil arch or the pile head in limit-state equilibrium models. Therefore, it is essential to develop an approach which can be readily adopted for piled embankment design.

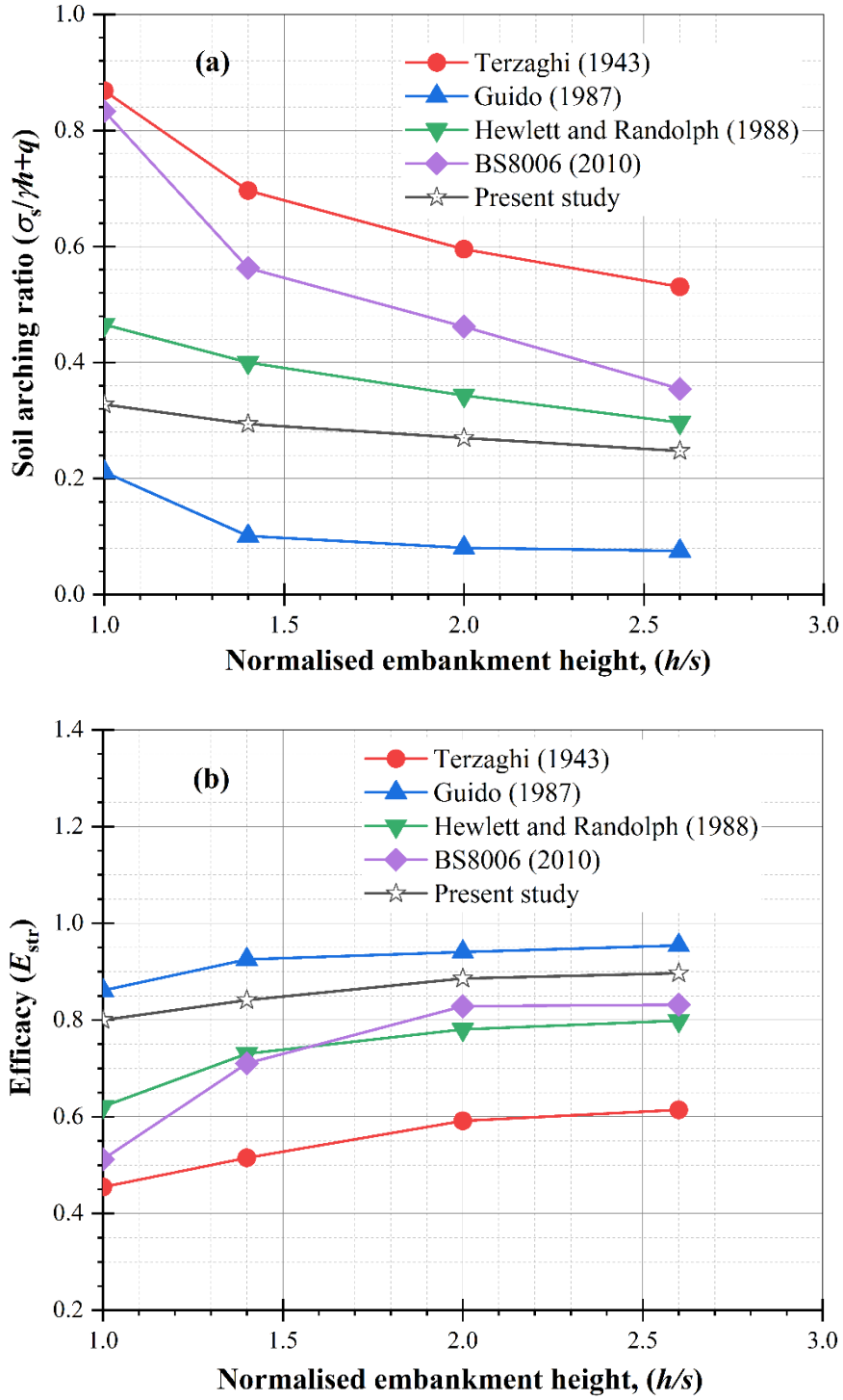

Figure 3.25: Review of available design approaches with present study, (a) soil arching ratio (*SAR*), and (b) efficacy (E_{str})

3.5 PRACTICAL IMPLICATIONS AND LIMITATIONS

Minimising differential settlement is the primary concern for the pile-supported embankment design, and it has been acknowledged that soil arching help to reduce the

differential settlement. In the literature, an optimum embankment height (h_{opt}) is introduced to account for soil arching beyond which differential settlement is minimal (Lai et al. 2018). In this chapter, the height of soil arching is given in terms of clear pile spacing (*s*-*d*), which can be used to determine the optimum embankment height. The parametric study is useful to identify the most critical piled embankment parameters and their correlation with the conditions mobilising soil arching. The practical implications of this chapter are as follows:

- The height of soil arching is summarised in Table 3.4, and it is verified with other published results. It is worth noting that the height of soil arching is 1.04 times of clear pile spacing (*s*-*d*), which is applicable to all considered pile spacing (i.e., 2.0 m, 2.5 m and 3.5 m). Above this embankment height (i.e., 1.04 times of clear spacing), the uniform settlement is observed. This implies that the h_{opt} should be equal to 1.04 times of clear pile spacing (*s*-*d*) for complete mobilisation of soil arching.
- It is noteworthy to mention that soil arching is concerned with the optimum embankment height. However, FEM results indicate that variations in the piled embankment parameters also have significant effects on the extent to which soil arching would be mobilised. Based on the parametric study results, it is evident that embankment modulus and friction angle play vital roles on the load transfer (e.g., soil arching) mechanism. Following relationships are established between soil arching ratio (*SAR*) and the embankment modulus and friction angle as below:

$$SAR = a\,(E_{em})^b + c \qquad \textbf{(3.5)}$$

where, a, b, c are coefficients and the values are $1.331e^{+6}$, -6.08, and 0.28, respectively. And,

$$SAR = -0.0061f' + 0.4791 \quad (\mathbf{3.6})$$

Therefore, current chapter is beneficial to identify optimum embankment height as a function of clear pile spacing, and the most critical design parameters to the optimise embankment design (refer to Equations (3.5 and 3.6).

Further, following are the limitations of this chapter which can be incorporated in future study:

- In this chapter, a linear elastic-perfectly plastic model with Mohr-Coulomb (MC) failure criterion was considered for soil. It is acknowledged that the use of the Mohr-Coulomb model can result in overprediction of strength at higher normal stresses. However, the expected normal stresses in a typical traffic scenario would not be too large in particular to the gravity loading analysis (self-weight of embankment). The low stress condition may not be true, during train loading when train-induced transient stresses attain peak values in the top layers of embankment. This is also evident in past through fully instrumented field studies in Australia (Indraratna et al. 2010; Nimbalkar and Indraratna 2016). In the present Chapter, the dynamic nature of train loading is not considered and hence the use of MC model was considered appropriate for the modelling. The use of MC model is also consistent with other past studies (Li et al. 2018; Ye et al. 2020). Ye et al. (2020) simulated embankment as linear elastic-perfectly plastic model with Mohr-Coulomb (MC) failure criterion considering surcharge. Li et al. (2018) simulated a ballasted railway track with Mohr-Coulomb and (MC) model for embankment considering train speed from 100 km/h to 440 km/h.

- The current chapter deals with the use of cohesive-frictional materials possessing high frictional strength and coarse-grained soil for embankment fill and gravel bed which can largely remain in a relatively dry state. The consolidation settlements are ignored in this study. However, the consolidation can be significant issue when dealing with soft saturated subsoils.

3.6 THREE-DIMENSIONAL (3D) UNIT CELL NUMERICAL MODELLING

The simulated unit cell in 2D plane strain is extended into 3D to investigated the soil arching. Figure 3.26 shows the FE model diagram of a simulated 3D unit cell with a 2D plane strain model. As shown in Figure 3.26(b), a square shape 3D unit cell is modelled which includes the effective region of four piles arranged in a square pattern. Half of the piles are modelled in a square shape with an equivalent width of a circular pile to avoid any convergence error in the simulation. The equivalent width of a pile is calculated with $0.886 \times D$, where D is the diameter of the pile.

The material properties, constitutive model, and element type are considered the same as in 2D planed strain condition. The bottom of the FE model is considered fixed. However, the vertical planes are restraint along their axis.

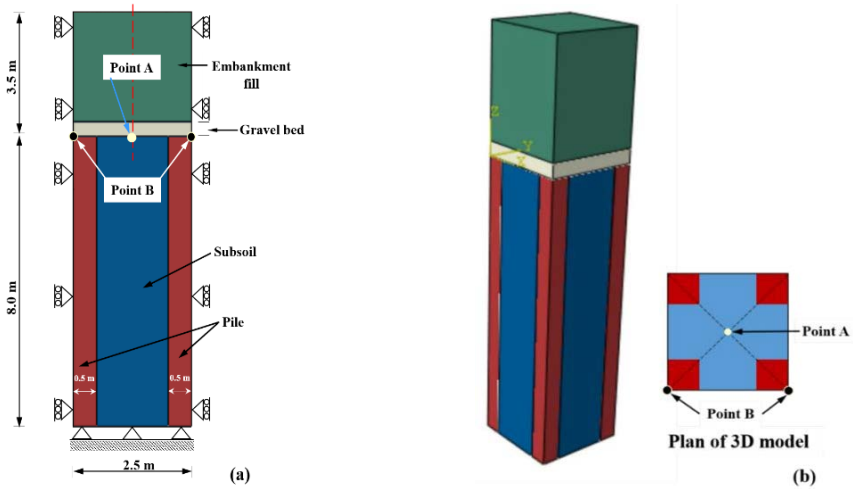

Figure 3.26: FE unit cell model in (a) 2D and (b) 3D

A comparison of vertical stress on point A (subsoil mid) is shown in Figure 3.27. It is found that the modelled until cell in 2D with EA method with 7% difference well match with the 3D unit cell. The EEM and EFS method show a consistent trend of vertical stress variation through the embankment height and a 24% difference with the 3D unit cell model. While the ARR method shows 22% difference with the 3D unit cell. Thus, it can be a further extension of the FE simulation in 3D. However, the 3D simulation is not considered in this study.

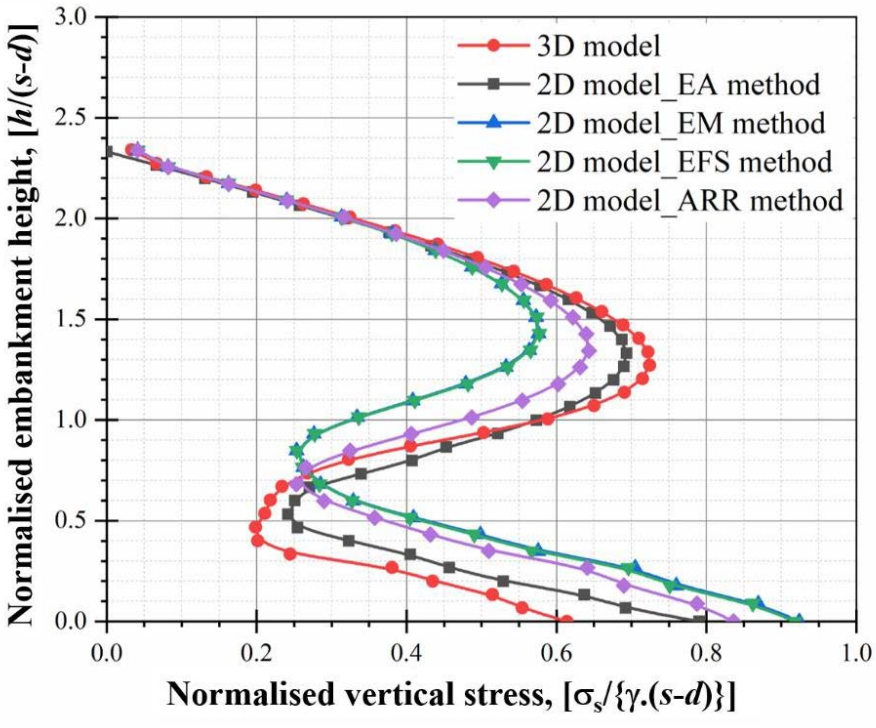

Figure 3.27: Comparison of vertical stress on subsoil in 2D and 3D FE model

3.7 SUMMARY

A numerical study on pile-supported railway embankment under the plane strain condition has been presented in this chapter. In addition, a comparison of the 2D model with the 3D unit cell has also been undertaken. The soil arching behaviour was investigated using the plane strain model results. The study was further expanded to a parametric study to investigate the influence on the size and shape of soil arching with varying piled-embankment parameters, pile spacing embankment height and geosynthetic layer.

Based on the FE analysis, the following summary may be drawn in details from the present chapter:

1) Soil arching was significantly affected by the pile-supported embankment properties.

- The soil arching ratio (*SAR*) decreases up to 61% with an increase in embankment modulus (E_{em}) from 15 to 30 MPa. While, the *SAR* decreases up to 30% with an increase in friction angle from 30° to 45°. Thus, it implies that the tenancy of stress transfer to pile increases with an increase in embankment modulus and friction angle. The effect of pile modulus is found negligible due to a very high modulus of pile. However, soil arching ratio increases up to 7% with an increase in dilation angle, at the lower friction angle.
- The effect of pile modulus on stress efficacy (E_{str}) is found to be negligible, while efficacy increases up to 87% with an increase in embankment modulus (E_{em}) from 15 to 30 MPa. Also, efficacy increases up to 20% with an increase in friction angle from 30° to 45° and the effect of dilation is found to be negligible.
- The maximum tension decreases up to 35% with an increase in embankment modulus (E_{em}) from 5 to 30 MPa. Further, the maximum tension decreases up to 54% with an increase in friction angle from 25° to 45°. However, the effect of pile modulus and dilation are found to be negligible. It implies that the geosynthetic layer is more contributing with less embankment modulus and friction angle.

Therefore, embankment modulus and friction angle are two major parameters that can affect mobilisation of the soil arching. However, the dilation angle has a negligible effect at a lower friction angle. In addition, the height of the embankment cannot adjust. However, this thesis investigates the effect of embankment height on soil arching before it is constructed.

2) The geosynthetic layer at the base of embankment encourages stress transfer to the pile head through the tension in geosynthetic layer.
    - The normalised vertical stress (N_{vs}) is observed less up to 10% at the subsoil top in the reinforced case compared to unreinforced. In contrast, it shows an increase of up to 19% below the outer boundary of soil arching at the pile top (above point B). Thus, it implies that geosynthetic layer improves the load transfer mechanism.
    - The total settlement reduces up to 10% with incorporating the geosynthetic layer at embankment base. Further, the stress concentration ratio (*SCR*) increases up to 21% in the reinforced case compared to unreinforced.
    - The stress concentration ratio (*SCR*) increases with an increase in the stiffness of geosynthetic layer (*J*) and after a certain value of stiffness (2500 kN/M for this study), it remains constant.

Thus, it is clear that the inclusion of a geosynthetic layer can enhance the soil arching and transfer more load on the pile top through the tension.

3) The soil arching was significantly affected by the embankment height and pile spacing.
    - The soil arching mobilisation increases with an increase of embankment height (*h*) until it is not fully mobilised, and after full mobilisation of soil arching negligible effect of embankment height is to be found (*h* = 5 m in this study). It is worth noting that the minimum embankment height for full mobilisation of soil arching should be 1.95-fold of clear pile spacing (*s*-*d*).

- The height of the soil arch (h_{arch}) is closely related to embankment height (h). For a specific pile spacing (s), it increases with an increase in embankment height up to a certain height (5·0 m in this Chapter) and then remains constant beyond this critical embankment height.
- The vertical stress on subsoil top increases up to 118% with a decrease in pile spacing from 3.5 to 2.5 m. Further, the total settlement decreases up to 42% with a decrease in pile spacing from 2.5 to 3.5 m. Thus, pile spacing should be limited for efficient load transfer to the pile top.
- For a specific embankment height, height of soil arching (h_{arch}) increases up to 35% with an increase in clear pile spacing (s-d) within the range from 1.5 to 3.5 m.

4) The shape of the soil arch is not semicircular with uniform thickness, rather, it follows the multi-arch theory.
   - The thickness of the arch is about 0.76 m at the crown of the arch. However, Hewlett and Randolph (1988) and BS8006-1 (2010) assumed that the shape of the arch is semicircular with a uniform thickness which is equal to half of the pile width. It evident that the shape of the arch is very similar to the multi-shell arching theory proposed by Kempfert et al. (2004). The formation of the soil arch starts from the lower boundary to the upper boundary. The shape and formation of the soil arch are still not understood well.

Thus, more research is needed on the shape and formation of the soil arch, in particular.

5) Comparison of the numerical results with the available design methods shows inconsistencies. Further research needs to be carried out in order to improve the available design and analytical methods.

CHAPTER 4

2D ANALYTICAL SCHEME OF SOIL ARCHING IN A PILE-SUPPORTED RAILWAY EMBANKMENT

In this chapter, a theoretical method is presented for the analysis of a pile-supported railway embankment in the two-dimensional (2D) condition. The key modification in this method is to consider the accurate evaluation of surcharge on the soil arching crown, coming from a railway corridor laying on the embankment top. In the past, a small value of surcharge is considered on the embankment top to represent the traffic loading and the same magnitude of surcharge is considered while deriving the vertical stress on the soil arching crown. However, the surcharge value is higher beneath a railway corridor (surcharge due to the railway track and a moving train) and the magnitude of this surcharge reduces with an increase in embankment depth. Thus, the surcharge magnitude at the soil arching crown should be smaller than the surcharge acting on the embankment top. The proposed method is validated by a field study and a full-scale model test and is found to be in good agreement with reasonable accuracy for both studies. In addition, it is also compared with other design methods such as Guido el al. (1987), Low et al. (1994) and BS8006 (2010). In particular, the proposed method enables a realistic approximation of vertical stress on the soil arching crown which can be useful in designing a pile-supported railway embankment.

4.1 INTRODUCTION

In a pile-supported railway embankment, most of the imposed load is transferred to the rigid pile through a shearing stress mechanism named the soil arching and tension action of the geosynthetic layer (Terzaghi 1943; Low et al. 1994; Zhuang et al. 2014). In the recent decade, several theoretical methods (Hewlett and Randolph 1988; Low et al. 1994; Kempfert et al. 2004; Van Eekelen et al. 2013; Pham 2020a) have which focus on the soil arching mechanism have been proposed. Hewlett and Randolph (1988) performed three-dimensional model tests and proposed a semi- spherical empirical model to describe soil arching without any reinforcement. Further, Low et al. (1994) extended Hewlett and Randolph's (1988) model and reported that the critical state of the embankment fill soil element would be either at the crown of the soil arch or just above the pile head. The BS8006 (2010) guideline for the design of the pile-supported embankment is based on Hewlett and Randolph's (1988) method. Kempfert et al. (2004) carried out 1: 3 model tests and proposed a design method. They suggested that, first, the load magnitude on soft soil without any reinforcement should be evaluated, and then the tension in reinforcement is estimated. The EBGEO (2011) guideline for the design of pile-supported embankment is based on this method. Further, Van Eekelen et al. (2013) proposed a new model as a concentric arch model which is the extended version of Hewlett and Randolph's (1988) and the EBGEO (2011) model. This model involves a set of concentric hemispheres arches. Pham (2020a) proposed a comprehensive design method to assess soil arching by combining the effect of soil layer, tension in the geosynthetic layer, subgrade reaction, interaction between geosynthetic layer and soil, and the consolidation of the subsoil under both the linear and nonlinear model. In addition, Fonseca and Palmeira (2019) carried out a series of large-scale tests and investigated the accuracy of the current analytical

methods. They found that the concentric arches theory-based methods, the modified British method (BS8006), and the German method (EBGEO) are in a good agreement with proposed method prediction. In the previous studies, either surcharge is neglected or the same surcharge acting on the embankment top is considered on the soil arching crown. However, the magnitude of the applied surcharge on the embankment top reduces with embankment depth.

In this chapter, Low et al.'s (1994) model in the two-dimensional (2D) plane strain condition is used. Based on Low et al.'s (1994) analysis, Abusharar et al. (2009) reported a simplified method for the analysis of a piled embankment. A uniform surcharge is considered on the embankment top and the surcharge acting on the soil arching crown is considered to be the same as the surcharge acting on the embankment top. The main refinement in this chapter is the inclusion of a uniform equivalent dynamic stress induced by a moving train on the embankment top, and the magnitude of this equivalent dynamic stress attenuation with embankment depth. In addition, the effect of an earthquake is also investigated. The proposed method can be used to assess the soil arching and tension in the geosynthetic layer. In addition, this method is compared with the field study and current design methods to validate its applicability.

4.2 THEORETICAL ANALYSIS OF SOIL ARCHING IN 2D

The proposed theoretical analysis is based on the following assumption:

(i) The embankment fill material is homogeneous, isotropic, and cohesionless: For the analysis of soil arching, it is assumed that the properties of the embankment are uniform throughout the entire embankment in all directions. In other words, a single material is considered for the entire embankment fill. Different material properties may lead to complexity in capturing soil arching in the

embankment fill. The embankment fill material is assumed to have no cohesion (i.e. no intermolecular force of attraction when water is added). Also, in cohesionless material, the tangential stress (σ_θ) = $K_p \times \sigma_r$. However, if we consider cohesive material, the tangential stress (σ_θ) = $K_p \times \sigma_r + 2 \times c \times (K_p)^{0.5}$ (Pham 2020a).

(ii) The subsoil is homogeneous, isotropic, and cohesive: In a pile-supported embankment, the settlement of subsoil is maximum at the centre of two adjacent piles and minimum near the pile top. It is possible when embankment fill acts as a perfectly flexible foundation resting on the subsoil (cohesive material). If the foundation (i.e. embankment fill) is subjected to a uniformly distributed load, the contact pressure will be uniform and the foundation will experience a sagging profile as reported in Das (2021).

(iii) Embankment fill and subsoil deforms vertically: Vertical settlement is more crucial for soil arching compared to the horizontal deformation of soil. In addition, the horizontal loads components can be affected to the soil arching. However, this thesis is limited to vertical load components only.

(iv) The deformation in piles is zero: The rigid pile is considered to develop sufficient shear stress due to the stiffness difference of the pile and subsoil.

(v) A smooth surface between piles and the surrounding subsoil (i.e., no friction): The skin friction between piles and the surrounding subsoil can affect the subsoil reaction (k_s). Thus, to avoid any difficulty it is assumed that there is no friction between the pile and subsoil.

(vi) Ratio of the embankment height (h) to the centre to centre pile spacing (s) is greater than 0.5: Hewlett and Randolph (1988) considered a semicircular arch with a diameter of semicircular arch is (s-d). So, the radius is 0.5(s-d), which

is equal to the minimum embankment height (h). Thus, the ratio $h/(s\text{-}d) = 0.5$ and this ratio should be larger than 0.5 for full soil arching development.

4.2.1 Theoretical analysis of soil arching in an unreinforced pile-supported railway embankment

The analytical solution is based on the semi-cylindrical arch model proposed by Low et al. (1994), which was extended by Abusharar et al. (2009) to a two-dimensional (2D) plane strain condition. The main refinement in the proposed analysis is the vertical stress at depth h' (i.e., the soil arching crown) below the embankment top due to the self-weight of the rail track (σ_{track}) and the moving train (σ_{train}), as shown in Figure 4.1.

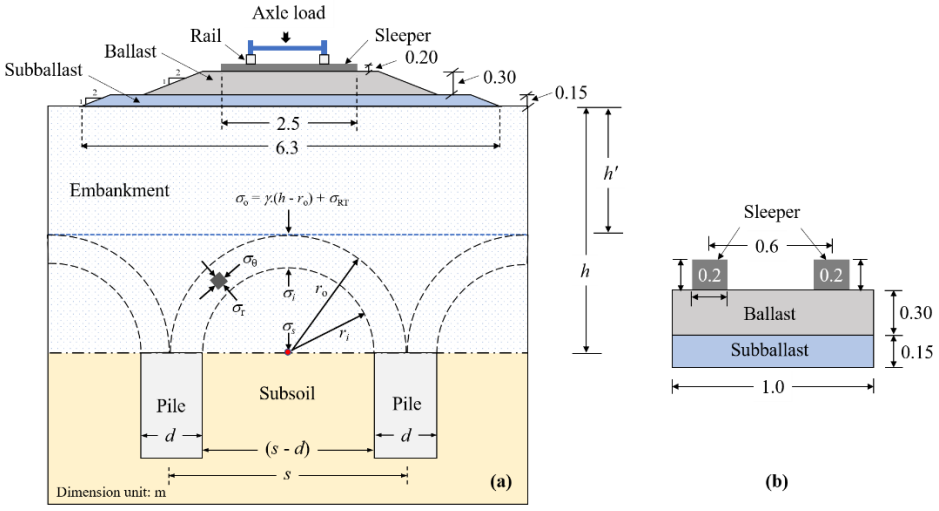

Figure 4.1: (a) Cross-sectional view of the pile-supported railway embankment; (b) Longitudinal view of the considered unit length with the sleeper

The radial equilibrium for an element in the semicircular arch is determined following (Low et al. 1994):

$$\frac{d\sigma_r}{dr} + \frac{\sigma_r - \sigma_\theta}{r} + \gamma = 0 \quad (4.1)$$

where σ_r = radial stress (kN/m^2); σ_θ = tangential stress (kN/m^2); r = radial distance (m); and γ = unit weight of embankment fill material (kN/m^3). For limit state analysis, the tangential stress (σ_θ) = $k_p.\sigma_r$; where $k_p = (1+\sin\phi)/(1-\sin\phi)$.

$$\frac{d\sigma_r}{dr} + \frac{\sigma_r(1-k_p)}{r} + \gamma = 0 \quad (4.2)$$

The general solution of Equation (4.2) is:

$$\sigma_r = \gamma.\left(\frac{r}{k_p - 2}\right) + C'.r^{(k_p-1)} \quad (4.3)$$

The boundary condition is at the soil arching crown, where $r = s/2$ and $\sigma_r = \gamma(h-s/2) + \sigma_{RT}$ and where σ_{RT} = total vertical stress on the soil arching crown due self-weight of the rail track and the moving train.

The vertical stress due to track (σ_{track}) is the component due to the self-weight of the rail, sleeper, ballast and subballast. Figure 4.1(a) shows the cross-section of considered railway embankment and Figure 4.1(b) shows the longitudinal view of the considered sleeper configuration. The calculation of σ_{track} is described in Table 4.1.

Table 4.1: Calculation of the surcharge on the embankment top

Material	Density (ρ), kg/m^3	Unit volume (V), m^3	Mass weight (kg)	Total weight (W_{track}), kN	Area where total weight applied, ($A_{\sigma track}$) m^2	Vertical stress (σ_{track}) due to self-weight of rail track on the embankment top, kPa
Rail (UIC-60)	-	-	60			
Sleeper	2350	0.2	470	41.59	6.3	6.60
Ballast	1700	1.23	2091			
Subballast	1800	0.9	1620			

The vertical stress due to the moving train (σ_{train}) is calculated using the trapezoidal approximation (2:1 method) (refer to Equation 3.7). The dynamic amplification factor (DAF) is calculated using the ORE method (refer to Equation 3.8). The vertical stress on the embankment top due the different train speed is listed in Table 4.2.

Table 4.2: Calculation of the moving train surcharge (σ_{train}) due to 25 t axle load

Train speed (V), km/h	Vertical stress (σ_{train}) due to moving on the embankment top, kPa
40	193.69
60	194.60
80	196.38
100	199.30
120	203.66

The radial stress (σ_r) is denoted as σ_o at the soil arching crown in the embankment. The imposed vertical stress due to the track and moving train is dissipates in trapezoidal form (using trapezoidal approximation) as shown in Figure 4.2. In this method, the stress dissipates with the depth in the form of a trapezoid that has 2:1 (vertical: horizontal) inclined sides. The imposed vertical stress due to the moving train is considered uniformly distributed at the embankment top for simplicity (Sadeghi 2008). A list of contact pressure distribution beneath the sleepers is reported in Sadeghi (2008). It also stated that a uniform contact pressure sleeper and ballast is considered to determine sleeper stresses for design.

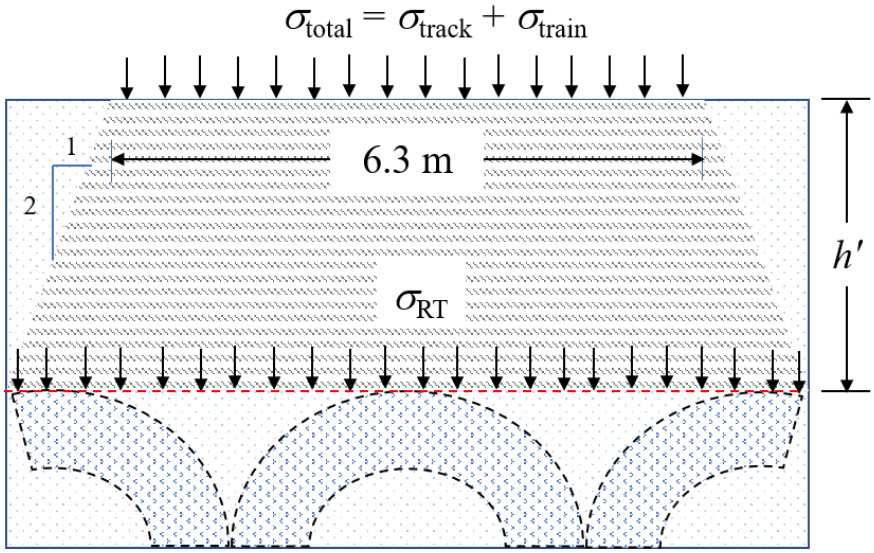

Figure 4.2: Vertical stress (σ_{RT}) at depth *h*' below the embankment top due to the self-weight of rail track and the moving train

Thus, the vertical stress on the soil arching crown (σ_{RT}) due to the rail track and moving train is:

$$\sigma_{RT} = \left(\frac{\left(\sigma_{track} \times A_{\sigma_{track}}\right) + \left(\sigma_{train} \times A_{\sigma_{train}}\right)}{A_{\sigma_{RT}}} \right) \quad \textbf{(4.4)}$$

where, $A_{\sigma track}$ and $A_{\sigma train}$ = the area of applied stress due to the track and train loading, respectively = area of embankment top (A_{Emtop}); $A_{\sigma RT}$ = area of applied stress on the soil arching crown.

Thus, the vertical stress (σ_i) is just below the inner boundary of the soil arching, where $r = (s\text{-}d)/2$, is

$$\frac{\sigma_i}{\gamma h} = \frac{(s-d)}{2h(k_p-2)} + \left(\frac{s-d}{s}\right)^{(k_p-1)} \left[1 - \frac{s}{2h}\left(1 + \frac{1}{k_p-2}\right) + \frac{\sigma_{RT}}{\gamma h}\right] \quad \textbf{(4.5)}$$

The vertical stress (σ_s) acting on the subsoil midway between the pile heads is:

$$\sigma_s = \sigma_i + \frac{\gamma(s-d)}{2} \quad \textbf{(4.6)}$$

$$\sigma_s = \frac{\gamma(s-d).(k_p-1)}{2.(k_p-2)} + \left(\frac{s-d}{s}\right)^{(k_p-1)} \left[\gamma h - \frac{\gamma.s}{2}\left(1 + \frac{1}{k_p-2}\right) + \sigma_{\mathrm{RT}}\right] \quad \textbf{(4.7)}$$

The stress efficacy (E_{str}) is defined as the portion of the embankment weight that is carried by the piles

$$E_{str} = 1 - \frac{\sigma_s.A_s}{(\gamma h+\sigma_{\mathrm{RT}}).A} \quad \textbf{(4.8)}$$

where A_s = area of clear spacing = (s-d) × 1 m^2 and A = area of centre to centre pile spacing = s × 1 m^2. The unit value is considered for the plane strain problem.

From Equation (4.7) and (4.8), the stress efficacy is:

$$E_{str} = 1 - \frac{(s-d)^2(k_p-1)}{2sh(k_p-2)} + \left(\frac{s-d}{s}\right)^{k_p} \left[1 - \frac{s}{2h}\left(1 + \frac{1}{k_p-2}\right) + \frac{\sigma_{\mathrm{RT}}}{\gamma h}\right] \quad \textbf{(4.9)}$$

For overall equilibrium condition

$$s(\gamma h + \sigma_{\mathrm{RT}}) = d.\sigma_p + (s-d).\sigma_s \quad \textbf{(4.10)}$$

The degree of load transfer is quantified using the stress concentration ratio (*SCR*):

$$SCR = \frac{\sigma_p}{\sigma_s} = \frac{s(\gamma h+\sigma_{\mathrm{RT}})-(s-d).\sigma_s}{d.\sigma_s} \quad \textbf{(4.11)}$$

4.2.2. Theoretical analysis of soil arching in a reinforced pile-supported railway embankment

In a reinforced pile-supported railway embankment, it is assumed that the deformed shape of the geosynthetic layer is a circular arc of radius *R* and the maximum deflection of *y* m in between the piles, as shown in Figure 4.3. The geosynthetic layer is laid down on a subsoil layer of depth 8 m and it is fixed at the edges of the pile heads. In addition,

a rigid interface of the geosynthetic layer with the pile head is considered to avoid any risk of puncturing or tearing the geosynthetic material. For simplicity, the creep effect is neglected during this analysis.

From Figure 4.3:

$$\sin\theta = \frac{4\left(\frac{y}{s-d}\right)}{1+4\left(\frac{y}{s-d}\right)^2} \tag{4.12}$$

Let $(y/(s\text{-}d)) = \beta$;

$$\sin\theta = \frac{4\beta}{1+4\beta^2} \tag{4.13}$$

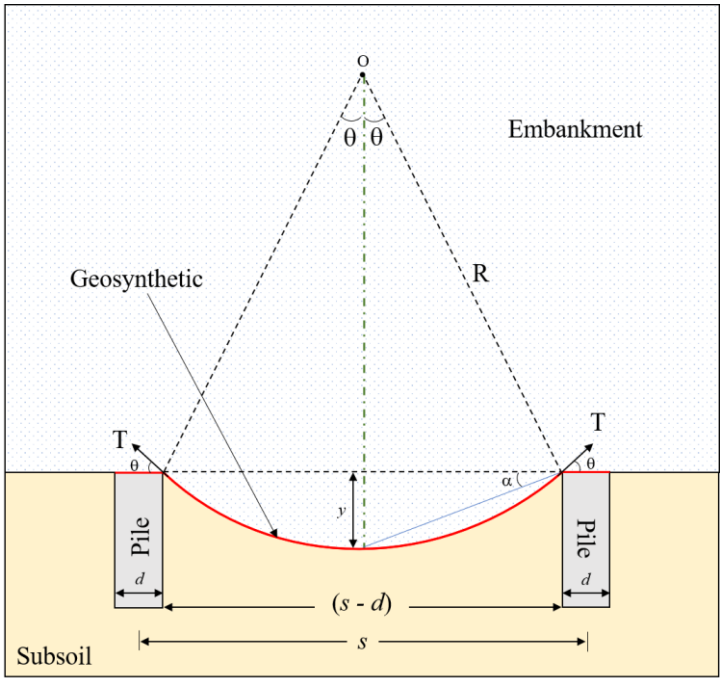

Figure 4.3: Deflection in the geosynthetic layer overlying the pile head and subsoil

$$\tan\alpha = \frac{y}{(s-d/2)} = 2\beta \tag{4.14}$$

From Equation (4.14), when α is very small; $\tan\alpha = \alpha$

$$\theta = 2\alpha = 2\tan^{-1}(2\beta) = 4\beta \tag{4.15}$$

The axial strain in geosynthetic layer (ε_{geo}) is:

$$\varepsilon_{geo} = \frac{\Delta(s-d)}{(s-d)} \tag{4.16}$$

From Equation (4.13) and (4.15):

$$\varepsilon_{geo} = 4\beta^2 \tag{4.17}$$

4.2.2.1 Vertical stress distribution on the geosynthetic layer in a reinforced pile-supported railway embankment

In recent decades, it has been argued that subsoil has a significant effect on the load-settlement behaviour of the geosynthetic layer (Chen et al. 2008; Rui et al. 2020). In this regard, a part of the vertical stress (σ_s) is borne by the geosynthetic layer (σ_{geo}), as shown in Figure 4.4:

$$\sigma_{geo} = \sigma_s - \sigma_{up} \tag{4.18}$$

where σ_s is the vertical stress on the top of the geosynthetic layer by the soil arching effect; σ_{up} is the upward vertical reaction stress on the bottom of the geosynthetic layer for the equilibrium condition.

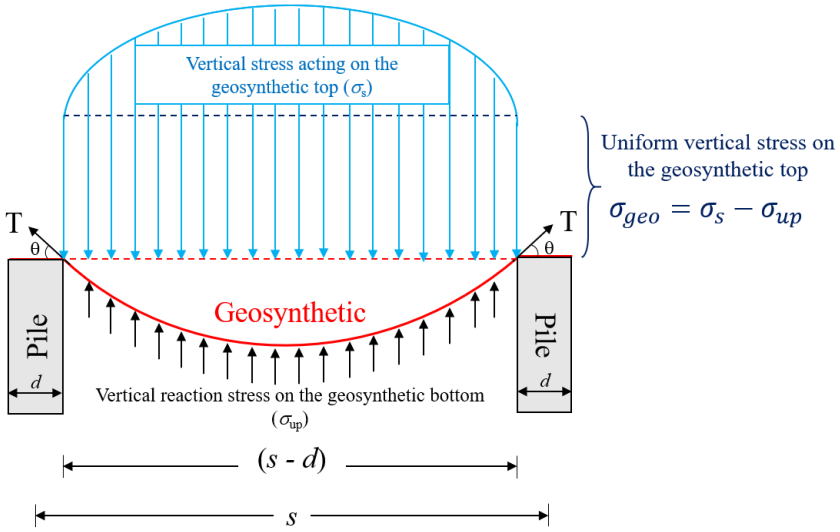

Figure 4.4: Vertical stress distribution on the geosynthetic layer and tension

In a pile-supported embankment, the subsoil has very complex load-settlement characteristics as it is nonlinear, anisotropic and heterogeneous. The vertical stress, coming from embankment fill including surcharge, which is carried by the geosynthetic layer is dependent on these load-settlement characteristics of subsoil. Consequently, it is very difficult to establish any mathematical formulation to predict the vertical stress on the geosynthetic layer. In this regard, a simple mathematical formulation often becomes essential with reasonable accuracy. Thus, in this study, the Winkler model is considered for subsoil. This model has already been used in several design guidelines such as EBGEO (2011) and CUR226 (2016). The upward vertical reaction stress on the bottom of the geosynthetic layer (σ_{up}) is calculated as:

$$\sigma_{up} = y.k_s = \frac{y.E_o}{D_{act}} \tag{4.19}$$

where y is the maximum deflection of geosynthetic layer; k_s is the modulus of the subgrade reaction; D_{act} is the active depth of subsoil (full depth of subsoil; Pham 2020a); and E_o is the one-dimensional modulus of the subsoil, which can be derived using Young´s modulus of the subsoil ($E_{subsoil}$) and Poisson´s ratio (v) as follows:

$$E_o = E_{subsoil}\left(\frac{(1-v)}{(1+v).(1-2v)}\right) \quad \textbf{(4.20)}$$

Thus, Equation (4.18) become:

$$\sigma_{geo} = \sigma_s - \left[\frac{y\,.\,E_o}{D_{act}}\right] \quad \textbf{(4.21)}$$

4.2.2.2 Tension in the geosynthetic layer

As subsoil deforms vertically, the strength of the geosynthetic layer is mobilized due to the vertical stress on the top of the geosynthetic layer. Consequently, it acts as a tensioned cable and results in reduced pressure on the subsoil. It is assumed that the deform shape of the geosynthetic layer is circular and the strain is uniformly distributed in the geosynthetic layer to simplify the analysis (Pham 2020b). However, prediction can differ using different deformation shape of geosynthetic layer. Initially, the geosynthetic layer is flat and its length is the same as the pile spacing (*s*). As shown in Figure 4.4, tension (*T*) in the geosynthetic layer can be determined as follows:

$$2T\sin\theta = \sigma_{geo}(s-d) \quad \textbf{(4.22)}$$

From Equation (4.21) and (4.22);

$$T = \frac{(s-d)(1+4\beta^2)}{8\beta}\left(\sigma_s - \left[\frac{y\,.\,E_o}{D_{act}}\right]\right) \quad \textbf{(4.23)}$$

4.2.2.3. Soil-geosynthetic layer interface

Skin friction along the interface of the geosynthetic layer also develops a part of the tension in the geosynthetic layer. Figure 3.5 shows the shear stress developed along with the geosynthetic layer interface and can be defined as:

$$\tau = \tau_{top} + \tau_{bottom} = \sigma_n \tan\delta \quad \textbf{(4.24)}$$

where σ_n is normal stress in the interface; δ is the friction angle between the soil and geosynthetic layer (tan $\delta = \lambda \tan\phi'$); ϕ' is the shearing resistance angle of the surrounding soil; and λ is a factor which lies between 0.7 to 0.9 depending on the type of soil (Di Donna et al. 2016). The value of λ is taken 0.8 for this study.

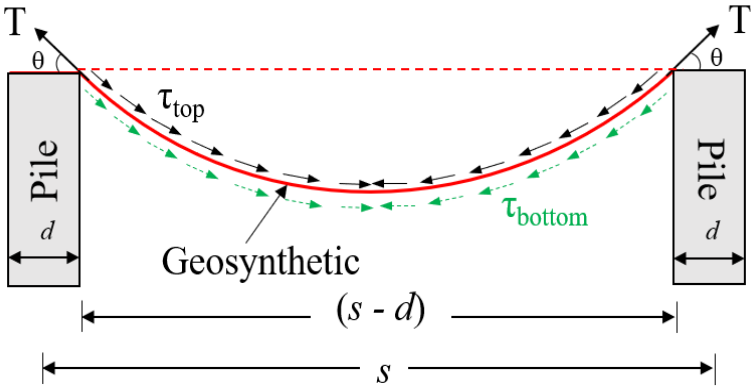

Figure 4.5: Shear stress developed at the soil-geosynthetic layer interface

The embankment and soft soil both contribute to the skin friction. Thus, the soil-geosynthetic layer interface shear stress for the embankment and subsoil are:

$$\tau_{top} = \sigma_s(\lambda . \tan \phi_{em}) \quad \textbf{(4.25)}$$

$$\tau_{bottom} = \sigma_{up}(\lambda . \tan \phi_{subsoil}) \quad \textbf{(4.26)}$$

where, ϕ_{em} and $\phi_{subsoil}$ is the shearing resistance angle of embankment fill and subsoil, respectively.

Substituting Equation (4.25) and (4.26) into (4.24):

$$\tau = \lambda . \left(\sigma_s . \tan \phi_{em} + \frac{y.E_o}{D_{act}} . \tan \phi_{subsoil}\right) \quad \textbf{(4.27)}$$

The tension in the geosynthetic layer is considered as a function of two strain components, one due to the load and the other due to the skin friction.

Thus,

$$T = J\,.\,\varepsilon_{geo} + \tau\frac{(s-d)}{4} \tag{4.28}$$

where, J is tensile stiffness of geosynthetic layer (kN/m).

Substituting Equation (4.17) and (4.27) into (4.28),

$$T = 4\beta^2 J\ + \frac{\lambda}{4}\left(\sigma_s.\tan\phi_{em} + \frac{y.E_o}{D_{act}}.\tan\phi_{subsoil}\right)(s-d) \tag{4.29}$$

With the combing of Equation (4.23) and (4.29),

$$A.\beta^3 + B.\beta^2 + C.\beta + D = 0 \tag{4.30}$$

where $A = 32.J + 4.(s-d).\frac{E_o}{D_{act}}$;

$B = 2.(s-d)^2.\lambda.\frac{E_o}{D_{act}}.\tan\phi_{subsoil} - 4.(s-d).\sigma_s$;

$C = 2.(s-d).\lambda.\sigma_s.\tan\phi_{em} + (s-d)^2.\frac{E_o}{D_{act}}$;

$D = -(s-d).\sigma_s$

The efficacy can be derived as Equation (4.8):

$$E_{str} = 1 - \frac{\sigma_{geo}.A_s}{(\gamma h+\sigma_{\mathrm{RT}}).A} \tag{4.31}$$

Now for overall equilibrium as Equation (4.10):

$$s(\gamma h + \sigma_{\mathrm{RT}}) = d.\sigma_p + (s-d).\sigma_{geo} \tag{4.32}$$

From Equation (4.32),

$$SCR = \frac{\sigma_p}{\sigma_{geo}} = \frac{s(\gamma h+\sigma_{\mathrm{RT}})-(s-d).\sigma_{geo}}{d.\sigma_{geo}} \tag{4.33}$$

4.3 VALIDATION OF THE PROPOSED ANALYTICAL METHOD

In this section, the proposed analytical model is validated with a full-scale model test and field test (Cao et al. 2016; Chen et al. 2016) in terms of the stress efficacy and maximum deflection in the geosynthetic layer. Full details of the site condition and the monitoring scheme are reported in Cao et al. (2016) and Chen et al. (2016). However, a brief description of the design parameters, used to validate the analytical model are given in Table 4.3.

Table 4.3: A brief of parameters used for validation of present analytical method

Parameters		Cao et al. (2016)	Chen et al. (2016)
Embankment	Height, h (m)	2.4	3.2
	Unit weight, γ (kN/m^3)	19.5	21.2
	Friction angle ϕ' (degree)	35	42
Subsoil	Active depth, D_{act} (m)	4.68	-
	Unit weight, γ (kN/m^3)	19.5	9.81
	Young's modulus of elasticity, E (MPa)	8.80	2
Pile	Width, d (m)	1	1
	Pile spacing, s (m)	1.6	1.8
Geosynthetic layer	Tensile stiffness, J (kN/m)	300*	2459#
Surcharge on the embankment top, σ_{total} (kPa)		48	12.25

*biaxial warp-knitting geogrid; #uniaxial geogrid used in the study

4.3.1 Field study (*Cao et al. 2016*)

Cao et al. (2016) investigated a field test on a high-speed railway embankment in Anhui province, China. The height and crown-width of the tested embankment were 2.4 m and 13.2 m, respectively. A backfill material of 3 m height with 16 kN/m^3 unit weight was used to mimic the surcharge and obtain precise results. The tested embankment was supported on cement-fly ash-gravel (CFG) piles. The pile spacing and width were 1.6 m and 1m, respectively. The subsoil properties were determined

using the static cone penetration test and the plated loading test. One geogrid layer was sandwiched into a highly frictional gravel layer. Field monitoring sensors were installed at various locations such as within the embankment fill, in the subsoil, and on the pile top to monitor the different aspects of the testing embankment.

The proposed analytical method is compared with the existing methods and the measured field data is summarised in Table 4.4. The proposed method is in good agreement with Cao et al.'s (2016) measured field data with a difference of 3.8% in terms of maximum tension in the geosynthetic layer. The stress efficacy and deflection are overestimated by the BS8006 (2010) method whereas Guido et al. (1987) underestimated the stress efficacy.

Table 4.4: Comparison of present method with Cao et al. (2016) measurement and other methods

Parameters	Guido et al. (1987)	Low et al. (1994)	Abusharar el al. (2009)	BS8006 (2010)	Present method	Measured field data (Cao et al. 2016)
Efficacy, E_{str}, (%)	80.31	92.14	94.90	97.77	94.59	90.4
Max. tension in geosynthetic layer, T (kN/m)	4.98	2.25	2.55	11.87	2.49	2.40
Max. deflection in geosynthetic layer, y (mm)	-	5.30	5.41	17.47	5.36	4.20

Figure 4.6 shows the relative error in the different methods with the measured stress efficacy by Cao et al. (2016). The proposed method is in good agreement with Cao et al.'s (2016) measured field data with a relative error of 4.6%. Guido et al. (1987) and BS8006 (2010) methods have a higher relative error by 11.56% and 8.15%, respectively whereas, Low et al.'s (1994) method is under the very less relative error

as it underestimated the stress efficacy. Abusharar et al.'s (2009) method has a 4.9 % relative error which is slightly higher than the proposed method.

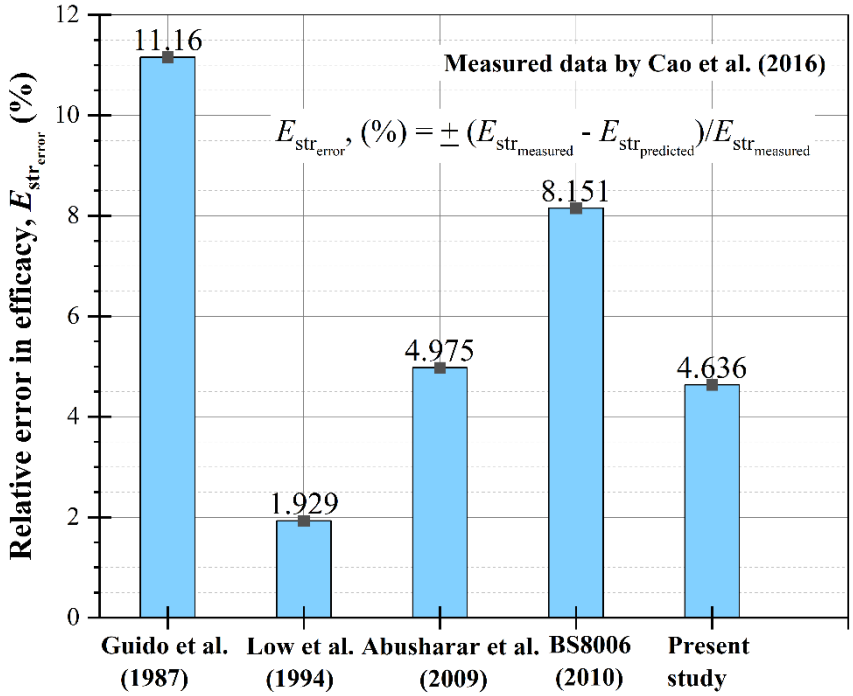

Figure 4.6: Relative error of different methods in predicting stress efficacy based on Cao et al. (2016)

4.3.2 Field study (*Chen et al. 2016*)

Chen et al. (2016) carried out a model test to assess the tension in a geosynthetic layer underneath the high-speed railway embankment. In this model test, water bags are used to represent the subsoil and control the differential settlement between the pile and adjacent subsoil. Therefore, support from the subsoil is assumed to be zero in this case.

The proposed analytical method is compared with the existing methods and the measured field data of Chen et al. (2016) as summarised in Table 4.5. The proposed method is in good agreement with Chen et al.'s (2016) measured field data with a difference of 0.38% in terms of stress efficacy. However, the difference in tension and

deflection in the geosynthetic layer is 37% and 14%, respectively. Guido et al. (1987) underestimated stress efficacy by 20%, whereas they overestimated tension in the geosynthetic layer by 99%. The BS8006 (2010) method overestimated the deflection in the geosynthetic layer by 25%.

Table 4.5: Comparison of present method with Chen et al. (2016) measurement and other methods

Parameters	Guido et al. (1987)	Low et al. (1994)	Abusharar el al. (2009)	BS8006 (2010)	Present method	Measured field data (Chen et al. 2016)
Efficacy, E_{str}, (%)	76.67	91.61	92.64	90.46	92.35	92.0
Max. tension in geosynthetic layer, T (kN/m)	35.77	24.21	24.79	26.63	24.60	17.93
Max. deflection in geosynthetic layer, y (mm)	-	39.69	40.16	43.66	40.01	35.0

The relative error in different methods with measured stress efficacy by Chen et al. (2016) is shown in Figure 4.7. It can be seen that the proposed method is in good agreement with Chen et al.'s (2016) measured data with a relative error of 0.38%. Guido et al.'s (1987) method demonstrates a higher relative error by 16.67% whereas the BS8006 (2010), and the methods by Low et al. (1994) and Abusharar el al. (2009) have a relative error of 1.67%, 0.42%, and 0.69%, respectively.

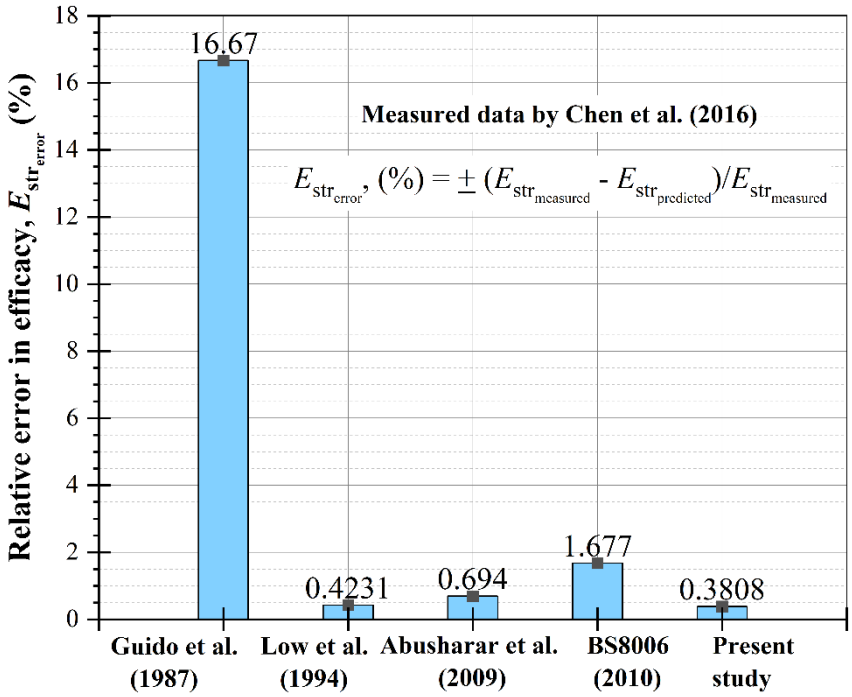

Figure 4.7: Relative error of different methods in predicting stress efficacy based on Chen et al. (2016)

In Cao et al. (2016) and Chen et al. (2016), a small surcharge value is considered, thus the difference in relative error is not greatly different between Abusharar et al.'s (2009) method and the proposed method. However, the difference between the relative error may increase with an increase in the surcharge value on the embankment top.

4.4 PARAMETRIC STUDY

In this section, the effect of different parameters of pile-supported railway embankments on soil arching using the proposed method is investigated in terms of stress concentration ratio, stress efficacy, deflection in geosynthetic layer, tension and axial strain in the geosynthetic layer. A train speed of 40 km/h and normalised embankment height (h/s-d) = 3 are considered to see the effect of other parameters except for train speed and embankment height, respectively. For general applicability,

embankment height is normalised by clear spacing (*s*-*d*) to see the effect of embankment height.

The embankment geometry parameters of Meena et al. (2020) are used as a reference case for the parametric study. The input parameters of Meena et al. (2020) are listed in Table 3.1. In addition, details of the considered parameters are as follows: (*i*) Embankment - height (h) = varies from 1 m to 15 m, unit weight (γ) = 20 kN/m^3, Young's modulus of elasticity (E) = 20 MPa, internal frictional angle (ϕ) = 30°, cohesion (c) = 0.1 kPa; (*ii*) Subsoil - depth (D_{sub}) = 8 m, unit weight (γ) = 18.4 kN/m^3, Young's modulus of elasticity (E) = 2.2 MPa, internal frictional angle (ϕ) = 22°, cohesion (c) = 8 kPa; and (*iii*) Pile - width (d) = 1 m, spacing (s) = 2.5 m; (*iv*) Geosynthetic layer (Secugrid^R 60/60Q1 @ 2 % strain @ rib thickness of 2 mm) - tensile stiffness (J) = 1000 kN/m.

4.4.1 Effect of embankment height

The effect of embankment height on the stress concentration ratio (*SCR*) for different ratios of pile width (d) to clear spacing (*s*-*d*) is shown in Figure 4.8. As shown in Figure 4.8(a) for unreinforced cases, the *SCR* increases with an increase in the ratio of d/(*s*-*d*). In addition, for a higher d/(*s*-*d*) ratio (1 in this study), the *SCR* initially slightly decreases, and after a certain normalised embankment height (3 in this study) it increases. The effect of embankment height is not prominent for a higher d/(*s*-*d*) ratio due to the higher value of surcharge on the embankment top. However, the *SCR* increases with an increase in embankment height for a lower d/(*s*-*d*) ratio. Similar results are reported in other studies (Abusharar et al. 2009; Van Eekelen et al. 2013).

Figure 4.8(b) shows the effect of embankment height on the *SCR* in reinforced cases. It can be seen that the *SCR* decreases with an increase in the ratio of d/(*s*-*d*) for

a smaller embankment height. However, it is likely to approach a limiting value for a larger embankment height, and it implies the critical height of soil arching. In addition, the *SCR* decreases with an increase in embankment height for a small *d*/(*s*-*d*) ratio and it increases with an increase in embankment height as the *d*/(*s*-*d*) ratio increases. This trend of the *SCR* is due to the presence of reinforcement at the base of the embankment. The *SCR* in the reinforced case is higher compared to the unreinforced case due to additional vertical stress on the pile head that is transferred from the geosynthetic layer. The geosynthetic layer enhances the stress concentration ratio by 125-500%.

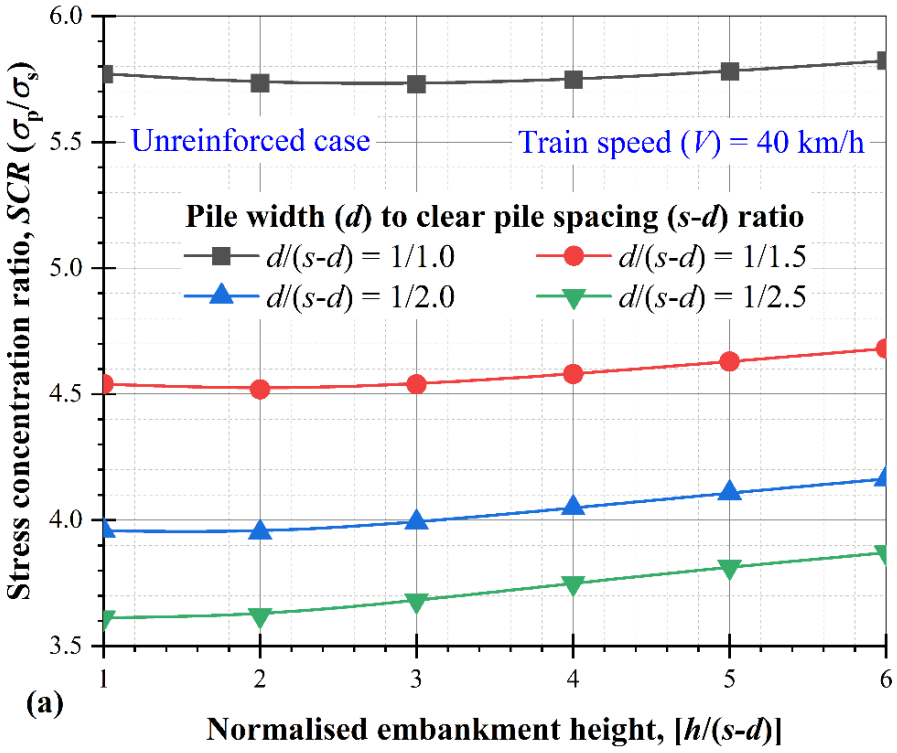

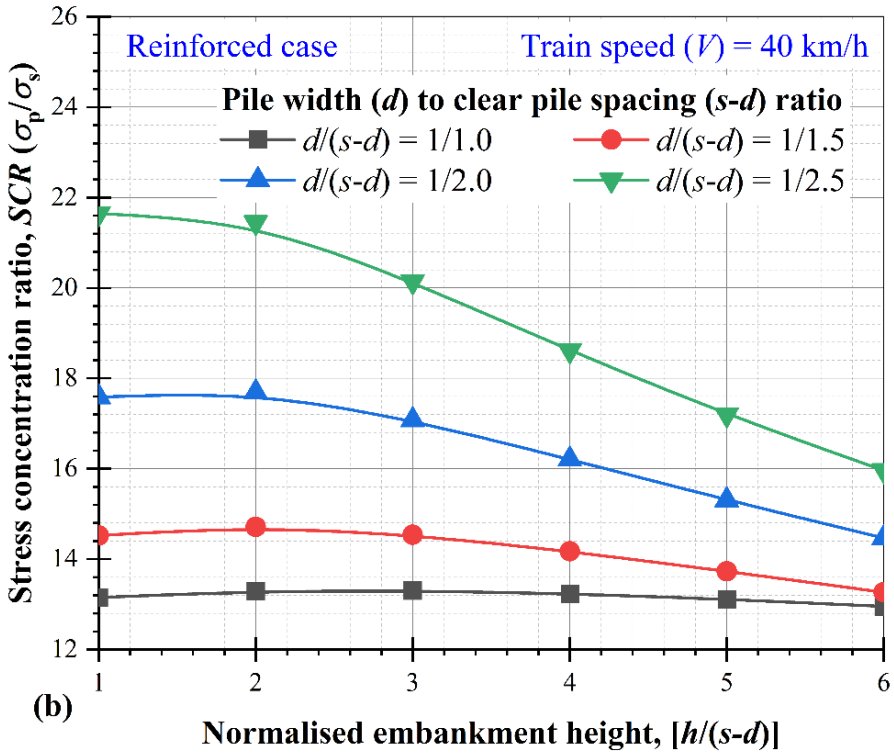

Figure 4.8: Effect of embankment height on the stress concentration ratio in (a) the unreinforced case; and (b) the reinforced case

Figure 4.9 shows the influence on stress efficacy (E_{str}) of embankment height for different $d/(s\text{-}d)$ ratios. For unreinforced cases, a negligible effect is found on stress efficacy due to a higher surcharge on the embankment top, as shown in Figure 4.9(a). However, it increases with an increase in embankment height for a small $d/(s\text{-}d)$ ratio, whereas Figure 4.9(b) shows the effect of embankment height on stress efficacy in the reinforced case. The E_{str} decreases with an increase in embankment height when the $d/(s\text{-}d)$ ratio decreases. The E_{str} in the reinforced case is higher compared to the unreinforced case due to additional vertical stress on the pile head that transfers from the geosynthetic layer. The geosynthetic layer enhances the E_{str} by 9-51%.

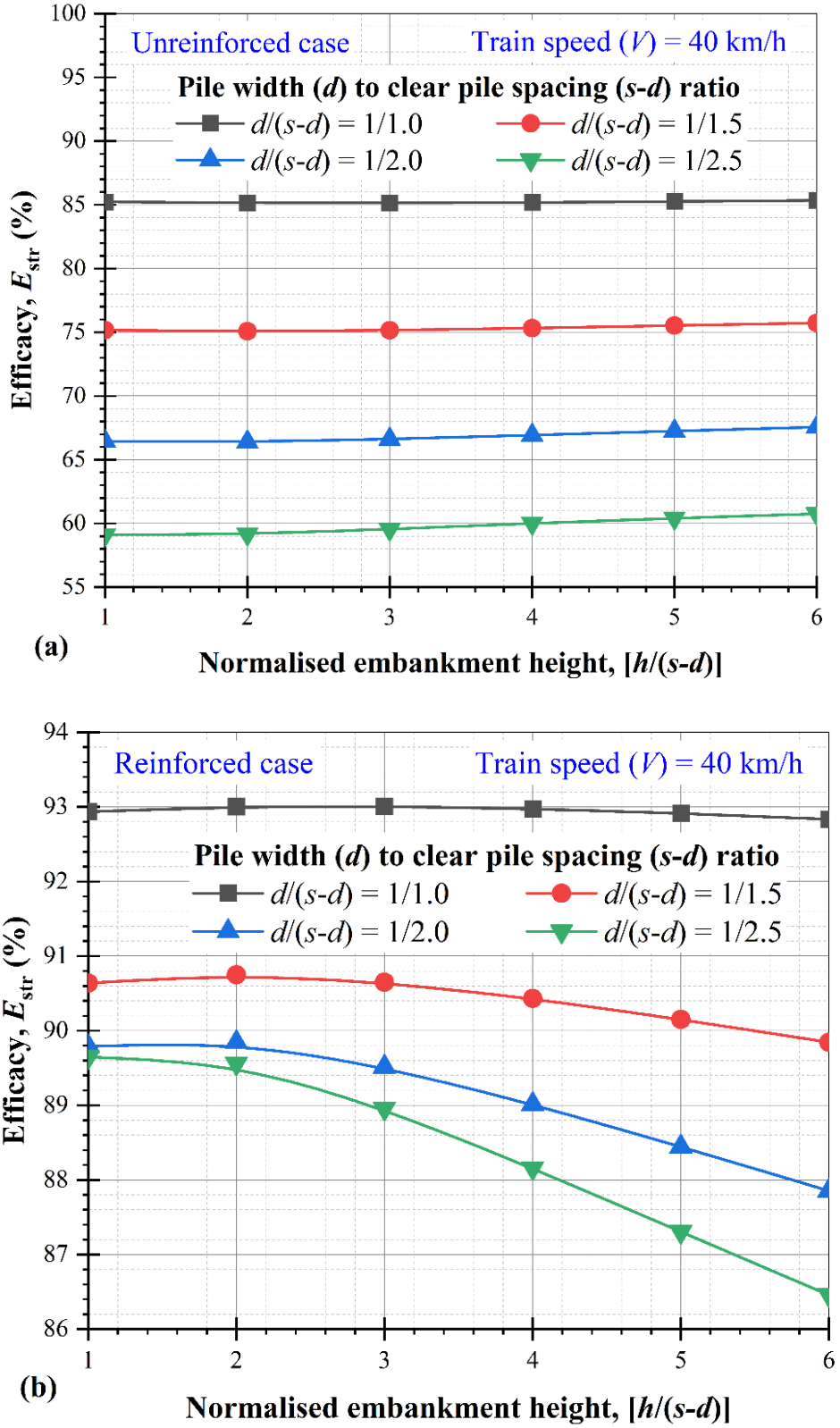

Figure 4.9: Effect of embankment height on efficacy in (a) the unreinforced case (b) the reinforced case

Figure 4.10 shows the effect of embankment height on tension (T) and axial strain (ε_{geo}) in the geosynthetic layer for different $d/(s\text{-}d)$ ratios. The same trend is found for both tension and axial strain in the geosynthetic layer, as shown in Figure 4.10 (a) and (b), respectively. The tension and axial strain in the geosynthetic layer decrease with an increase in the $d/(s\text{-}d)$ ratio, and both increase with an increase in embankment height. Zhuang et al. (2014) reported similar results. However, a negligible effect is found at a higher $d/(s\text{-}d)$ ratio due to a lower deflection in the geosynthetic layer.

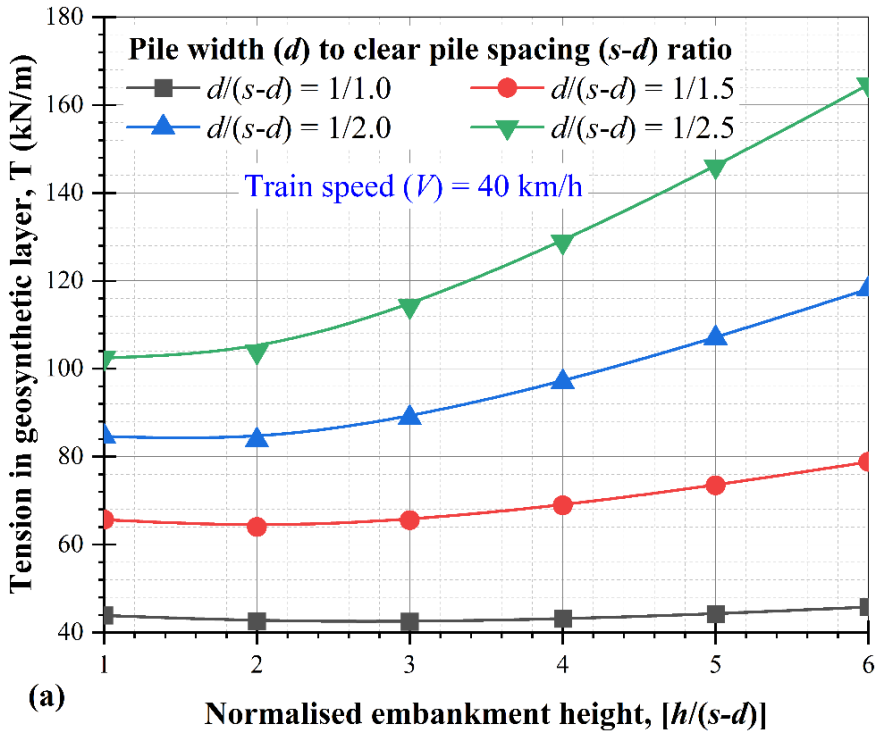

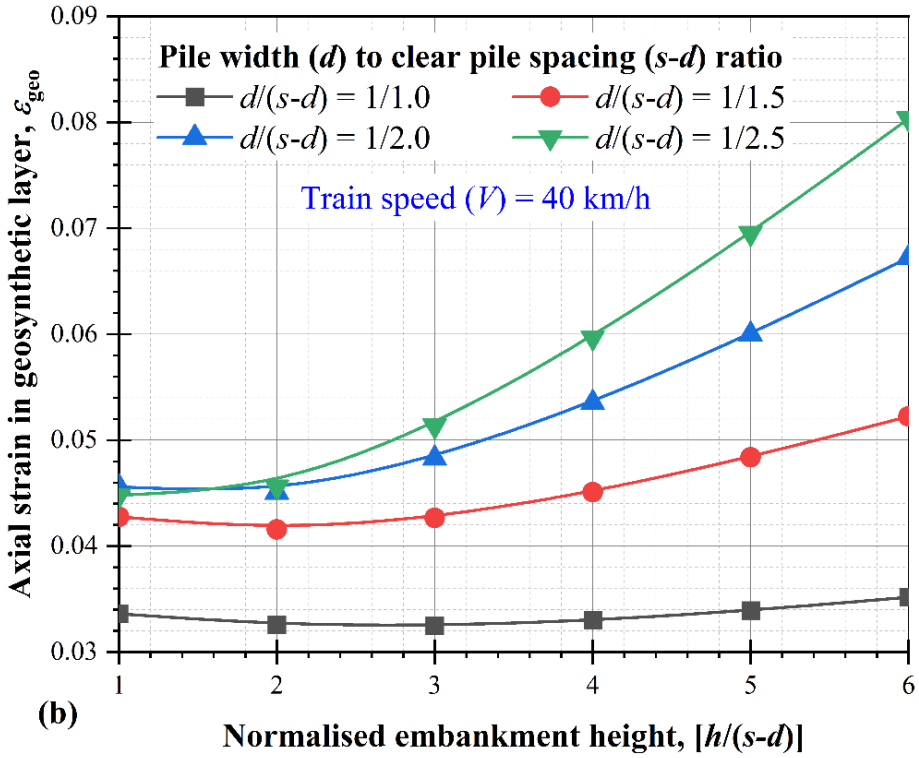

Figure 4.10: Effect of embankment height on (a) tension, and (b) axial strain in the geosynthetic layer

Figure 4.11 demonstrates the effect of embankment height on the maximum deflection (y) in the geosynthetic layer. It is evident that the maximum deflection decreases with an increase in the $d/(s\text{-}d)$ ratio and increases with an increase in embankment height. Similar results are reported by Pham (2020a). However, deflection in the geosynthetic layer remains the same at all embankment heights for a higher $d/(s\text{-}d)$ ratio due to the small pile spacing.

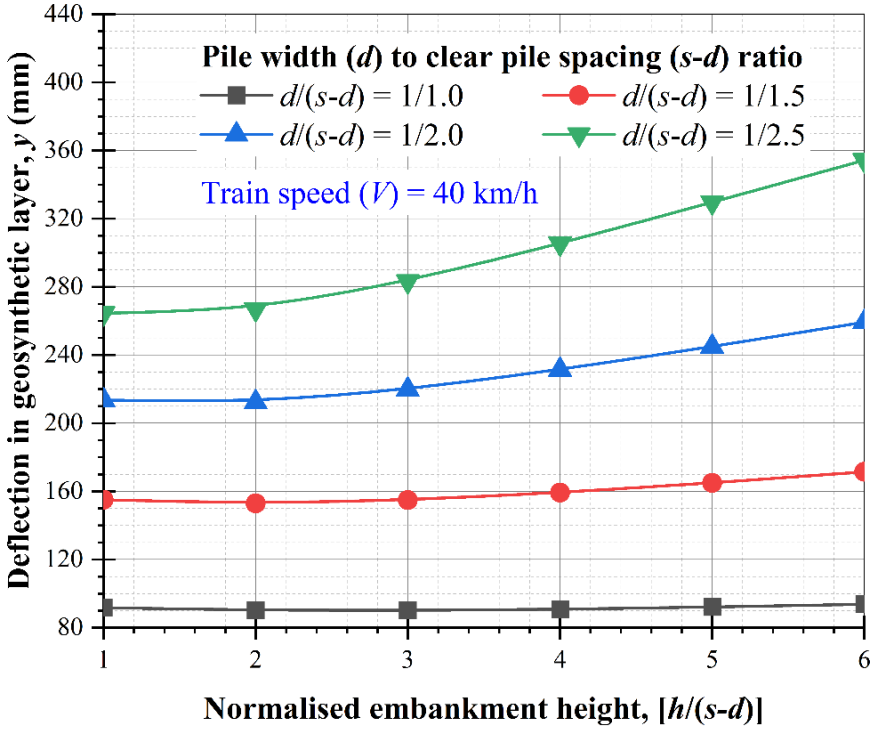

Figure 4.11: Effect of embankment height on deflection in the geosynthetic layer

4.4.2 Effect of the one-dimensional modulus of subsoil

The subgrade reaction of the subsoil, which can be derived from the one-dimensional modulus of subsoil (E_o), plays a major role in the settlement of embankment fill and load support on the subsoil. Therefore, it is important to investigate the effect of the one-dimensional modulus of the subsoil.

Figures 4.12 shows the effect of the one-dimensional modulus of subsoil (E_o) on the stress concentration ratio for different $d/(s\text{-}d)$ ratios. For an unreinforced case, as shown in Figure 4.12(a), the *SCR* increases with an increase in the $d/(s\text{-}d)$ ratio. However, there is no change in the *SCR* by changing the one-dimensional modulus of the subsoil. This may be because the subsoil makes no contribution in the unreinforced case, whereas in the reinforced case, as shown in Figure 4.12(b), the *SCR* slightly increases with an increase in the $d/(s\text{-}d)$ ratio for a smaller E_o value (0.5 MPa for this study) and it decreases with an increase in the $d/(s\text{-}d)$ ratio for a higher E_o value (3.0

MPa for this study). The geosynthetic layer transfers the majority load to the pile top by the membrane effect when an increase in the $d/(s\text{-}d)$ ratio is at a small value of E_o. while, for a higher value of the E_o, the contribution of the geosynthetic layer is not fully utilized as the subsoil is sufficiently stiff to support the imposed load. Thus, the *SCR* increases with a decrease in the $d/(s\text{-}d)$ ratio at a higher value of the E_o.

A higher *SCR* is observed in the reinforced case compared to the unreinforced case due to the presence of a geosynthetic layer which transfers an extra load on the pile top. This implies that in reinforced cases, the subsoil significantly contributes to the load transfer mechanism. Also, it is worth noting that reinforcement plays a crucial role for very compressible subsoil (e.g. E_o = 0.5 MPa for this study).

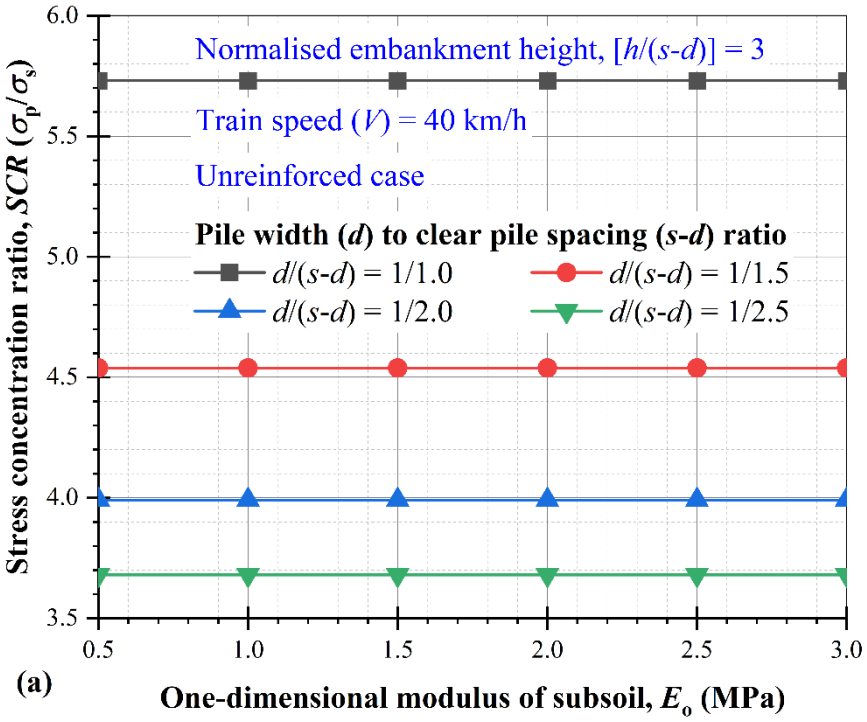

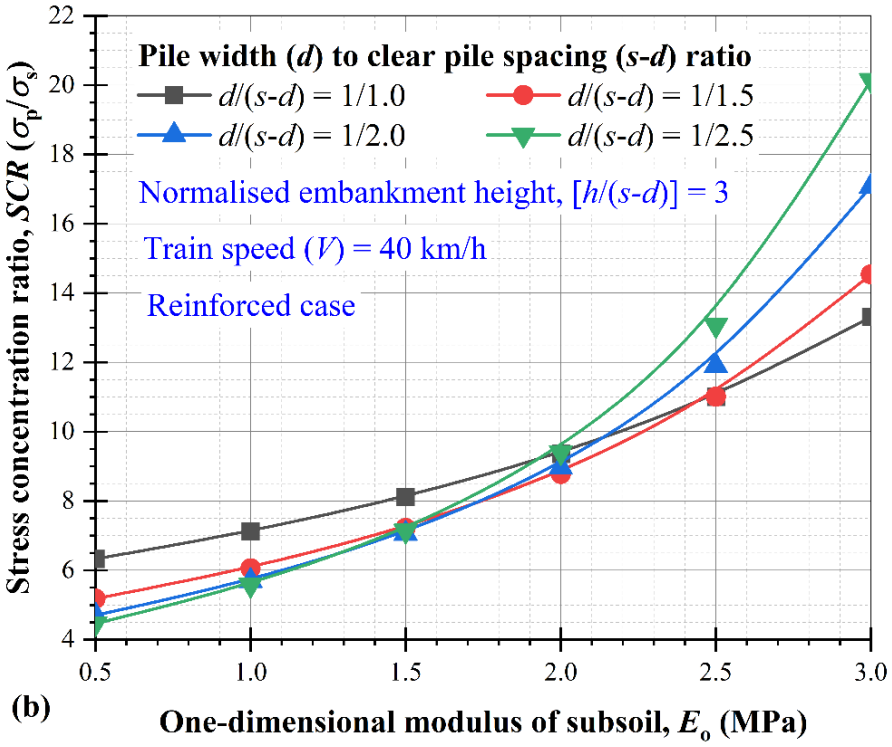

Figure 4.12: Effect of the one-dimensional modulus of the subsoil on the stress concentration ratio in (a) the unreinforced case; and (b) the reinforced case

The effect of the one-dimensional modulus of subsoil (E_o) on stress efficacy for different $d/(s\text{-}d)$ ratios is shown in Figures 4.13. The unreinforced case (refer to Figure 4.13a) follows the same trend as shown in Figure 4.12(a) for the SCR, whereas in the reinforced case as shown in Figure 4.13(b), the stress efficacy increases with an increase in the $d/(s\text{-}d)$ ratio and E_o. The stress efficacy increases for different $d/(s\text{-}d)$ by 7.5 - 39%. However, it is likely to approach a limiting value for a high value of the E_o, which implies that the subsoil is sufficiently stiff to support the imposed load and reinforcement is not necessary for stiff subsoil.

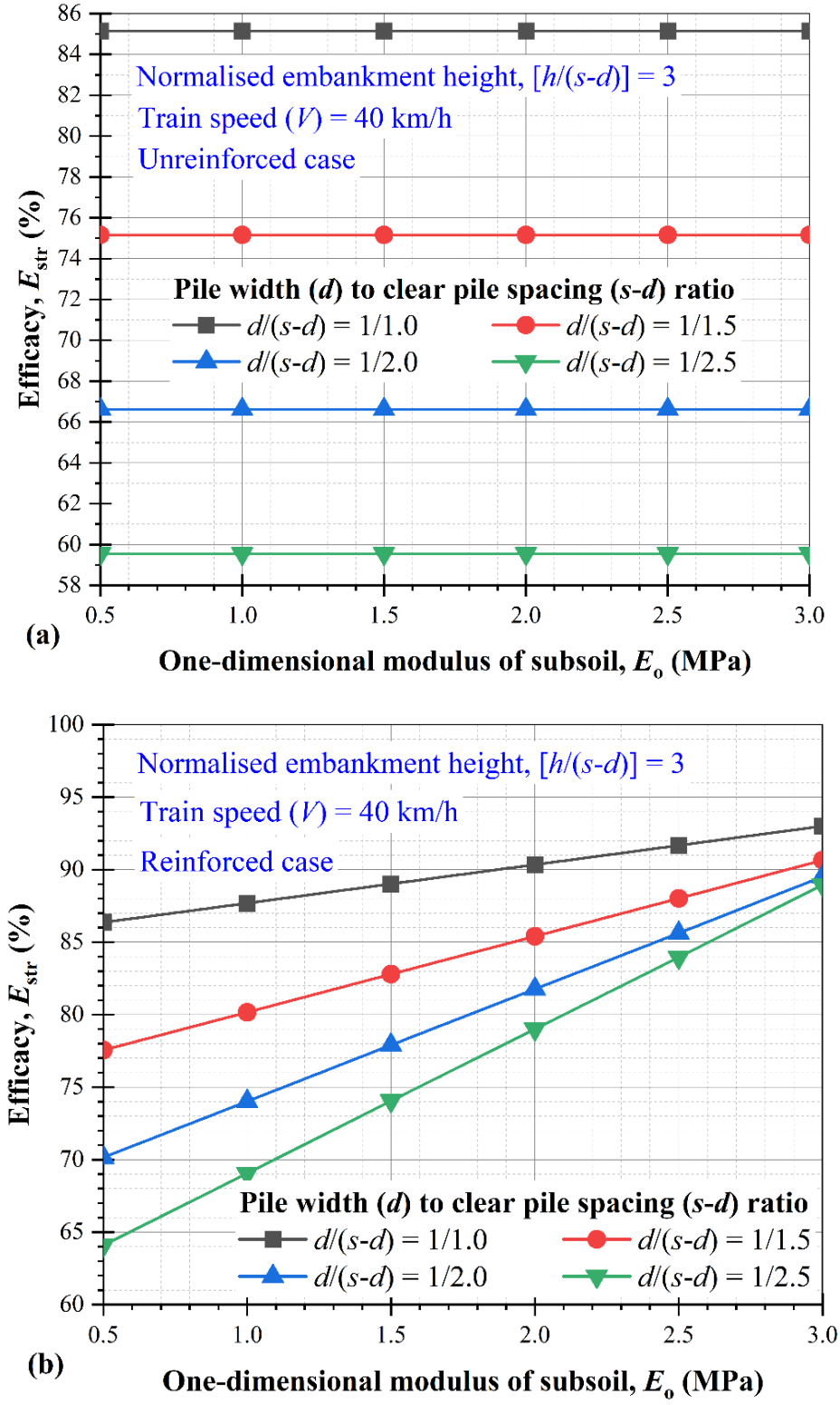

Figure 4.13: Effect of the one-dimensional modulus of subsoil on stress efficacy in (a) the unreinforced case; and (b) the reinforced case

Figure 4.14 shows the effect of the one-dimensional modulus of subsoil on tension (T) in the geosynthetic layer for different $d/(s\text{-}d)$ ratios. The tension in the geosynthetic layer decreases by up to 70% with an increase in the $d/(s\text{-}d)$ ratio and E_o, and after approaching a higher value of E_o it is likely to remain a limiting value.

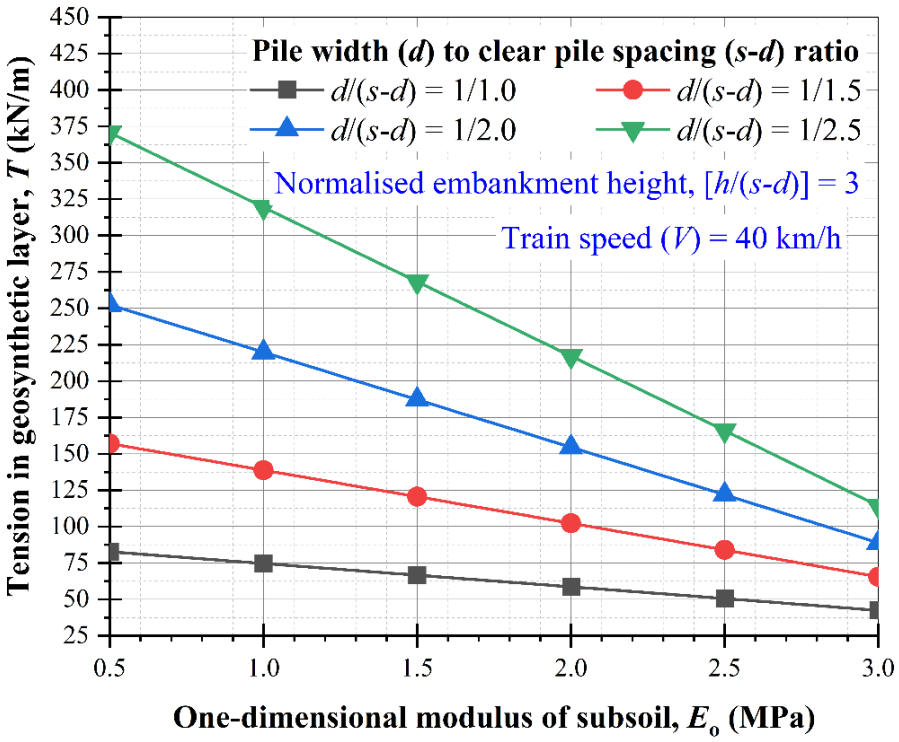

Figure 4.14: Effect of the one-dimensional modulus of subsoil on the tension in the geosynthetic layer

The effect of the one-dimensional modulus of the subsoil on the geosynthetic layer deflection is shown in Figure 4.15. The geosynthetic layer deflection decreases with an increase in the $d/(s\text{-}d)$ ratio and E_o. Further, it is likely to approach a limiting value with an increasing the E_o. A similar result is reported in (Zhuang et al. 2014; Pham 2020a). However, Pham (2020a) reported the effect of the one-dimensional modulus in terms of subgrade reaction (k_s).

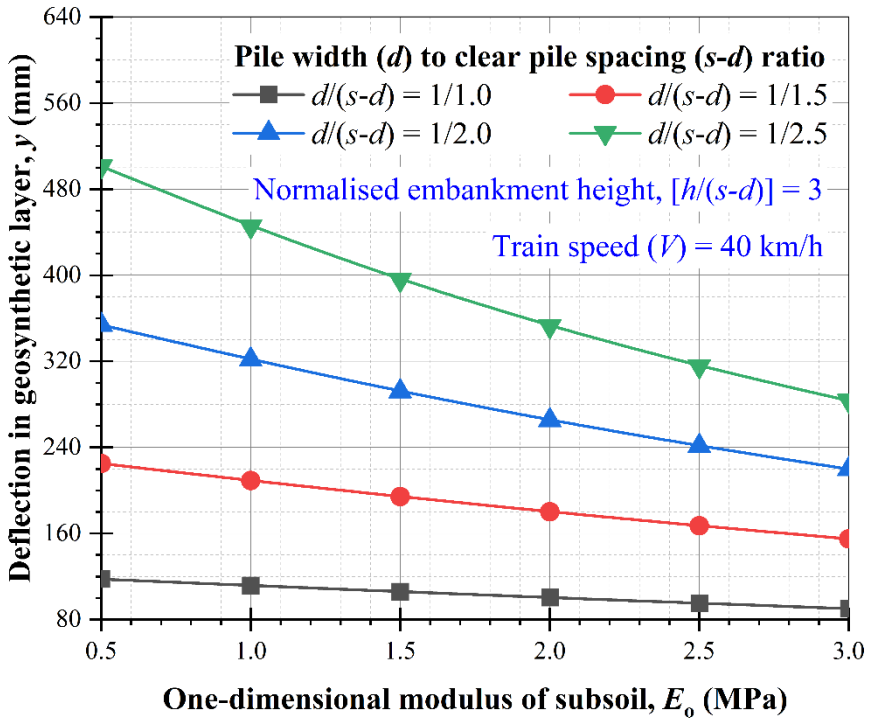

Figure 4.15: Effect of the one-dimensional modulus of subsoil on deflection in the geosynthetic layer

4.4.3 Effect of the tensile stiffness of the geosynthetic layer

Currently, the existing design methods do not incorporate the effect of tensile stiffness of the geosynthetic layer although the membrane behaviour of the geosynthetic layer also depends on the tensile stiffness of the geosynthetic layer. Therefore, the effect of tensile stiffness of the geosynthetic layer is investigated here.

As shown in Figure 4.16(a), it is evident that the *SCR* decreases with an increase in the *d*/(*s*-*d*) ratio and the tensile stiffness of the geosynthetic layer. There is an inconsistent trend at zero tensile stiffness although at a high tensile stiffness, it is probably approaching a limiting value. Figure 4.16(b) shows the effect of tensile stiffness of the geosynthetic layer on stress efficacy. Stress efficacy increases with an increase in the *d*/(*s*-*d*) ratio and decreases with an increase in the tensile stiffness of the geosynthetic layer.

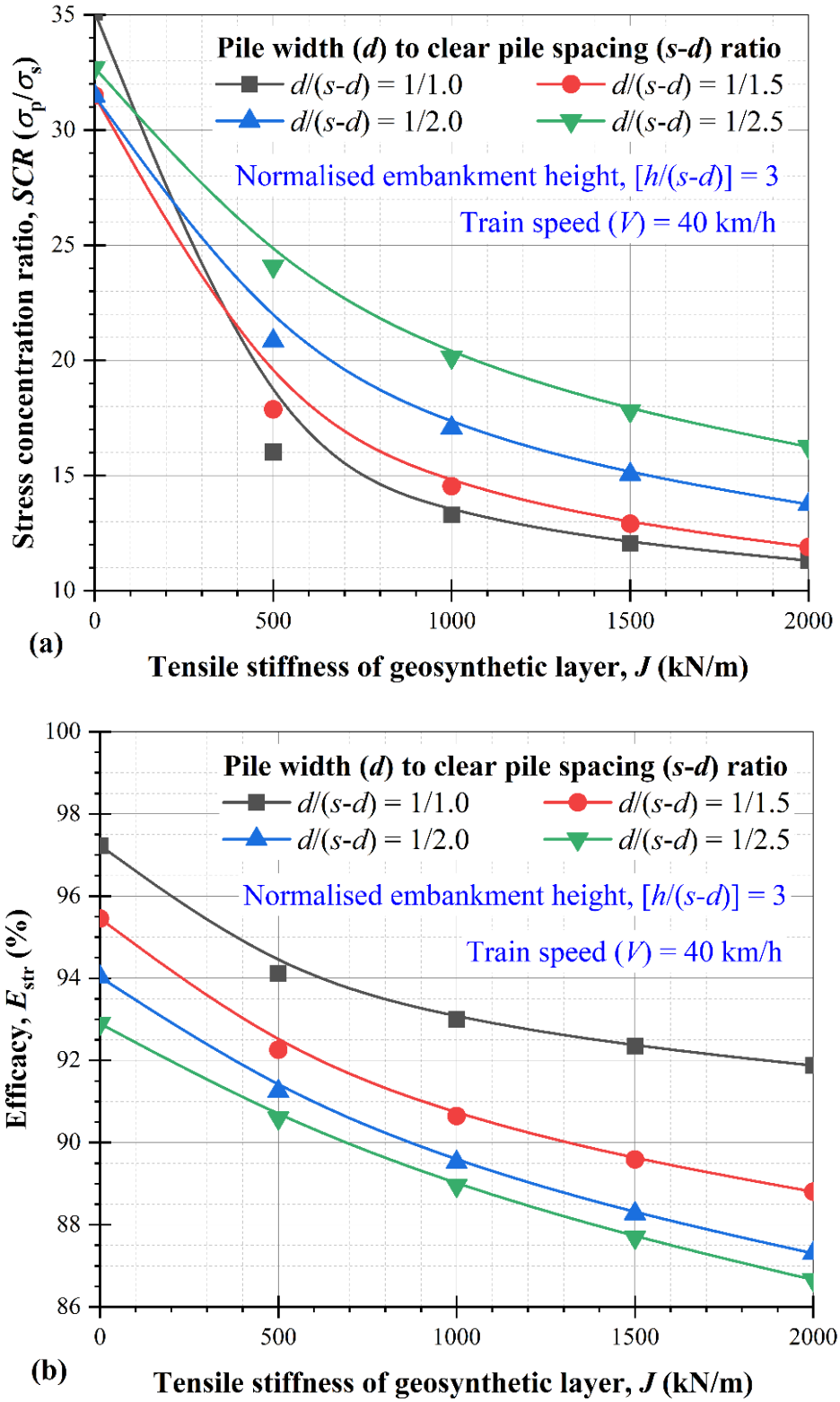

Figure 4.16: Effect of tensile stiffness of the geosynthetic layer on (a) the stress concentration ratio; and (b) the stress efficacy

Figure 4.17 demonstrates the effect of tensile stiffness of the geosynthetic layer on geosynthetic layer deflection. The deflection in geosynthetic layer (y) decreases with an increase in the $d/(s\text{-}d)$ ratio and the tensile stiffness of the geosynthetic layer. It decreases by up to 20% with an increase in tensile stiffness from 0 to 2000 kN/m which implies that as pile spacing decreases and the tensile stiffness of the geosynthetic layer increases, the membrane behaviour of the geosynthetic layer becomes effective, consequently, less deflection in the geosynthetic layer occurs.

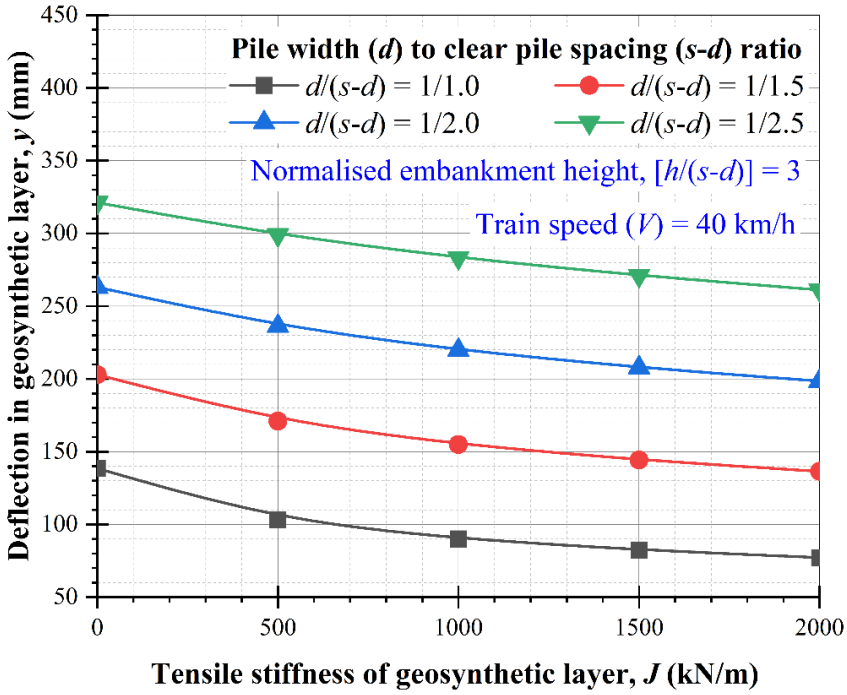

Figure 4.17: Effect of tensile stiffness of the geosynthetic layer on deflection in the geosynthetic layer

The effect of the tensile stiffness of the geosynthetic layer on the tension and axial strain in the geosynthetic layer is shown in Figure 4.18. As shown in Figure 4.18(a), the tension in the geosynthetic layer decreases with an increase in the $d/(s\text{-}d)$ ratio, and it increases by up to 150% with an increase in the tensile stiffness of the geosynthetic layer from 0 to 2000 kN/m, whereas the axial strain decreases by up to

45% with an increase in the tensile stiffness of the geosynthetic layer from 0 to 2000 kN/m, as shown in Figure 4.18(b). Similar results are found in (Zhuang et al. 2014; Pham 2020a).

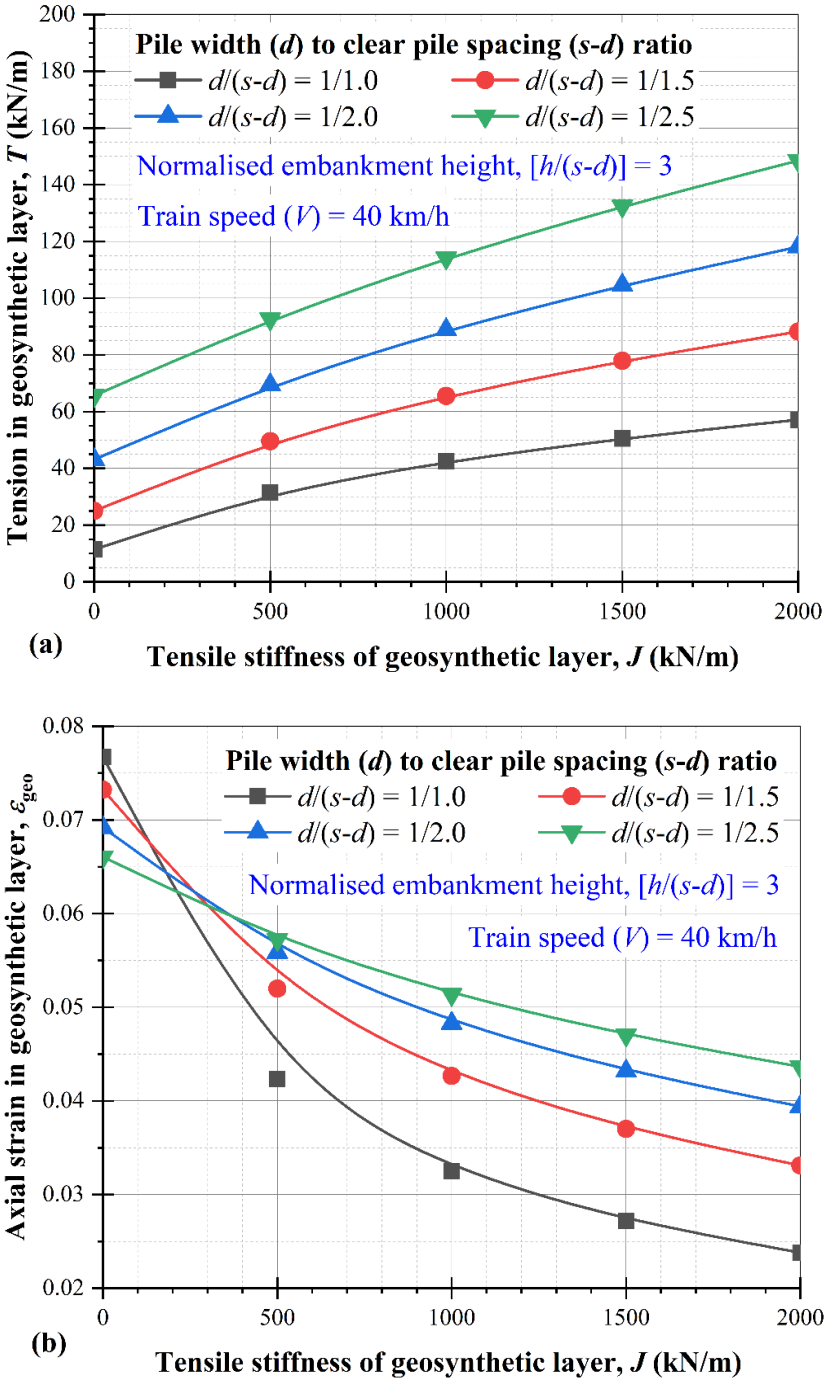

Figure 4.18: Effect of tensile stiffness of the geosynthetic layer on (a) tension; and (b) axial strain in the geosynthetic layer

4.4.4 Effect of equivalent dynamic load induced by different train speed

Increasing the train speed leads to an increase in the surcharge on the embankment top, which can influence soil arching mobilisation. Therefore, the effect of train speed is crucial in a pile-supported railway embankment which is investigated here.

Figure 4.19 shows the effect of train speed on the stress concentration ratio. For the unreinforced case as shown in Figure 4.19(a), the *SCR* increases with an increase in the train speed at a small embankment height. This implies that the majority of stress is transferred to the pile head at a small embankment height. However, it increases with an increase in embankment height and is likely to approach a limiting value at a large embankment height. In contrast, as shown in Figure 4.19(b), the *SCR* decreases with an increase in the train speed at a small embankment height for the reinforce case, and then it decreases with a further increase in embankment height and is likely to approach a limiting value at a large embankment height. This may be due to the membrane behaviour of the geosynthetic layer.

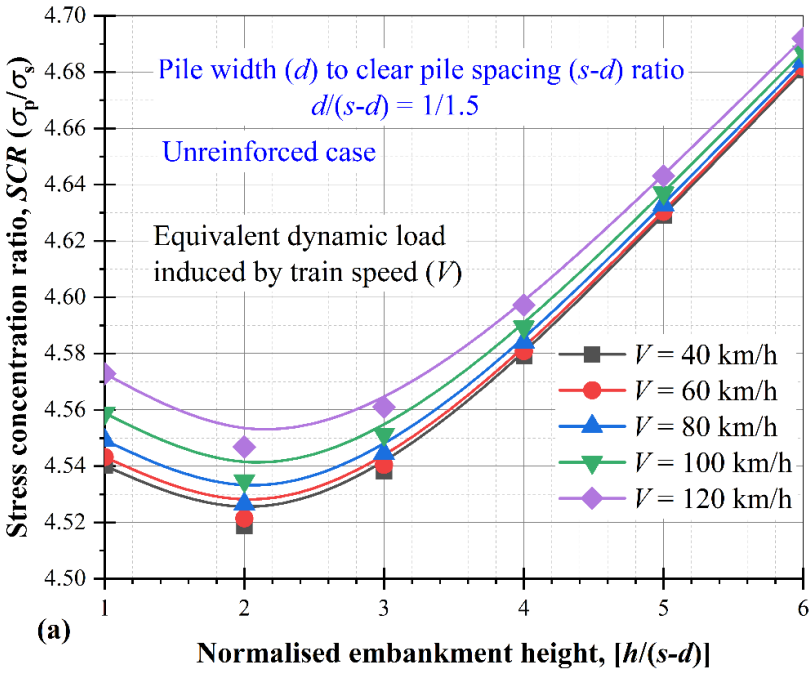

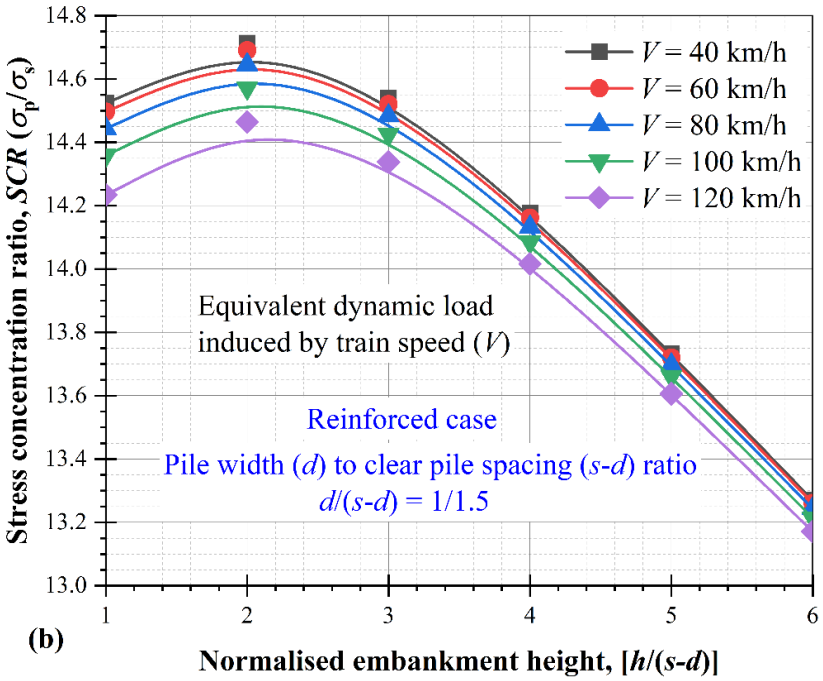

Figure 4.19: Effect of equivalent dynamic load induced by different train speed on the stress concentration ratio in (a) the unreinforced case, and (b) the reinforced case

The effect of train speed on stress efficacy is shown in Figure 4.20. It can be seen that the trend shown in Figure 4.20 is similar to that in Figure 4.19. For the unreinforced case shown in Figure 4.20(a), the stress efficacy increases with an increase in the train speed at a small embankment height. In contrast, it decreases with an increase in the train speed (refer Figure 4.20b). Further, it is likely to approach a limiting value at a large embankment height.

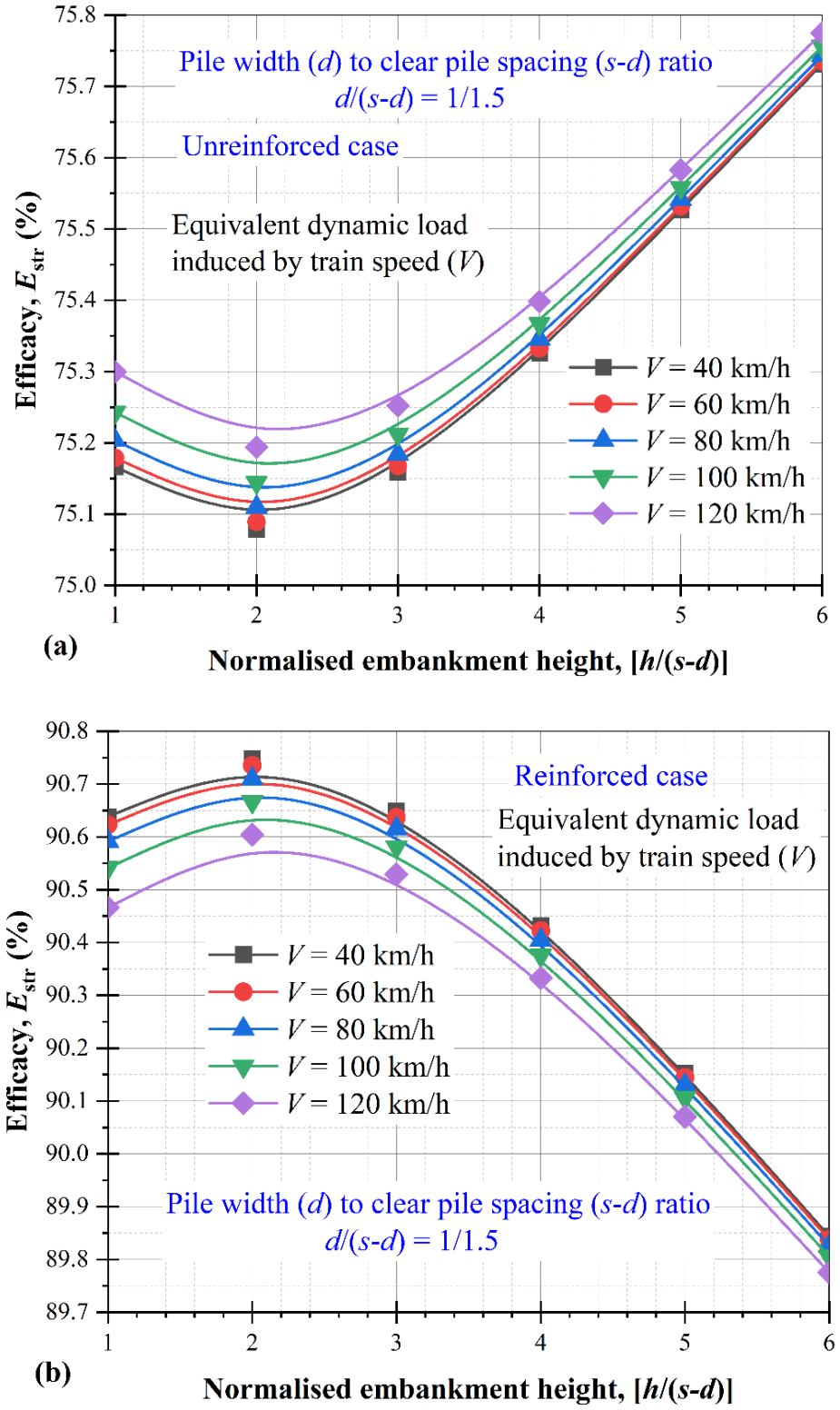

Figure 4.20: Effect of equivalent dynamic load induced by different train speed on stress efficacy in (a) unreinforced, and (b) reinforced case

Figure 4.21 demonstrates the effect of train speed on the geosynthetic layer deflection. It can be seen that at a small embankment height, the deflection in the geosynthetic layer increases with an increase in the train speed although it increases with an increase in embankment height and reaches a limiting value at a large embankment height.

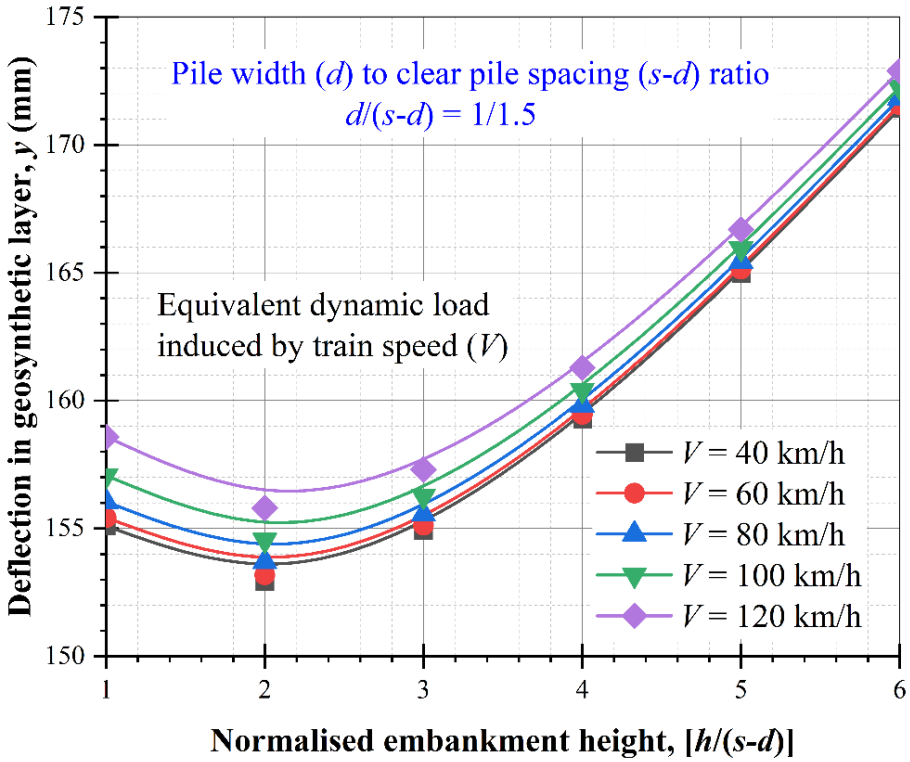

Figure 4.21: Effect of equivalent dynamic load induced by different train speed on deflection in the geosynthetic layer

4.5 THEORETICAL ANALYSIS OF SOIL ARCHING IN A PILE-SUPPORTED EMBANKMENT CONSIDERING AN EARTHQUAKE

In the earthquake condition, additional loading is applied on the embankment top. The earthquake loading is determined using the pseudo-static approach (Son et al. 2010). In addition, Kelesoglu and Cinicioglu (2010) reported the soil stiffness parameter (k_{soil})

which represents time depend behaviour of system under the earthquake-induced load. The soil stiffness parameter is defined as (Kelesoglu and Cinicioglu 2010):

$$k_{soil} = \left(\frac{K}{\Delta_{lateral}}\right)\sigma_v \quad \textbf{(4.34)}$$

where K is the lateral stress coefficient, $\Delta_{lateral}$ is the lateral displacement. Initially, it is assumed that embankment fill is in rest condition (i.e., K = 0.5, as explained in chapter 3).

The horizontal acceleration (A_h) can be determine as (Kramer 1996):

$$A_h = k_h \times g \quad \textbf{(4.35)}$$

where k_h is the coefficient of horizontal acceleration, and g is the gravity.

Further, the vertical acceleration (A_v):

$$A_v = k_v \times g \quad \textbf{(4.36)}$$

where k_v is the coefficient of vertical acceleration.

For simplicity, it is assumed that a uniform force (F) is applied on the embankment lateral side as shown in Figure 4.22.

Thus,

$$F = m \times a \quad \textbf{(4.37)}$$

where m is the mass of the embankment, and a is the horizontal acceleration which is equal A_h. Equation (4.35) and (4.36) used to calculate the horizontal acceleration.

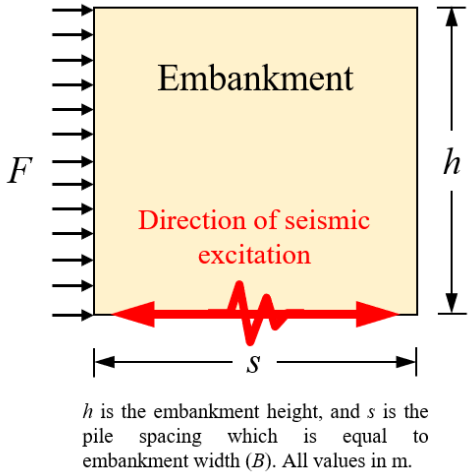

Figure 4.22: Schematic diagram of an embankment under the seismic excitation

Using Equation 4.37, the horizontal stress (σ_h) in the embankment can be calculated as:

$$\sigma_h = \frac{F}{A} \tag{4.38}$$

where *a* is the area of the embankment.

The later stress coefficient at rest (K_o) is:

$$k_o = \frac{\sigma_h}{\sigma_v} \tag{4.39}$$

Thus, from Equation 4.38 and 4.39, the vertical stress due to an earthquake is:

$$\sigma_v = \frac{(F/A)}{k_o} \tag{4.40}$$

In this study, friction angle of embankment fill is 30°. Thus, K_o is 0.5, and Equation (4.40) become:

$$\sigma_{v_{EQ}} = \frac{F}{0.5 \times A} \tag{4.41}$$

Equation (4.41) is the additional vertical stress which is acting on the embankment top due to a seismic excitation. In addition, the magnitude of earthquake can induce appreciable impact on the analysis. The earthquake magnitude is calculated using $a_h=k_hg$, which is varied with the value of k_h.

4.5.1 In unreinforced pile-supported railway embankment

In the unreinforced condition with an earthquake, Equation 4.7 modified as:

$$\sigma_s = \frac{\gamma(s-d).(k_p-1)}{2.(k_p-2)} + \left(\frac{s-d}{s}\right)^{(k_p-1)} \left[\gamma h - \frac{\gamma.s}{2}\left(1+\frac{1}{k_p-2}\right) + \left(\sigma_{\mathrm{RT}} + \sigma_{v_{EQ}}\right)\right] \qquad \textbf{(4.40)}$$

From Equation (4.11), the stress concentration ratio (*SCR*) is:

$$SCR = \frac{\sigma_p}{\sigma_s} = \frac{\left(s\left(\gamma h+\left(\sigma_{\mathrm{RT}}+\sigma_{v_{EQ}}\right)\right)-(s-d)\sigma_s\right)}{d.\sigma_s} \qquad \textbf{(4.41)}$$

Figure 4.23 shows the effect of vertical acceleration (A_v) on the *SCR*. It can be seen that the *SCR* increases by up to 7.7% with an increase in the vertical acceleration (A_v) from 0.0g to 0.3g. In addition, it also increases with an increase of embankment height, and likely to approaching a limiting value at normalised embankment of 6. For without earthquake case (i. e., A_v = 0.0g), the *SCR* initially slightly decreases, and after a certain normalised embankment height (2 in this study) it increases. In addition, the effect of embankment height is not prominent due to a higher surcharge imposed on the embankment top.

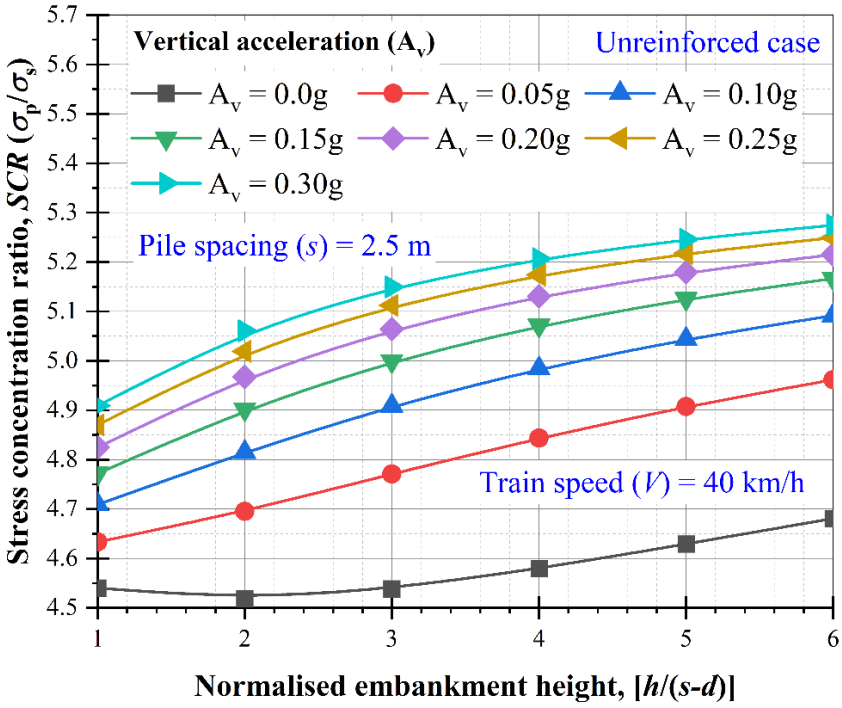

Figure 4.23: Effect of vertical acceleration on the stress concentration ratio in the unreinforced condition

4.5.2 In reinforced pile-supported railway embankment

During an earthquake, the vertical stress which is acting on the geosynthetic layer top (Equation 4.21) is modified using Equation 4.40. In addition, the *SCR* can be calculated using Equation 4.33.

The effect of vertical acceleration on the *SCR* is shown in Figure 4.24. It can be observed that the *SCR* decreases by up to 53% with an increase in the vertical acceleration (A_v) from 0.0g to 0.3g. However, it is likely to an approach a limiting value for a larger embankment height. For without earthquake case (i. e., A_v = 0.0g), the *SCR* initially slightly increases, and after a certain normalised embankment height (2 in this study) it decreases. In addition, the *SCR* in the reinforced case is higher compared to the unreinforced case due to additional vertical stress on the pile head that is transferred from the geosynthetic layer.

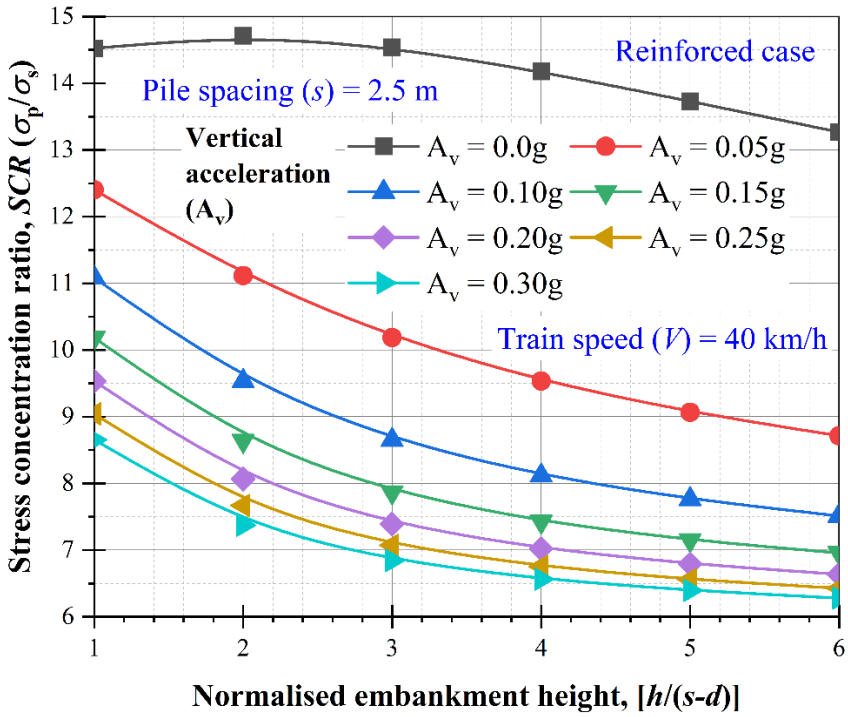

Figure 4.24: Effect of vertical acceleration on the stress concentration ratio in the reinforced condition

Figure 4.25 shows the influence of vertical acceleration on the tension in geosynthetic layer. It can be seen that tension in the geosynthetic layer increases by up to 1150% with an increase the vertical acceleration (A_v) from 0.0g to 0.3g. This increment is in tension is more pronounced at a higher embankment height. This implies that the tension in geosynthetic layer increases with an increase in the embankment height.

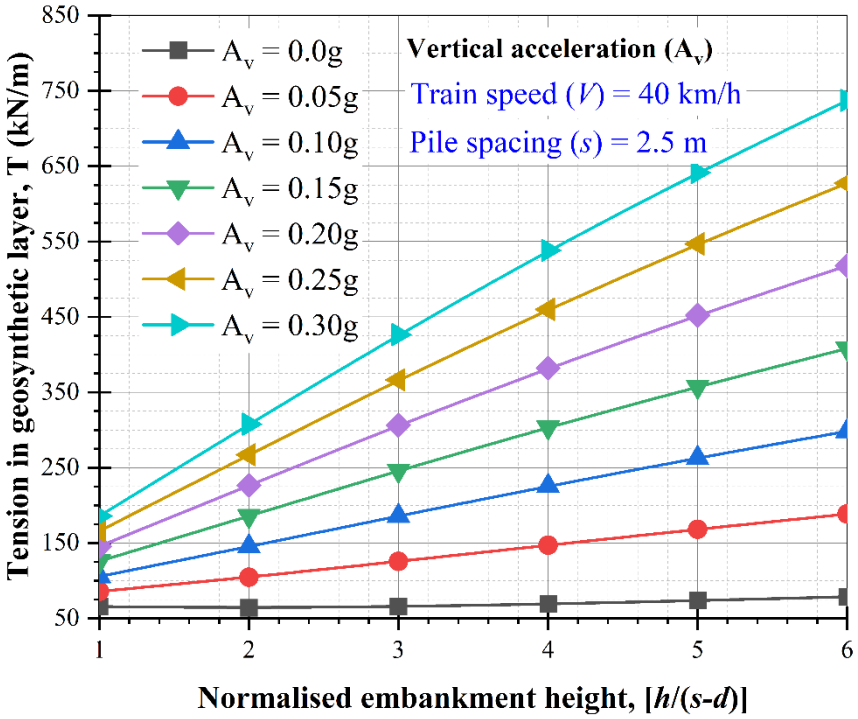

Figure 4.25: Effect of vertical acceleration on the tension in a geosynthetic layer

4.6 SUMMARY

In this chapter, a theoretical method is presented for the analysis of a pile-supported railway embankment based on Low et al.'s (1994) method. The key modification in this method is to consider the precise value of vertical stress on the soil arching crown which should be less compared to the surcharge imposed on the embankment top. The proposed method is validated by a field study and a full-scale model test and is found to be in good agreement with reasonable accuracy for both studies. In addition, it is also compared with other design methods such as Guido el al. (1987), Low et al. (1994) and BS8006 (2010). In particular, the proposed method enables a realistic approximation of vertical stress on the soil arching crown which can be useful in designing a pile-supported railway embankment.

The results demonstrate that the performance of a pile-supported railway embankment is significantly affected by various pile-supported railway embankment

parameters such as clear pile spacing, embankment height, subsoil compression modulus, tensile stiffness of the geosynthetic layer and train speed. Based on the present method, following findings can be drawn:

1) Vertical load carried by the pile top increases with an increase in the embankment height (h) and ratio of pile width (d) to clear pile spacing (s-d).
    - In unreinforced cases, the stress concentration ratio (SCR) increases up to 60% with an increase in the ratio of d/(s-d). The effect of embankment height is not prominent for a large d/(s-d) ratio due to the higher value of surcharge on the embankment top. While, In the reinforced case, the SCR decreases up to 40% with an increase in the ratio of d/(s-d). For a lower d/(s-d) ratio, the SCR decreases up to 26% with an increase in normalised embankment height from 1 to 6. An increment in the ratio of d/(s-d) represented a decrease in the pile spacing from 3.5 to 2 m and vice versa.
    - A negligible effect of embankment height is found on stress efficacy (E_{str}) due to a higher surcharge on the embankment top in unreinforced case. Whereases, the efficacy increases up to 42% with a decrease in pile spacing from 3.5 to 2 m. In reinforced case, the stress efficacy increases up to 8% with a decrease in pile spacing from 3.5 to 2 m, and it decreases with an increase in normalised embankment height from 1 to 6 for small d/(s-d) ratio.
    - The tension and axial strain in geosynthetic layer decrease up to 60% with an increase in the d/(s-d) ratio (refer to decrease in pile spacing) at smaller normalised embankment height. While both tension and axial strain in geosynthetic layer increases up to 40% with an increase in

normalised embankment height from 1 to 6. It implies that geosynthetic layer is more prominent for large pile spacing and embankment height.

Therefore, it can be concluded that soil arching significantly affected by embankment height and pile spacing.

2) The geosynthetic layer plays a crucial role in the load transfer mechanism, especially for a large pile spacing and for very compressible subsoil (e.g. E_o = 0.5 MPa for this study).
    - In reinforced case, the geosynthetic layer enhances the stress concentration ratio by 125-500% compared to unreinforced case. While the stress efficacy enhances up to 51% by the inclusion of geosynthetic layer. Thus, geosynthetic layer is prominent for large pile spacing (3.5 m for this study) and very compressible subsoil (0.5 MPa for this study).
    - It is evident from results that the stress concentration ratio (*SCR*) and efficacy (E_{str}) decrease up to 64% and 10%, respectively with an increase in tensile stiffness of geosynthetic layer (J) from 0 to 2000 kN/m. It implies that as tensile stiffness of geosynthetic layer increases, the membrane behaviour of geosynthetic layer becomes effective, consequently, less deflection in geosynthetic layer occur and the geosynthetic layer can carry more load which reduced load transfer from the subsoil to pile top.

Therefore, in the reinforced case, the extra load is transferred to the pile top from the subsoil and the soil arching enhance more. In addition, number of piles can be reduced with the inclusion of geosynthetic layer resulting in a more economic design of pile-supported embankment.

3) The subsoil contributed a significant role in the reinforced pile-supported embankment and it cannot be ignored during the design of a piled embankment.
    - For unreinforced case, no change has been found in the stress concentration ratio (*SCR*) and efficacy (E_{str}) by changing the one-dimensional modulus of subsoil. While, the stress concentration ratio increases up to 400% with an increase of compression modulus of subsoil (E_o) from 0.5 to 3 MPa.
    - Further, the efficacy (E_{str}) increases up to 38% with an increase in the compression modulus of subsoil. Although, it is likely to approach a limiting value for a higher E_o, which implies that the subsoil is sufficiently stiff to support the imposed load. Also, reinforcement is not necessary for stiff subsoil.
    - It is also evident that tension in geosynthetic layer (*T*) decreases up to 70% with an increase in the E_o, and after approaching a higher value of E_o it is likely to remain a limiting value. It implies that when the compression modulus of the subsoil is increasing the deflection in geosynthetic layer is reduced due to sufficient stiffness of subsoil.

Therefore, the one-dimensional modulus of subsoil (E_o) plays a major role in the settlement of embankment fill and load support on the subsoil. It is important to investigate the effect of the one-dimensional modulus of subsoil.

4) Imposed load on the embankment top induced by different train speed is also influence the load transfer mechanism. However, in this study, the imposed load by 40 km/h train speed is much higher thus the effect of the imposed load is not fully justified here.

In this chapter, moving train load is considered as an equivalent dynamic load. The equivalent dynamic load is equal to the weight of the train multiplied by a dynamic amplification factor (DAF), which accounts for the dynamic effects due to the moving train. Therefore, the true dynamic nature of traffic loading is needed to be investigated further.

5) An earthquake applied additional vertical load on the soil arching which can derived and considered in the analytical method.
    - For the unreinforced condition, the *SCR* increases by up to 7.7% with an increase in the vertical acceleration (A_v) from 0.0g to 0.3g.
    - For the reinforced condition, the *SCR* decreases by up to 53% with an increase in the vertical acceleration (A_v) from 0.0g to 0.3g, and it is likely to an approach a limiting value for a larger embankment height.
    - The tension in the geosynthetic layer increases by up to 1150% with an increase the vertical acceleration (A_v) from 0.0g to 0.3g.

This chapter discussed the force-based method for seismic analysis of a pile-supported embankment. However, recently the displacement-based approach is becoming popular (Son et al. 2010; Kelesoglu and Cinicioglu 2010; Deng et al. 2014). The analytical method proposed in this chapter provides a simple approach for design engineers. In chapter 6, a series of numerical simulations have been undertaken to understand the effect of an earthquake on both stress and accumulated displacement in the pile-supported embankment.

In addition, the 2D analytical method which is presented in this chapter is extended into a 3D analytical method for soil arching in the next chapter.

CHAPTER 5

A 3D ANALYTICAL ASSESSMENT OF SOIL ARCHING IN A PILE-SUPPORTED RAILWAY EMBANKMENT

This chapter covers an analytical method of soil arching for a pile-supported railway embankment in a three-dimensional (3D) condition. A uniform surcharge value is considered on the embankment top to represent the rail track and moving train induced load. The applied surcharge by the moving train is equivalent in dynamic nature, as explained in chapter 3. The accurate evaluation of the surcharge on the soil arching crown is considered. The accuracy of the proposed method is assessed with a field study and some existing empirical methods.

5.1 INTRODUCTION

Pile-supported embankments are a feasible solution for the construction of transport infrastructures on soft soil. As stated in chapter 2, soil arching occurs within the embankment fill due to the stiffness difference between the rigid pile and adjacent soft soil which has been well acknowledged in the past (Hewlett and Randolph 1988; Low et al. 1994; Abusharar et al. 2009; Zhuang et al. 2014). Further, the inclusion of the geosynthetic layer minimises the settlements and improves the load transfer mechanism by the membrane effect (Zhuang and Wang 2017).

Several analytical methods (Hewlett and Randolph 1988; Zhuang et al. 2014;

Zhang et al. 2016; Pham 2020a) have been reported to study soil arching in the 3D condition. Hewlett and Randolph (1988) carried out model tests and proposed a semi-spherical empirical method in the 3D condition to describe soil arching without any reinforcement. Further, Zhuang et al. (2014) extended Hewlett and Randolph's method and investigated two critical failure regions (at the soil arching crown and at the pile top) without any surcharge on the embankment top. Zhang et al. (2016) reported a field study and a 3D analytical method considering the triangular arrangement of a pile. The proposed analytical method is assessed with the existing empirical methods and field data with no surcharge on the embankment top and a good agreement with existing methods and field data was found in terms of pile efficacy and tension in the geosynthetic layer. Pham (2020a) reported a comprehensive analytical method considering the effect of soil layer, tension in the geosynthetic layer, subgrade reaction, interaction between the geosynthetic layer and soil, and the consolidation of the subsoil under both a linear and nonlinear nature. However, the precise estimation of a train-induced surcharge on the soil arching crown in the 3D condition has not been investigated yet.

The main objective of this chapter is to study soil arching, considering the precise value of the surcharge on the soil arching crown, coming from the railway corridor lying down on the embankment top. Two critical regions (at the soil arching crown and at the pile top) within soil arching are investigated to determine the most critical region in the 3D condition.

5.2 3D ANALYTICAL METHOD FOR GRPS RAILWAY EMBANKMENTS

The proposed analytical method is based on the same assumptions as followed in the chapter 4.

5.2.1 Theoretical analysis of soil arching in an unreinforced pile-supported railway embankment

Hewlett and Randolph (1988) and Low et al. (1994) carried out model tests and proposed a theoretical method for the assessment of load transfer in a pile-supported embankment by assuming the limit equilibrium state of embankment fill. The proposed analysis follows Hewlett and Randolph's (1988) method where the failure of the soil arch is either at the soil arching crown or at the pile top. The crown of the soil arching is dominated by the performance of the pile-supported embankment at the low embankment height relative to the pile spacing (i.e., $h < s$) while the failure region transfers towards the pile head as the embankment height increases. Therefore, the failure of the soil arching should be derived from both regions (i.e., at the pile head and the soil arching crown) and a relatively larger value should be considered to estimate the load transfer to the pile head. Vertical stress on the subsoil is estimated for both conditions in the following two subsections.

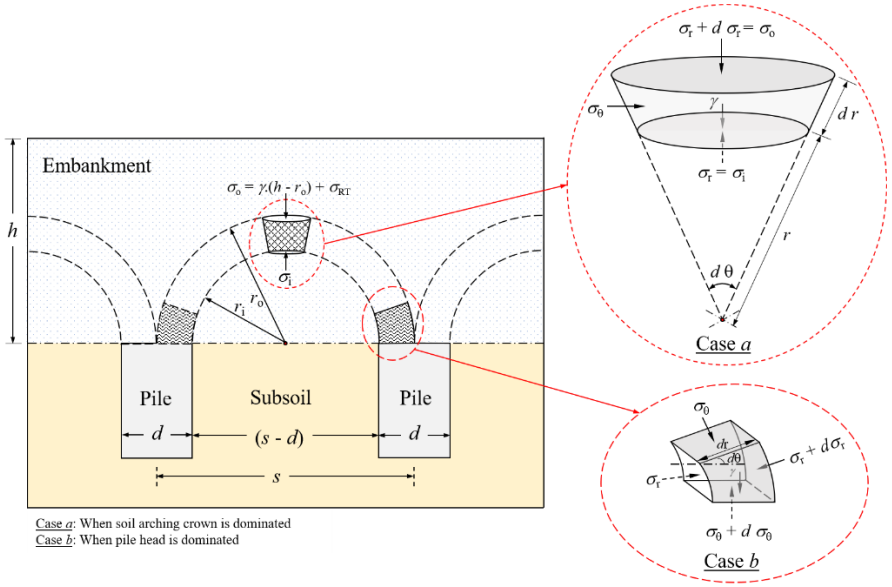

Figure 5.1: Stress distribution on a three-dimensional (3D) element of soil arching (modified from Hewlett and Randolph 1988)

5.2.1.1 Soil arching in the three-dimensional (3D) condition when the arching crown is critical

The radial equilibrium for an element resting on the crown of soil arching (refer Figure 5.1; case *a*) is calculated using Equation 4.1:

$$\frac{d\sigma_r}{dr} + \frac{2(\sigma_r - \sigma_\Theta)}{r} + \gamma = 0 \qquad \textbf{(5.1)}$$

where σ_r = radial stress (kN/m^2); σ_θ = tangential stress (kN/m^2); r = radial distance (m); and γ= unit weight of embankment fill material (kN/m^3). For a limit state analysis, the tangential stress (σ_θ) = $k_p.\sigma_r$; where k_p = (1+sinϕ)/ (1-sinϕ).

$$\frac{d\sigma_r}{dr} + \frac{2.\sigma_r(1-k_p)}{r} + \gamma = 0 \qquad \textbf{(5.2)}$$

The general solution of Equation (5.2) is:

$$\sigma_r = \gamma.\left(\frac{r}{2.k_p - 3}\right) + C'.r^{2(k_p-1)} \qquad \textbf{(5.3)}$$

The boundary condition at the soil arching crown, where $r = s/\sqrt{2}$ and $\sigma_r = \gamma(h - s/\sqrt{2}) + \sigma_{RT}$ (Van Eekelen et al. 2013; Zhuang et al. 2014). Hewlett and Randolph (1988) considered a hemispherical shape of soil arching in the 3D condition and the radius of the outer boundary of soil arching is $r = s/\sqrt{2}$, where σ_{RT} = total vertical stress on the soil arching crown due to the self-weight of the rail track and the equivalent dynamic load on the embankment top (refer to Equation 4.4).

In this chapter, the equivalent dynamic load due to train (σ_{train}) will be the same as that obtained in chapter 4 (refer to Table 4.2). However, the stress coming from the

3D geometry of the track will be changed. The vertical stress due to the track is shown in Table 5.1.

Table 5.1: Calculation of the track surcharge on the embankment top

Material	Density (ρ), kg/m^3	Unit volume (V), m^3	Mass weight (kg)	Total weight (W_{track}), kN	Area where total weight applied, ($A_{\sigma track}$) m^2	Vertical stress (σ_{track}) due to self-weight of rail track on the embankment top, kPa
Rail (UIC-60)	-	-	60			
Sleeper	2350	1.1	2585	255.21	39.69	6.43
Ballast	1700	7.75	13173.3			
Subballast	1800	5.67	10206			

After deriving the constant of integration (C'), the radial stress at the soil arching crown is:

$$\sigma_r = \gamma.\left(\frac{r}{2k_p-3}\right) + \left(\frac{\sqrt{2}\,r}{s}\right)^{2.(k_p-1)}\left[\gamma h - \gamma\frac{s}{\sqrt{2}}\left(\frac{2k_p-2}{2k_p-3}\right) + \sigma_{\mathrm{RT}}\right] \qquad \textbf{(5.4)}$$

where, σ_{RT} is calculated in Equation 4.4.

Now, the vertical stress (σ_i) just below the inner boundary of the soil arching, where $r = (s - d)/\sqrt{2}$, is:

$$\sigma_i = \gamma\left(\frac{(s-d)}{\sqrt{2}\,(2k_p-3)}\right) + \left(\frac{s-d}{s}\right)^{2(k_p-1)}\left[\gamma h - \gamma\frac{s}{\sqrt{2}}\left(\frac{2k_p-2}{2k_p-3}\right) + \sigma_{\mathrm{RT}}\right] \qquad \textbf{(5.5)}$$

The vertical stress (σ_s) acting at the base of embankment on geosynthetic layer is:

$$\sigma_{geo} = \sigma_i + \frac{\gamma(s-d)}{\sqrt{2}} \qquad \textbf{(5.6)}$$

$$\sigma_s = \gamma \frac{(s-d)}{\sqrt{2}}\left(\frac{2k_p-2}{2k_p-3}\right) + \left(\frac{s-d}{s}\right)^{2(k_p-1)}\left[\gamma h - \gamma \frac{s}{\sqrt{2}}\left(\frac{2k_p-2}{2k_p-3}\right) + \sigma_{\mathrm{RT}}\right] \quad \textbf{(5.7)}$$

5.2.1.2 Soil arching in the three-dimensional (3D) condition when the pile head is critical

The radial equilibrium for an element resting on the pile head (refer Figure 5.1; case *b*) is determined as

$$\frac{d\sigma_r}{dr} + \left(\frac{\sigma_r - \sigma_\Theta}{r}\right) = 0 \quad \textbf{(5.8)}$$

Substituting σ_θ value from Equation (5.2)

$$\frac{d\sigma_r}{dr} + \left(\frac{\sigma_r(1-k_p)}{r}\right) = 0 \quad \textbf{(5.9)}$$

Solving Equation (5.9) using boundary condition for radial stress at pile head (r = (s-d)/2)

$$\sigma_r = k_p\, \sigma_s \left(\frac{s-d}{2r}\right)^{(1-k_p)} \quad \textbf{(5.10)}$$

Total force acting on the pile head (P) which is arranged in a square pattern is obtained by

$$P = 4.\left(\int_{\frac{(s-d)}{2}}^{\frac{s}{2}} \sigma_\Theta \,.\, dA_{pile}\right) \quad \textbf{(5.11)}$$

$$P = 2\,\sigma_{geo}.s.(s-d)\left(\frac{k_p}{k_p+1}\right)\left[\left(\frac{s}{s-d}\right)^{k_p} - 1 - k_p.\left(\frac{d}{s}\right)\right] \quad \textbf{(5.12)}$$

Now for overall equilibrium

$$(\gamma h + \sigma_{\mathrm{RT}}).s^2 = P + \sigma_s(s^2 - d^2) \quad \textbf{(5.13)}$$

or

$$(\gamma h + \sigma_{\mathrm{RT}}).s^2 = d.\sigma_p + (s^2 - d^2).\sigma_s \quad \textbf{(5.14)}$$

From Equation (5.12) and (5.13), the vertical stress (σ_{geo}) acting at the base of embankment on geosynthetic layer can be obtained:

$$\sigma_{geo} = (\gamma h + \sigma_{\mathrm{RT}}) / \left\{ \left(\frac{s^2-d^2}{s^2}\right) + \left(\frac{2k_p}{k_p+1}\right) \left[\left(\frac{s-d}{s}\right)^{(1-k_p)} - \left(\frac{s-d}{s}\right)\left(\frac{s+k_p.d}{s}\right) \right] \right\} \quad \textbf{(5.15)}$$

Derivation of the equations 5.4 to 5.15 is listed in the Appendix A.

5.2.2 Theoretical analysis of soil arching in a GRPS railway embankment

In this study, the geosynthetic layer is assumed to be placed at the base of the embankment and fixed on the pile head. It is assumed that the geosynthetic layer is deflected as a parabola shape and induced tension (T) can be derived as (Zhuang et al. 2014):

$$T = 0.125\sigma_{geo}\left(\frac{l^2}{y}\right) \quad \textbf{(5.16)}$$

where T is the tension in geosynthetic layer; σ_{geo} is the vertical stress in the geosynthetic layer; l is the actual span of the geosynthetic layer; and y is the maximum deflection in the geosynthetic layer. The span of the geosynthetic layer (l) is the average value of the minimum clear pile spacing (i.e., s-d) and maximum clear pile spacing (i.e., $\sqrt{2}(s$-$d)$) as shown in Figure 5.2. Thus, the tensile force in the geosynthetic layer under the 3D condition can be obtained by the plane strain condition.

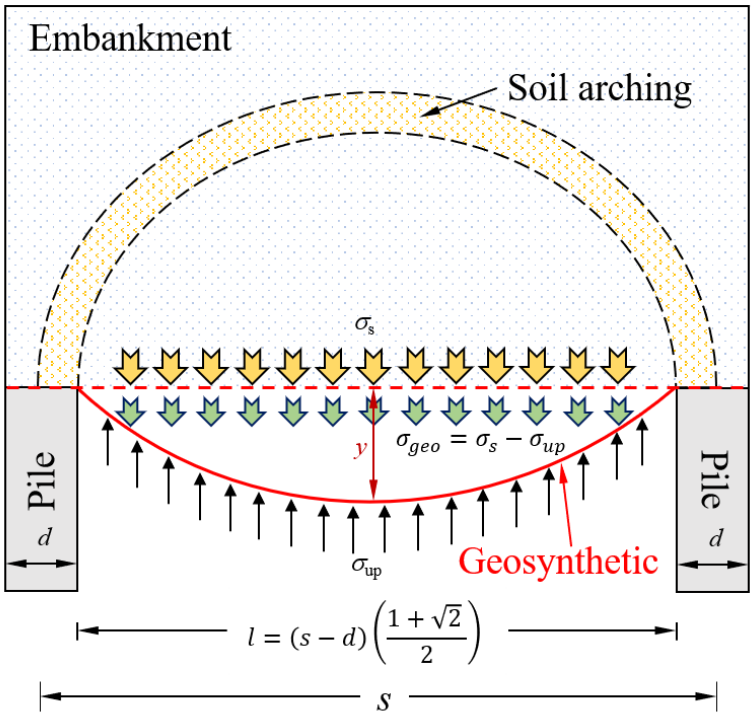

Figure 5.2: Vertical stress formation in a reinforced case of pile-supported embankment

Based on the deflection in the geosynthetic layer, axial strain can be expressed as:

$$\varepsilon_{geo} = 2.67\left(\frac{y}{l}\right)^2 \quad \textbf{(5.17)}$$

The tension in the geosynthetic layer is developed by two strain components, one due to the load and the other due to the skin friction:

$$T = J\,.\,\varepsilon_{geo} + \tau\frac{(s-d)}{4} \quad \textbf{(5.18)}$$

where J is the tensile stiffness of the geosynthetic layer (kN/m).

In this chapter, skin friction is neglected avoid any complexity due to 3D geometry (Chen et al. 2008). In addition, Zhuang and Wang (2017) reported that pile-subsoil interaction can be categorised into three sections: (i) negative skin friction up to a certain depth of pile head which attains a maximum value, (ii) a transition zone, skin

friction changes negative to positive up to maximum value, (iii) skin friction reduces up to a specific value at the pile bottom. Thus, Equation (5.18) becomes:

$$T = J \,.\, \varepsilon_{geo} \tag{5.19}$$

From Equation (5.17) and (5.19), the vertical stress on the geosynthetic layer is:

$$\sigma_{geo} = 21.34\, J \left(\frac{y^3}{l^4}\right) \tag{5.20}$$

In the reinforced case, the actual vertical stress carried by the subsoil is in equilibrium with the upward vertical reaction stress on the bottom geosynthetic layer (σ_{up}), calculated based on the one-dimensional compression modulus of the subsoil:

$$\sigma_{up} = y_s . k_s = \frac{y.E_o}{D_{act}} \tag{5.21}$$

where y_s is the maximum deformation of the subsoil top (in this study, $y_s = y$); k_s is the modulus of the subgrade reaction; D_{act} is the active depth of the subsoil (full depth of subsoil for this study); and E_o is the one-dimensional modulus of the subsoil, which can be derived using Young′s modulus of the subsoil ($E_{subsoil}$) and Poisson's ratio (v) as follows:

$$E_o = E_{subsoil} \left[\frac{(1-v)}{(1+v).(1-2v)}\right] \tag{5.22}$$

The overall equilibrium condition is shown in Figure 4.4 and Equation (4.18)

$$\sigma_{geo} + \sigma_{up} - \sigma_s = 0 \tag{5.23}$$

Substituting Equation (5.20) and (5.21) into (5.23),

$$21.34\, J \left(\frac{y^3}{l^4}\right) + \frac{y.E_o}{D_{act}} - \sigma_s = 0 \tag{5.24}$$

Using Equation (5.24), the maximum deflection in the geosynthetic layer can be obtained using a third-degree cubic equation and then the other unknown parameters can be calculated.

5.2.3 Soil arching indices

The stress efficacy (E_{str}) is defined as the portion of the embankment weight that carried by the piles:

$$E_{str} = 1 - \frac{\sigma_v A_s}{(\gamma h + \sigma_{RT}).A} \quad \textbf{(5.25)}$$

where σ_v is the vertical stress at the embankment base (in unreinforced case = σ_s and in reinforced case = σ_{up}); A_s = area of clear spacing = (s^2-d^2) and A = area of centre to centre pile spacing = s^2.

From Equation (5.14), the stress concentration ratio (*SCR*) is as follows:

$$SCR = \frac{\sigma_p}{\sigma_v} = \frac{(\gamma h + \sigma_{RT}).s^2 - (s^2 - d^2).\sigma_v}{d.\sigma_v} \quad \textbf{(5.26)}$$

Further, the soil arching ratio (*SAR*) is defined as the ratio of vertical stress on the subsoil top (σ_s) to the vertical stress induced by the self-weight of the embankment and applied surcharge on the embankment top ($\gamma h + \sigma_{total}$). Its value lies between 0 to 1. The 0 value indicates that the whole vertical load is transferred to the pile head, whereas *SAR* = 1 indicates that the vertical stress on the subsoil top is equal to the overburdened stress.

$$SAR = \frac{\sigma_v}{\gamma h + \sigma_{RT}} \quad \textbf{(5.27)}$$

5.3 VALIDATION OF THE PROPOSED ANALYTICAL METHOD

In this section, the proposed analytical method is validated against a model test conducted by Xu et al. (2015). Details of the site condition and monitoring scheme are reported in Xu et al. (2015). However, a brief of the parameters that are used to validate the analytical model is given in Table 5.2.

Table 5.2: A brief of the parameters used to validate the proposed 3D analytical method.

Parameters	Xu et al. (2015)
Embankment height, h (m)	0.4
Unit weight of embankment fill, γ (kN/m^3)	17.9
Friction angle of embankment fill, ϕ' (degree)	38
Modulus of the subgrade reaction, k_s (kPa/ m^3)	350
Pile diameter width, d (m)	0.3
Centre to centre pile spacing, s (m)	0.5
Tensile stiffness of geosynthetic layer (biaxial PP geogrid), J (kN/m)	500
Surcharge on the embankment top, σ_{total} (kPa)	71

A comparison of the proposed method with the existing methods and field data is shown in Table 5.3. It is found that the proposed method is a good match with a 2.4% difference against the field data in terms of stress efficacy. The proposed method achieves a lower value of the stress efficacy compared to Xu et al.'s (2015) field data. However, the maximum tension and deflection in the geosynthetic layer (biaxial PP geogrid) is higher than the measured data. In addition, the existing methods also show the overestimated predictions.

Table 5.3: Comparison of present method with Xu et al. (2015) measurement and other methods

Parameters	BS8006 (2010)	EBGEO (2011)	Zhuang et al. (2014)	CUR226 (2016)	Present method	Measured field data (Xu et al. 2015)
Efficacy, E_{str}, (%)	72.60	77.90	70.30	84.90	74.20	76.00
Max. tension in geosynthetic layer, T (kN/m)	7.40	26.20	2.20	2.60	1.40	0.80
Max. deflection in geosynthetic layer, y (mm)	5.4	12.6	4.2	4.3	2.9	2.0

5.4 PARAMETRIC STUDY

The effect of the pile-supported railway embankment parameters using the proposed analytical method on soil arching is investigated here. A train speed of 40 km/h and a normalised embankment height (h/s-d) = 3 are considered to see the effect of other parameters, except for train speed and embankment height, respectively. For general applicability, embankment height is normalised by clear spacing (s-d) to see the effect of embankment height. Moreover, the most critical region for soil arching failure is investigated by comparing both cases (i.e., soil arching failure at the crown or at the pile head).

Meena et al.'s (2020) study is used as a reference case for the parametric study. The input parameters of Meena et al. (2020) are listed in Table 3.1. In addition, details of the considered parameters are as follows: (*i*) Embankment - height (h) = varies from 1 m to 15 m, unit weight (γ) = 20 kN/m^3, Young's modulus of elasticity (E) = 20 MPa, internal frictional angle (ϕ) = 30°, cohesion (c) = 0.1 kPa; (*ii*) Subsoil - depth (D_{act}) = 8 m, unit weight (γ) = 18.4 kN/m^3, Young's modulus of elasticity (E) = 2.2 MPa, internal frictional angle (ϕ) = 22°, cohesion (c) = 8 kPa; and (*iii*) Pile - width (d) = 1

m, spacing (*s*) = 2.5 m; (*iv*) Geosynthetic layer (Secugrid^{R} 60/60Q1 @ 2 % strain @ rib thickness of 2 mm) - tensile stiffness (*J*) = 1000 kN/m.

5.4.1 Effect of embankment height

Figures 5.3 - 5.6 show the effect of embankment height (*h*) on the soil arching indices and tension in the geosynthetic layer for different ratios of pile width (*d*) to clear spacing (*s*-*d*). The effect of embankment height on the stress concentration ratio (*SCR*) is shown in Figure 5.3. As shown in Figure 5.3(a) for an unreinforced case, the *SCR* increases by up to 57% with an increase in the ratio of *d*/(*s*-*d*) from 0.4 (i.e., 1/2.5) to 1 (i.e., 1/1) for both failure regions (failure at the soil arching crown and the pile head). Also, it increases by up to 20% with an increase in the normalised embankment height from 1 to 6 in the case of failure occurring at the soil arching crown. However, in the case of soil arching failure at the pile head, the *SCR* is not influenced by embankment height.

The effect of embankment height on the *SCR* for a reinforced case is shown in Figure 5.3(b). It can be seen that at both failure regions, the *SCR* increases by up to 58% with an increase in the normalised embankment height from 1 to 6 and the ratio of *d*/(*s*-*d*) from 0.4 (i.e., 1/2.5) to 1 (i.e., 1/1). However, in the case of failure at the pile head, the *SCR* is slightly affected by embankment height. Thus, the inclusion of reinforcement at the base of the embankment enhances the load transfer mechanism and prevents the failure of soil arching at the pile head.

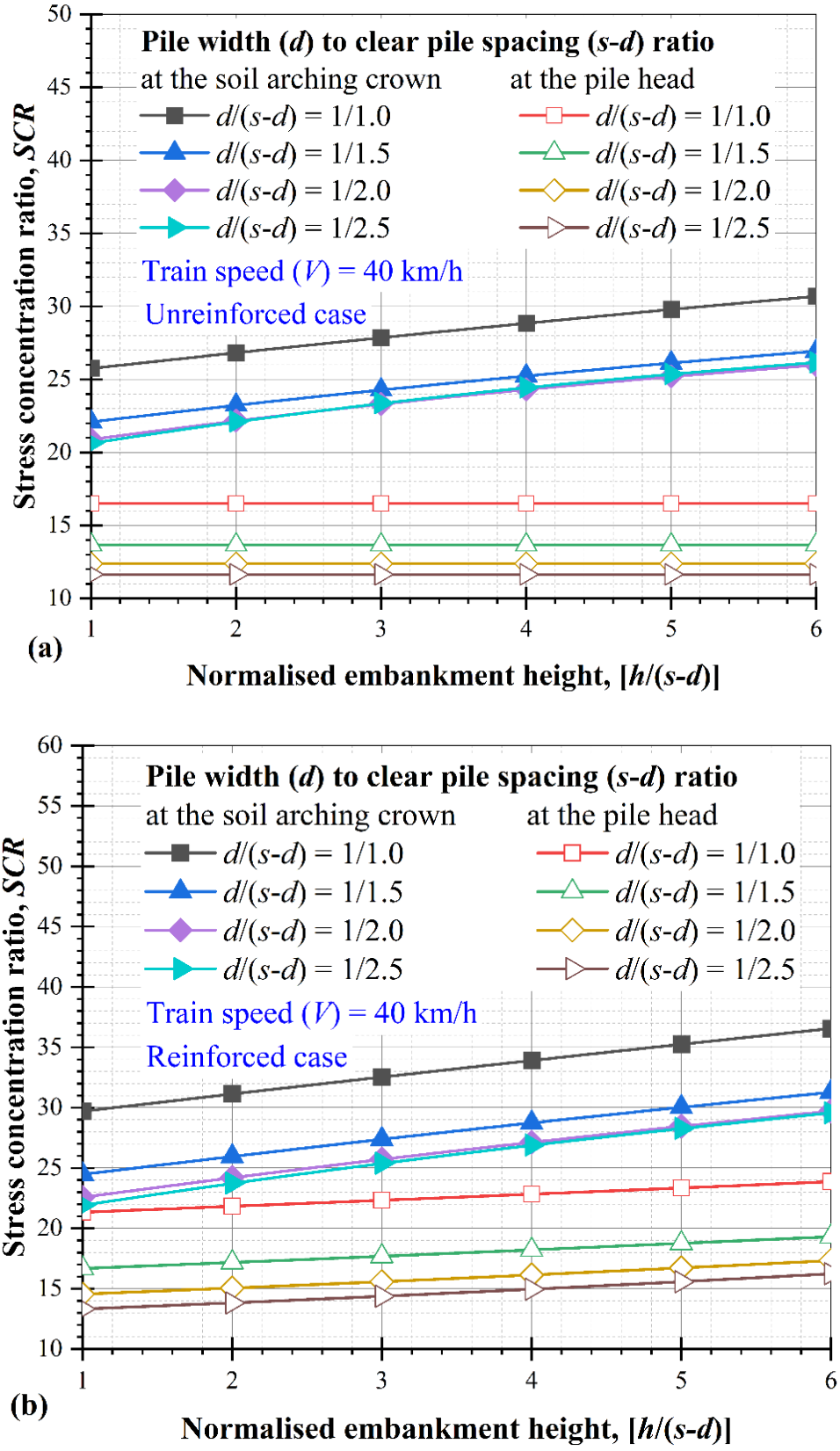

Figure 5.3: Effect of embankment height on the stress concentration ratio in (a) the unreinforced case, and (b) the reinforced case

Figure 5.4 shows the effect of embankment height on stress efficacy (E_{str}). It can be seen from Figure 5.4(a) that in the unreinforced case, the E_{str} increases by up to 68% with an increase in the ratio of $d/(s\text{-}d)$ from 0.4 to 1 for both failure regions (failure at the soil arching crown and the pile head). In the case of failure at the soil arching crown, the E_{str} increases by up to 7% with an increase in the normalised embankment height from 1 to 6. However, embankment height has not been found to have a significant effect on failure at the pile head.

For the reinforced case, the effect of embankment height on the stress efficacy is shown in Figure 5.4(b). The E_{str} increases by up to 36% with an increase in the ratio of $d/(s\text{-}d)$ from 0.4 to 1 for both failure regions (failure at the soil arching crown and the pile head).

It is worth noting in Figure 5.3 and Figure 5.4 that the *SCR* and E_{str}, respectively in the case of failure at the pile head is less compared to the case of failure at the soil arching crown which implies that failure at the pile head is the more critical region for soil arching. This argument is in good agreement with Zhuang et al. (2010).

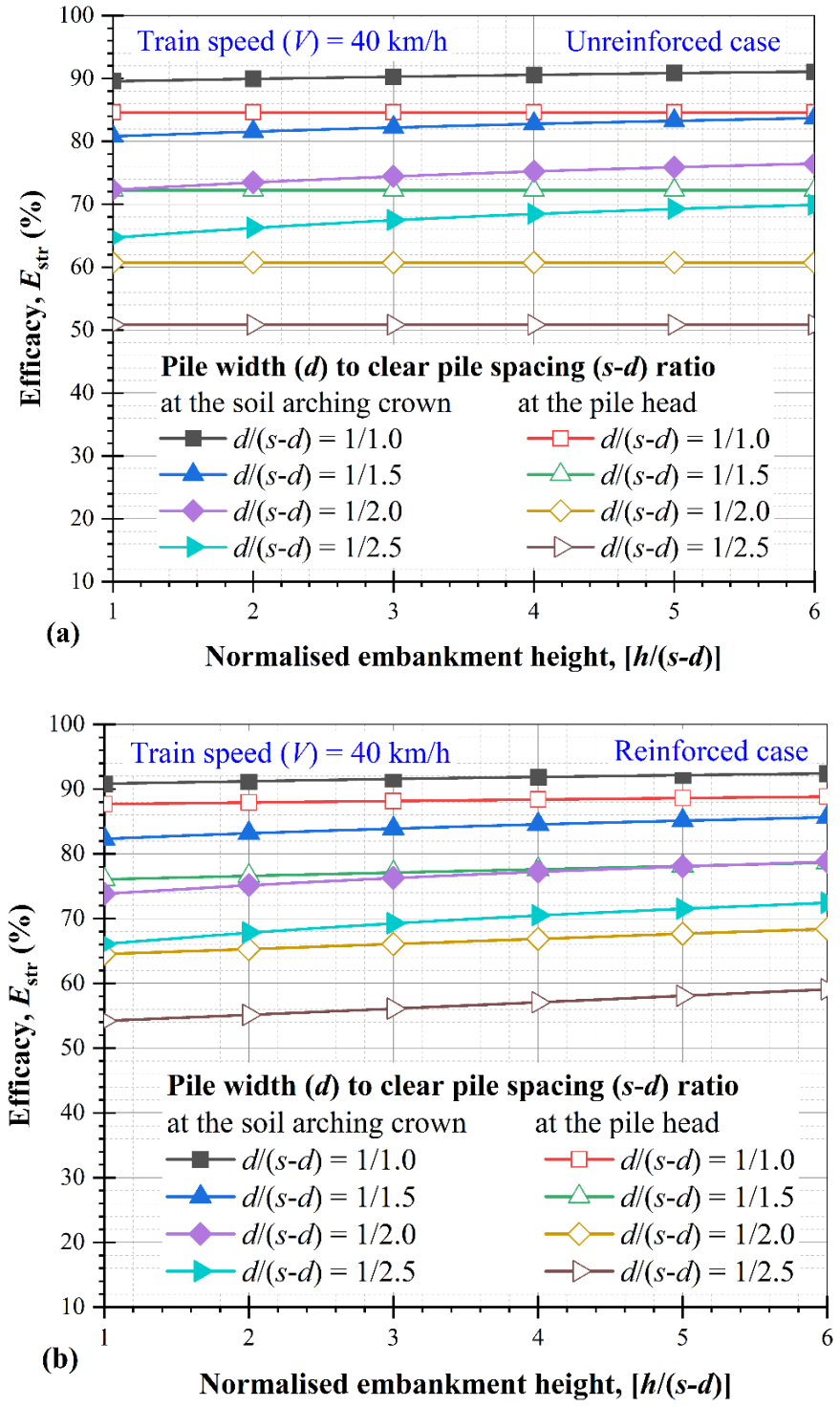

Figure 5.4: Effect of embankment height on stress efficacy in (a) the unreinforced case, and (b) the reinforced case

Figure 5.5 shows the effect of embankment height on the soil arching ratio (*SAR*). Figure 5.5(a) shows that in the unreinforced case, the *SAR* decreases by up to

62% with an increase in the ratio of $d/(s\text{-}d)$ from 0.4 to 1 for both failure regions (failure at the soil arching crown and the pile head). Also, it increases by up to 12% with an increase in the normalised embankment height from 1 to 6 in the case of failure occurring at the soil arching crown. However, in the case of soil arching failure at the pile head, the *SAR* is not influenced by embankment height.

The effect of embankment height on the *SAR* for the reinforced case is shown in Figure 5.5(b). It can be seen that at both failure regions, the *SAR* decreases by up to 12% with an increase in the normalised embankment height from 1 to 6 and the ratio of $d/(s\text{-}d)$ from 0.4 to 1. As shown in Figure 5.5(b), the *SAR* value in the reinforced case is lower than the unreinforced case (refer to Figure 5.5(a)), which implies that subsoil significantly contributes to the vertical equilibrium and reinforcement enhances the load transfer mechanism to the pile top.

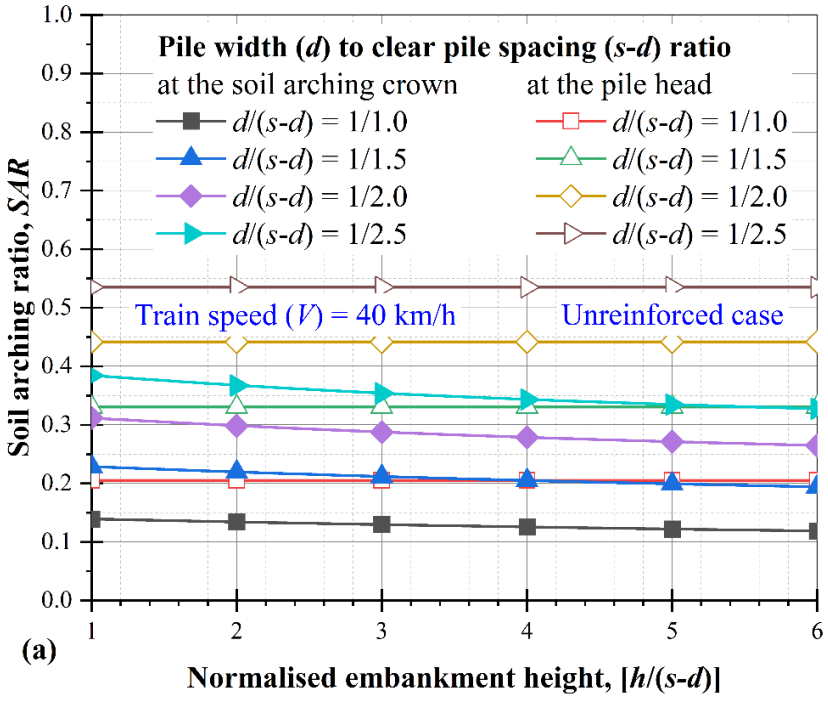

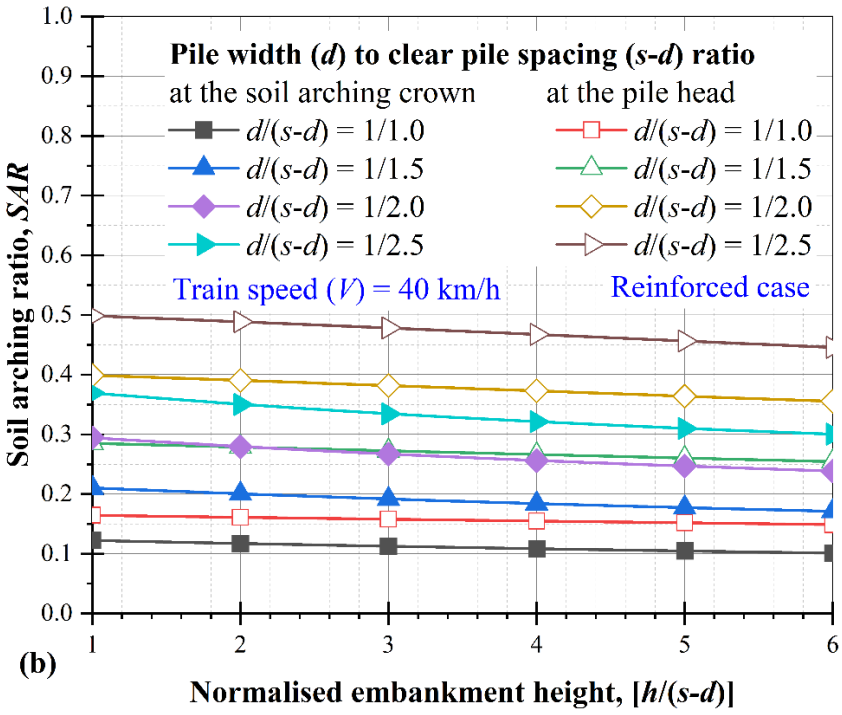

Figure 5.5: Effect of embankment height on the soil arching ratio in (a) the unreinforced case, and (b) the reinforced case

Figure 5.6 illustrates the effect of embankment height on tension in the geosynthetic layer. It can be seen that tension in the geosynthetic layer decreases by up to 62% with an increase in the ratio of $d/(s\text{-}d)$ from 0.4 to 1 for both failure regions (failure at the soil arching crown and the pile head), whereas it increases by up to 135% with an increase in the normalised embankment height from 1 to 6. The tension in the geosynthetic layer is more noticeable for a small ratio of $d/(s\text{-}d)$. It can also be seen that for the same $d/(s\text{-}d)$ ratio, the tension in the geosynthetic layer is higher in the case of failure at the pile top compared to failure at the soil arching crown.

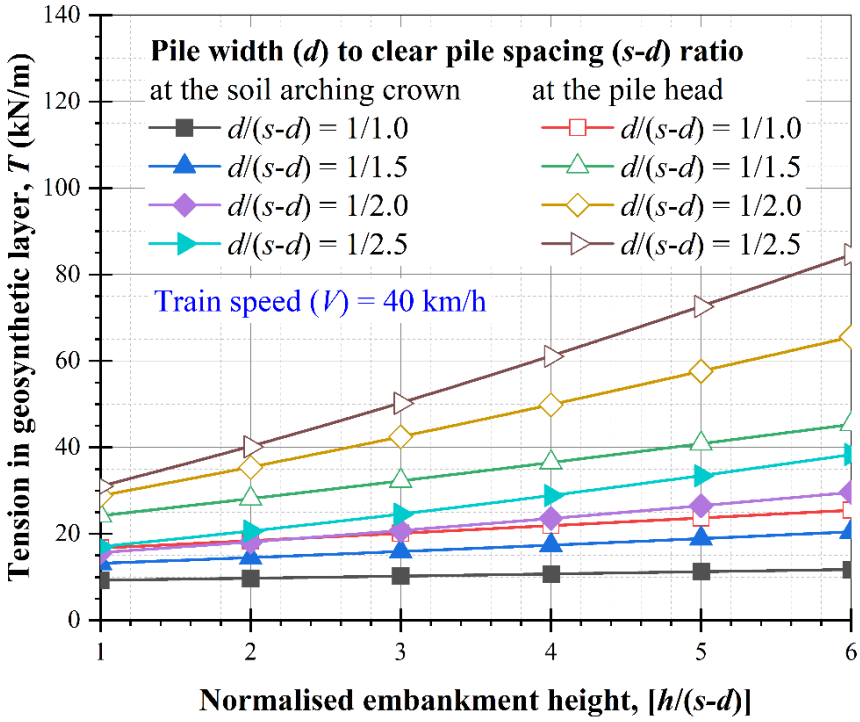

Figure 5.6: Effect of embankment height on tension in the geosynthetic layer

5.4.2 Effect of the one-dimensional modulus of subsoil

The effect of one-dimensional modulus of subsoil (E_o) on soil arching indices and tension in the geosynthetic layer for different ratios of pile width (d) to clear spacing (s-d) is shown in Figures 5.7 - 5.10. The effect of E_o on the stress concentration ratio is shown in Figure 5.7. For the unreinforced case as shown in Figure 5.7(a), no change has been found in the *SCR* with a variation in E_o whereas Figure 5.7(b) shows the effect of E_o on *SCR* for the reinforced case. It can be seen that the *SCR* decreases by up to 72% with an increase in the E_o from 0.5 MPa to 3.0 MPa. However, the *SCR* increases by up to 43% and 38% for the unreinforced and reinforced case, respectively with an increase in the ratio of d/(s-d) from 0.4 to 1 and is likely to approach a limiting value for a higher E_o value of the subsoil.

Thus, this implies that the subsoil plays a major role in the load transfer mechanism, especially in the reinforced case. A comparison of Figure 5.7(a) and 5.7

(b) shows that the role of the geosynthetic layer is more pronounced for very compressible subsoil (0.5 MPa in this study).

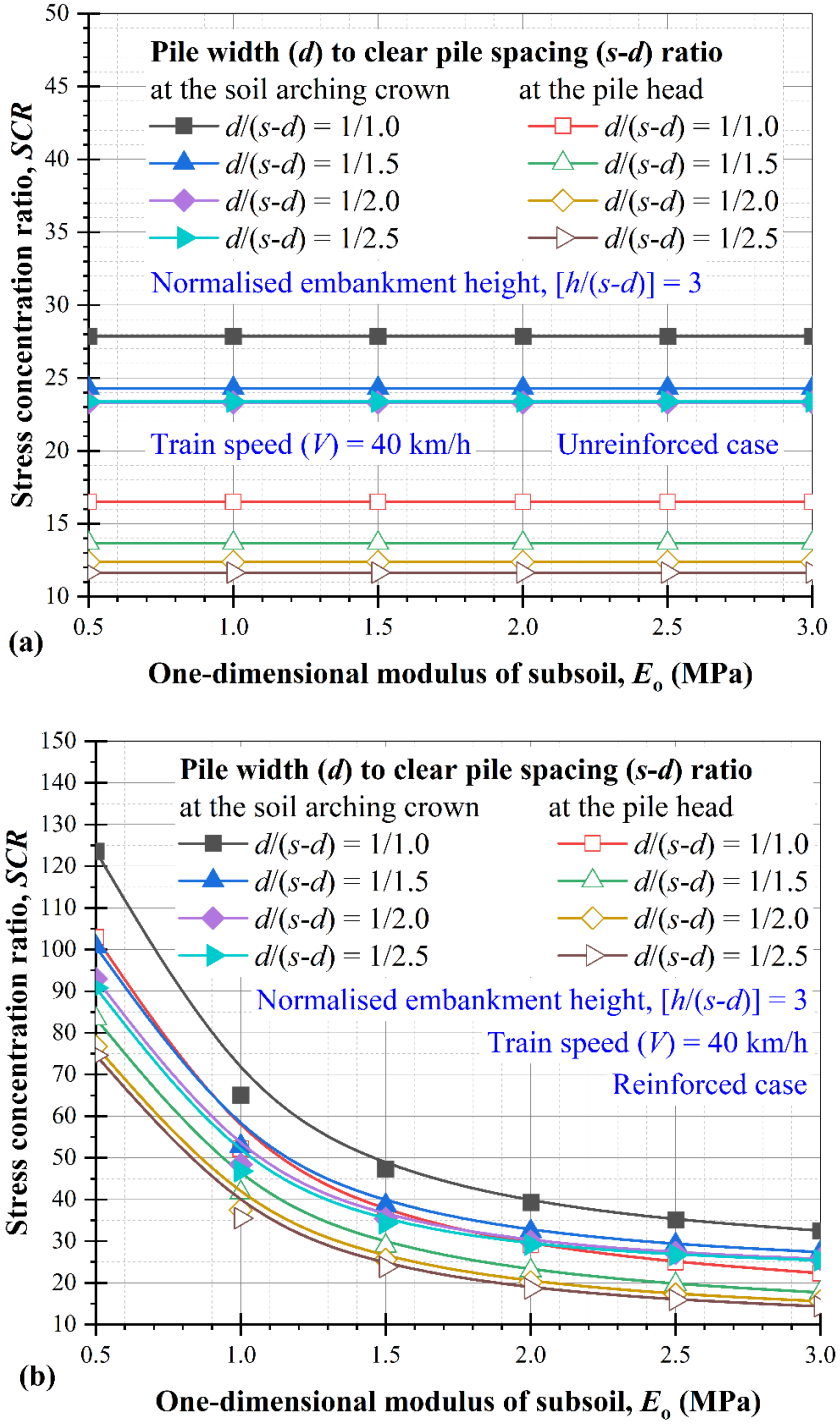

Figure 5.7: Effect of one-dimensional modulus of subsoil on stress concentration ratio in (a) the unreinforced case, and (b) the reinforced case

Figure 5.8(a) shows the effect of E_o on stress efficacy (E_{str}) in the unreinforced case. It can be seen that the E_{str} is not affected by the one-dimensional modulus of subsoil (E_o) as the subsoil makes no contribution in the unreinforced case, whereas in the reinforced case, as shown in Figure 5.8(b), the E_{str} decreases by up to 24% with an increase in the E_o from 0.5 MPa to 3.0 MPa. However, a variation in efficacy is more noticeable for the small $d/(s\text{-}d)$ ratio (0.4 in this study) and failure at the pile head case. It is also worth noting that the efficacy is likely to approach a limiting value at a small value of E_o. Thus, this implies that the efficiency of load transfer to pile top is influenced by the subsoil characteristic.

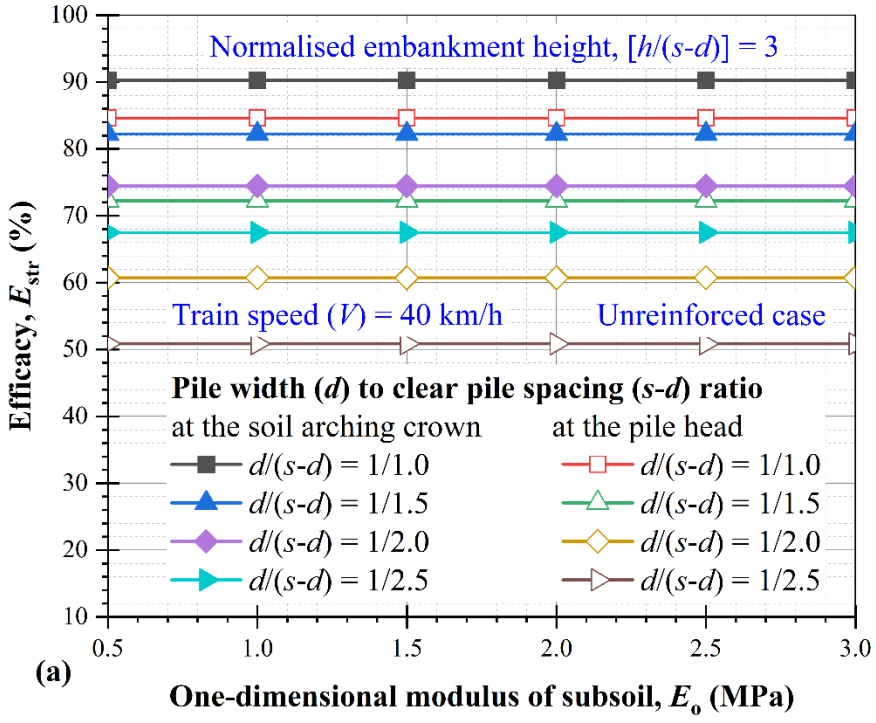

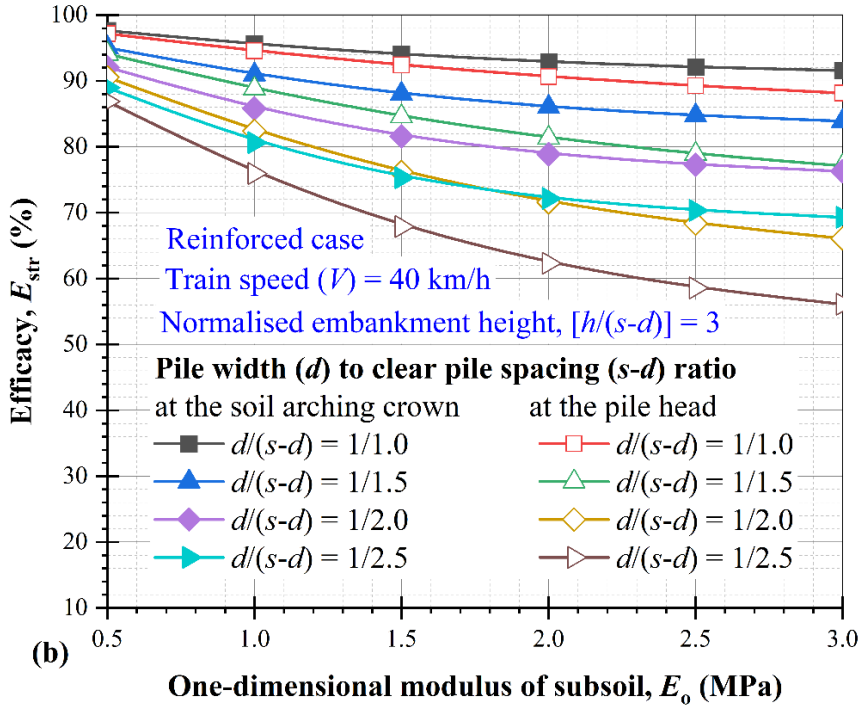

Figure 5.8: Effect of one-dimensional modulus of subsoil on stress efficacy in (a) the unreinforced case, and (b) the reinforced case

In the unreinforced case, the effect of the one-dimensional modulus of the subsoil on the *SAR* is shown in Figure 5.9(a). The *SAR* decreases by up to 57% and 63% for failure occurring at the crown and pile head, respectively with an increase in the ratio of $d/(s\text{-}d)$ from 0.4 to 1, while it remains constant with the variation of the E_o from 0.5 MPa to 3.0 MPa.

Further, the effect of the one-dimensional modulus of the subsoil on the *SAR* in the reinforced case is shown in Figure 5.9(b). The *SAR* increases by up to 200% with an increase in the E_o from 0.5 MPa to 3.0 MPa for both failure regions (failure at the soil arching crown and the pile head). However, a small $d/(s\text{-}d)$ ratio is more prominent and the *SAR* is likely to approach a limiting value at the same ratio. The value of *SAR* in the reinforced case is smaller compared to unreinforced case which implies that reinforcement improves the load transfer from subsoil to pile top.

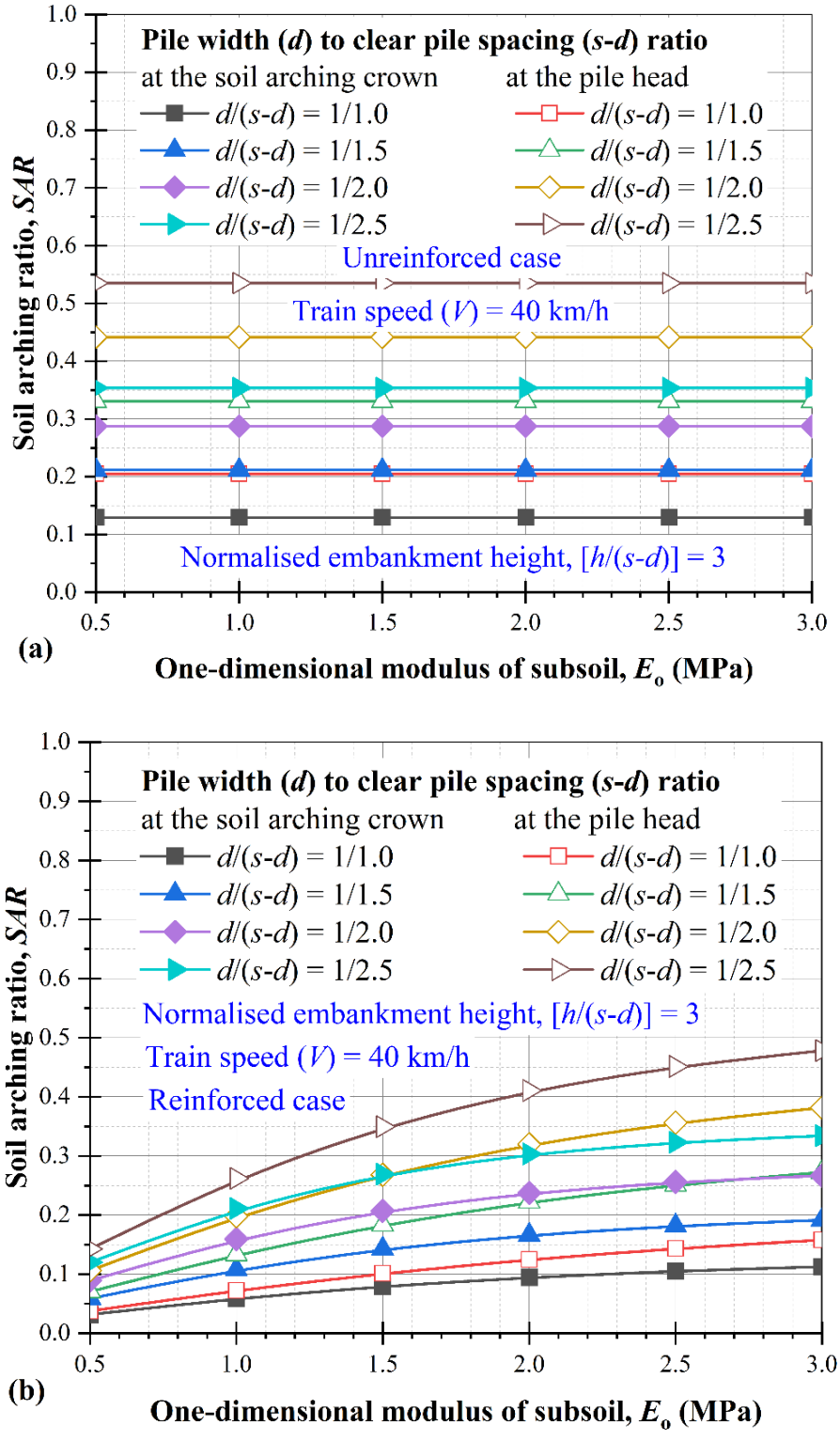

Figure 5.9: Effect of one-dimensional modulus of subsoil on the soil arching ratio in (a) the unreinforced case, and (b) the reinforced case

Figure 5.10 illustrates the effect of the one-dimensional modulus of subsoil on tension in the geosynthetic layer. The tension in the geosynthetic layer decreases with

an increase in the ratio of $d/(s\text{-}d)$ from 0.4 to 1. In addition, it decreases by up to 76% and 72% for failure occurring at the crown and pile head, respectively with an increase in the E_o from 0.5 MPa to 3.0 MPa for both failure regions (failure at the soil arching crown and the pile head). The tension in the geosynthetic layer is more noticeable for small one-dimensional modulus of subsoil and the ratio of $d/(s\text{-}d)$. For a large value of the E_o, it is likely to approach a limiting value which implies that the geosynthetic layer is more significant for very compressive subsoil. It can also be seen that for the same $d/(s\text{-}d)$ ratio, the tension in the geosynthetic layer is higher in the case of failure at the pile top compared to failure at the soil arching crown.

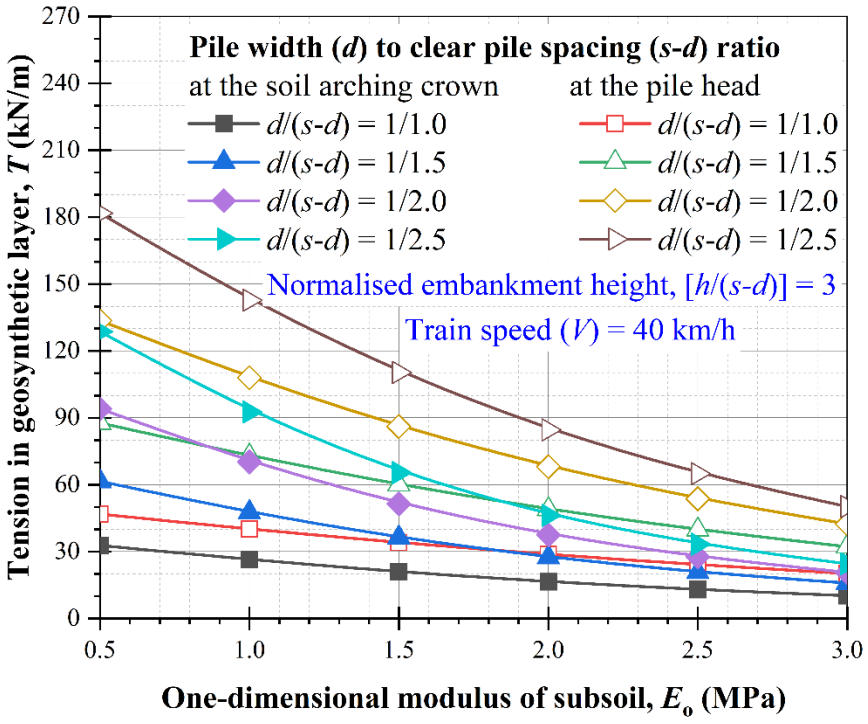

Figure 5.10: Effect of one-dimensional modulus of subsoil on tension in the geosynthetic layer

5.4.3 Effect of tensile stiffness of the geosynthetic layer

The effect of tensile stiffness of the geosynthetic layer (J) on soil arching indices and tension in the geosynthetic layer for different ratios of pile width (d) to clear spacing

(*s-d*) is shown in Figures 5.11 - 5.14. The effect of tensile stiffness (*J*) on the stress concentration ratio is shown in Figure 5.11. It can be seen that the *SCR* increases by up to 28% for a failure occurring at arching crown, while it increases by up to 62% for a failure occurring at the pile head with an increase in tensile stiffness (*J*) from 0 to 2000 kN/m. It is also evident that the *SCR* increases with an increase in the ratio of *d*/(*s-d*) from 0.4 to 1.

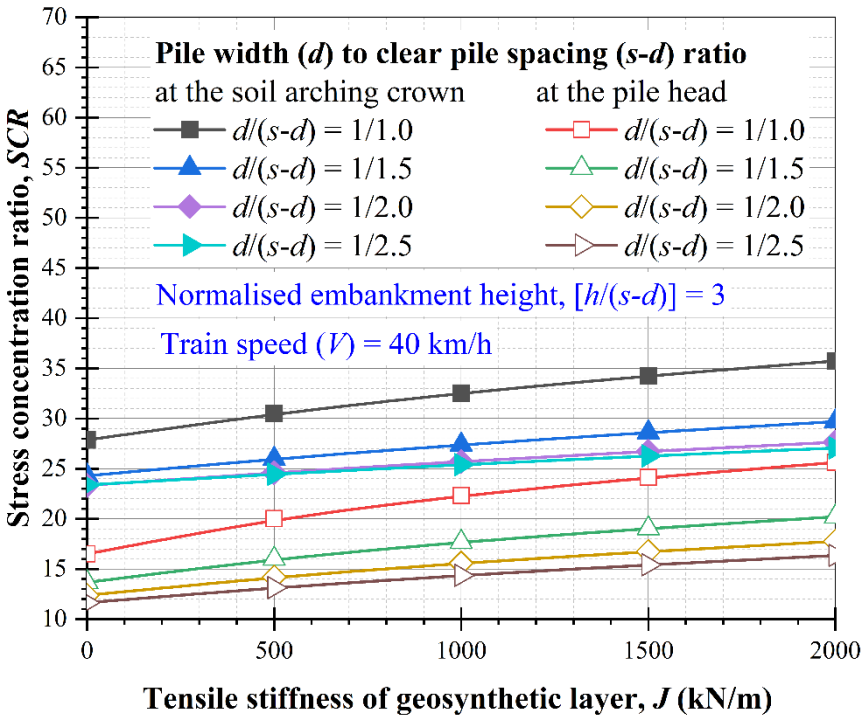

Figure 5.11: Effect of tensile stiffness of the geosynthetic layer on the stress concentration ratio in the reinforced case

Figure 5.12 shows the effect of tensile stiffness of the geosynthetic layer on the efficacy. The E_{str} increases by up to 32% and 70% for a failure occurring at the crown and pile head, respectively with an increase in the ratio of *d*/(*s-d*) from 0.4 to 1. The effect of tensile stiffness of the geosynthetic layer is more prominent on a small *d*/(*s-d*) ratio.

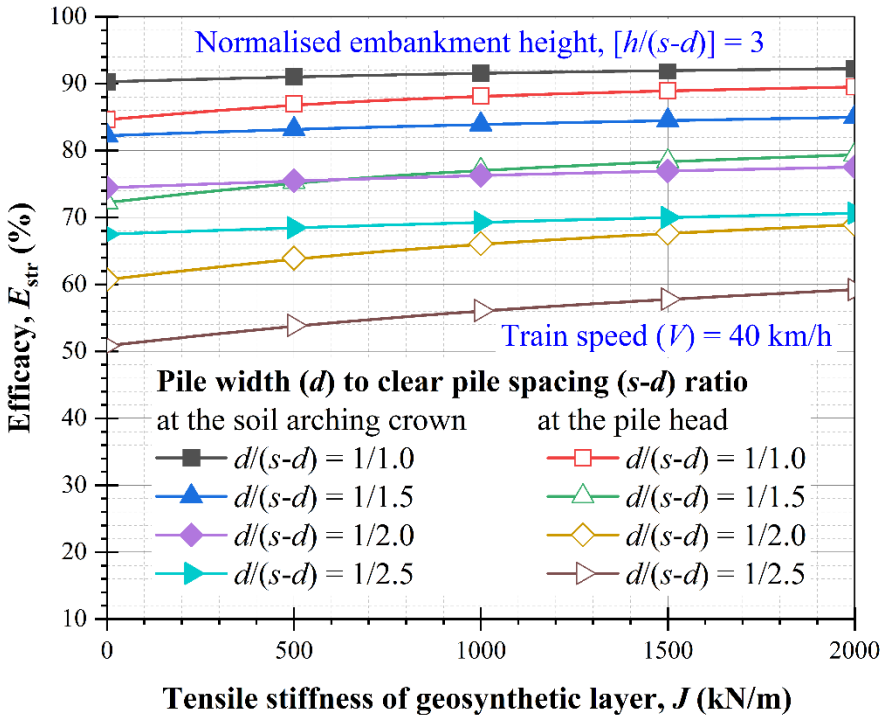

Figure 5.12: Effect of tensile stiffness of the geosynthetic layer on the stress efficacy in the reinforced case

Figure 5.13 illustrates the effect of the *J* on the *SAR*. The *SAR* decreases by up to 18% with an increase in the *J* from 0 to 2000 kN/m in the case of a failure occurring at the pile head, whereas there was a negligible effect in the case of a failure occurring at the soil arching crown. A comparison with Figure 5.9(b) shows that the one-dimensional modulus of the subsoil contributes significantly to the load transfer mechanism.

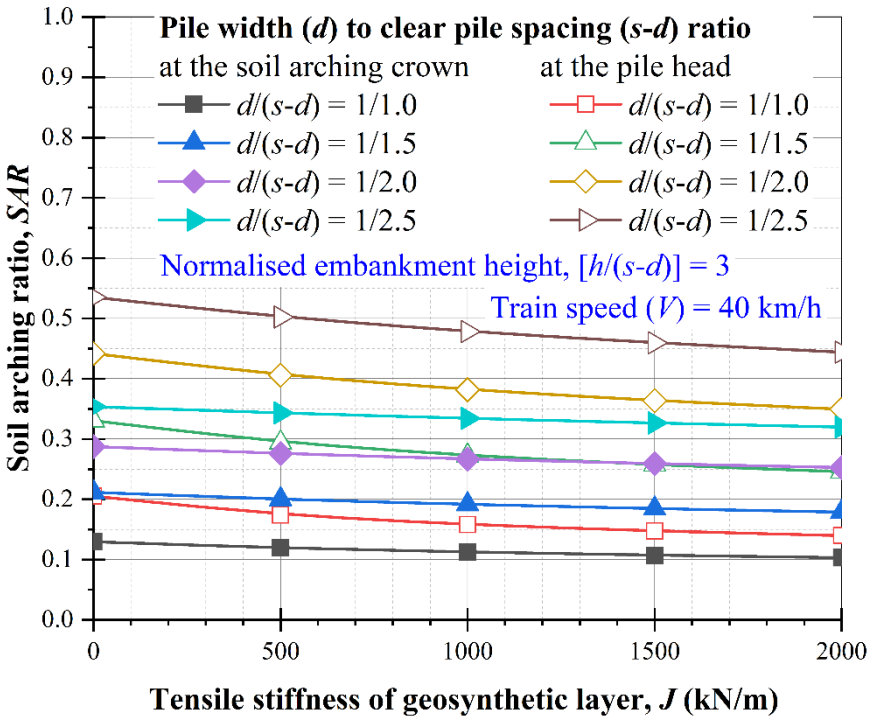

Figure 5.13: Effect of tensile stiffness of the geosynthetic layer on the soil arching ratio in the reinforced case

Figure 5.14 illustrates the effect of tensile stiffness of the geosynthetic (J) on tension in the geosynthetic (T). The tension in geosynthetic layer decreases with an increase in the J and the ratio of $d/(s\text{-}d)$ from 0.4 to 1. The tension in the geosynthetic layer is more prominent for the large tensile stiffness of the geosynthetic layer and a small ratio of $d/(s\text{-}d)$. For a small value of J, it is approaching zero which implies that higher stiffness of the geosynthetic layer is more significant for soil arching. It can also be seen that for the same $d/(s\text{-}d)$ ratio, tension in the geosynthetic layer is higher in the case of failure at the pile top compared to failure at the soil arching crown.

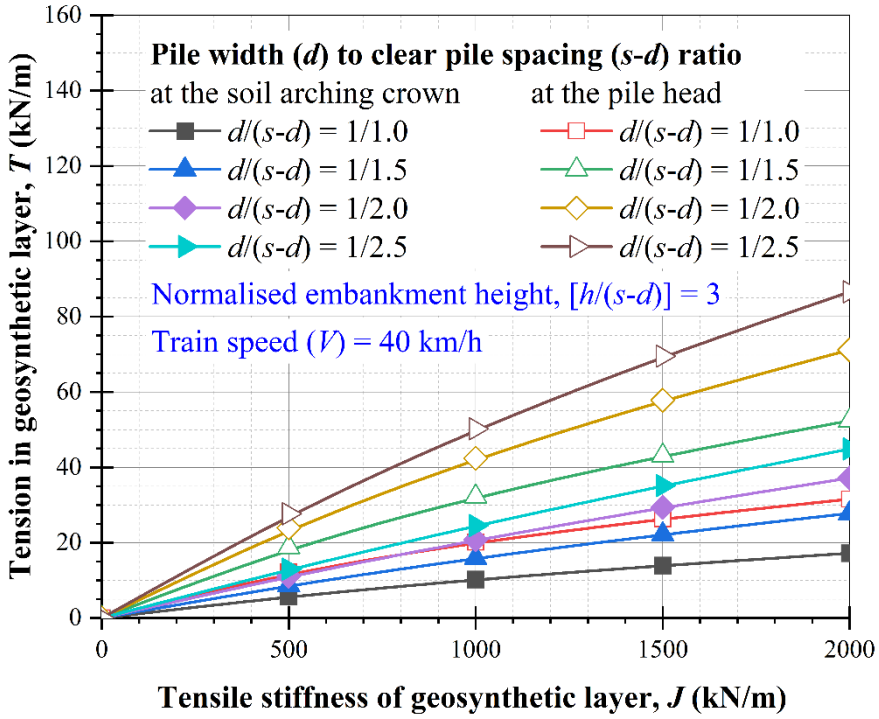

Figure 5.14: Effect of tensile stiffness of the geosynthetic layer on tension in the geosynthetic layer

5.4.4 Effect of equivalent dynamic load induced by different train speed

The effect of train speed (V) on soil arching indices and tension in the geosynthetic layer for different ratios of pile width (d) to clear spacing (s-d) is shown in Figures 5.15 - 5.18. Figure 6.15(a) shows the effect on the *SCR* in the unreinforced case. It can be seen that the *SCR* increases by up to 2% for failure occurring at the crown with an increase in the ratio of $d/(s\text{-}d)$ from 0.4 to 1. However, it remains constant for the case where failure occurs at the pile head. Moreover, in the crown failure case, the *SCR* increases with an increase in the normalised embankment height which is similar to the result shown in Figure 5.3(a). It is also evident that pile head failure is critical compared to arching crown failure as the *SCR* value for the pile head failure case is lower than for the soil arching crown case.

In the reinforced case, as shown in Figure 5.15(b), a similar trend to Figure 5.15(a) can be seen. However, the *SCR* value is higher in the reinforced case compared

to the unreinforced case due to the inclusion of the geosynthetic layer which enhances the load transfer from the subsoil to the pile top.

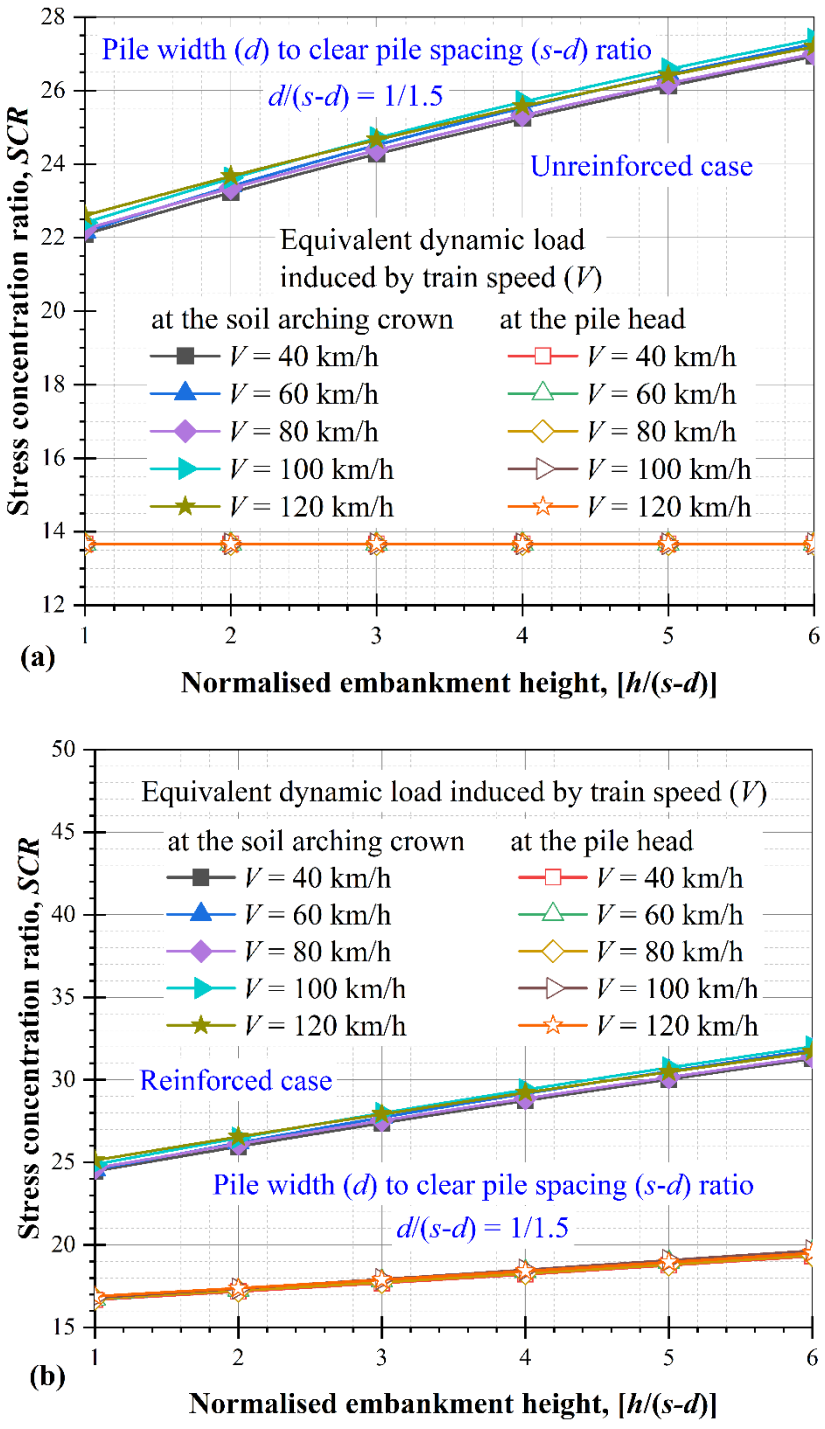

Figure 5.15: Effect of train speed on the stress concentration ratio in (a) the unreinforced case, and (b) the reinforced case

The effect of train speed on stress efficacy in the unreinforced case is shown in Figure 5.16(a). Train speed has a negligible effect on stress efficacy with an increase in the ratio of $d/(s\text{-}d)$ from 0.4 to 1, although in the crown failure case, the E_{str} increases with an increase in normalised embankment height. It is also evident that the pile head failure is critical compared to arching crown failure as the E_{str} value for the pile head failure case is lower than the soil arching crown case.

Figure 5.16(b) shows a similar trend to Figure 5.16(a). However, the E_{str} value is higher in the reinforced case compared to the unreinforced case due to the inclusion of the geosynthetic layer which enhances the load transfer from the subsoil to the pile top.

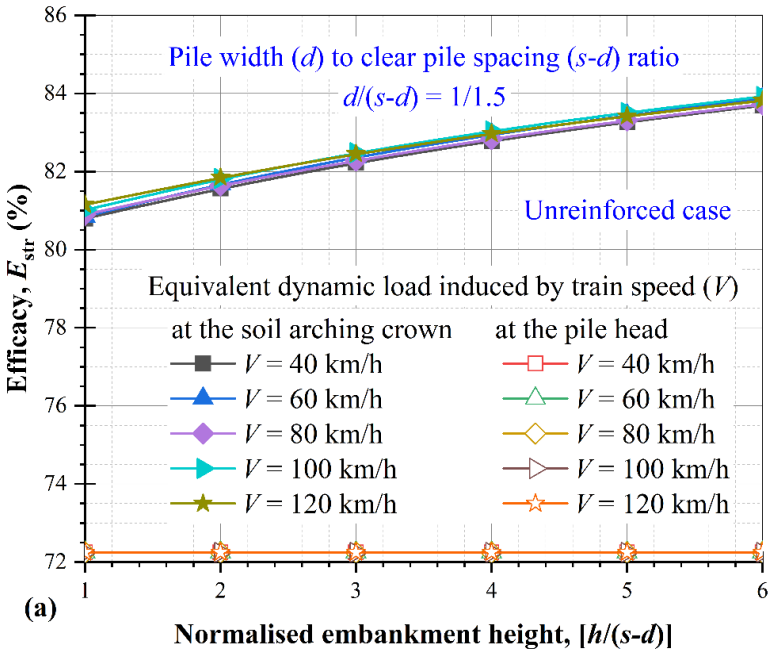

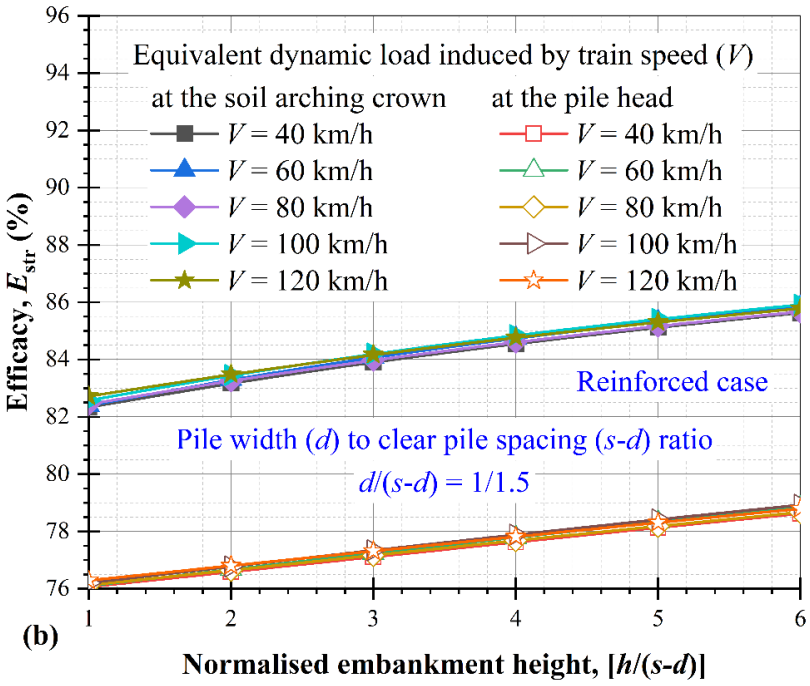

Figure 5.16: Effect of train speed on stress efficacy in (a) the unreinforced case, and (b) the reinforced case

Figure 5.17 shows the effect of train speed on the *SAR*. It can be seen that train speed has a negligible effect on the *SAR* for both unreinforced and reinforced cases (refer to Figure 5.17(a) and (b), although in the crown failure case, the *SAR* decreases with an increase in the normalised embankment height. Pile head failure is critical compared to arching crown failure as the *SAR* value for the pile head failure case is higher than the soil arching crown case. Also, the *SAR* value is lower in the reinforced case compared to the unreinforced case due to the inclusion of the geosynthetic layer which enhances the load transfer from the subsoil to the pile top.

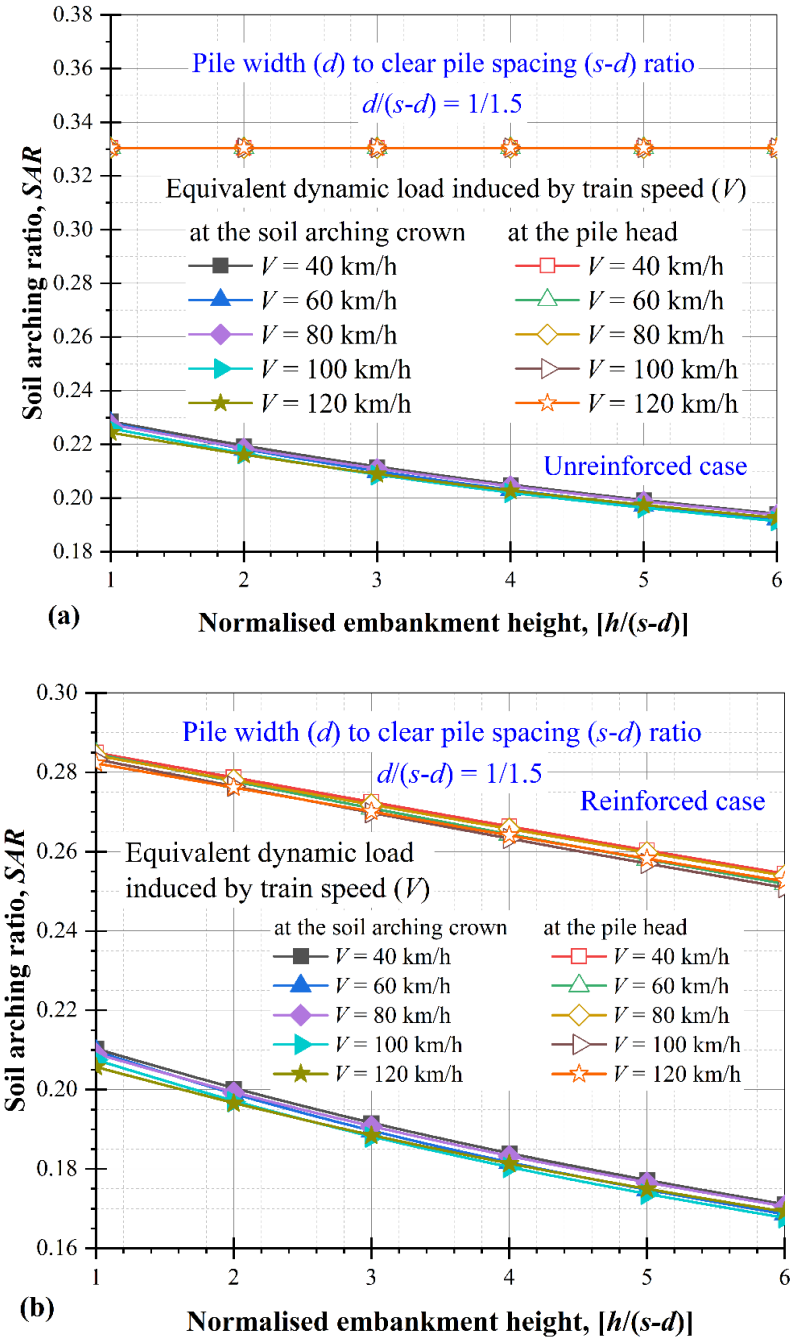

Figure 5.17: Effect of train speed on the soil arching ratio in (a) the unreinforced case, and (b) the reinforced case

Figure 5.18 illustrates the effect of train speed (V) on tension in the geosynthetic (T). The tension in the geosynthetic layer is not affected by a variation in train speed, although in the crown failure case, the T is much more prominent and increases with an increase in the normalised embankment height. The T value for the

pile head failure case is lower than for the soil arching crown case.

It is worth noting that the surcharge induced by different train speeds does not significantly influence soil arching due to a higher value. However, if we consider a small value of surcharge we can see the effect of the surcharge which can be considered by different train speeds.

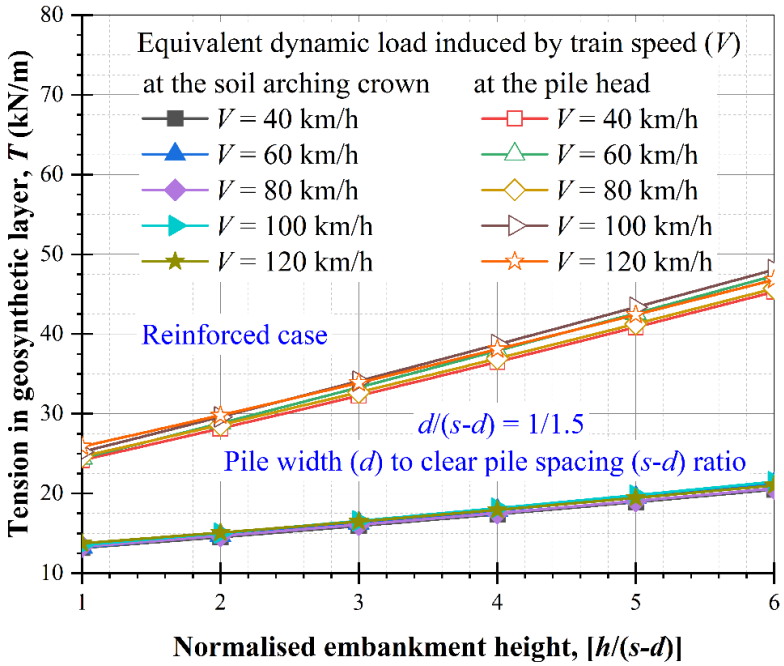

Figure 5.18: Effect of train speed on tension in the geosynthetic layer

5.5 SUMMARY

In this chapter, an 3D analytical method considering the accurate evaluation of surcharge over the soil arching crown is proposed. The accuracy of the proposed method is assessed using a field study and a few existing empirical methods and it is found to be in good agreement with both studies. In particular, the present method enables a realistic approximation of vertical stress on the soil arching crown which can be useful to design a pile-supported railway embankment.

The analysis results show that the performance of soil arching is significantly affected by several parameters of the pile-supported railway embankment such as clear pile spacing, embankment height, subsoil compression modulus, tensile stiffness of geosynthetic and train speed. Based on the present method, the following findings are made:

1) The failure of soil arching at the pile top is critical in the 3D condition, whereas the soil arching failure at crown is more critical in the 2D condition.
2) The soil arching phenomena increase with an increase in the ratio of pile width (d) to clear pile spacing (s-d), which implies that pile spacing is a key parameter for efficient soil arching. The soil arching enhances up to 30% in terms of stress efficacy under the effect of different pile-supported railways embankment parameters.
3) The geosynthetic layer and compression modulus of subsoil significantly contribute to the load transfer likely to be for large pile spacing and very compressive subsoil (e.g. E_o = 0.5 MPa for this study). The soil arching increases up to 26% with the inclusion of a geosynthetic layer resting at the base of the embankment and it increases up to 43% with an increase the E_o from 0.5 to 3.0 MPa.
4) The surcharge induced by a railway corridor resting on the embankment is also influenced to the soil arching mechanism. However, due to a higher surcharge value, the effect of surcharge induced by different train speeds is not fully captured in this chapter.

The next chapter is covered the numerical simulation of soil arching under the earthquake condition.

CHAPTER 6

INVESTIGATION OF SOIL ARCHING IN A PILE-SUPPORTED EMBANKMENT UNDER THE EARTHQUAKE

The seismic assessment of soil arching is covered in this chapter. It primarily focuses on the different aspects of soil arching under seismic excitation for both unreinforced and reinforced cases. Subsequently, the most influential parameters of the pile-supported embankment, as explained in chapter 3, are investigated.

6.1 INTRODUCTION

The geosynthetic-reinforced pile-supported (GRPS) embankments provide feasible solutions for railroad construction on soft soil due to their rapid construction and less differential settlements. In GRPS embankments, soil arching is a key mechanism for load transfer from the subsoil to the pile top. Several finite element method (FEM) based numerical studies (Han and Gabr 2002; Huang et al. 2009; Nunez et al. 2013; Meena et al. 2020) and model tests (Chen et al. 2010; Iglesia et al. 2014; Fagundes et al. 2017; Rui et al. 2019) have been conducted to investigate the soil arching under the static loading condition.

The dynamic behaviour of soil arching has also been investigated under cyclic loading, representing traffic loading, in a few recent studies (Han et al. 2015; Niu et al. 2018; Pham and Dias 2019). Han et al. (2015) conducted a series of model tests and

FEM-based numerical simulations and found that the reinforcement and subsoil characteristics can enhance soil arching mobilisation under dynamic loading. Niu et al. (2018) reported that the height of soil arching is reduced under the dynamic load induced by a high-speed train compared to the static loading condition. Pham and Dias (2019) investigated the behaviour of a GRPS embankment subjected to cyclic loading. However, the seismic analysis of soil arching is yet to be investigated for GRPS embankments.

Although Australia is widely recognised as a seismically non-active country, small to moderate seismic activities continue to occur (Daniell and Love 2010). The locations of these seismic events in Australia are illustrated in Figure 6.1 and Table 6.1 details these events. This study analyses the impact of seismic activity on GRPS embankments.

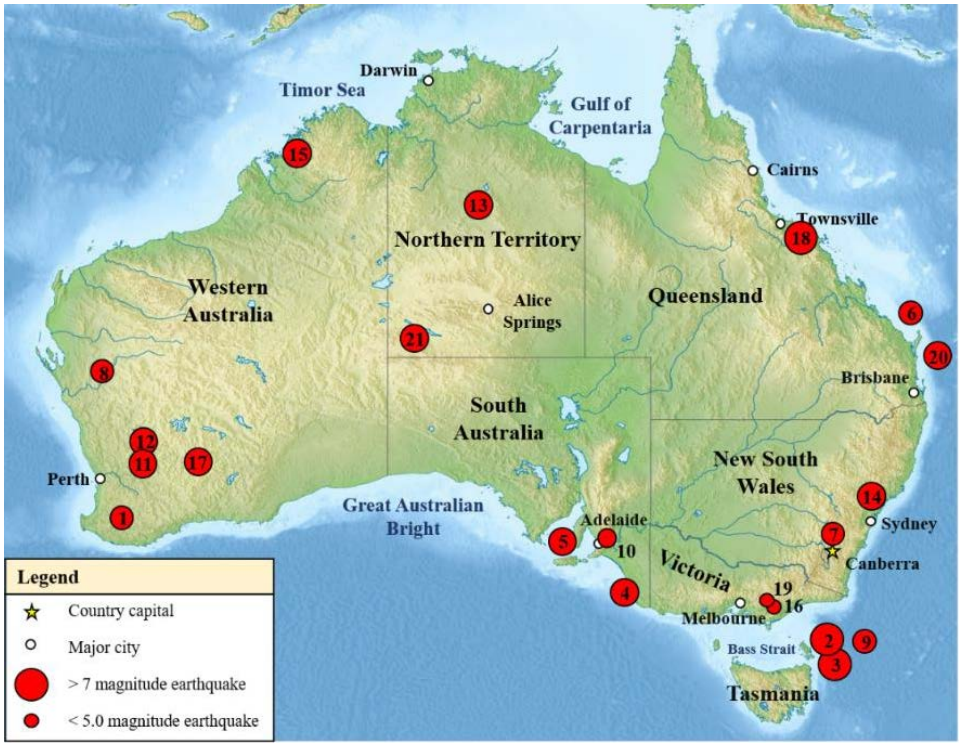

Figure 6.1: Locations of the key seismic events in Australia (map modified from Geoscience Australia)

Table 6.1: Seismic events in Australia and territories (Meena and Nimbalkar 2019)

Location No. in Figure 6.1	Year	Location	State	Magnitude (M_L)
1.	2018	Lake Muir	Western Australia	5.3
2.	2016	Petermann Ranges	Northern Territory	6.1
3.	2015	Offshore East of Fraser Island	Queensland	5.4
4.	2012	Moe	Victoria	5.4
5.	2011	Near Bowen	Queensland	7.1
6.	2010	Kalgoorlie	Western Australia	5.0
7.	2000	Boolarra South	Victoria	5.0
8.	1997	Collier Bay	Western Australia	6.2
9.	1989	Newcastle	New South Wales	5.4
10.	1988	Tennant Creek	Northern Territory	6.6
11.	1979	Cadoux	Western Australia	6.1
12.	1968	Meckering	Western Australia	6.5
13.	1954	Adelaide	South Australia	5.4
14.	1946	Offshore East of Flinders Island	Tasmania	5.8
15.	1941	Meeberrie	Western Australia	6.3
16.	1934	Gunning	New South Wales	5.6
17.	1918	Offshore Gladstone	Queensland	6.0
18.	1902	Warooka	South Australia	6.0
19.	1897	Offshore Beachport	South Australia	6.5
20.	1892	Tasman Sea NE	Tasmania	6.9
21.	1885	Tasman Sea	Tasmania	6.8

6.2 NUMERICAL MODELLING

The finite element (FE)-based commercial software ABAQUS (2018) is used to assess soil arching under the earthquake condition. The key points of the FE analysis, such as the analysed area, soil constitutive model, element type, interface, boundary condition, loading and modelling procedure are detailed in this section.

6.2.1 Geometric profile of FE model

As shown in Figure 3.1, the same central part of a typical pile-supported railway embankment is considered for the earthquake analysis. However, the FE model consists of a hard stratum underlain by subsoil and end-bearing piles. The pile length and subsoil depth are the same (8 m). The pile spacing (s) and diameter (D) are 2 m to 3.5 m and 1 m, respectively. An embankment fill, including a 400 mm thick gravel

layer, is laid over the pile foundation. A 2 mm thick geosynthetic layer is sandwiched between two gravel bed layers in the reinforced condition. First, a 200 mm thick gravel layer is placed on the piled improved subsoil area, then the geosynthetic layer is laid without any physical damage. Another 200 mm layer of thick gravel is placed on the geosynthetic top to achieve the required thickness of the gravel layer (i.e., 400 mm). The embankment height (h) varies from 2.5 m to 6.5 m.

6.2.2 Boundary condition, element type and interface

As explained in chapter 2, the adoption of the infinite element boundary can reduce the wave reflection from the model boundaries during the seismic analysis. The four-node plane strain element with reduced integration (CPE4R) is used for the finite domain of the FE model, whereas the four-node plane strain linear infinite element (CINPE4) is used for the infinite domain. In addition, the interaction between the pile and surrounding soil is stimulated using the basic Coulomb friction model (Potyondy 1961).

6.2.3 Constitutive model, material parameters and damping

The Mohr-Coulomb (MC) constitutive model is chosen for embankment fill, gravel layer and hard stratum, whereas the Modified Cam Clay (MCC) model is used for the subsoil. The piles and geosynthetic layer are considered to follow an isotropic linear elasticity. The Young′s modulus of pile (E_p) and geosynthetic layer are 20 GPa, and 500 MPa, respectively. The biaxial geogrid @ 5 % tensile strength with a rib thickness of 2 mm is used as a geosynthetic layer for the reinforced case. Table 6.2 illustrates the material properties used for the seismic analysis.

Table 6.2: Material properties used for the seismic analysis

Material properties	Embankment fill	Gravel bed	Subsoil	Hard stratum
Constitutive model	MC	MC	MCC	MC
Unit weight, γ (kN/m^3)	20	21	18.4	21
Young's modulus, E (MPa)	20	25	-	500
Poisson's ratio, v	0.25	0.25	0.30	0.30
Effective cohesion c′ (kPa)	1	1	-	1
Effective friction angle, ϕ' (degree)	30	35	-	45
Effective dilation angle, ψ (degree)	0	5	-	-
Critical-state stress ratio, M	-	-	1.2	-
Logarithmic hardening constant, λ	-	-	0.06	-
Logarithmic bulk modulus, k	-	-	0.012	-
Initial yield surface size, a_o (kPa)	-	-	103	-
Void ratio at unit pressure, e_1	-	-	0.87	-
Initial void ratio, e_o	-	-	0.45	-
Geosynthetic stiffness, J (kN/m) = $E \times t_{geo}$	1000			

In the dynamic or seismic analysis of soil, energy dissipation occurs, which is referred to as hysteretic damping. This damping can significantly influence the FE model's response. The indefinite travel of stress waves without changing amplitude is not possible in real soil (Kramer 1996). The amplitude of the stress waves is reduced with distance in the soil. The possible reason for this reduction may be material or geometric damping. Material damping is mainly associated with soil properties such as friction and sliding in the inter-particles pore fluid viscosity. The viscous damping is commonly used to characterise this damping. Due to the material damping of soil, the elastic energy of the stress waves decreases with the distance, resulting in the amplitude of stress waves also being reduced (Bakr and Ahmad 2018). Consequently, the elastic energy per unit volume (specific energy) can also reduce due to the geometry of the material, which is known as geometric damping. Rayleigh damping is commonly used as geometric damping.

Rayleigh damping is subjected to viscus damping where energy is resealed from a finite source, ranging from large-scale earthquake fault to small-scale vibrating

foundation (Kramer 1996). Rayleigh damping instead of viscous damping is used in the FE analysis to obtain a correct response from the FE model during these types of analyses. Rayleigh damping is obtained as in Nimbalkar et al. (2012):

$$[C] = \alpha[M] + \beta[K'] \tag{6.1}$$

where $[C]$ is the damping matrix, $[M]$ is the mass matrix, $[K']$ is the stiffness matrix, α and β are the damping coefficients calculated as:

$$\alpha = 2 \times \left(\frac{\omega_i.\omega_j}{\omega_i+\omega_j}\right) \times \xi_0 \tag{6.2}$$

$$\beta = \left(\frac{2}{\omega_i+\omega_j}\right) \times \xi_0 \tag{6.3}$$

where α and β are obtained using the first two vibration modes i and j, respectively; ω_i and ω_j are the angular frequencies of the vibrating material and ξ_o is the damping ratio.

The angular frequencies (ω_n) of the selected vibration modes are calculated as in (Kramer 1996; Nimbalkar et al. 2012)

$$\omega_n = \frac{\pi V_s}{2h'}(2n-1) \tag{6.4}$$

where V_s is the shear wave velocity, h' is material height, and n is mode number (referred to as i and j in this study). The damping ratio (ξ_o) is assumed to be 3% to compute the damping coefficients α and β (Bi et al. 2020). In addition, the stiffness (k) and damping (c) coefficients are determined as:

$$k = \frac{0.4E(1-v)}{h'(1+v)(1-2v)} \tag{6.5}$$

$$c = \sqrt{\frac{E\rho}{(1+v)(1-v)}} \tag{6.6}$$

where E is the elastic modulus, v is Poisson's ratio, ρ is the density of particular

material. The values of the different parameters which are used to determine shear wave velocity (V_s), stiffness (k) and damping coefficient (c) are listed in Table 6.3.

Table 6.3: Parameter values to determine the shear wave velocity, stiffness and damping coefficient

Parameters	Material			
	Embankment	Gravel bed	Subsoil	Hard stratum
Height, h' (m)	3.1	0.4	8	0.5
Young's modulus, E (N/m^2) × 10^6	20	25	10	250
Density, ρ (kg/m^3)	2039.44	2141.41	1876.30	2141.41
Poisson's ratio, (υ)	0.25	0.25	0.30	0.30
Shear wave velocity, V_s (m/s)	62.63	68.34	45.30	211.90

Material response in seismic analysis depends on its dynamic characteristics. Therefore, it is crucial to determine the Rayleigh damping coefficients precisely. The choice of targeted modal periods for the determination of Rayleigh damping parameters is dependent on the modal periods of the considered structure. Table 6.4 shows the dynamic parameters used in the FE model to compute the Rayleigh damping coefficients.

Table 6.4: Dynamic parameters used for the seismic analysis

Material type	Stiffness coefficient, k (10^8) (N/m)	Damping coefficient, c (10^6) (Ns/m)	Angular frequencies (rad/s)		Rayleigh damping coefficient	
			ω_1	ω_2	α	β
Embankment fill	0.03	0.21	31.74	158.68	1.5868	0.00032
Gravel bed	0.30	0.24	268.36	1341.76	13.4178	0.00004
Subsoil	0.01	0.14	8.89	44.45	0.4445	0.00112
Hard stratum	2.69	0.77	665.71	3328.53	33.2853	0.00002

6.2.4 Seismic input

A few Australian earthquakes followed similar seismic parameters to the Christchurch 2011 earthquake (Meena and Nimbalkar 2019). Therefore, the acceleration time history of the Christchurch 2011 earthquake is chosen in this study. Only horizontal acceleration is considered for an earthquake excitation. The magnitude of this earthquake was 6.3 M_L on the Richter scale with 0.34g peak ground acceleration (PGA) for 30 s (refer to Figure 6.2a). Fast Fourier transform (FFT) analysis is conducted to obtain the dominant frequency (f_{eq}) of the input earthquake time history (refer to Figure 6.2b). In the literature, none of the studies has investigated the seismic assessment of soil arching. Thus, this thesis mainly focuses on the soil arching behaviour under a seismic condition. According to seismic zones and relevant ground motion parameters the mobilization of soil arching. The use of earthquake records obtained from single accelerogram is the first step which is deemed suitable for the model validation, in light of the absence of comprehensive earthquake records obtained from multiple accelerograms in the literature.

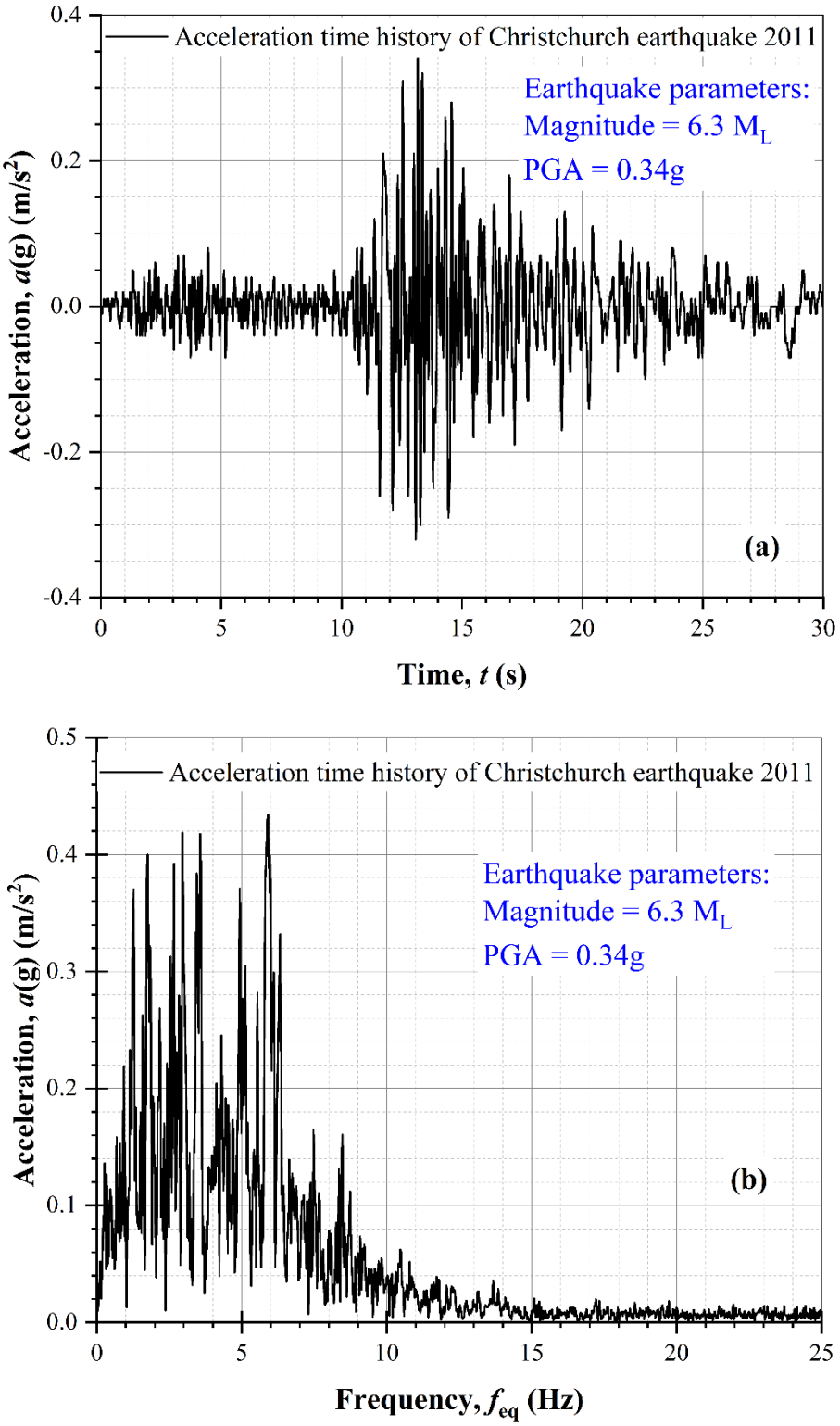

Figure 6.2: (a) Horizontal acceleration time history of the Christchurch 2011 earthquake, and (b) Fast Fourier transform amplitude of the Christchurch 2011 earthquake

6.2.5 FE simulation procedure

The numerical analysis starts by establishing the initial stress in the subsoil using the

geostatic step. The installation of the rigid piles and the stage construction of the pile-supported embankment, including the gravel bed and geosynthetic layer, are simulated in the following steps. After attaining full embankment height, the horizontal acceleration time history of the Christchurch 2011 earthquake is applied at the base of the FE model. In this Chapter, dynamic implicit analysis procedure is used for the dynamic analysis. The meshed profile of finite element is shown in Figure 6.3.

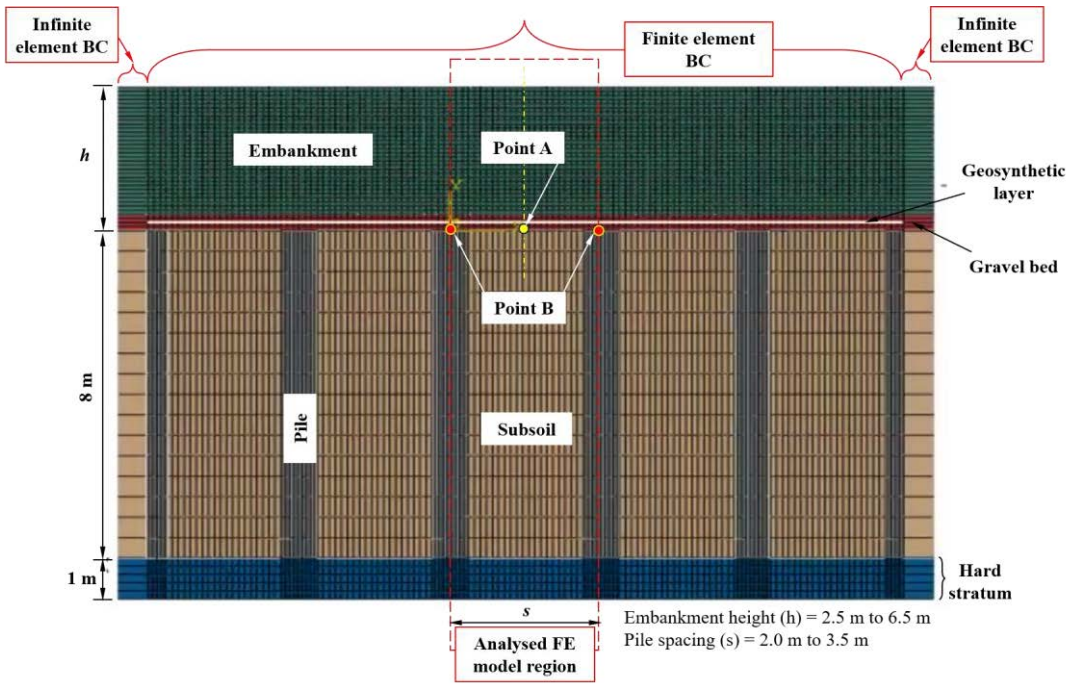

Figure 6.3: Mesh profile of the FE model

6.3 MODEL VALIDATION

None of the existing studies validate the numerical simulation of soil arching assessment in the earthquake condition. However, verification of material models with the existing static or dynamic triaxial tests could be useful. Such model verification is the future scope of this thesis.

6.4 RESULTS AND DISCUSSION

6.4.1 Vertical stress

Figure 6.4 shows the contours of vertical stress in the unreinforced condition at different time instances (i.e., 0, 13.16, and 30 s) above points A and B referred to in Figure 3.1. The embankment height (h) and vertical stress (σ) are normalised by clear pile spacing (s-d) and $\gamma(s$-$d)$, respectively, for the sake of general applicability. The normalised vertical stress on the subsoil is 0.89 when there is no earthquake (i.e., $t = 0$ s) whereas it increases to 1.67 at the end of an earthquake (i.e., $t = 30$ s). At $t = 0$ s, the soil arching zone lies between 0.32 - 0.59 of the normalised embankment height, while no soil arching zone is formed at t = 30 s. The normalised vertical stress has a negligible effect on the pile top. This implies that the vertical stress on the subsoil increases when the duration of an earthquake increases, disturbing the soil arching mobilisation.

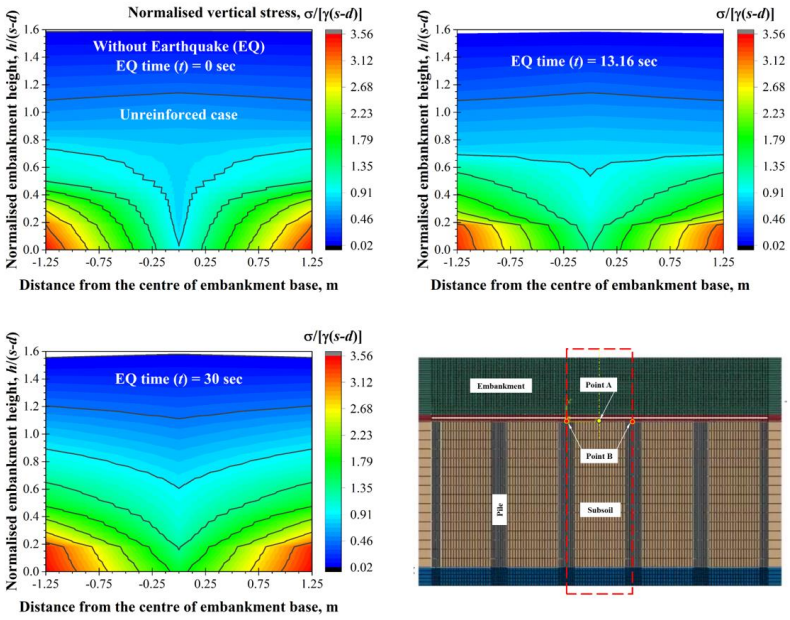

Figure 6.4: Vertical stress contour for different time instances

A comparison of the vertical stress contours in the unreinforced and reinforced case at t = 30 s is shown in Figure 6.5. In the unreinforced case, as shown in Figure 6.5(a), the normalised vertical stress on the subsoil is 1.67, similar to Figure 6.4 at *t* = 30 s. It decreases to 1.17 in the reinforced case, and the soil arching zone lies in between 0.36 - 0.50 of the normalised embankment height (referred to Figure 6.5b). In addition, the normalised vertical stress on the pile top decreases to 2.8. Thus, this implies that a reinforcement layer at the embankment base improves the soil arching mobilisation at time (*t*) 30 s.

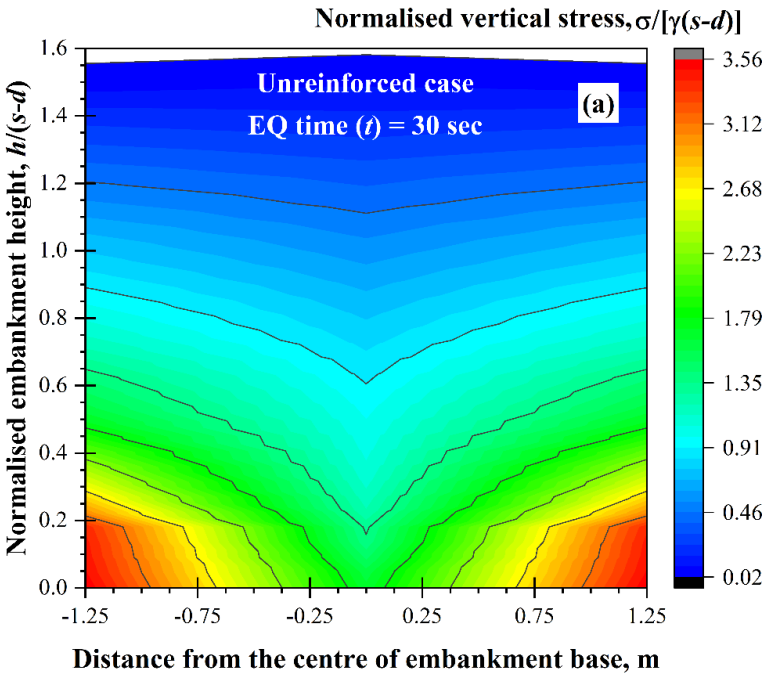

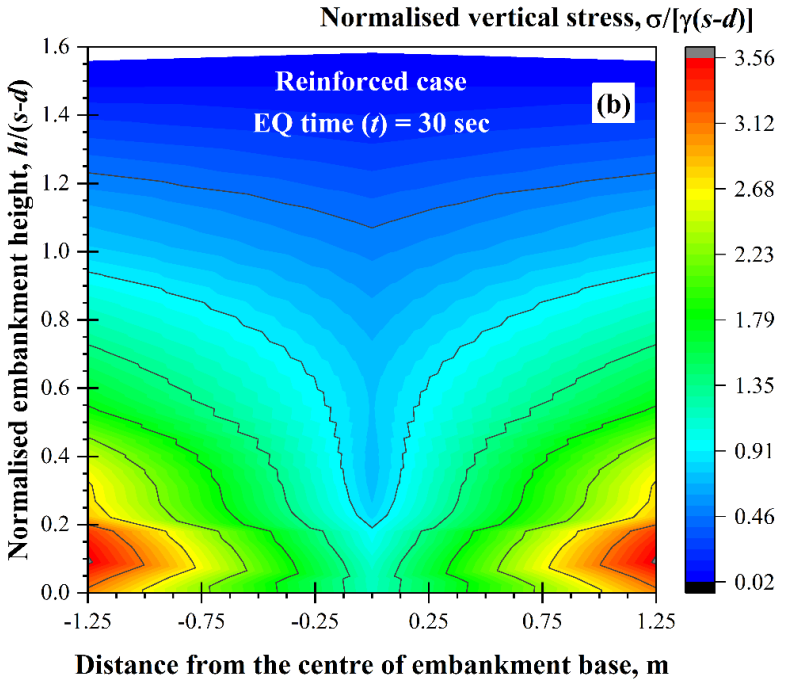

Figure 6.5: Vertical stress contour at earthquake time (t) = 30 s for (a) the unreinforced case, and (b) the reinforced case

As illustrated in Figures 6.4 and 6.5, the vertical stress on the subsoil and pile is altered during an earthquake excitation time (t). Therefore, it is crucial to examine the time history of vertical stress during an earthquake. Figure 6.6 shows the normalised vertical stress time history on the subsoil and pile for both unreinforced and reinforced cases during the earthquake. The vertical stress on the subsoil and pile are designated by amid and above the pile, respectively. In the unreinforced case, the normalised vertical stress on the subsoil starts at 0.89 and slightly increases by up to 11 s. Subsequently, it significantly increases in the time frame of 11-14 s. The input acceleration has a maximum intensity in this time frame. The normalised vertical stress gradually increases further increase in an earthquake time and attains a maximum of 1.67 at 30 s. In the reinforced case, the normalised vertical stress decreases by up to 11% and 30% at 0 s and 30 s, respectively. However, it follows the same trend.

In contrast, the normalised vertical stress on the pile is 3.56 at 0 s in the

unreinforced case. It is consistent up to 11 s, and suddenly it is disturbed (i.e., initially it increases and then decreases) in the time frame of 11-14 s. The normalised vertical stress decreases further increase in an earthquake time and decreases to 3.40 at 30 s whereas in the reinforced case, the normalised vertical stress increases by up to 8.6% at 0 s and decreases by up to 30% at 30 s.

It is worth noting that in both the unreinforced and reinforced cases, vertical stress is transferred to the pile before 11 s while after that, the vertical stress on the subsoil and pile is approaching close, which ruins the soil arching mobilisation.

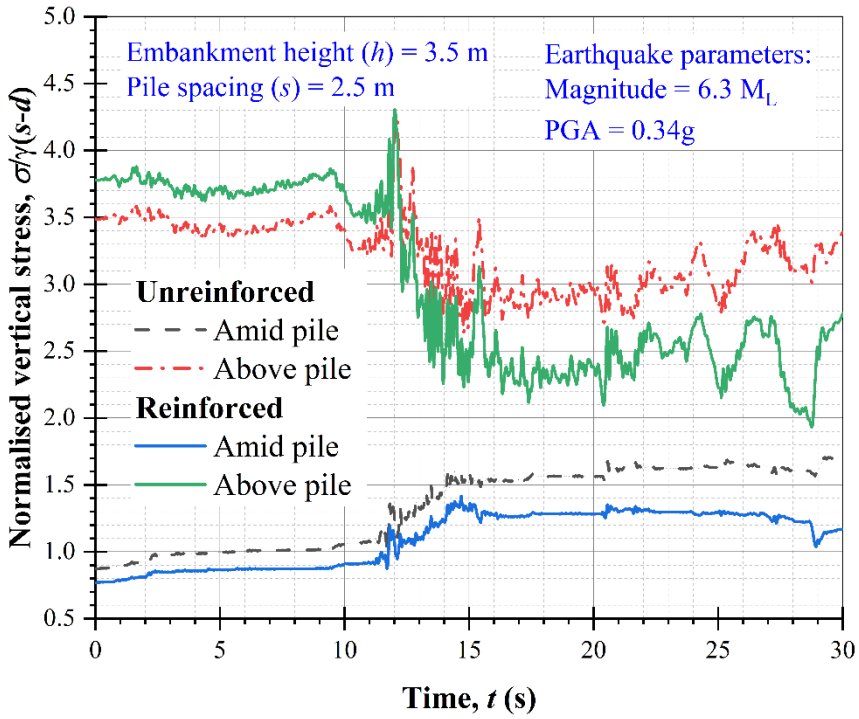

Figure 6.6: Normalised vertical stress on the subsoil and pile during the earthquake

6.4.2 Settlement

Figure 6.7 shows the settlement contours of the embankment in the unreinforced condition at different time instances (i.e., 0, 13.16, and 30 s). The normalised settlement of the subsoil top is 0.4 when there is no earthquake (i.e., t = 0 s), whereas

it increases to 2.52 at the end of the earthquake (i.e., t = 30 s). However, the settlement on the pile top is negligible. When there is no earthquake, a uniform settlement is observed above the normalised embankment height is 0.8. This embankment height is known as the plane of equal settlement. However, embankment settlement increases and the plane of equal settlement is ruined by a further increase in t.

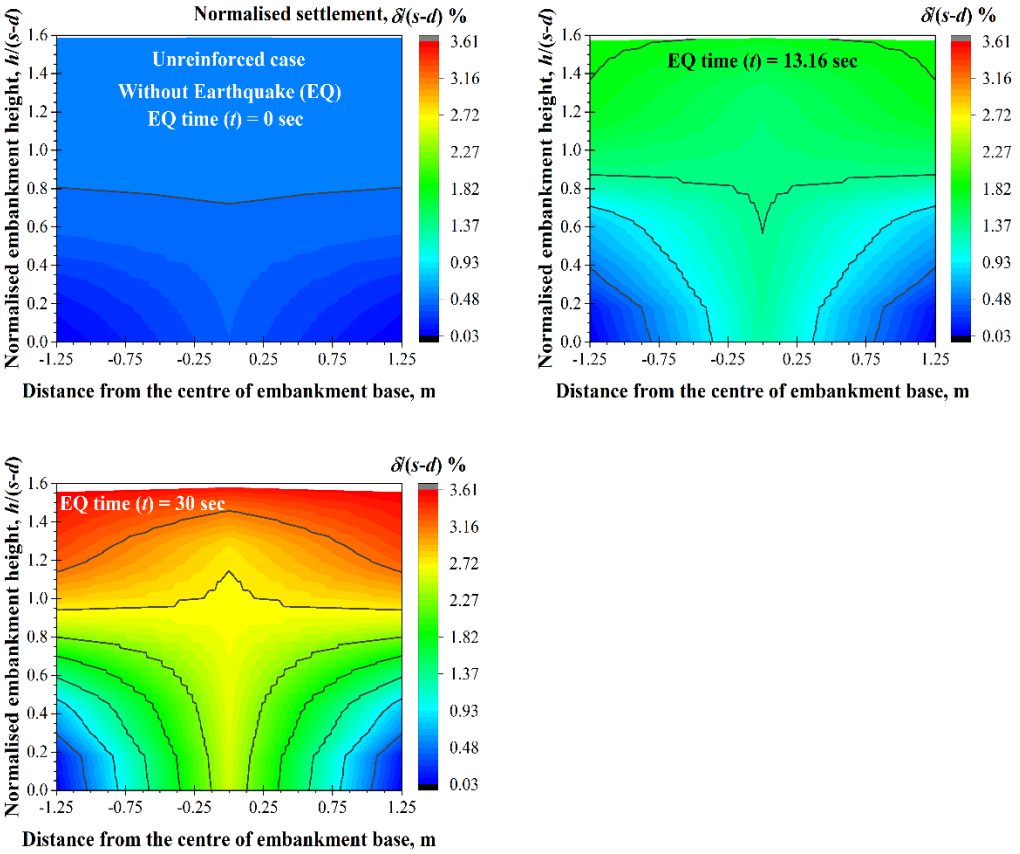

Figure 6.7: Settlement contour for different time instances

Figure 6.8 shows the effect of reinforcement on embankment settlement at t = 30 s. The unreinforced case (Figure 6.8a) is the same as that shown in Figure 6.7 at t = 30 s, with a normalised settlement of 2.52 at the subsoil top, whereas as shown in Figure 6.8b, it reduces to 2.10 with the inclusion of a reinforcement layer. In addition, the settlement on the embankment top is also reduced by up to 20%. This implies that

reinforcement reduces the settlement during the earthquake, which can prevent the potential failure of the embankment.

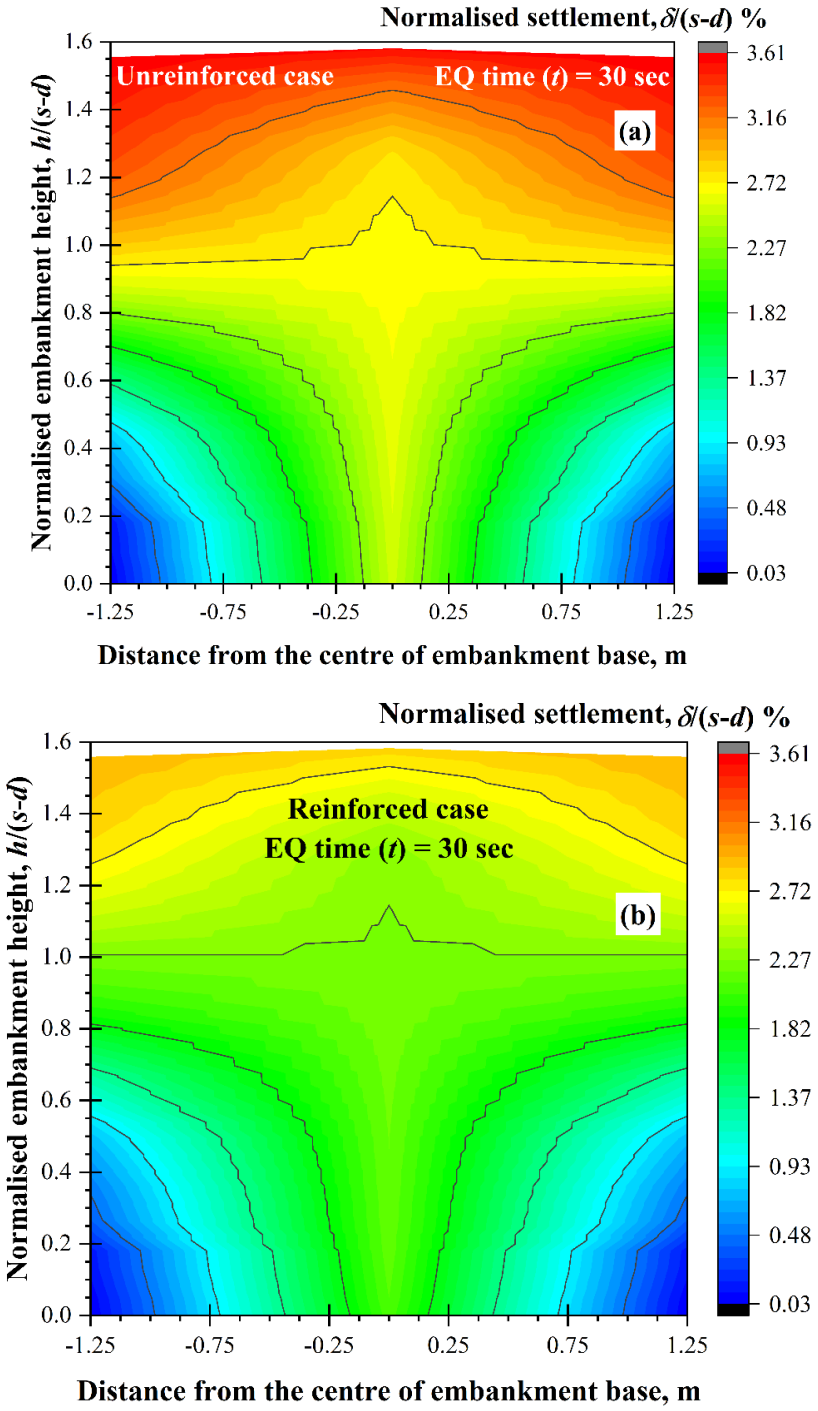

Figure 6.8: Settlement contour at earthquake time (t) = 30 s for (a) the unreinforced case, and (b) the reinforced case

Figure 6.9 shows the effect of an earthquake on embankment settlement on the subsoil and pile top for both the unreinforced and reinforced cases. The settlement is normalised for the general applicability. In the unreinforced case, the normalised settlement starts at 0.4 at t = 0 s. It considerably increases after 11 s and reaches 2.52 at the end of the earthquake (i.e., t = 30 s). In contrast, the normalised settlement starts at 0.35 at t = 0 s. and reduces by up to 17% (i.e., 2.10) at the end of the earthquake. The settlement on the pile top is negligible in both cases.

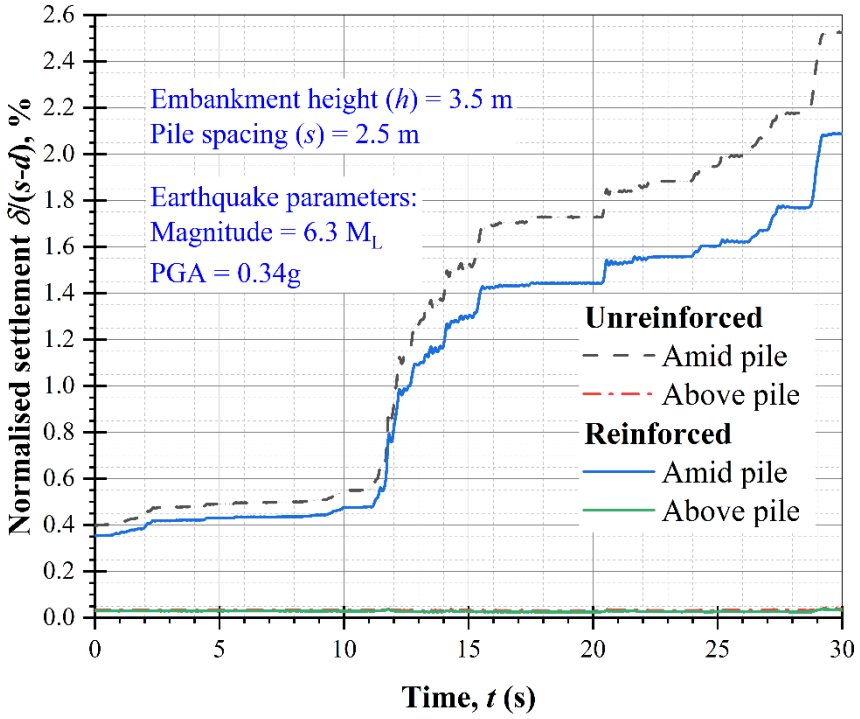

Figure 6.9: Normalised settlement on the subsoil and pile top during the earthquake

6.4.3 Soil arching indices

6.4.3.1 Stress concentration ratio (SCR)

Figure 6.10 shows the stress concentration ratio during the earthquake. A higher *SCR* representing more stress is transferred from the subsoil to the pile top. In the unreinforced case, the *SCR* is initiated with 4 at t = 0 s. It gradually decreases with an

increase in time by up to 11 s. However, the *SCR* value drastically decreases within the time frame of 11 s to 15 s, and it reaches 2 at the end of the earthquake.

In contrast, the *SCR* is introduced with 4.9 in the reinforced case, and reducing to 2.40 at the end of earthquake, although there is a negligible difference in the *SCR* within the time frame of 12 s to 27 s in both the unreinforced and reinforced cases. The *SCR* value is 22.5% higher in the reinforced case compared to the unreinforced case at $t = 0$ s. This implies that stress transfer from the subsoil to the pile top decreases with an increase in earthquake time. Also, more stress is transferred to the pile top in the reinforced case compared to the unreinforced case.

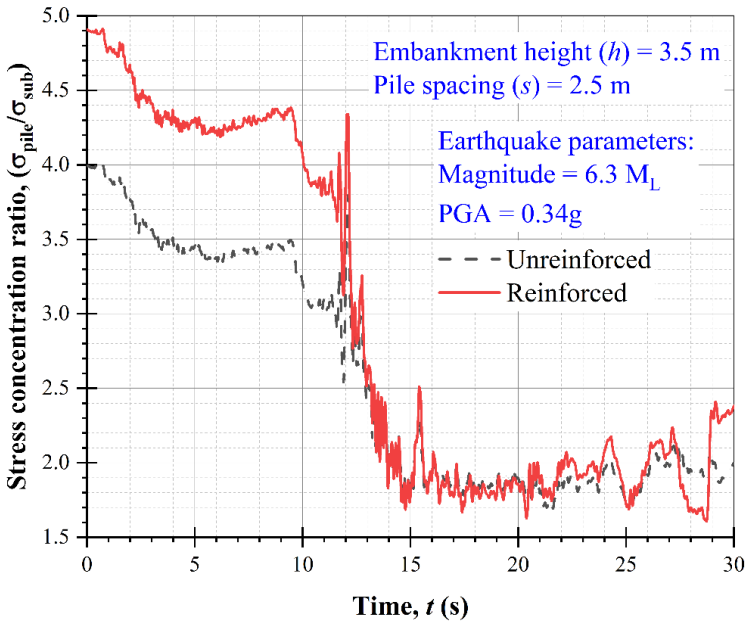

Figure 6.10: Stress concentration ratio time history during the earthquake

6.4.3.2 Soil arching ratio (*SAR*)

A profile of the soil arching ratio during the earthquake in the unreinforced and reinforced cases is shown in Figure 6.11. The value of *SAR* varied between 0 to 1. The unit value of *SAR* represents no soil arching, whereas zero denotes the complete

mobilisation of soil arching. In the unreinforced case, *SAR* starts at 5.5, increasing with an increase in earthquake time. In the time frame of 12 to 14 s, it reaches the unit value. After 20 s, it crosses the unit value of *SAR* and reaches 1.07 at the end of the earthquake. This implies that the degree of soil arching decreases with an increase in earthquake time, and after 20 s, there is no soil arching mobilisation, whereas in the reinforced case, it starts from 4.75 and increases to 15 s time, and after that, it remains consistent with further increases in the earthquake time. However, it slightly decreases at 27 s and drops to 0.73 at the end of the earthquake. It is observed that a reinforced layer enhances the degree of soil arching by up to 14% and 32% at the t = 0 s and 30 s, respectively.

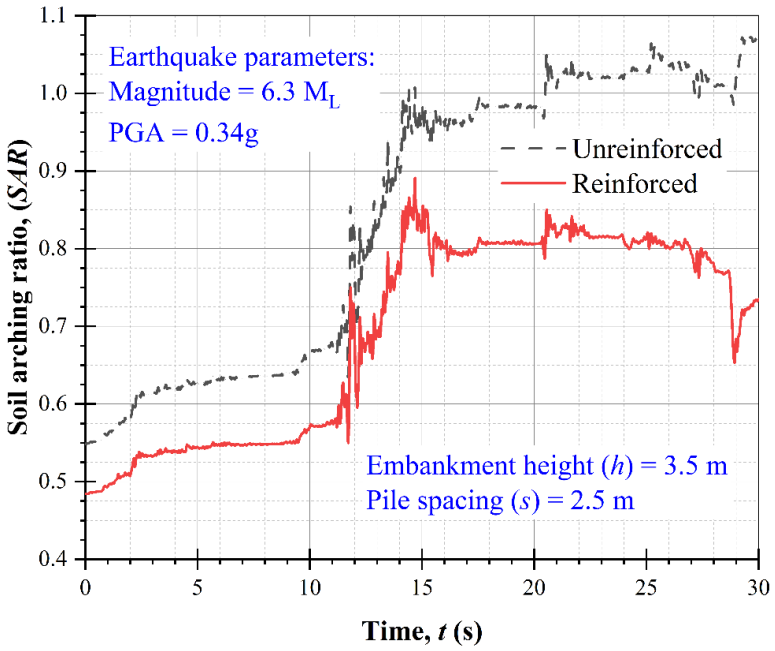

Figure 6.11: Soil arching ratio time history

6.5 PARAMETRIC STUDY

As previously discussed, a reinforcement layer enhances the performance of soil arching during an earthquake. Therefore, only a reinforced case is considered for the

parametric study. Only one parameter is varied at a time, while the others remain the same to investigate the effect of particular parameters.

6.5.1 Effect of embankment height and pile spacing

Figures 6.12 - 6.16 show the effect of embankment height and pile spacing on different aspects of soil arching. The embankment height varies from 2.5 m to 6.5 m, whereas pile spacing is 2 m to 3.5 m. The earthquake time (t) = 30 s is taken to investigate the effect of embankment height and pile spacing. Figure 6.12 illustrates the effect of embankment height (h) and pile spacing (s) on the normalised vertical stress on the subsoil. It is observed that the normalised vertical stress increases by up to 110% with an increase in embankment height from 2.5 m to 6.5 m. However, it decreases by 52% with an increase in pile spacing from 2 m to 3.5 m. The semicircular shape of soil arching is mobilised with a higher radius in pile spacing 2 m compared to other pile spacing. Therefore, more load is observed at the subsoil top in pile spacing 2 m.

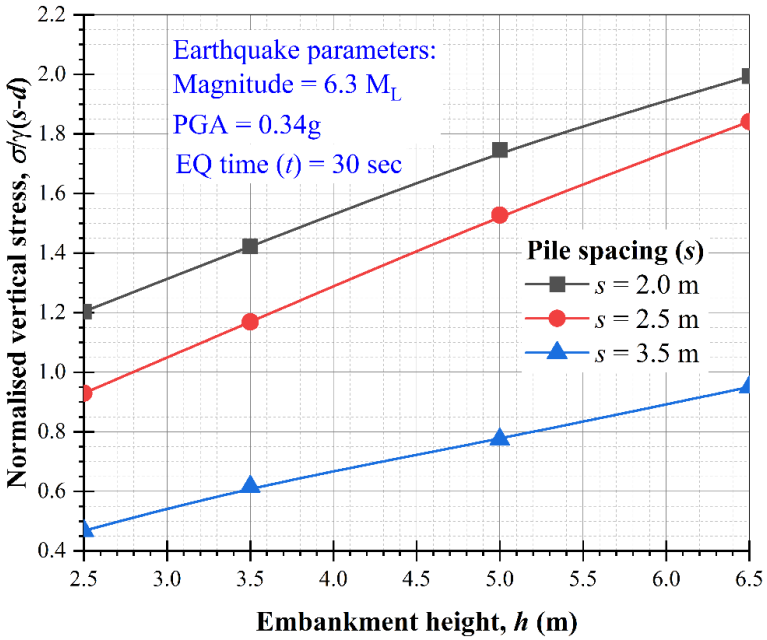

Figure 6.12: Effect of embankment height and pile spacing on normalised vertical

stress on the subsoil at the end of the earthquake

The effect of embankment height and pile spacing on normalised settlement is shown in Figure 6.13. The normalised settlement increases by up to 87% with an increase in embankment height from 2.5 m to 6.5 m, whereas it increases by up to 76% with an increase in pile spacing from 2 m to 3.5 m.

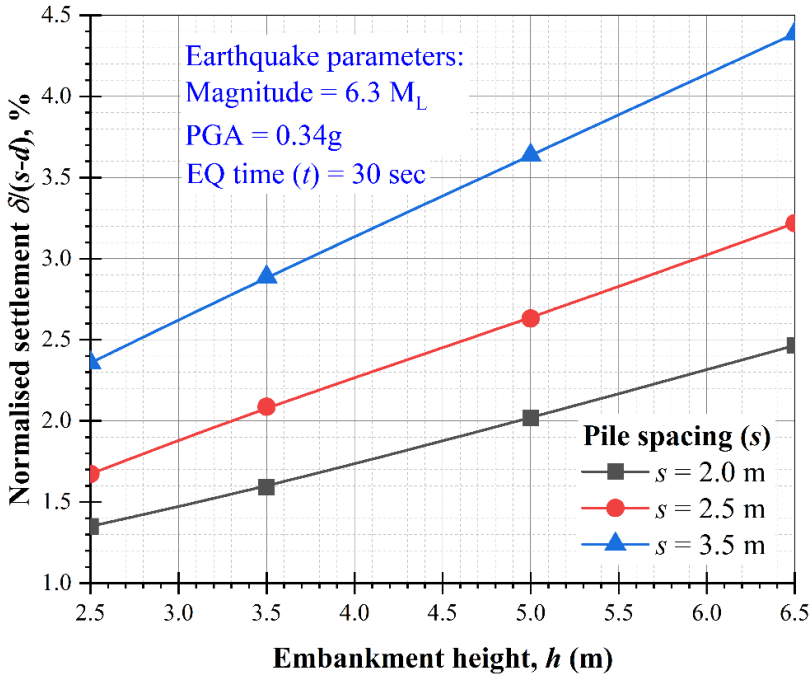

Figure 6.13: Effect of embankment height and pile spacing on the normalised settlement of the subsoil top at the end of earthquake

Figure 6.14 shows the influence of embankment height and pile spacing on the maximum tension in the geosynthetic layer which increases by up to 108% with an increase in both embankment height and pile spacing. A higher tension is observed for larger pile spacing. This implies that the function of the geosynthetic layer is more pronounced in a higher pile spacing.

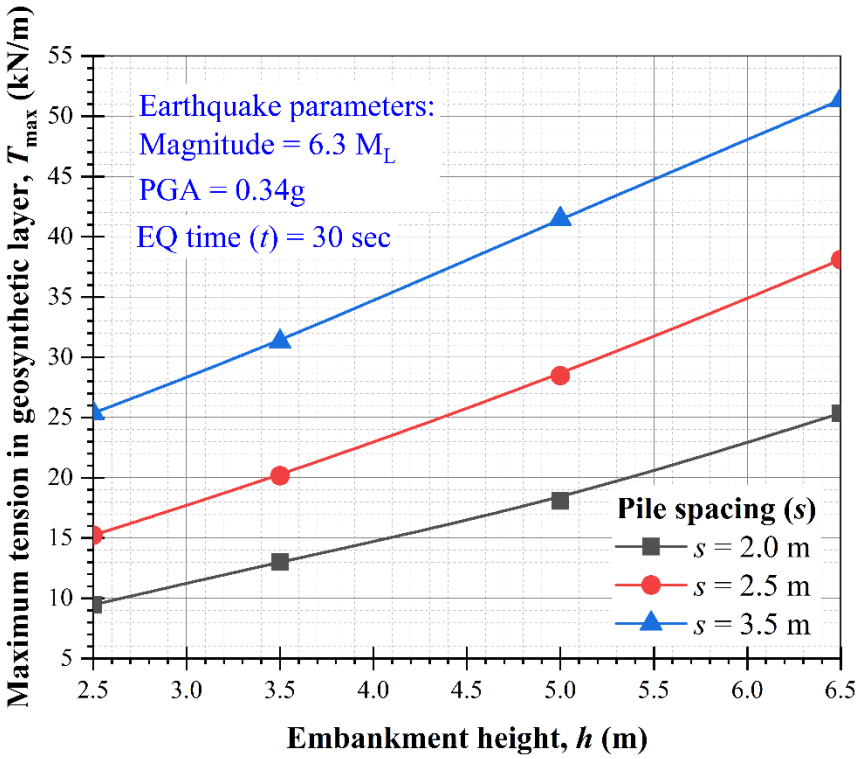

Figure 6.14: Effect of embankment height and pile spacing on maximum tension in the geosynthetic layer at the end of the earthquake

The effect of embankment height and pile spacing on soil arching indices; stress concentration ratio (*SCR*), and soil arching ratio (*SAR*) are shown in Figures 6.15 and 6.16, respectively. In Figure 6.15, for pile spacing 2 m and 2.5 m, the *SCR* increases by up to 42% with an increase in embankment height of 2.5 m to 6.5 m. However, pile spacing of 3.5 m has a negligible effect. Also, the *SCR* increases by up to 77.5% with an increase in pile spacing at a larger embankment height. As shown in Figure 6.16, the *SAR* decreases by up to 70% with an increase in embankment height of 2.5 m to 6.5 m. The reduction in *SAR* is higher in smaller pile spacing which implies that smaller pile spacing enhances the degree of soil arching. It can also be observed that the *SAR* increases by up to 500% with an increase of pile spacing from 2 m to 3.5 m at a larger embankment height.

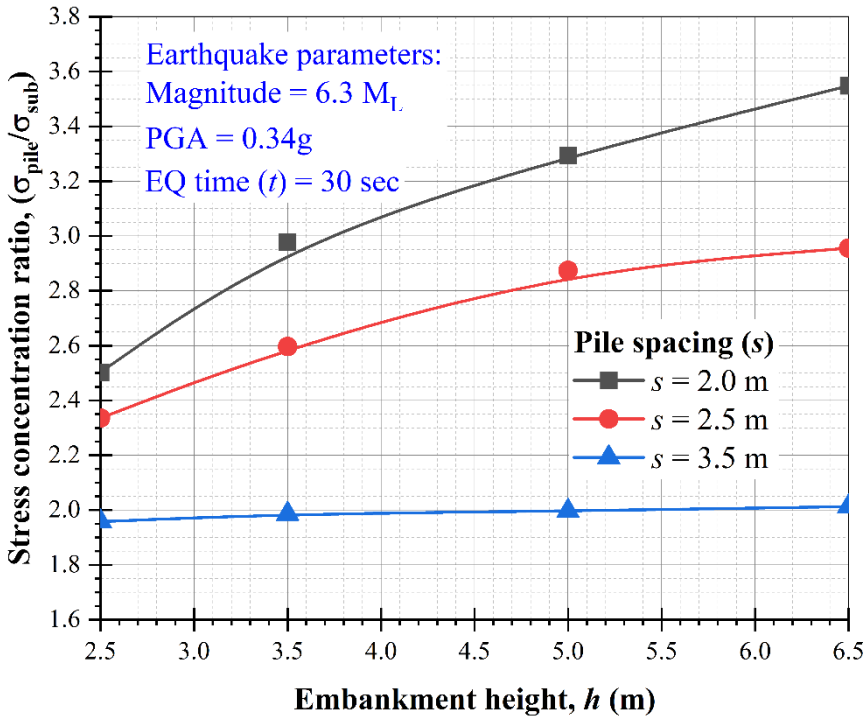

Figure 6.15: Effect of embankment height and pile spacing on the stress concentration ratio at the end of the earthquake

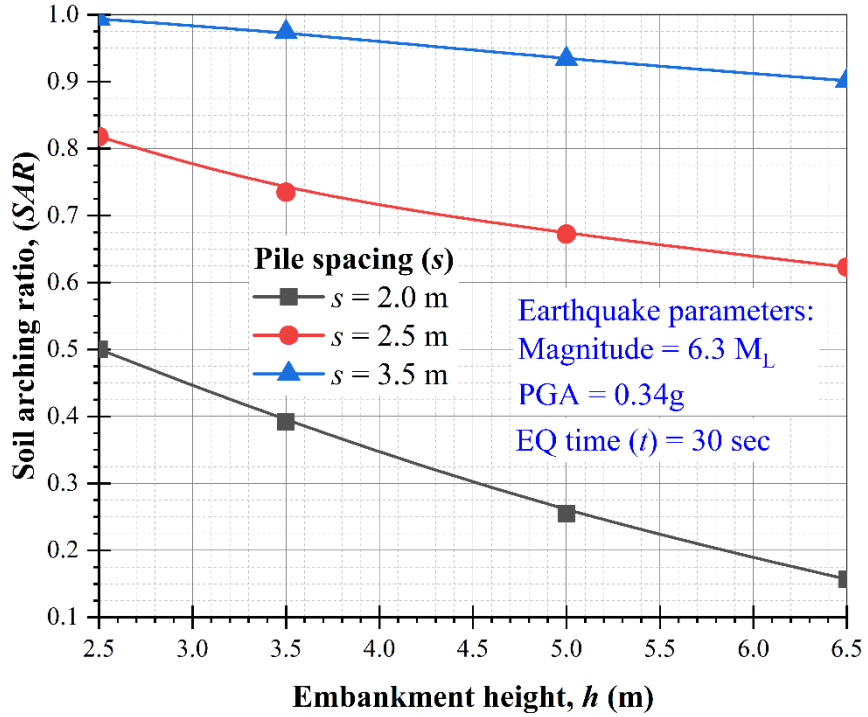

Figure 6.16: Effect of embankment height and pile spacing on the soil arching ratio at the end of the earthquake

6.5.2 Effect of the embankment modulus and friction angle

Figures 6.17-6.21 show the effect of embankment modulus (E_{em}) and friction angle (ϕ') on different aspects of soil arching. The embankment modulus varies from 15 MPa to 30 MPa, and the friction angle is 30° to 45°. Figure 6.17 shows the effect of the embankment modulus and friction angle on the normalised vertical stress acting on the subsoil during the earthquake. Figure 6.17(a) shows that from 0 s to 11 s, the normalised vertical stress decreases by up to 16%, increasing the embankment modulus from 15 MPa to 30 MPa. After 11 s, the embankment modulus has a negligible effect on normalised vertical stress. This implies that the embankment modulus reduces the vertical stress on the subsoil in the initial phase of an earthquake.

In contrast, Figure 6.17(b) shows that the normalised vertical stress on the subsoil decreases by up to 37%, increasing the friction angle from 30° to 45°. The normalised vertical stress reduction is more pronounced at the end of the earthquake. This implies that the friction angle is an effective parameter that can enhance soil arching even in the earthquake.

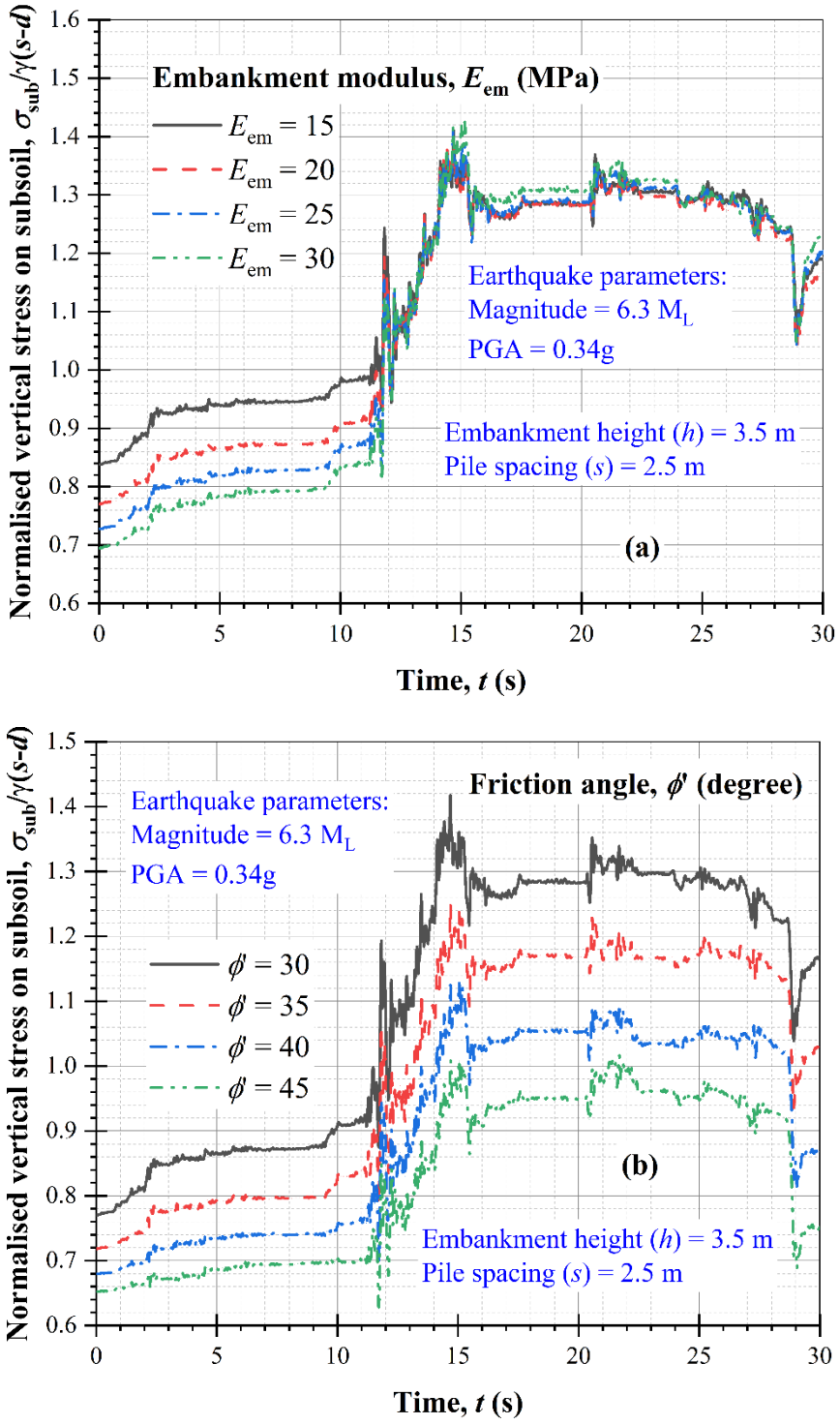

Figure 6.17: Effect on normalised vertical stress due to (a) embankment modulus, and (b) friction angle

The effect of the embankment modulus and friction angle on normalised settlement of subsoil during the earthquake is shown in Figure 6.18. As observed in Figure 6.18(a), the embankment modulus has a negligible effect on normalised

settlement. The normalised settlement increases by up to 500% with an increase in earthquake time from 0 to 30 s. As shown in Figure 6.18(b), the normalised settlement decreases by up to 24% with an increase in the friction angle from 30° to 45°. The reduction in the settlement is more noticeable at the end of the earthquake.

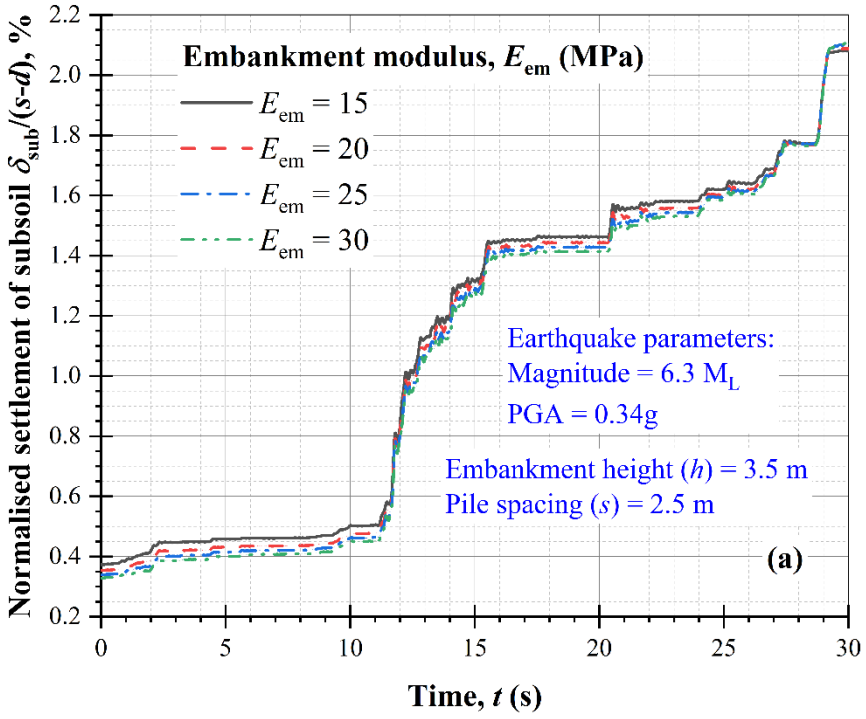

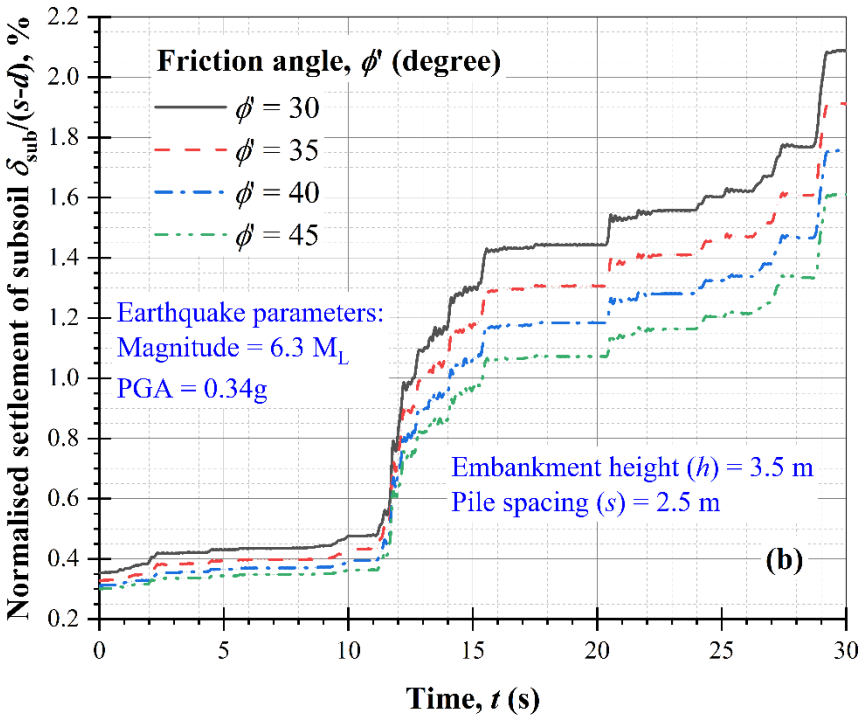

Figure 6.18: Effect on normalised settlement due to (a) embankment modulus, and (b) friction angle

Figure 6.19 shows the effect of the embankment modulus and friction angle on maximum tension (T_{max}) in a geosynthetic layer. It is observed in Figure 6.19(a) that the embankment modulus has a negligible effect on the maximum tension in a geosynthetic layer. However, the T_{max} increases by up to 975% with an increase in earthquake time from 0 s to 30 s. However, the T_{max} decreases by up to 19% with an increase in friction angle from 30° to 45° (refer to Figure 6.19b). This is due to improved embankment quality, leading to less deformation and thus less tension in the geosynthetic layer.

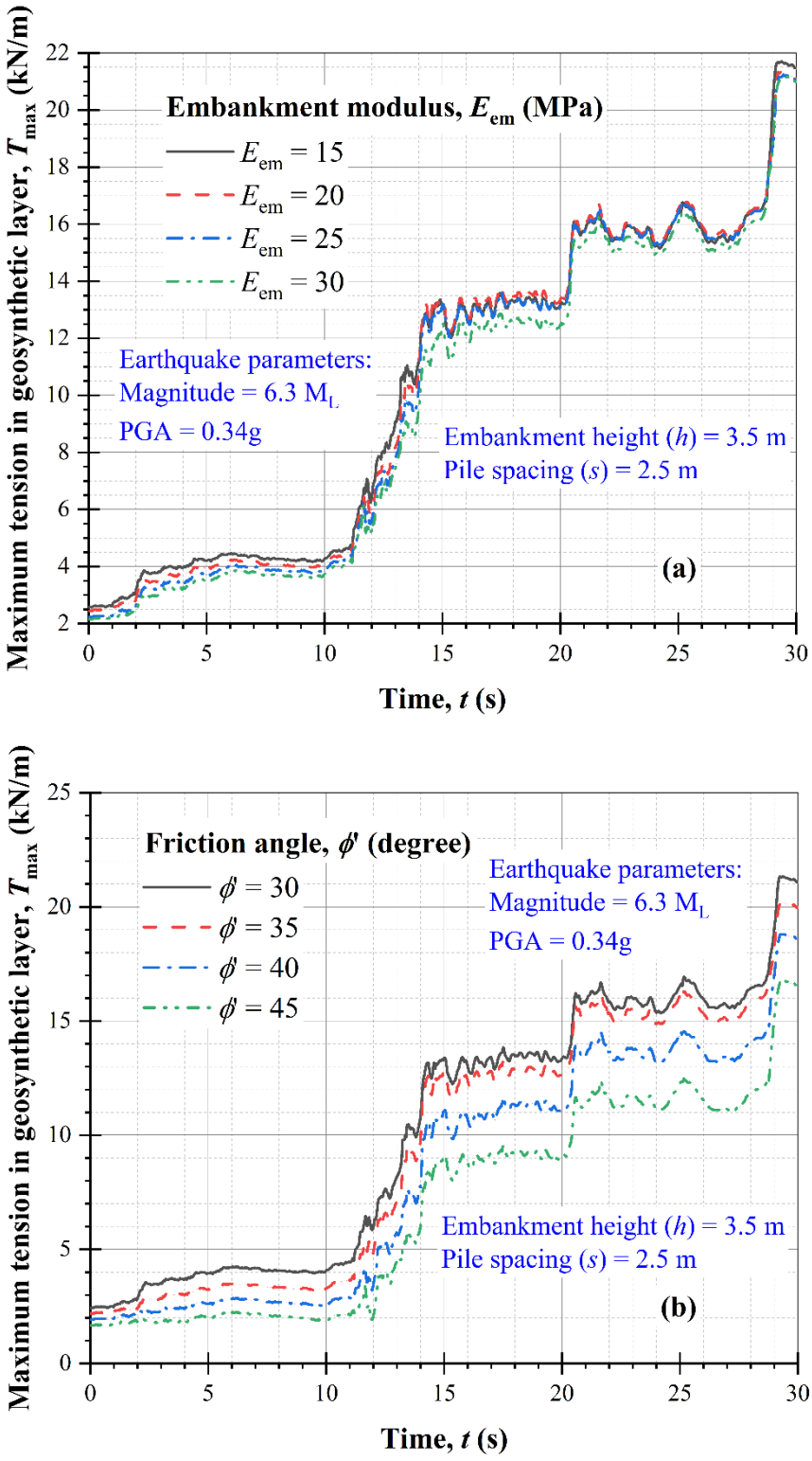

Figure 6.19: Effect on maximum tension in the geosynthetic layer due to (a) embankment modulus, (b) friction angle

The effect of the embankment modulus and friction angle on the stress concentration ratio (*SCR*) is shown in Figure 6.20. As shown in Figure 6.20(a), from

0 s to 11 s, it increases by up to 51% with an increase in the embankment modulus from 15 MPa to 30 MPa. However, the embankment modulus has a negligible effect after 11 s, and it decreases by up to 61% at the end of the earthquake. This implies that the embankment modulus is effective for the stress transfer to pile in the initial phase of an earthquake. In contrast, as shown in Figure 6.20(b), the friction angle significantly affects the *SCR*. The *SCR* increases by up to 273% with an increase in the friction angle from 30° to 45°. The effect of the friction angle is more pronounced at the end of the earthquake.

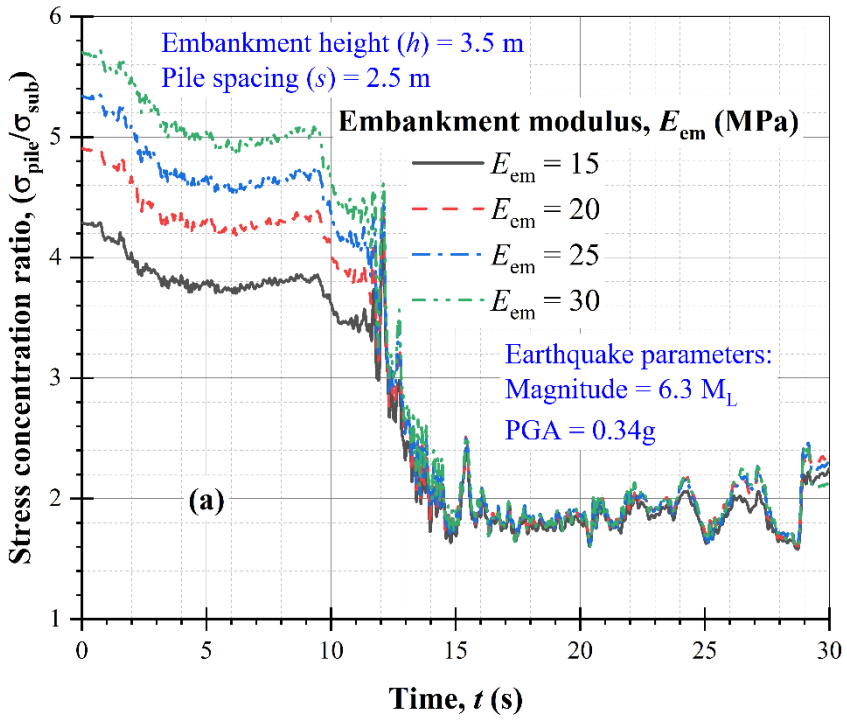

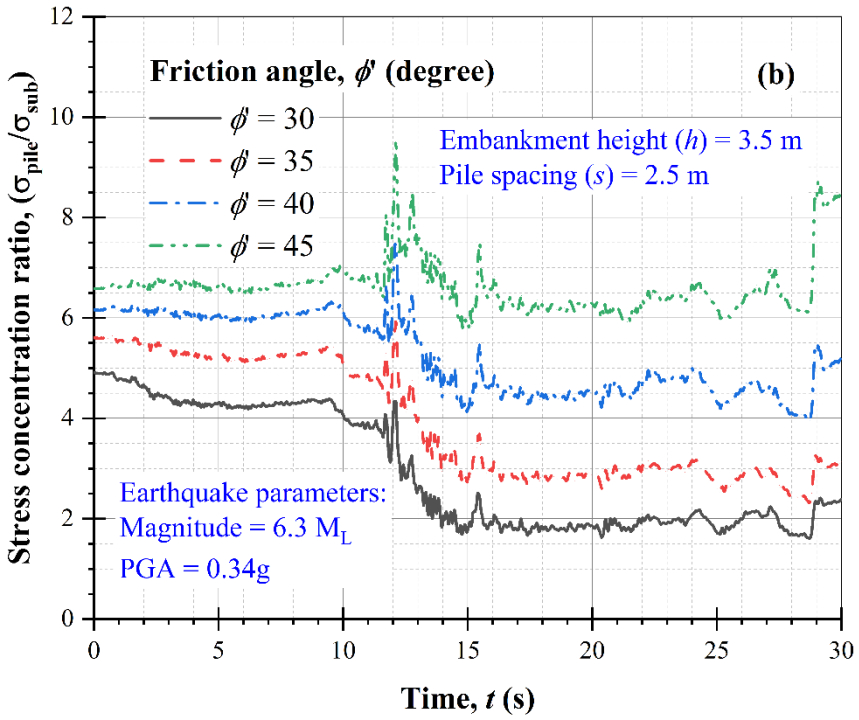

Figure 6.20: Effect on stress concentration ratio due to (a) embankment modulus, (b) friction angle

Figure 6.21 shows the effect of the embankment modulus and friction angle on *SAR*. As shown in Figure 6.21(a), from 0 s to 11 s, it decreases by up to 15% with an increase of the embankment modulus from 15 MPa to 30 MPa. However, the embankment modulus has a negligible effect after 11 s and it increases by up to 77% at the end of the earthquake. This implies that after 11 s, the soil arching is not full mobilised. However, it decreases by up to 35% with an increase in the friction angle from 30° to 45° (referring to Figure 6.21b). The *SAR* approaching a smaller value with an increase in the friction angle further indicates that the degree of soil arching mobilisation is improving by increasing the friction angle.

It is worth noting from Figures 6.17-6.21 that the friction angle is an effective parameter in an earthquake. The friction angle should be higher to reduce the potential failure of pile-supported embankment during an earthquake.

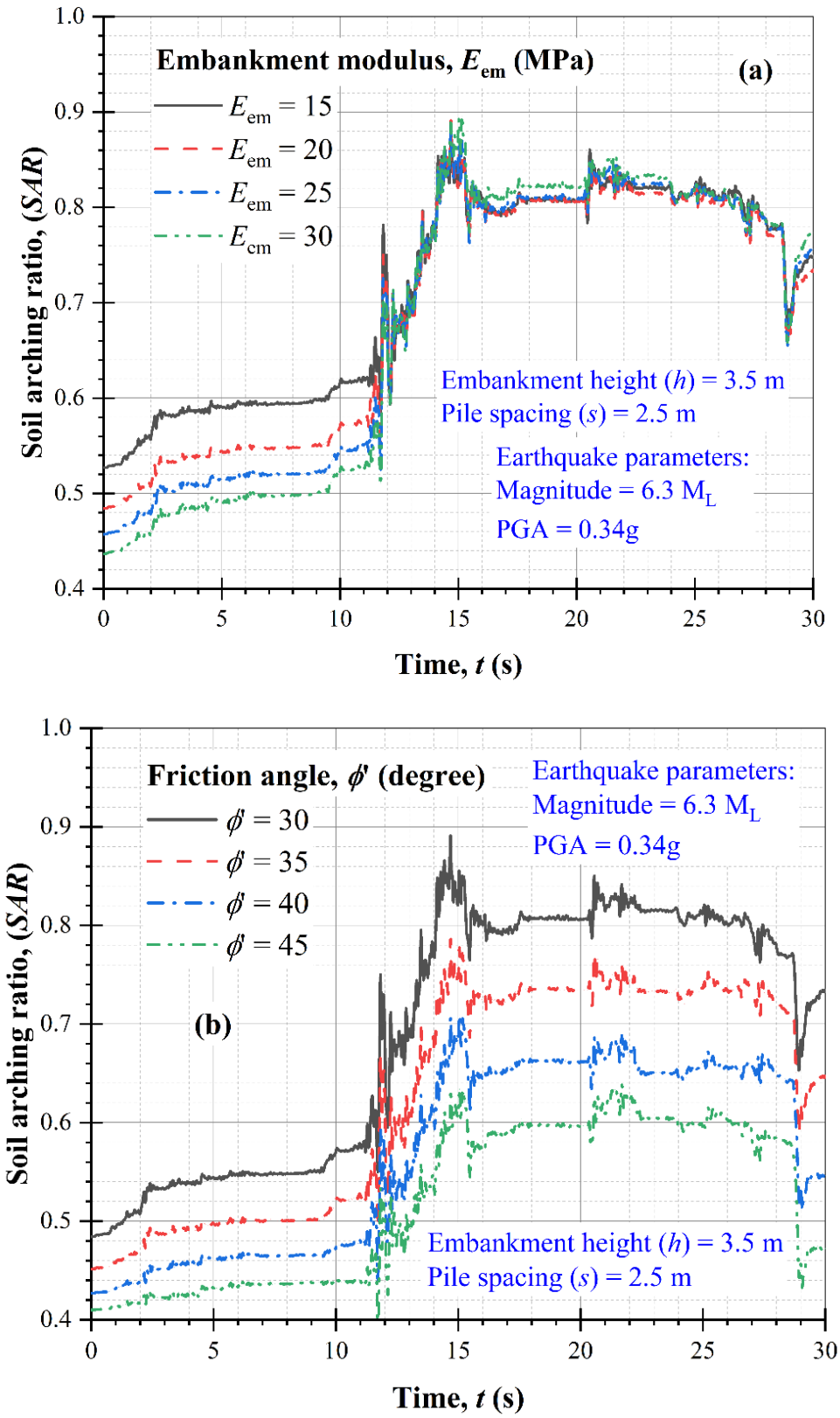

Figure 6.21: Effect on soil arching ratio due to (a) embankment modulus, (b) friction angle

6.5.3 Effect of tensile stiffness of the geosynthetic layer

Figures 6.22-6.26 show the effect of tensile stiffness of the geosynthetic layer (J) on different soil arching aspects. The effect of tensile stiffness on normalised vertical stress acting on the subsoil is shown in Figure 6.22. The normalised vertical stress decreases by up to 19% with an increase in tensile stiffness from 500 kN/m to 2000 kN/m. The reduction in normalised vertical stress is pronounced at the end of the earthquake. This implies that sufficient tensile stiffness of a geosynthetic reduces stress on the subsoil and enhances soil arching.

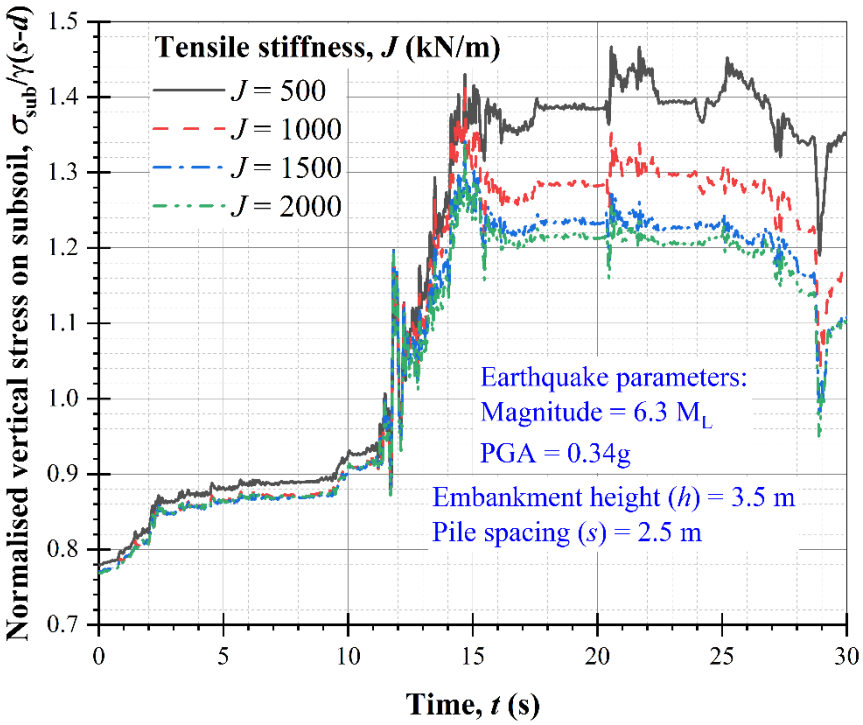

Figure 6.22: Effect of geosynthetic tensile stiffness normalised vertical stress acting on the subsoil

Figure 6.23 shows the effect of tensile stiffness on settlement. It is observed that initially, there is no effect of tensile stiffness on the settlement. However, at the end of the earthquake, the settlement decreases by up to 11 %, increasing geosynthetic tensile stiffness from 500 kN/m to 2000 kN/m.

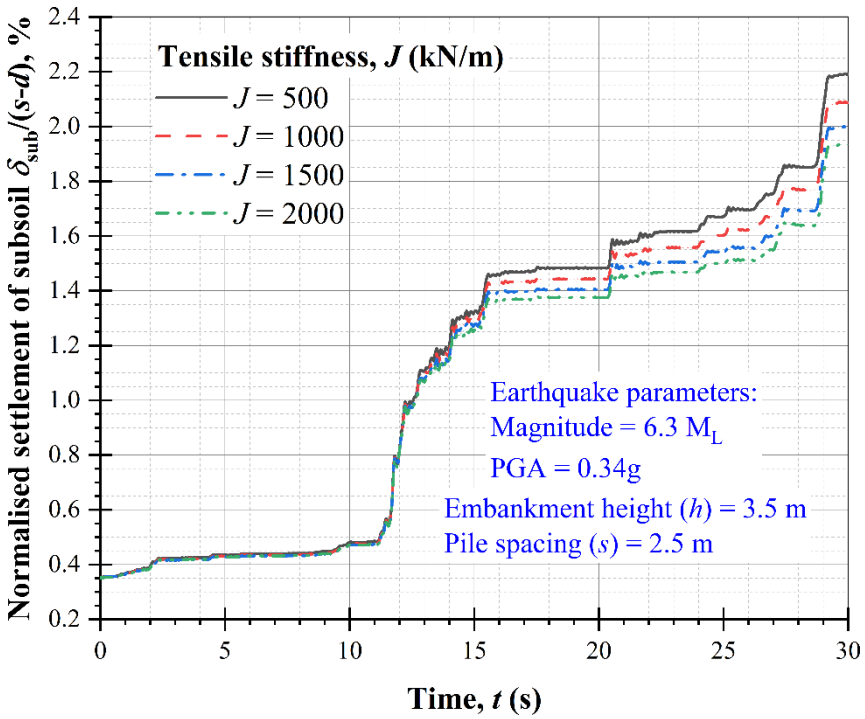

Figure 6.23: Effect of geosynthetic tensile stiffness on normalised settlement of subsoil

The influence of geosynthetic tensile stiffness on the maximum tension (T_{max}) is shown in Figure 6.24. The T_{max} increases by up to 93% with an increase in tensile stiffness from 500 kN/m to 2000 kN/m. The maximum tension in the geosynthetic layer is more pronounced at the end of the earthquake.

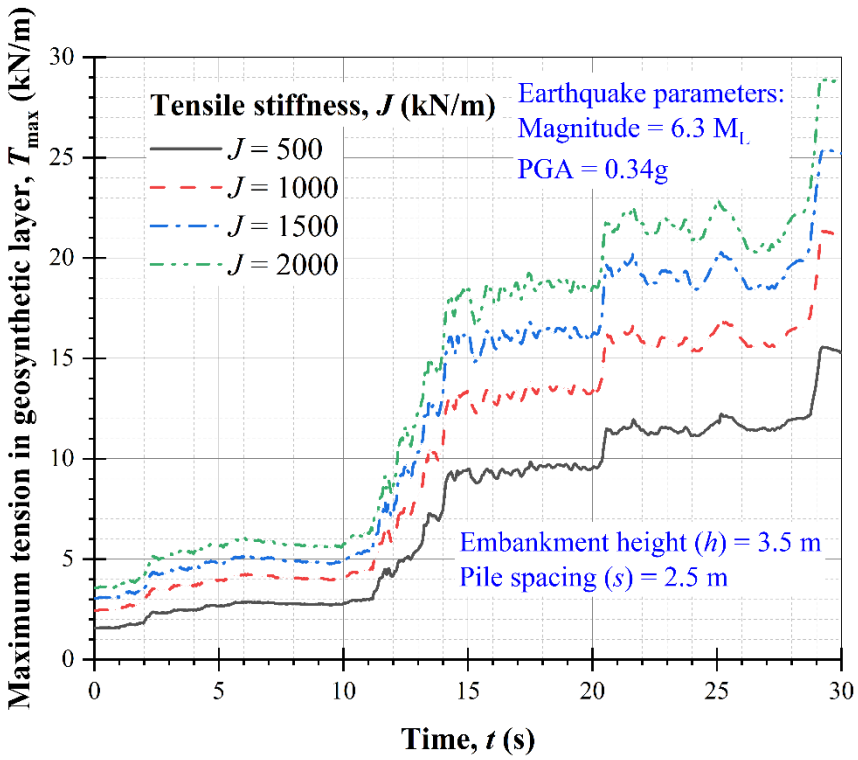

Figure 6.24: Effect of geosynthetic tensile stiffness on maximum tension in the geosynthetic layer

As shown in Figure 6.25, the effect of geosynthetic tensile stiffness on stress concentration ratio (*SCR*) is found to be negligible. The *SCR* starts at 4.9 and decreases with an increase in earthquake time, decreasing to 2.2 at the end of the earthquake. Figure 6.26 shows the influence on the soil arching ratio (*SAR*). The *SAR* decreases by up to 18% with an increase in tensile stiffness from 500 kN/m to 2000 kN/m. This implies that the degree of soil arching mobilisation improves with the higher tensile stiffness of the geosynthetic layer.

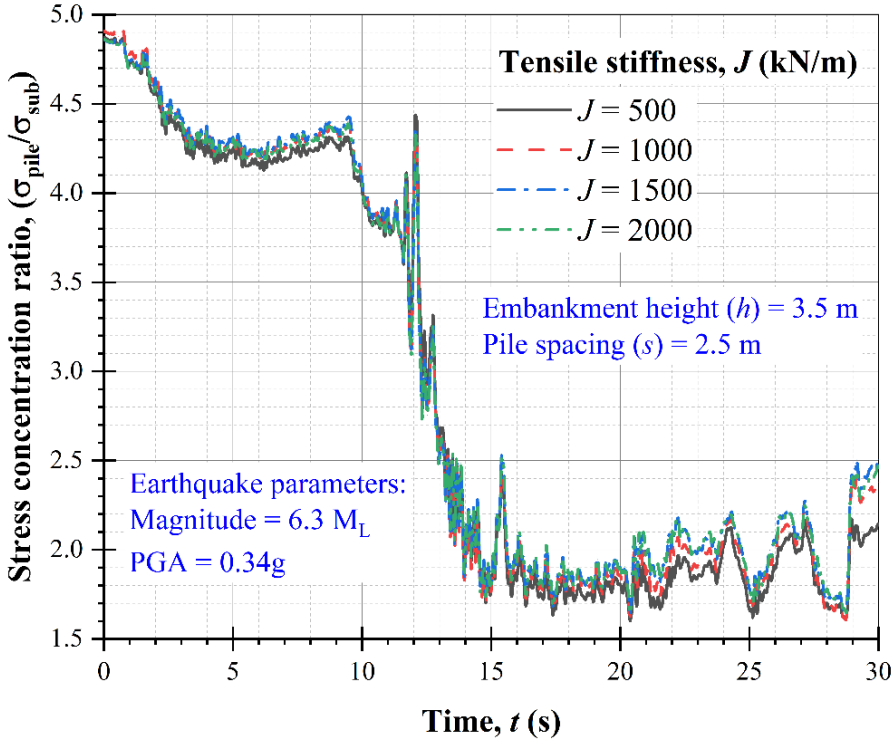

Figure 6.25: Effect of geosynthetic tensile stiffness on the stress concentration ratio

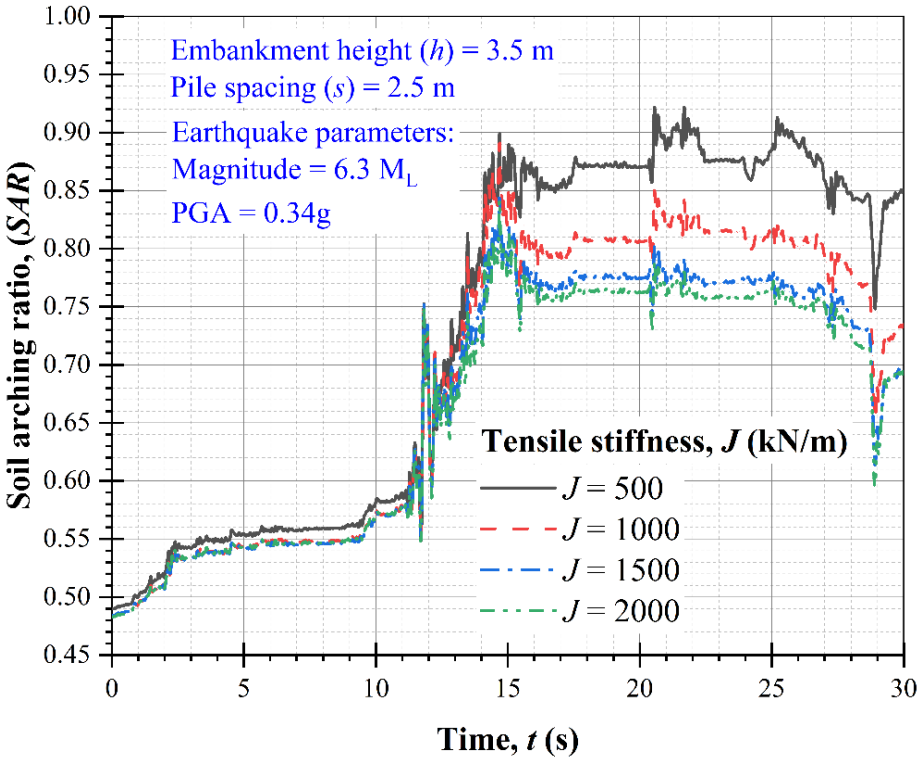

Figure 6.26: Effect of geosynthetic tensile stiffness on the soil arching ratio

6.5.4 Effect of the amplitude of input seismic excitation

This study uses the horizontal acceleration time history of the Christchurch 2011 earthquake. However, input peak ground acceleration (PGA) is scaled from 0.1g to 0.5g to investigate the effect of earthquake amplitude. The effect of earthquake magnitude could be different from PGA. Kramer (1996) is reported a relationship between PGA and different magnitude. However, this thesis is limited to the different PGA. The dominant frequency (f_{eq}) is fixed at 5.91 Hz. Figures 6.27-6.34 show the effect of earthquake amplitude on the different soil arching aspects.

Figure 6.27 shows the contours of normalised vertical stress for different PGA at t = 30 s. It is observed that the normalised vertical stress on the subsoil increases by up to 23% with an increase in input amplitude from 0.1g to 0.5g, whereas it decreases by up to 17% on the pile top. This implies that the input amplitude can be one of the reasons for the potential failure of soil arching. Therefore, soil arching behaves according to the earthquake scenario.

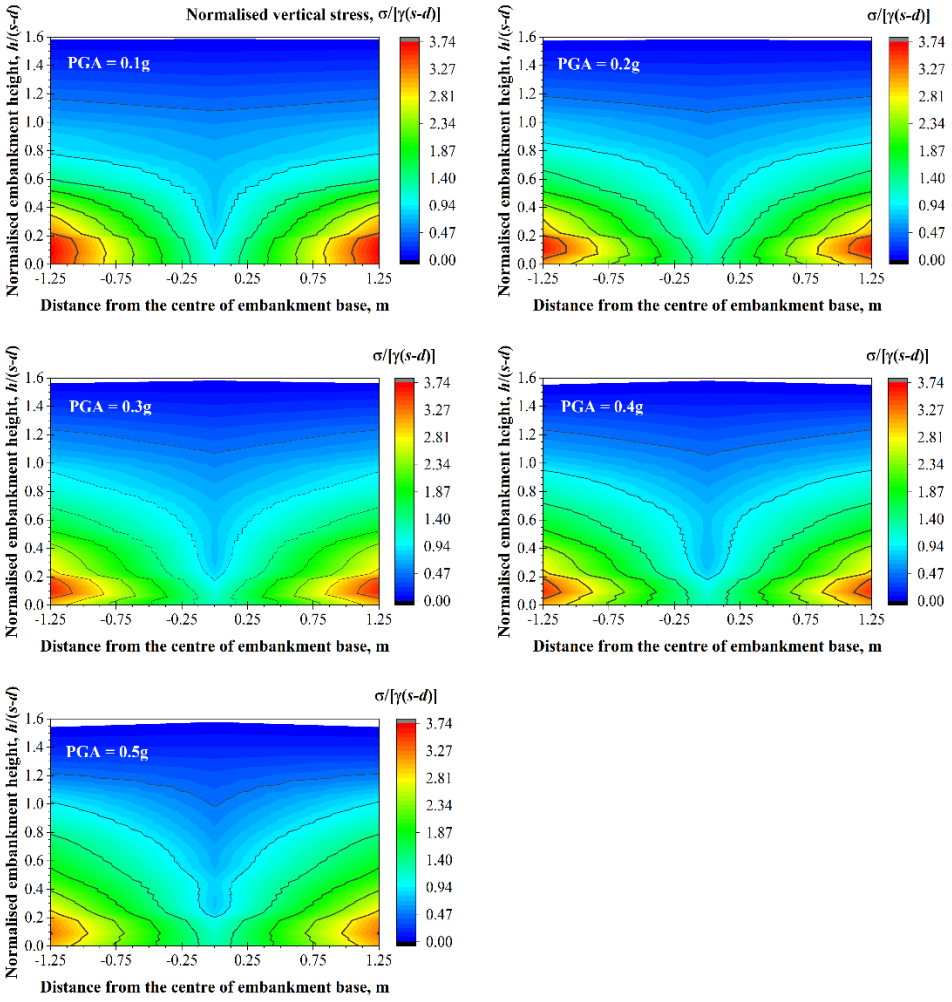

Figure 6.27: Vertical stress contour for different peak ground acceleration

The profile of normalised vertical stress acting on the subsoil during the earthquake with different PGA is shown in Figure 6.28. At t = 0 s, the normalised vertical stress is observed at 7.75 for all considered PGAs. However, it increases with an increase of PGA with respect to time. The normalised vertical stress consistently increases for all considered PGAs by up to 11 s, and subsequently, a sudden jump is observed. The normalised vertical stress increases by up to 26% with an increase of PGA from 0.1g to 0.3g. A further increase in PGA leads to failures of soil arching, and less vertical stress is observed at the end of the earthquake for PGA = 0.5g.

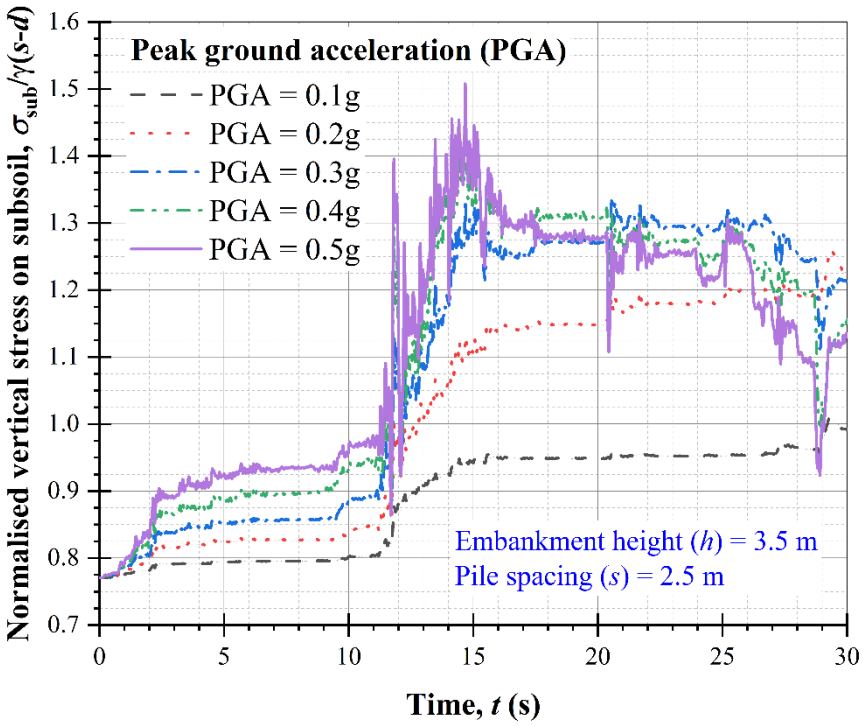

Figure 6.28: Effect of peak ground acceleration on the normalised vertical stress acting on the subsoil

The effect of the peak ground acceleration on normalised settlement couture at t = 30 s is shown in Figure 6.29. The normalised settlement on the subsoil increases by up to 433%, increasing PGA from 0.1g to 0.5g, while no difference is found on the pile top. This implies that the amplitude of input acceleration can be a major concern for GRPS embankment and soil arching failure. In addition, the effect of PGA on normalised settlement of subsoil during the earthquake is shown in Figure 6.30. It increases slightly to 11 s, and it drastically increases by up to 433% with an increase in PGA from 0.1g to 0.5g.

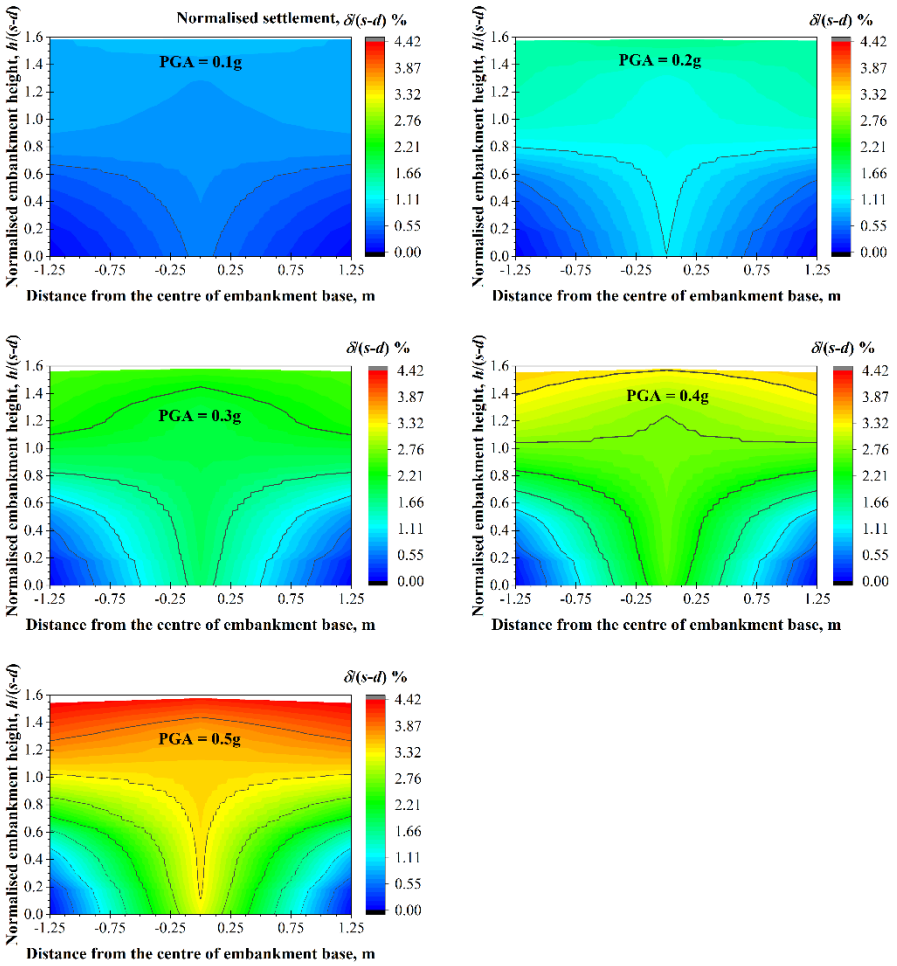

Figure 6.29: Normalised settlement contours for different peak ground acceleration

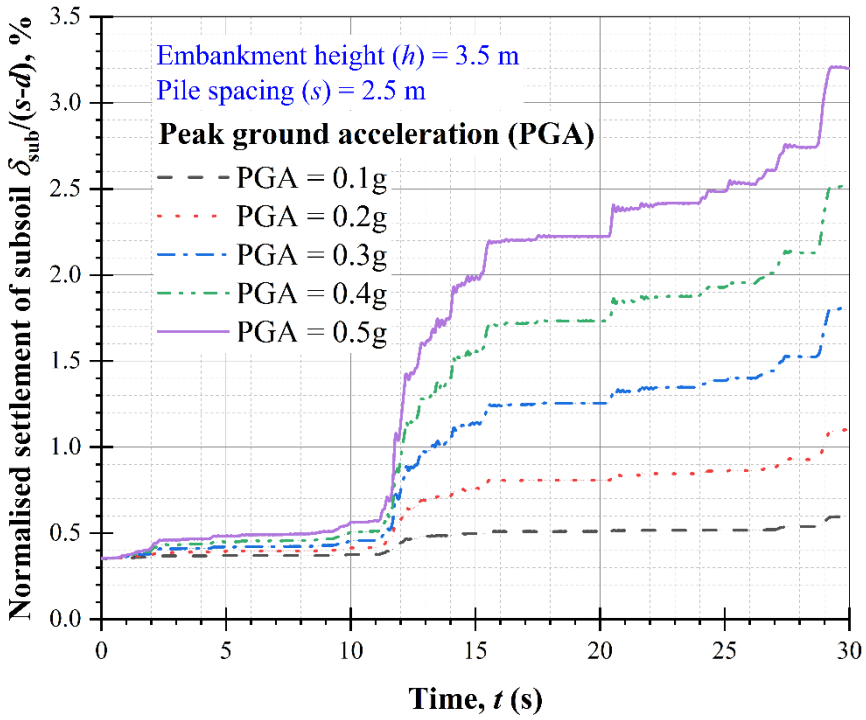

Figure 6.30: Normalised settlement of subsoil for different peak ground acceleration

Figure 6.31 shows the effect of PGA on maximum tension in a geosynthetic layer during the earthquake. The maximum tension initiates with 0.3 kN/m at t = 0 s for all considered PGAs. It increases with respect to time and a higher PGA leads to higher maximum tension in the geosynthetic layer. Also, at t = 30 s, it increases by up to 298%, increasing PGA from 0.1g to 0.5g.

Figure 6.32 illustrates the effect of PGA on the tension throughout a geosynthetic layer. Nonuniform distribution of tension is observed throughout the geosynthetic layer. Two peak values of tension are observed for a specific PGA near the inner edges of adjacent pile heads. The left side peak tension is smaller compared to the right side. This may be due to the earthquake excitation. For PGA = 0.1g, the tension in the geosynthetic layer increases to its maximum value from the outer to the inner edge of piles. Subsequently, it decreases to zero up to the middle of the geosynthetic layer, whereas for the other PGA values, it increases up to the maximum

and then decreases in the middle of the geosynthetic layer. Notably, the tension in the geosynthetic layer increases by up to 500% near the inner edges of the pile heads with an increase in PGA from 0.1g to 0.5g.

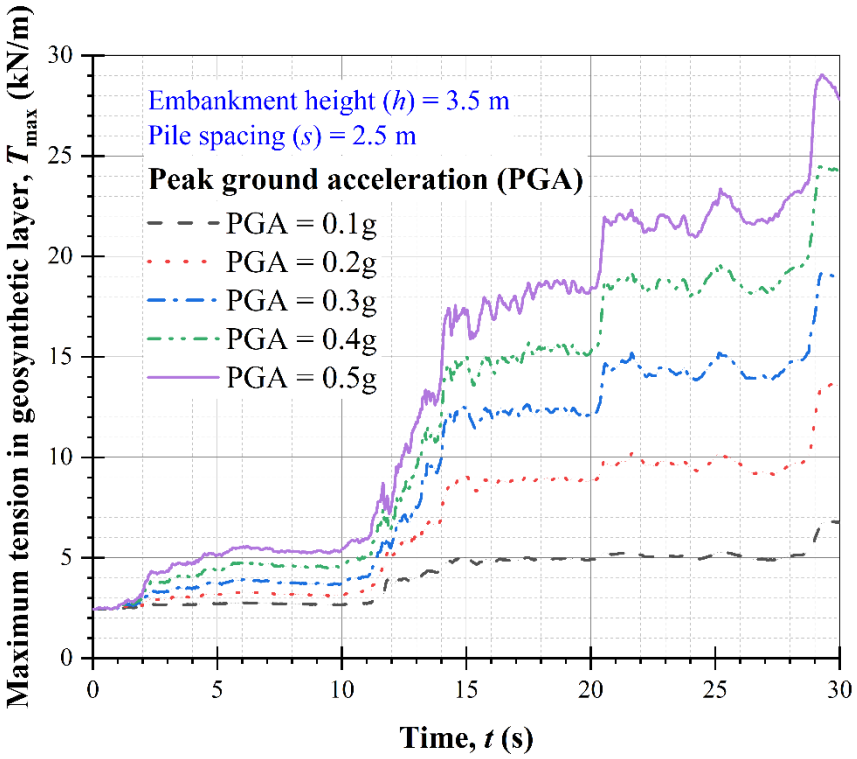

Figure 6.31: Effect of peak ground acceleration on maximum tension in the geosynthetic layer

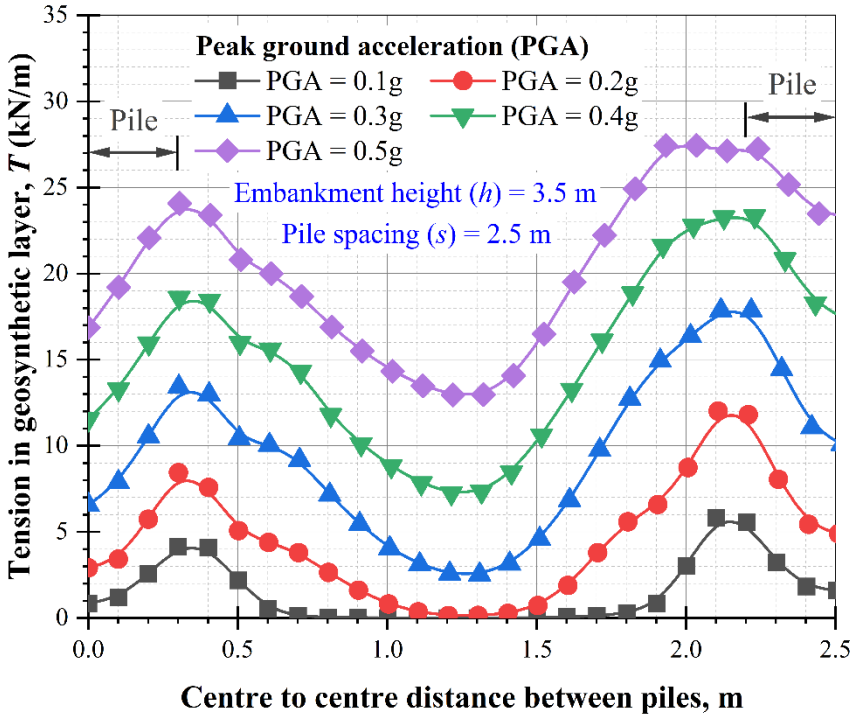

Figure 6.32: Effect of peak ground acceleration on tension in a geosynthetic layer

Figure 6.33 shows the effect of PGA on the *SCR*. The *SCR* starts with 0.49 and decreases with respect to time. It decreases by up to 34% with an increase in PGA from 0.1g to 0.5g. A higher reduction up to 0.3g PGA is observed. A further increase in PGA has a negligible effect on the *SCR*. This implies that the stress does not transfer to the pile top, and soil arching is not mobilising, thereby increasing PGA.

The effect of PGA on the *SAR* is shown in Figure 6.34. The *SAR* starts at 0.48 and increases with respect to time. It increases by up to 25% with an increase in PGA from 0.1g to 0.5g. A higher increment of up to 0.3g PGA is observed. The *SAR* decreases with further increases in PGA. This implies that the degree of soil arching deteriorates with an increase in PGA.

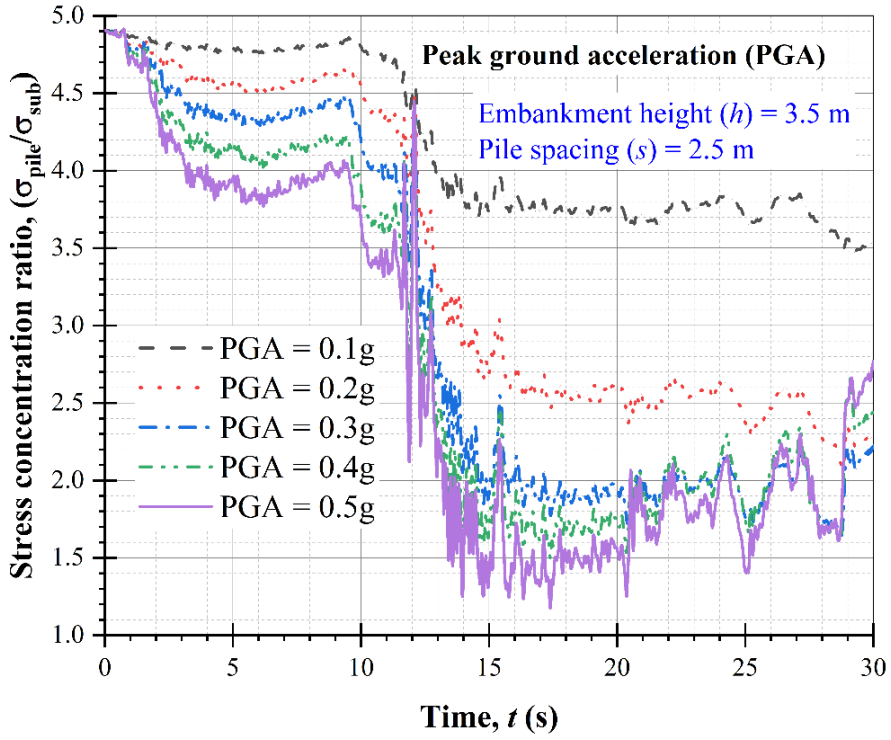

Figure 6.33: Effect of peak ground acceleration on the stress concentration ratio

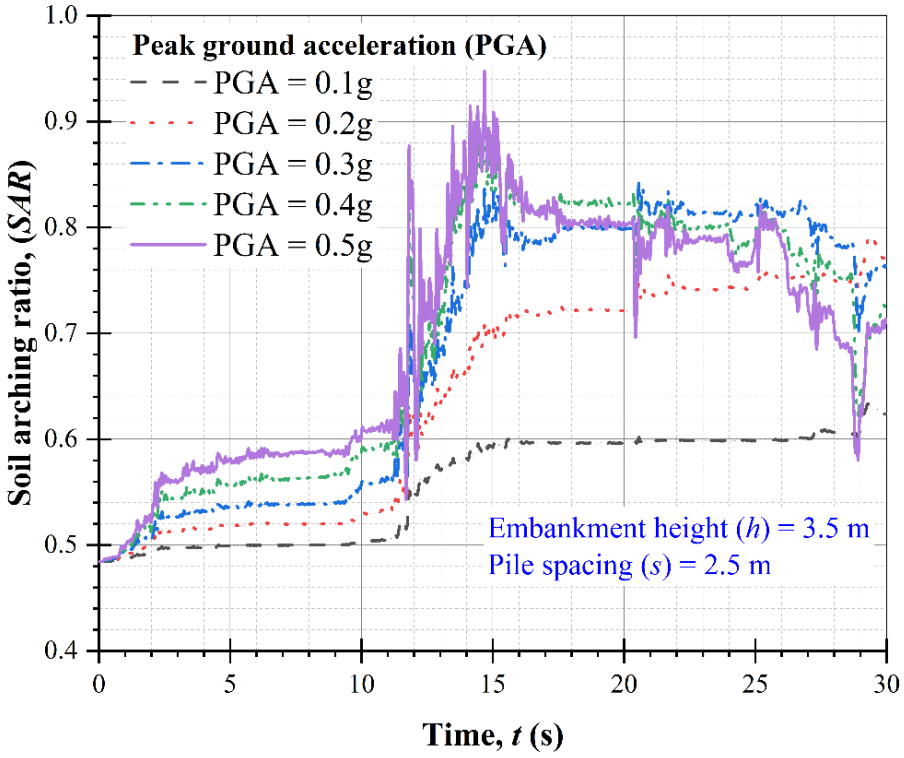

Figure 6.34: Effect of peak ground acceleration on the soil arching ratio

It is worth noting that in all cases of parametric study, the input accelerogram is not exciting the FE model with the maximum PGA at t = 11 s. It implies that the FE model does not get amplified at t = 11 s, and it can be used for further investigation of seismic behaviour of soil arching.

6.6 SUMMARY

This chapter reports on a seismic assessment of soil arching in a pile-supported embankment. Primarily, soil arching is investigated under earthquake excitation. Further, it extends to a parametric study to see the influence of different parameters of a pile-supported embankment on soil arching under seismic excitation. Based on the numerical analysis, a summary of this chapter is as follows:

1) The load transfer mechanism is significantly affected by the pile-supported embankment parameters.
    - Embankment modulus has a negligible effect on settlement. However, it decreases by up to 24% with an increase in the friction angle from 30° to 45°. This reduction in the settlement is more noticeable at the end of the earthquake.
    - The maximum tension in a geosynthetic layer is not affected by the embankment modulus. However, it decreases by up to 19% with an increase in the friction angle from 30° to 45°.
    - The maximum tension in a geosynthetic layer does not affect by embankment modulus. However, it decreases up to 19% with an increase in friction angle from 30° to 45°.
    - The stress concentration ratio (*SCR*) initially increases by up to 51% with an increase in the embankment modulus from 15 MPa

to 30 MPa. However, the embankment modulus has a negligible effect after 11 s, whereas it increases by up to 273% with an increase in the friction angle from 30° to 45°. The effect of the friction angle is more pronounced at the end of the earthquake.

Therefore, the friction angle is the most sensitive parameter of a pile-supported embankment which significantly affects soil arching during the earthquake.

2) The geosynthetic layer at the base of the embankment encourages stress transfer to the pile head through the tension in the geosynthetic layer.
    - The settlement of the subsoil top reduces by up to 17% with the inclusion of a geosynthetic layer at the base of the embankment.
    - The *SCR* value is 22.5% higher in the reinforced case compared to the unreinforced case at $t = 0$ s. However, there is a negligible difference in the *SCR* after 11 s in both the unreinforced and reinforced cases.
    - A reinforced layer enhances the degree of soil arching by up to 14% and 32% at the $t = 0$ s and 30 s, respectively.

Thus, it is clear that the inclusion of a geosynthetic layer can enhance soil arching under the earthquake condition and transfer more load on the pile top through the tension.

3) Soil arching is significantly affected by the amplitude of the input earthquake.
    - Vertical stress increases by up to 26% with a PGA increase from 0.1g to 0.3g. A further increase in PGA leads to failures in soil arching, and less vertical stress is observed at the end of earthquake for PGA = 0.5g. Also, the settlement increases by up to 433% with an increase in PGA from 0.1g to 0.5g.

- The maximum tension in the geosynthetic layer increases by up to 298%, increasing PGA from 0.1g to 0.5g.
- The *SCR* decreases by up to 34% with an increase in PGA from 0.1g to 0.5g. A higher reduction by up to 0.3g PGA is observed. A further increase in PGA has a negligible effect on the *SCR*. This implies that the stress does not transfer to the pile top and soil arching is not mobilising, thereby increasing PGA.

Thus, it is evident that the peak horizontal acceleration of an earthquake significantly affects soil arching.

In chapter 3, the true dynamic nature of traffic loading and soil arching is investigated under the equivalent dynamic load. Therefore, moving train load and dynamic response of soil is considered in chapter 7, and the soil arching is numerically investigated.

CHAPTER 7

INVESTIGATION OF SOIL ARCHING IN A PILE-SUPPORTED RAILWAY EMBANKMENT UNDER THE MOVING TRAIN LOAD

7.1 INTRODUCTION

Rail transport is the economic backbone of many countries, including Australia. Moreover, the Australian economy is largely dependent on railroad network which traverse the Australian coastal regions containing soft soil. As discussed earlier, pile-supported embankments have the potential to improve the unfavourable characteristics of soft soil. In the pile-supported railway embankments, soil arching reduces the load and settlement on the subsoil. However, the soil arching can get affected by the moving train in a railway embankment. Therefore, the effect of moving train on the soil arching in a pile-supported railway embankment cannot be ignored. Studies of the soil arching under static loading are well acknowledged. However, the dynamic behaviour of the soil arching under the moving train loading is limited.

In this chapter, a two-dimensional (2D) numerical simulation is carried out to demonstrate the effect of moving train induced loading on the soil arching. Subsequently, parametric study is performed to investigate the effect of different parameters of pile-supported railway embankment. A relationship between optimum embankment height and clear pile spacing is also established, which can be beneficial for the professionals.

7.2 FINITE ELEMENT METHOD (FEM) SIMULATION

7.2.1 Brief description

The numerical simulation is carried out using FEM based software ABAQUS (2018). As shown in Figure 7.1, the central portion of a typical pile-supported railway embankment is considered to investigate the effect of moving train on the soil arching. The geometric profile of the considered portion of pile-supported railway embankment is the same as used in chapters 3, and 6 (static and seismic analysis, respectively).

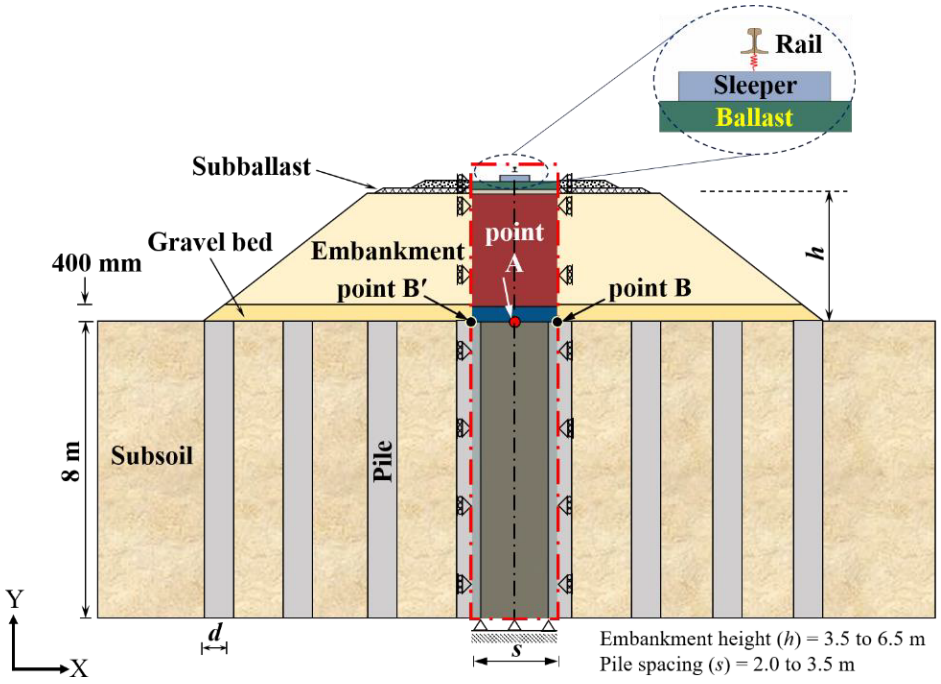

Figure 7.1: A typical cross section of pile-supported embankment including FE simulated model

The boundary conditions, element type, interface between pile and surrounding soil, soil constitutive model, material properties and damping are the same as considered during the seismic analysis in chapter 6. Additionally, Drucker-Prager constitutive soil model is used for the ballast and subballast. Sleeper and rail are modelled as linear elastic materials. The rail pad is modelled as spring dashpot with

stiffness of 1.20 E +06. The material properties for rail track are listed in Table 7.1.

Table 7.1: Material properties of rail track

Material properties	Subballast	Ballast	Sleeper	Rail
Constitutive model	Drucker-Prager	Drucker-Prager	linear elastic	linear elastic
Unit weight, γ (kN/m^3)	21	16	23	75.51
Young's modulus, E (MPa)	100	125	25.5×10^3	206000
Poisson's ratio, v	0.30	0.25	0.20	0.30
Friction angle, ϕ' (degree)	38	45	-	-
Dilation angle, ψ (degree)	8	15	-	-

The dynamic response of a material is different from static response, and for dynamic analysis, it is important to determine the Rayleigh damping coefficients. The dynamic parameters used to compute the Rayleigh damping coefficients for rail track material are listed in Table 7.2. The damping ratio (ξ_o) is assumed as 3% to compute the damping coefficients α and β (Bi et al. 2020). However, the Rayleigh damping coefficients for other material of pile-supported embankment is the same as determined in chapter 6.

Table 7.2: Dynamic parameters of ballast and subballast used in numerical simulation for moving train*

Dynamic parameters		Material	
		Ballast	Subballast
Modulus of elasticity, E (MPa)		125	100
Stiffness coefficient, k (10^8) (N/m)		2.00	3.59
Damping coefficient, c (10^5) (Ns/m)		4.56	4.82
Angular frequencies (rad/s)	ω_1	0.94	1.41
	ω_2	4.68	7.06
Rayleigh damping coefficient	α	0.0469	0.0706
	β	0.00001	0.00001

* Dynamic parameters for other track materials are the same as those used in chapter 6 hence not provided here again.

7.2.2 Moving train load

The dynamic load induced by a moving train is simulated by specifying the nodal force as a function of time history in a triangular pattern. This loading procedure is similar to Hall (2003). In this study, axle load of 25 ton with eight moving carriages including 32 wheels are considered for the moving train load calculation (refer Figure 7.2a). In addition, Figure 7.2(b) shows the loading pattern of a moving train at the 40 km/h speed. The moving train load is applied at the mid of the rail top as shown in Figure 7.1.

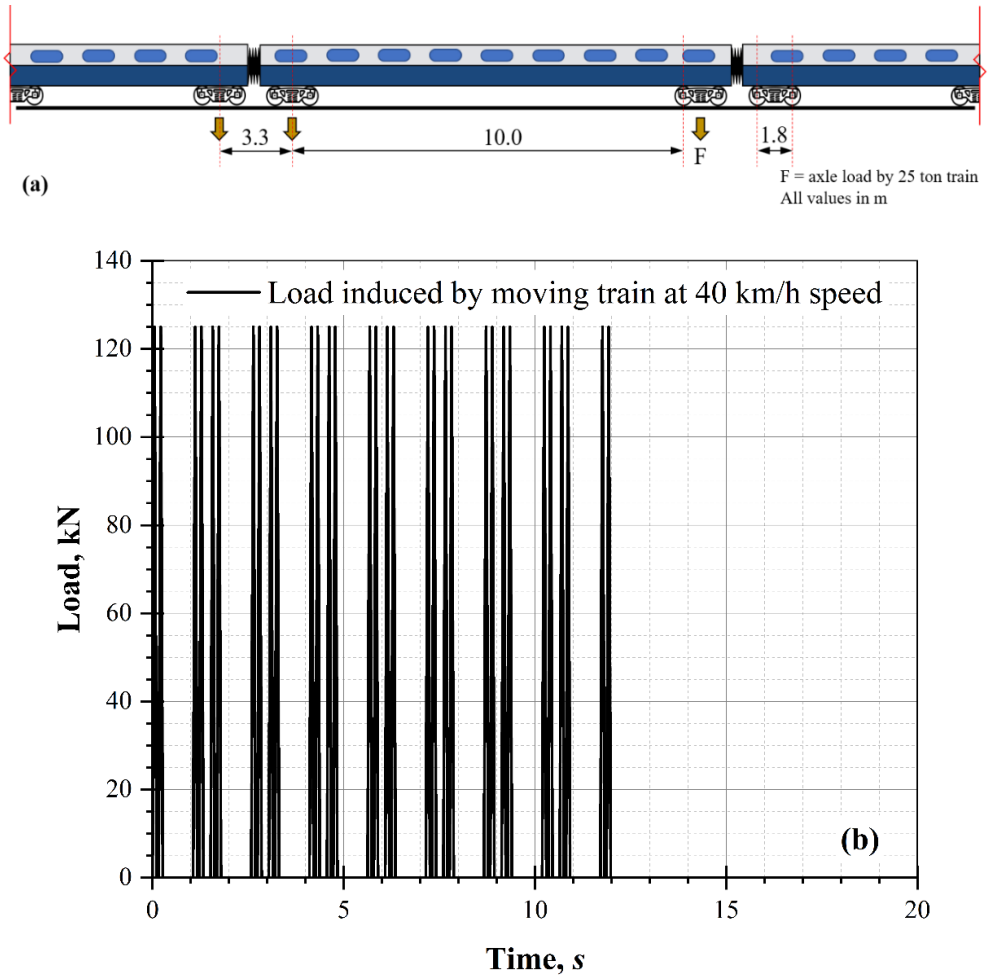

Figure 7.2: (a) Description of considered train configuration for moving train load calculation (b) Loading pattern induced by a train moving at 40 km/h train speed

7.2.3 Numerical analysis procedure

The numerical simulation initiated with establishing the geostatic stress condition in the subsoil. Further, installation of piles and stage construction of embankment including gravel bed with geosynthetic layer is proceed in the static general steps. After the achieving desired height of the embankment, 150 mm thick subballast and 300 mm thick ballast layers are modelled on the embankment top. Subsequently, sleeper with rail is simulated in the next step. The rail and sleeper are connected by a spring dashpot which is represented as a rail pad. Afterwards, a moving train load is imposed on the rail top using a dynamic implicit step for a time instant (Zhuang and Wang 2018; Pham et al. 2020). During the dynamic implicit step, the smaller time step (i.e., 0.002 s) is used to achieve a good convergence.

7.3 VALIDATION OF FE MODELLING

Accuracy of the FE model has been investigated by comparing of the analytical model and field measurement reported Yang and Yau (1997) and Paixão et al. (2014), respectively. The model calibration is already explained in chapter 3. Therefore, only model validation is covered in this chapter. Figure 7.3 shows a comparison of the beam displacement reported in Yang and Yau (1997) and the FE simulation result. The model parameters are taken the same as reported in Yang and Yau (1997). It can be seen that the present numerical simulation follows the same trend of displacement in the beam. The present numerical simulation shows an acceptable agreement with 11% difference compared to Yang and Yau (1997).

In addition, as shown in Figure 7.4, the FE model is also compared with the field data reported by Paixão et al. (2014). They reported the rail displacement at different sections of the railway track, under the Portuguese passenger train. Two

underpasses (i. e., UP1 and UP2) are considered to investigate the dynamic response of rail track. In this study, field measurement of the UP2 underpass rail track is considered for comparison purpose. Figure 7.4 shows a comparison of the rail displacement between field data and the FE result at the S1 section, resting on the embankment soil. The FE model result is in an acceptable agreement with the field measurement. Thus, Figures 7.3 and 7.4 confirm that the present FE model can predict the response of the pile-supported railway embankment with reasonable accuracy.

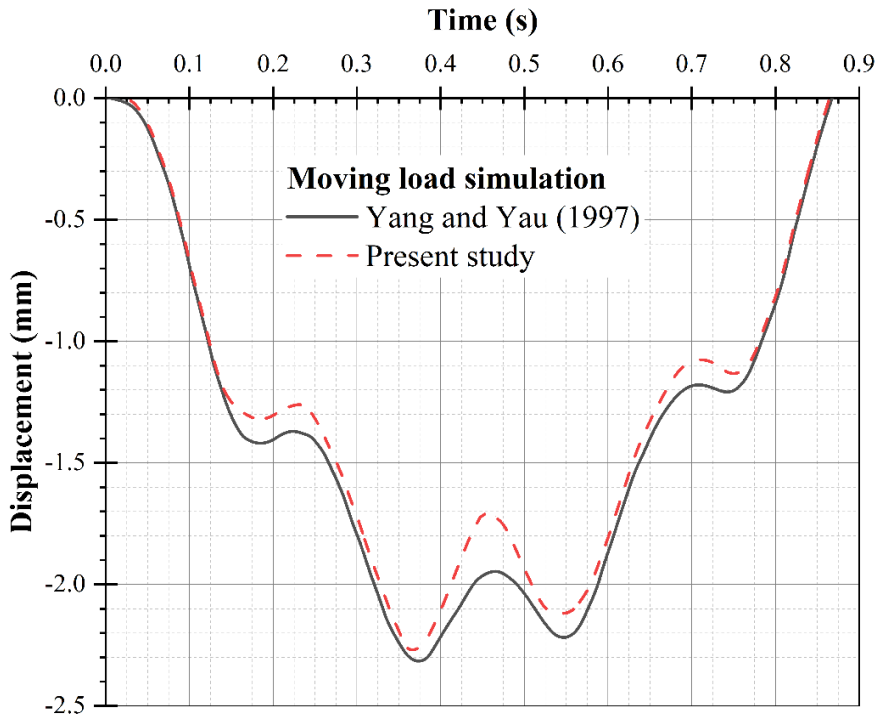

Figure 7.3: Comparison of vertical displacement of a beam with the data reported by Yang and Yau (1997)

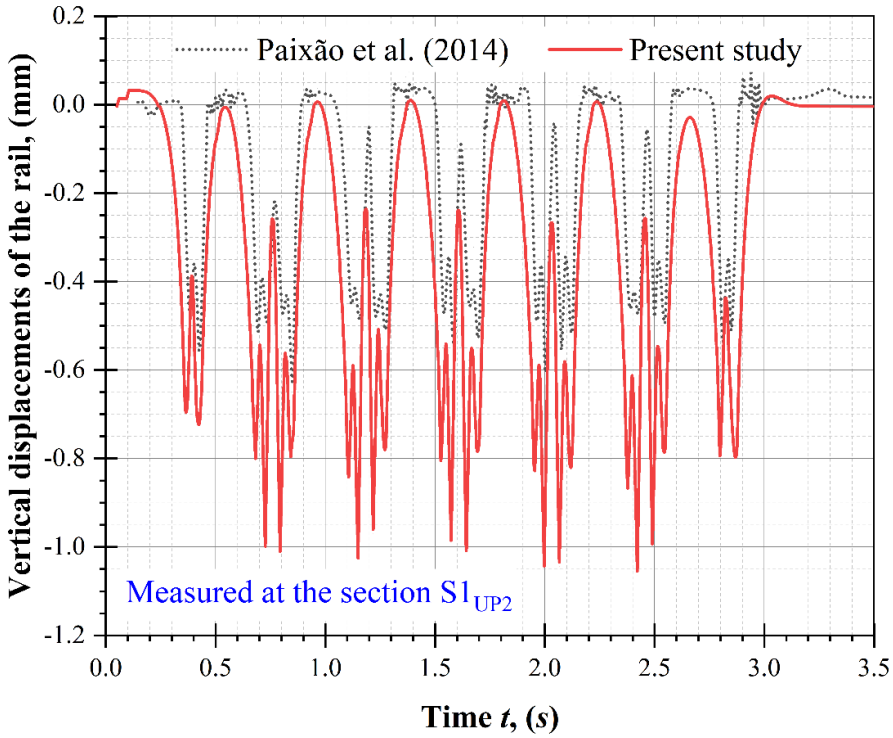

Figure 7.4: Comparison of vertical displacement of rail with the data reported by Paixão et al. (2014)

7.4 RESULTS AND DISCUSSION

After the validation of moving train load, it is crucial to investigate the effect of moving train load on the soil arching phenomenon in a pile-supported railway embankment. The vertical stress and settlement can be attended as the soil arching investigation.

7.4.1 Vertical stress

Figure 7.5 shows vertical stress distribution for both reinforced and unreinforced conditions under the embankment construction and a moving train at the speed of 40 km/h. To investigate the vertical stress in both conditions, the embankment height and pile spacing are considered as 3.5 m and 2.5 m, respectively. The normalised vertical stress starts with the 2 s representing gravel bed including the geosynthetic layer is

laid. Subsequently, for both reinforced and unreinforced conditions, it gradually increases with respect to time up to 11 s on the subsoil and piles. However, a higher normalised vertical stress can be seen on the pile top due to the soil arching. In the reinforced condition, the normalised vertical stress reduces up to 15% on the subsoil compared to the unreinforced condition. Whereas, it increases up to 10% on the pile top. It implies that the reinforced layer reduces the vertical stress on subsoil by transferring it to the pile top. In addition, it is also worth noting that the soil arching zone expands by the inclusion of a geosynthetic layer.

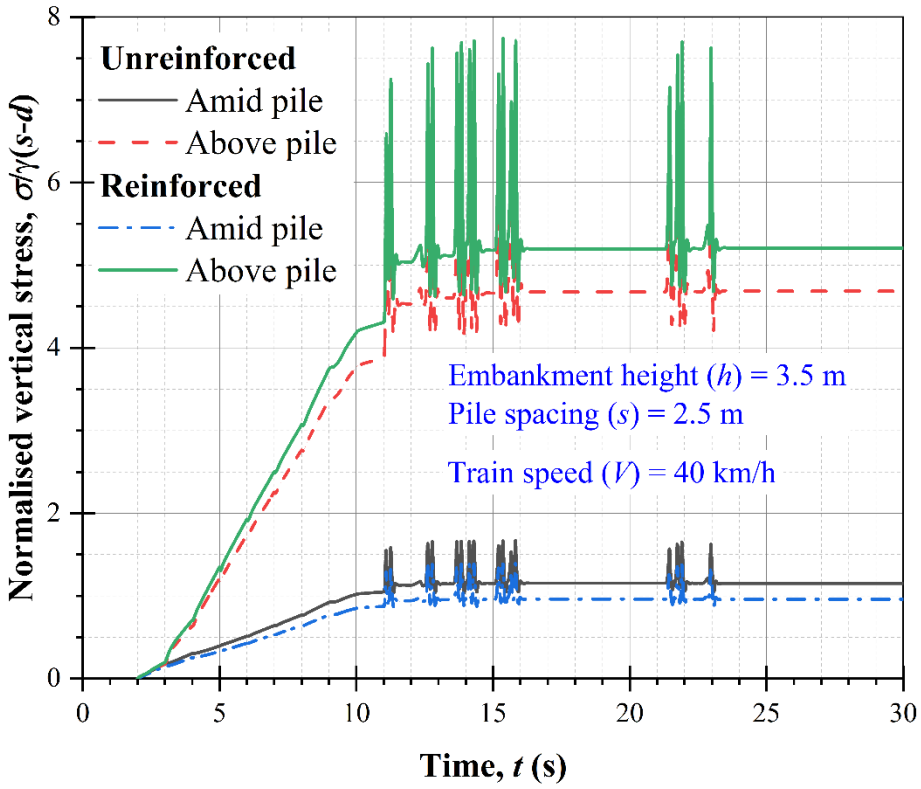

Figure 7.5: Normalised vertical stress distribution under the embankment construction and moving train loading

7.4.2 Settlement

Settlement of embankment fill at the pile top and subsoil are shown in Figure 7.6. It can be seen that the settlement on the subsoil gradually increases with respect to time

up to 11 s. Subsequently, it fluctuated due to the moving train load up to 23 s and then attained maximum value of 0.56 normalised settlement. The settlement of subsoil decreases up to 18% by the inclusion of a geosynthetic layer at the base of embankment. However, a negligible settlement is found on the pile top for both unreinforced and reinforced conditions.

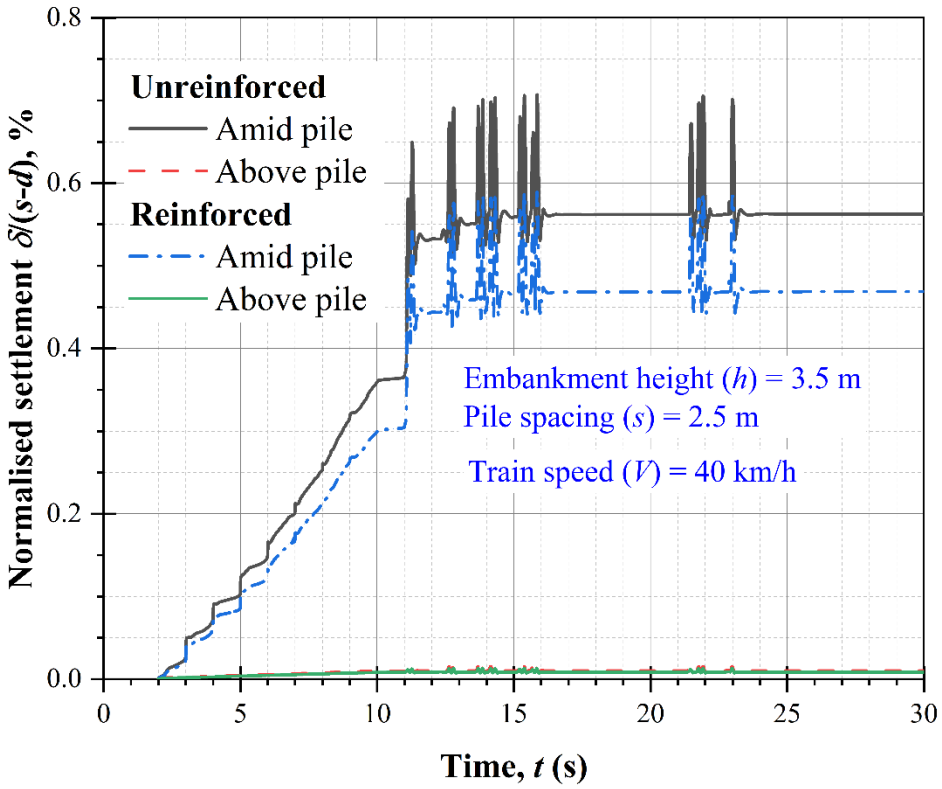

Figure 7.6: Normalised settlement under the embankment construction and moving train loading

7.5 PARAMETRIC STUDY

It is evident that the inclusion of a reinforcement layer at the base of embankment fill is beneficial for the load transfer from the subsoil to the pile top. Consequently, the parametric study is incorporated only for the reinforced condition. Only one parameter is changed at a time to see the effect of specific parameters.

7.5.1 Effect of pile spacing (*s*) *and embankment height* (*h*)

Soil arching effected by pile spacing and embankment height. Figures 7.7-7.10 show the effect of pile spacing and embankment height on the vertical stress, settlement, stress efficacy and maximum tension in geosynthetic layer. The pile spacing is varied from 2.0 m to 3.5 m while embankment height ranged between 2.5 to 6.5 m. The load induced by a train at 40 km/h speed is considered on the rail top.

The effect of pile spacing and embankment height on the vertical stress acting on the subsoil is shown in Figure 7.7. The vertical stress is normalised by $\gamma(s\text{-}d)$ for general applicability. It can be seen that the normalised vertical stress increases up to 220% with an increase of embankment height from 2.5 to 6.5 m for pile spacing 2.0 m. In addition, it increases up to 250% with an increase of pile spacing from 2.0 m to 3.5 m. It implies that the vertical stress on subsoil increases with an increase of embankment height and pile spacing. In addition, the soil arching zone increases for smaller pile spacing which helps to soil arching mobilisation.

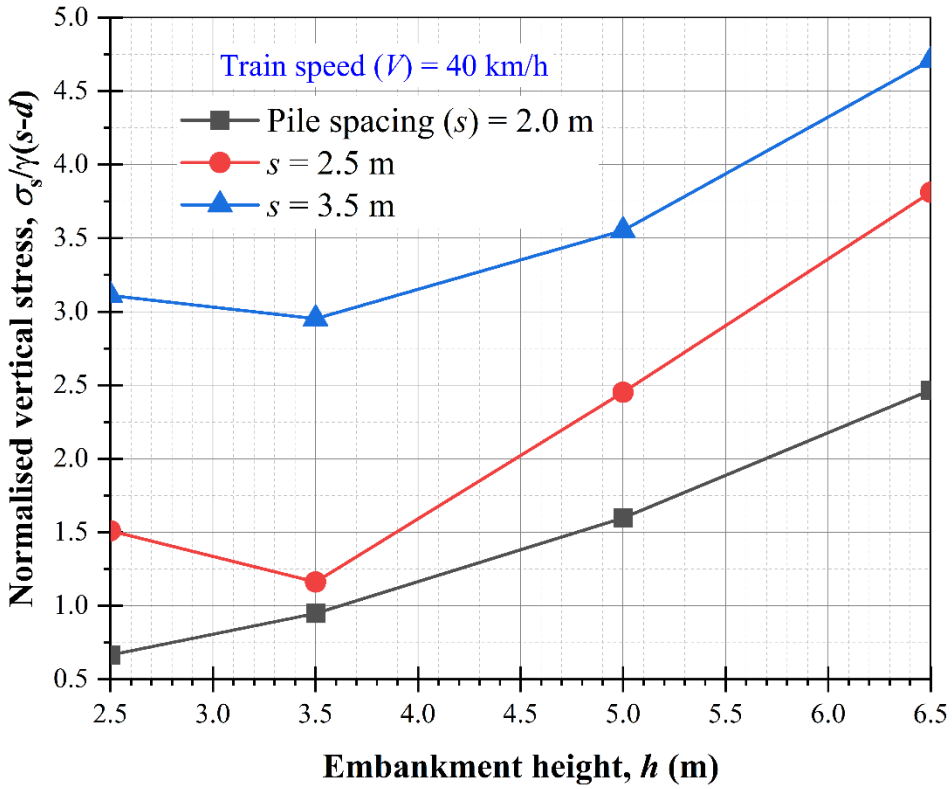

Figure 7.7: Effect of embankment height and pile spacing on normalised vertical stress at the subsoil top

Figure 7.8 shows the effect of pile spacing and embankment height on normalised settlement. The normalised settlement increases up to 600% with an increase of embankment height from 2.5 m to 6.5 m. In addition, the normalised settlement increases up to 114% with an increase pile spacing from 2.0 m to 3.5 m.

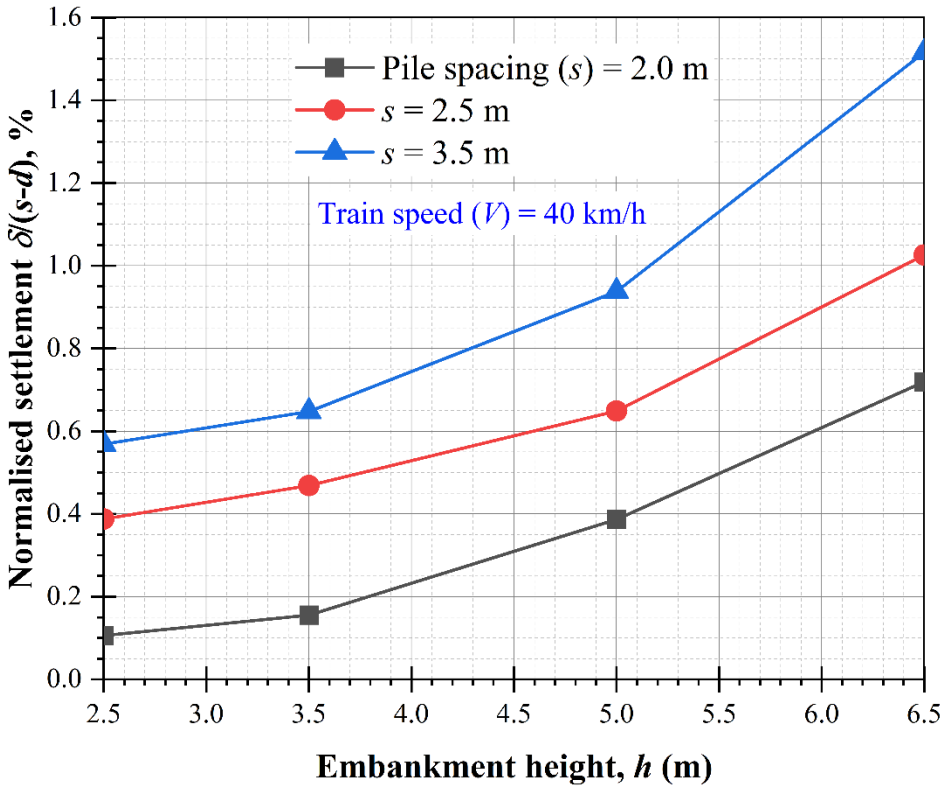

Figure 7.8: Effect of embankment height and pile spacing on normalised settlement of subsoil

Stress efficacy corresponding to different embankment heights (h) and pile spacing (s) is shown in Figure 7.9. The stress efficacy increases up to 44% with an increase of embankment height 2.5 m to 6.5 m for the pile spacing 2.0 m. In addition, it decreases up to 62% with an increase of pile spacing from 2.0 m to 3.5 m. Thus, it is evident that most of the load is transferred to the piles at smaller pile spacing and optimum embankment height (i.e., 5 m for this study).

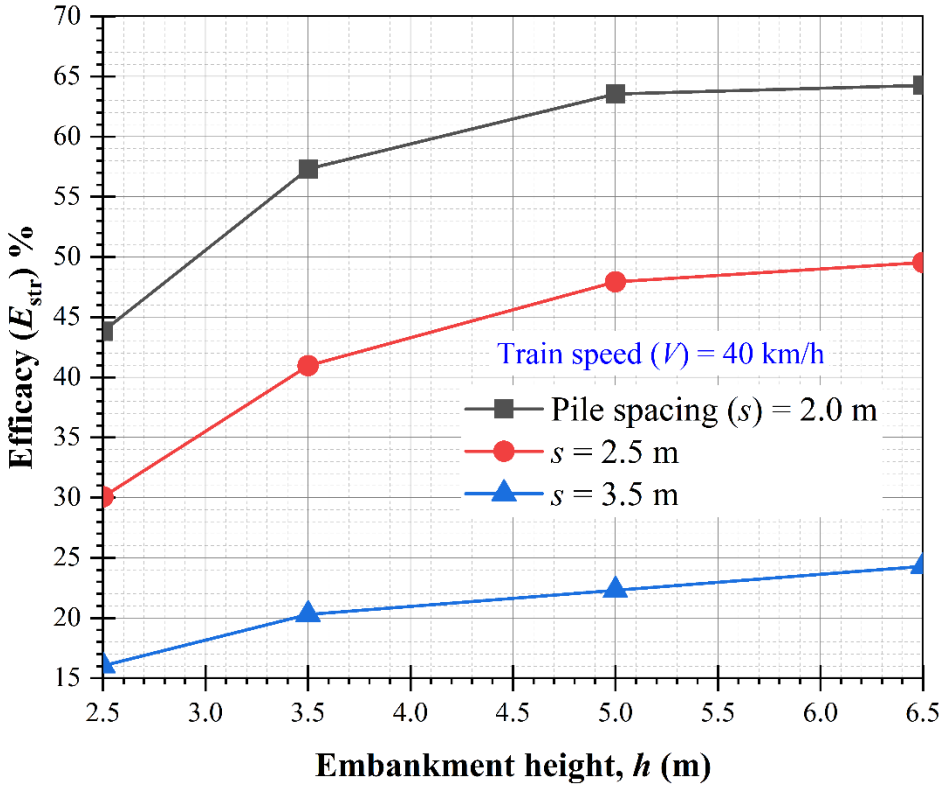

Figure 7.9: Effect of embankment height and pile spacing on stress efficacy

The effect of pile spacing and embankment height on maximum tension in geosynthetic layer is shown in Figure 7.10. It is can be seen that the maximum tension is increases up to 87% with an increase in embankment height from 2.5 m to 6.5 m. In addition, it increases up to 100% with an increase in pile spacing from 2 m to 3.5 m at large embankment height. The function of reinforced layer is more effective in a large pile spacing and embankment height.

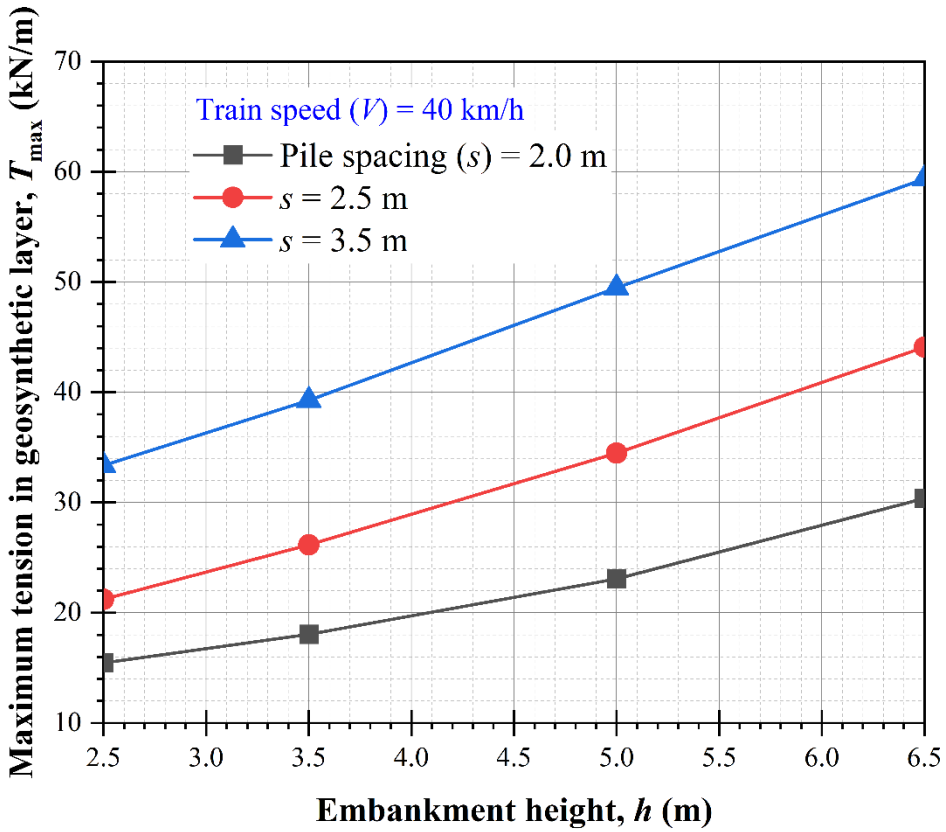

Figure 7.10: Effect of embankment height and pile spacing on maximum tension in geosynthetic layer

7.5.2 Effect of the embankment modulus and friction angle

The effect of pile-supported embankment parameters such as pile and embankment modulus, and friction and dilation angle illustrate in this section. The embankment height and train speed are considered as 3.5 m and 40 km/h, respectively to see the effect of these parameters. Figure 7.11 shows the effect of pile and embankment modulus on the stress efficacy for different pile spacing. It can be seen that the stress efficacy increases up to 28% with an increase of embankment modulus (E_{em}) from 15 to 30 MPa. However, pile modulus has a negligible effect on stress efficacy. The smaller pile spacing (i.e., 2.0 m for this study) shows a higher stress efficacy and it decreases with an increase of pile spacing.

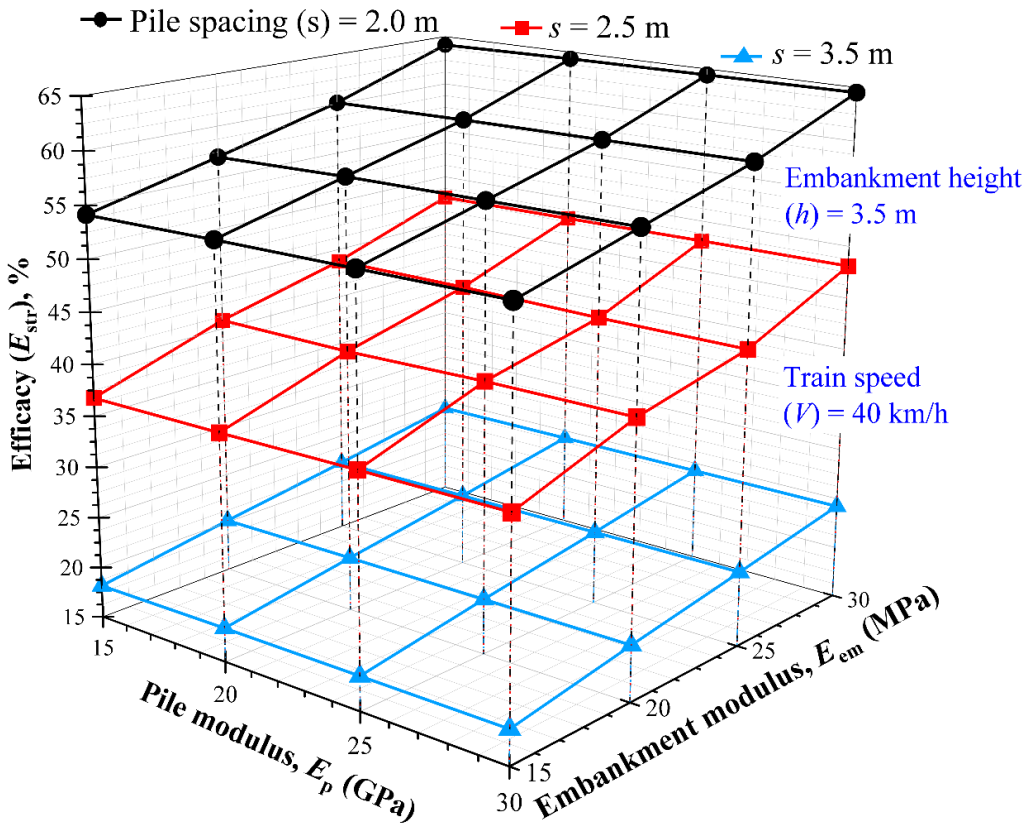

Figure 7.11: Effect of pile and embankment modulus spacing on stress efficacy

The influence of friction and dilation angle on stress efficacy is shown in Figure 7.12. It shows that stress efficacy increases up to 45% with an increase in friction angle from 30° to 45°. While the effect of dilation angle is found to be negligible. It is worth noting that smaller pile spacing shows higher stress efficacy. It implies that pile spacing should be optimum for efficient load transfer from subsoil to the pile.

In addition, it is clear from Figures 7.11 and 7.12 that embankment modulus and friction angle are the effective parameters of embankment fill for soil arching, and these both should be higher for fully mobilisation of soil arching. The same trend of efficacy is observed in chapter 3 under the equivalent dynamic load. However, a higher efficacy is observed in the moving train load compared to the equivalent dynamic load.

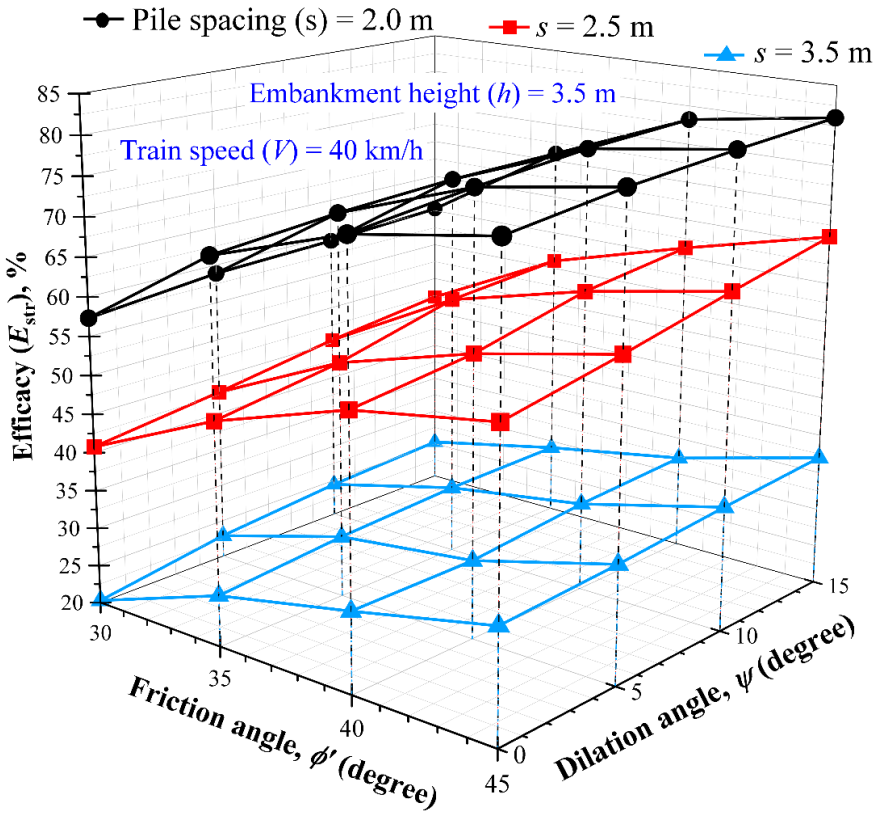

Figure 7.12: Effect of friction and dilation angle on stress efficacy

Further, the effect of embankment modulus and friction angle on the settlement of embankment base is shown in Figure 7.13. The effect of embankment modulus (E_{em}) on settlement is illustrated in Figure 7.13(a). A negligible settlement is found on the pile top, while it increases with an increase of centre to centre distance up to half of the pile spacing. The maximum settlement occurs at half of the pile spacing. It decreases up to 55% with an increase of embankment modulus (E_{em}) from 15 to 30 MPa. Figure 7.13(b) shows the effect of friction angle on the settlement profile at the embankment base. It can be seen that the maximum settlement, which occurs at the mid of pile spacing, decreases up to 46% with an increase in friction angle from 30° to 45°. In addition, the difference in settlement profile is decreases with an increase of embankment modulus and friction angle, which implies that an optimum value of embankment modulus and friction angle is required for efficient soil arching.

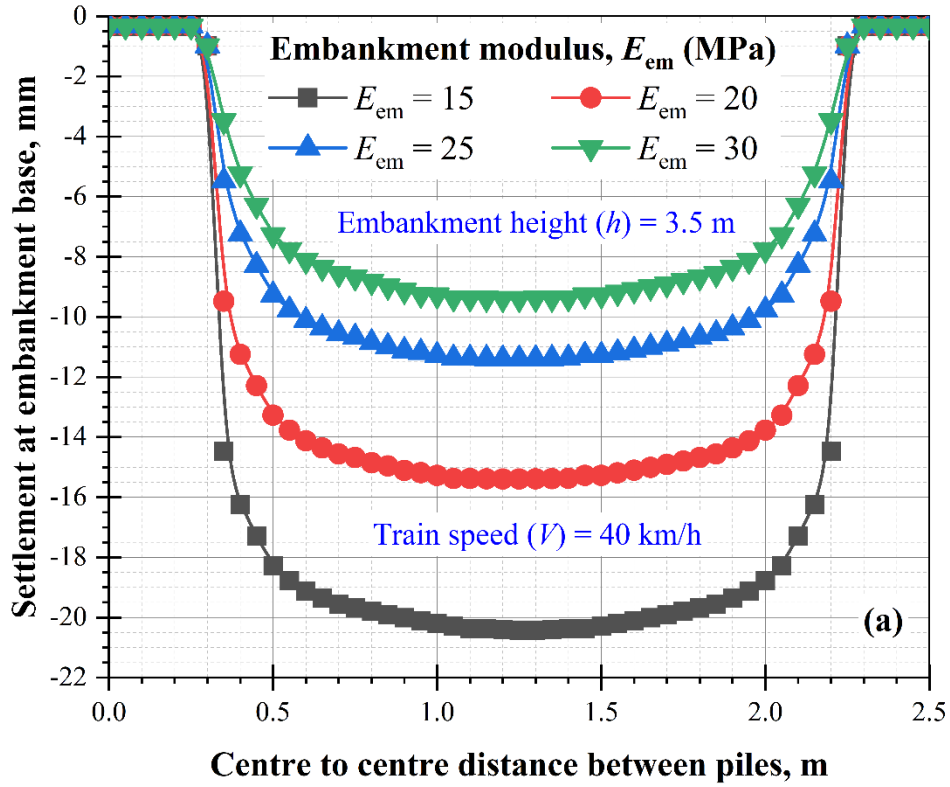

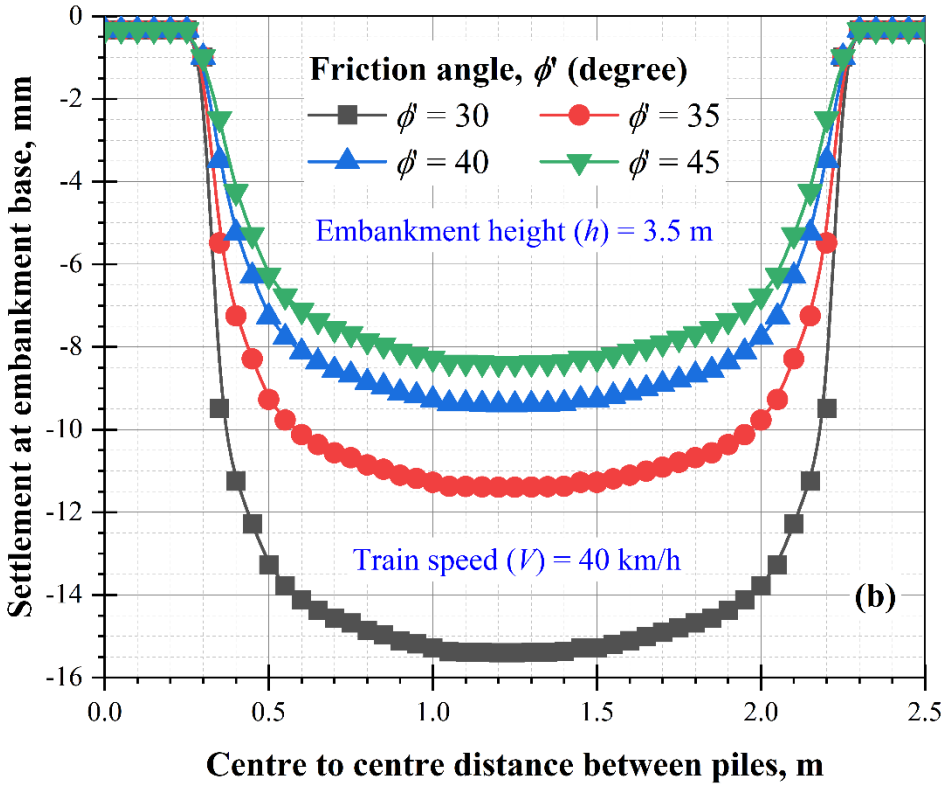

Figure 7.13: Effect of (a) embankment modulus and (b) friction angle on the settlement at the base of embankment

Figure 7.14 shows the effect of embankment modulus and friction angle on the tension in geosynthetic layer. As shown in Figure 7.14(a), the maximum tension occurs near the inner edge of piles and it decreases up to 30% with an increase of embankment modulus from 15 MPa to 30 MPa. Whereas, the maximum tension in geosynthetic layer decreases up to 40% with an increase of friction angle from 30° to 45°(refer to Figure 7.14b). The tension in the geosynthetic layer decreases with an increase of embankment modulus and friction angle which helps in load transfer to pile through the soil arching.

Thus, it is evident that embankment modulus and friction angle are important parameters of the embankment which can affect the load transfer mechanism including the soil arching even in the moving train condition.

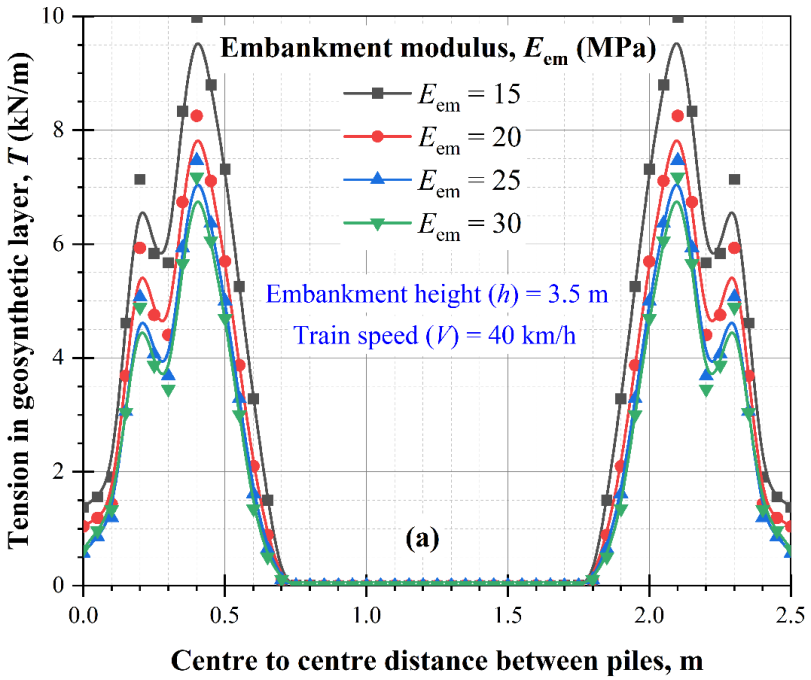

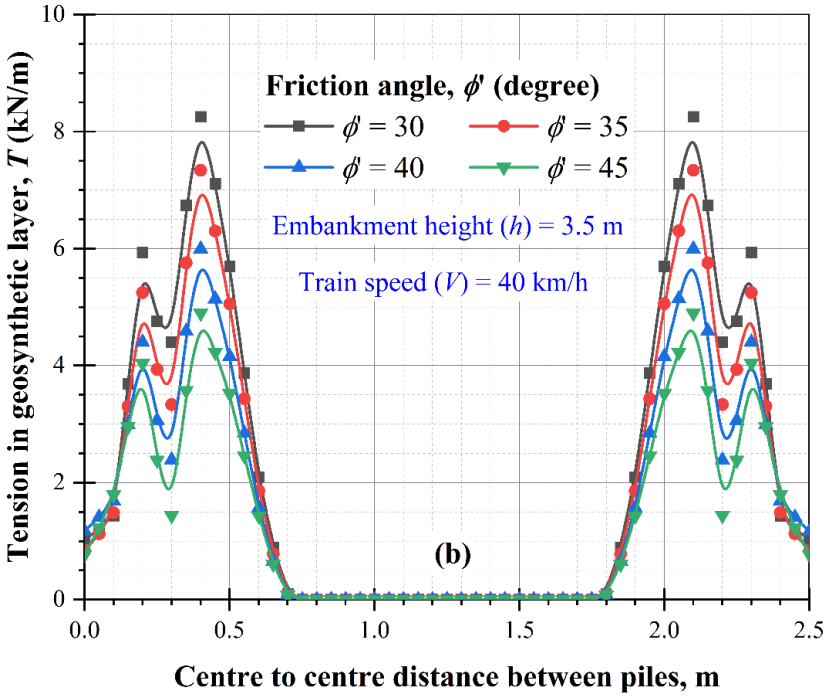

Figure 7.14: Effect of (a) embankment modulus and (b) friction angle on the tension in geosynthetic layer

7.5.3 Effect of the train speed

Figures 7.15-7.18 show the effect of train speed on soil arching. Figure 7.15 shows the lateral stress coefficient plotted on the vertical profile at subsoil and pile top. The lateral stress coefficient represents the ratio of horizontal to vertical stress as explained earlier in chapter 3. Embankment height (h) and pile spacing (s) is considered as 3.5 m and 2.5 m, respectively to see the effect of train speed.

Figures 7.15(a) shows the lateral stress coefficient (K) profiles for a range of train speed plotted with vertical distance upwards from the base of the embankment (h) normalised by (s-d). The profile of lateral stress coefficient under the moving train load does not follow to lateral stress coefficient in static condition. The lateral stress coefficient (K) profile initiate with 0.7 for moving train at the speed of 40 km/h. Subsequently, it approaches the active stage of lateral stress coefficient (K_o) at the normalised embankment height of 1.1, and with a further decrease in normalised

embankment height of 0.95, it attained at the lateral stress coefficient of 0.4. Up to this normalised embankment height, the lateral stress coefficient profile is shifted toward the active stage (K_o) with an increase in moving train load. This variation in the lateral stress coefficient is due to the influence of the dynamic load induced by the moving train. For normalised embankment height ($h/(s\text{-}d)$) < 0.95, lateral stress coefficient (K) is tens to approach at passive stage (K_p) up to ($h/(s\text{-}d)$) = 0.35. However, it is not approaching at passive stage due to the dynamic load induced by the moving train. Subsequently, the lateral stress coefficient (K) decreases until the embankment base for all moving train load which attribute the inner arch of soil arching. In addition, it is worth nothing that the zone of lateral stress coefficient at rest to passive stage is decreases with an increase in moving train load. Thus, it implies that the vertical stress significantly affected by the load induced by a moving train.

Figure 7.15(b) shows the lateral stress coefficient at pile top. It can be seen that the lateral stress coefficient profile gets disturbed and tends to rest at active stage. Due to the load induced by the moving train, the horizontal stress is disturbed up to 0.8 normalised embankment height from the embankment top.

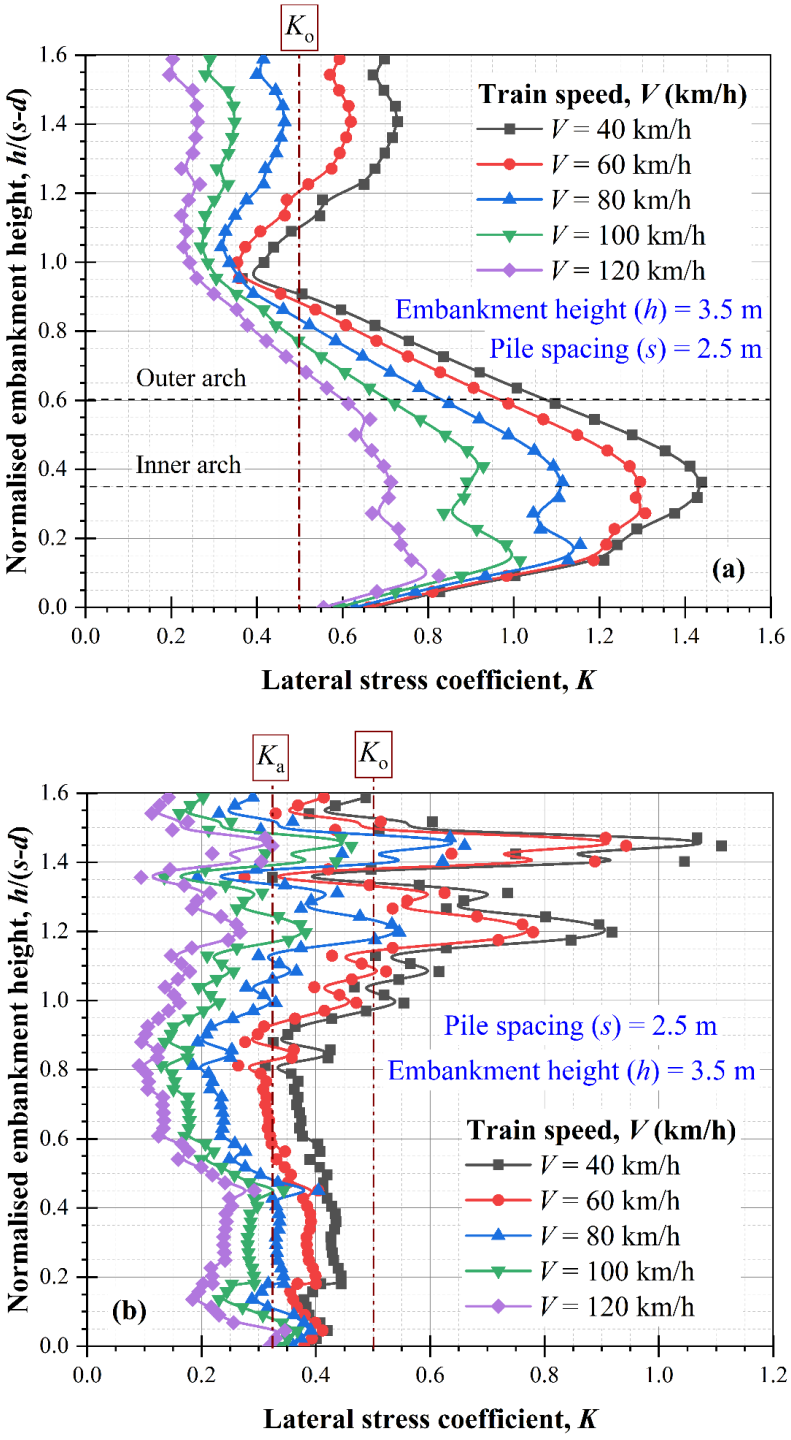

Figure 7.15: Effect of train speed on the Lateral stress coefficient (K) (a) at subsoil, (b) at pile top

Figure 7.16 shows the settlement time history on the subsoil for different load induced by different moving train. The embankment height and pile spacing are considered as 3.5 and 2.5 m, respectively. Time is normalised to evaluate the accurate

settlement value under the train pass with different speed. It can be seen that settlement on subsoil increases up to 220% with an increase in load induced by the moving train from 40 km/h to 120 km/h. The settlement is varied by the moving train and maximum occur under the wheel passages. In addition, a content settlement occurs after the train passage.

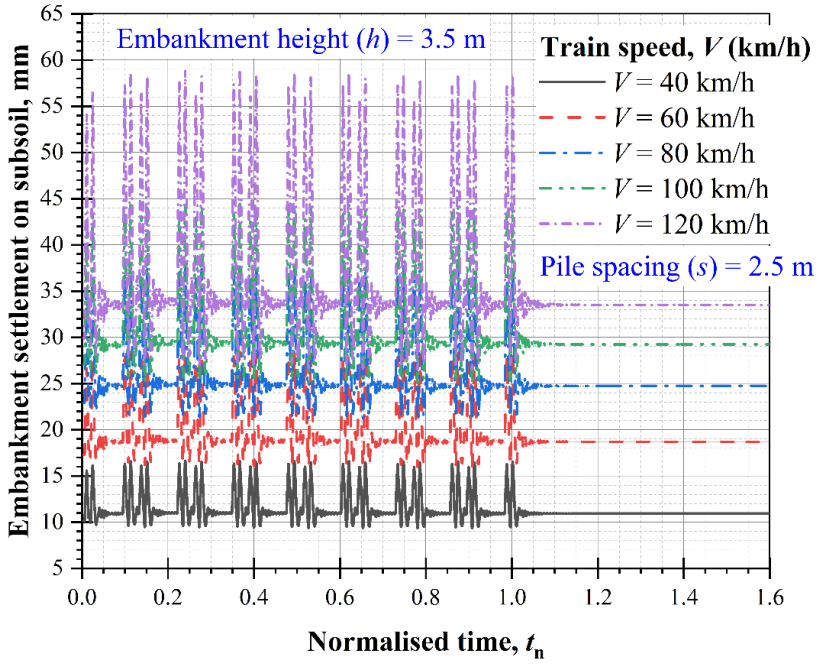

Figure 7.16: Effect of train speed on the embankment settlement on the subsoil

Influence of train speed on the stress efficacy is shown in Figure 7.17 for a range of pile spacing. In this study, pile spacing of 2 m is shown the higher stress efficacy. However, it decreases up to 69% with an increase in pile spacing (s) from 2 to 3.5 m. After the train speed of 100 km/h, the stress efficacy decreases due to higher load in the embankment top. However, this reduction in stress efficacy is more pronounced in the large pile spacing. It implies that pile spacing should be optimum for efficient load transfer from subsoil to pile.

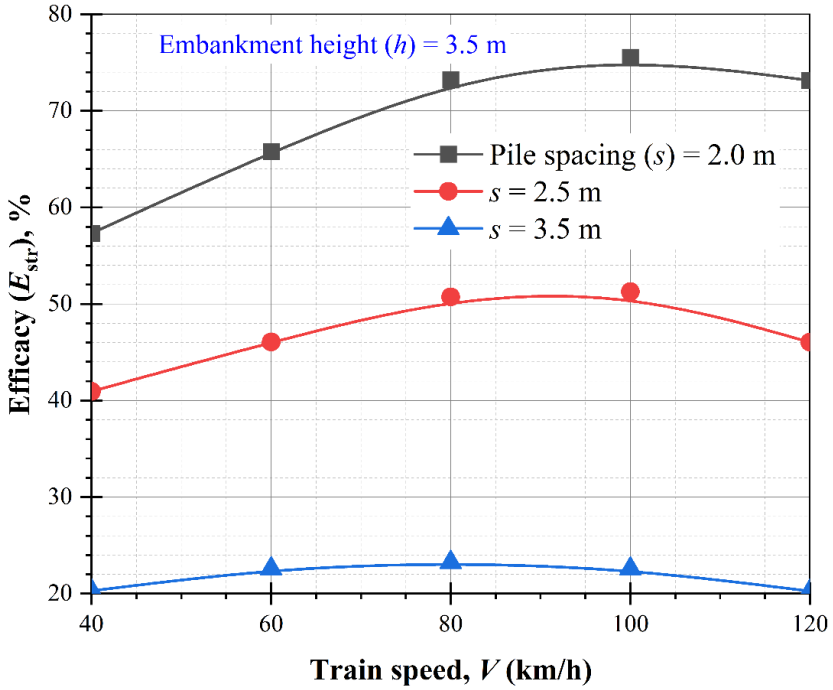

Figure 7.17: Effect of train speed on stress efficacy

The effect of moving train load on the tension in geosynthetic layer is shown in Figure 7.18. It is evident that maximum tension which occurs near the inner edge of piles increases up to 162% with an increase in train speed from 40 to 120 km/h. This is due to an increase in vertical stress on the subsoil with an increase in train speed. In addition, the function of the geosynthetic layer is more significant under the higher train speed.

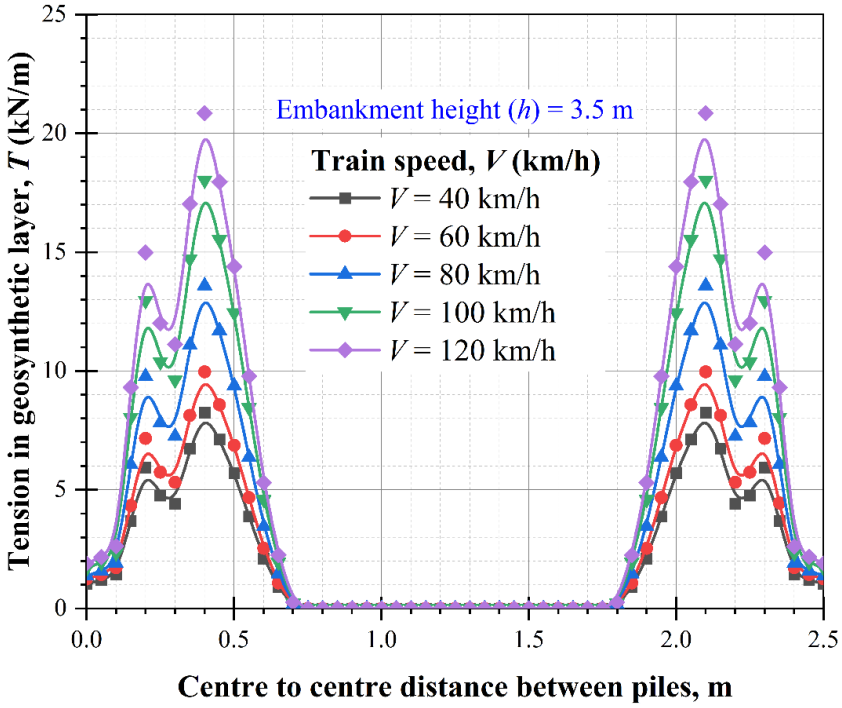

Figure 7.18: Effect of train speed on tension in geosynthetic layer

7.6 SUMMARY

In this chapter, a series of 2D numerical simulations of a pile-supported railway embankment is carried out to investigate the soil arching under the moving train load. The moving train load is validated against the existing literature which served as the basis of further analysis. Based on the numerical results, following summary may be drawn in the details:

1) The soil arching is significantly affected by different parameters of pile-supported embankment.
    - The vertical stress increases up to 250% with an increase of embankment height (h) from 2.5 to 6.5 m and pile spacing (s) from 2 to 3.5 m. The soil arching zone increases for smaller pile spacing which helps to soil arching mobilisation.
    - In addition, the stress efficacy also increases up to 44% with an

increase of embankment height 2.5 m to 6.5 m for the pile spacing 2.0 m. Thus, it is evident that most of the load is transferred to the piles at smaller pile spacing and optimum embankment height (i.e., 5 m for this study).

- Maximum settlement of subsoil decreases up to 55% with an increase of embankment modulus (E_{em}) from 15 to 30 MPa. Whereas it decreases up to decreases up to 40% with an increase of friction angle from 30° to 45°.

Thus, pile-supported parameters such as embankment height, pile spacing, embankment modulus and friction angle are the major parameters that can affect the soil arching in the moving train loading.

2) The load induced by the moving train at different speed is also affected to soil arching.
    - The zone of lateral stress coefficient at rest to passive stage is decreases with an increase in moving train load.
    - The settlement on subsoil increases up to 220% with an increase in load induced by the moving train from 40 km/h to 120 km/h.
    - A smaller pile spacing of 2 m shows the higher stress efficacy under the different train speed. However, after the train speed of 100 km/h, the stress efficacy decreases and it is more pronounced in the large pile spacing (i.e., 3.5 m in this study).
3) The inclusion of a geosynthetic layer at the base of embankment improve the load transfer to the pile top.
    - The maximum tension in geosynthetic layer increases up to 162% with an increase in train speed from 40 to 120 km/h. It implies that

the function of the geosynthetic layer is more significant under the higher train speed.

- Further, the maximum tension in geosynthetic layer decreases with an increase of embankment modulus and friction angle which helps in load transfer to pile through the soil arching.

CHAPTER 8

CONCLUSIONS AND RECOMMENDATIONS

This chapter covers the general conclusions and summarised the major findings from this research study. Directions for future research regarding this research are outlined in the last section of this chapter.

8.1 CONCLUSIONS

The soil arching mechanism is significantly investigated by many researchers. However, Seismic assessment of soil arching and accurate evaluation of vertical stress on the soil arching are not yet to be investigated. The solution of these issues is explored using FEM based software ABAQUS in the current research study. A unit cell of the pile-supported railway embankment is simulated in this study. Different parameters of GRPS embankments are assessed and investigated the influence on the soil arching. Based on the results of this study, the following conclusions could be delivered:

8.1.1 Soil arching in a pile-supported railway embankment

- The pile spacing embankment height, embankment modulus and friction angle are the most critical embankment parameters which can influence the soil arching. The dilation angle has a negligible effect at a lower friction angle.
- The geosynthetic layer at the base of embankment encourages stress transfer

to the pile head through the tension in geosynthetic. The application of geosynthetic layer is more notable for large pile spacing.

- The shape of the soil arch is not semicircular with uniform thickness, rather, it follows the multi-arch theory proposed by Kempfert et al. (2004). Thus, more research is needed on the shape and formation of the soil arch, in particular.
- Comparison of the numerical results with the existing design methods show inconsistencies which may lead for further research.

8.1.2 2D analytical scheme of soil arching in a pile-supported railways embankment

- The vertical load carried by the pile increases with an increase in the embankment height (h) and ratio of pile width (d) to clear pile spacing (s-d).
- The geosynthetic reinforcement plays a crucial role in the load transfer mechanism, especially for a large pile spacing and for very compressible subsoil (e.g. E_o = 0.5 MPa for this study). Due to membrane effect of geosynthetic, the extra load is transferred to the pile top from the subsoil and enhance the soil arching. In addition, number of piles can be reduced with the inclusion of geosynthetic reinforcement resulting in a more economic design of pile-supported embankment.
- The subsoil contributed a significant role in the reinforced pile-supported embankment and it cannot be ignored during the design of a piled embankment.
- Imposed load on the embankment top induced by different train speed is also influence the load transfer mechanism. However, in this study, the imposed load by 40 km/h train speed is much higher thus the effect of the imposed load is not fully justified here.

8.1.3 3D analytical assessment of soil arching in a pile-supported railway embankment

- The failure of soil arching at the pile top is critical in the 3D condition, whereas the soil arching failure at crown is more critical in the 2D condition.
- The soil arching phenomena increase with an increase in the ratio of pile width (*d*) to clear pile spacing (*s*-*d*), which implies that pile spacing is a key parameter for efficient soil arching.
- The geosynthetic reinforcement and compression modulus of subsoil significantly contribute to the load transfer likely to be for large pile spacing and very compressive subsoil.

8.1.4 Investigation of soil arching in a pile-supported embankment under the earthquake

- During the earthquake, embankment modulus has negligible effect on the settlement. However, it decreases with an increase in friction angle and it is more noticeable at the end of earthquake. Therefore, friction angle is the most sensitive parameter of a pile-supported embankment which significantly affects the soil arching during the earthquake.
- The geosynthetic layer at the base of embankment encourages stress transfer to the pile head through the tension in geosynthetic and enhance the soil arching under the earthquake.
- The efficiency of soil arching mobilisation depends on the peak horizontal acceleration of an earthquake. Increase in peak horizontal acceleration may leads to the failures of soil arching.

8.1.5 Investigation of soil arching in a pile-supported embankment under the moving train load

- The dynamic behaviour of soil arching is different from static behaviour. In addition, it is significantly affected by different parameters of pile-supported embankment. Higher vertical stress on subsoil is observed in dynamic loading induced by moving train compared to the static surcharge imposed on the embankment top.
- The soil arching zone reduces with an increase in train speed. Smaller pile spacing encourages soil arching even in the dynamic loading induced by a moving train. Consequently, the settlement of subsoil reduces.
- Tension in geosynthetic layer increases with an increase in train speed, which improve the load transfer mechanism. In addition, the function of the geosynthetic layer is more significant under the higher train speed.

This thesis emphasises to accurate evaluation of vertical stress on the soil arching top. Chapter 4 and 5 is beneficial to calculate the vertical stress on the soil arching top. In addition, the seismic behaviour of soil arching should be considered during the design of a pile-supported embankment. It is worth noting from chapter 6 that the mobilisation of soil arching decreases according to the PGA during seismic excitation. A geosynthetic layer improves the performance of a pile-supported embankment even during the seismic activity. Therefore, this thesis has practical importance for design of a pile-supported embankment. In addition, this thesis suggested an optimize values of strength and stiffness parameters such as friction angle and elastic modulus of embankment which leads to cost effective and safe design.

8.2 RECOMMENDATIONS FOR FURTHER RESEARCH

The current study mainly focused on the seismic assessment of soil arching and precise evaluation of vertical stress on the soil arching using FEM and existing method. In this study a 2D unit cell is numerically simulated under the drained condition. This research study can be further extended considering limitations which are discussed in chapter 1. In the continuation to extend this research study following points can be considered in the future research:

- In this thesis, soil arching is investigated using a unit cell neglecting the slope of the embankment which can affect the overall performance of GRPS embankments. Thus, it is important to simulate a full-scale 3D numerical model of the GRPS embankment to assess each aspect. In addition, a single rail track is considered to avoid any complicity in stress calculation. However, commonly GRPS railways embankments have a double rail track which can be investigated in the future study to see the effect of rail track lines on the soil arching.
- The seismic response of a soil embankment and pile foundation is highly influenced by the frequency of ground excitation and amplification of inertial forces. A preliminary result is shown in this direction in section 4.5 of this thesis. It can be extended in future work with the effect of the frequency of ground excitation and the amplification of inertial forces.
- Analytical solution proposed in the Chapter 5 can be compared with a FEA in the future work.
- During an earthquake, the soil behaviour depends on the characteristics of the soil. In reality, subsoil properties can be varied with respect to subsoil layer depth. In this thesis, a uniform profile of subsoil is taken. However, it can be

extended in future studies taking a different subsoil profile.

- Considering different frequency ground motions could be useful for assessing the earthquake response of pile supported railway embankment.
- Effect of pore water pressure can be considered, as the pore water pressure influenced to lead transfer mechanism and overall performance of GRPS embankments.
- The seismic response of pile-supported railway embankments can be assessed under the different amplification of earthquake forces.
- The numerical investigation of earthquake assessment on soil arching should be verified using some field test.

REFERENCES:

Abaqus, V. 2013-18, 6.13-18, *Online Documentation Help*, Theory manual: Dassault Systèmes.

Abusharar, S.W. Zheng, J.J. Chen, B.G. & Yin, J.H. 2009, 'A simplified method for analysis of a piled embankment reinforced with geosynthetics', *Geotextiles and Geomembranes*, vol. 27, no. 1, pp. 39-52.

Almeida, M.S.S. Ehrlich, M. Spotti, A.P. & Marques, M.E.S. 2007, 'Embankment supported on piles with biaxial geogrids', *Proceedings of the Institution of Civil Engineers-Geotechnical Engineering*, vol. 160, no. 4, pp. 185-192.

Anh Tran, Q. Villard, P. & Dias, D. 2019, 'Discrete and continuum numerical modeling of soil arching between piles', *International Journal of Geomechanics*, vol. 19, no. 2, pp. 04018195.

Aqoub, K. Mohamed, M. & Sheehan, T. 2020, 'Quantitative analysis of shallow unreinforced and reinforced piled embankments with different heights subject to cyclic loads: experimental study', *Soil Dynamics and Earthquake Engineering*, vol. 138, pp. 106277.

Ariyarathne, P. Liyanapathirana, D.S. & Leo, C.J. 2013, 'Comparison of different two-dimensional idealizations for a geosynthetic-reinforced pile-supported embankment', *International Journal of Geomechanics*, vol. 13, no. 6, pp. 754-768.

ASIRI, P. 2012, *Recommandations pour la conception, le dimensionnement, l'exécution et le contrôle de l'amélioration des sols de fondation par inclusions rigides*. Presses des Ponts, (in French).

Bakr, J. & Ahmad, S.M., 2018, 'A finite element performance-based approach to correlate movement of a rigid retaining wall with seismic earth pressure', *Soil Dynamics and Earthquake Engineering*, vol. 114, pp. 460-479.

Bao, N. Wei, J. Chen, J.F. & Stephen, A. 2021, 'Investigation of Soil Arching under Cyclic Loading Using the Discrete Element Method', *International Journal of Geomechanics*, vol. 21, no. 7, pp. 04021117.

Bergado, D.T. & Teerawattanasuk, C. 2008, '2D and 3D numerical simulations of reinforced embankments on soft ground', *Geotextiles and Geomembranes*, vol. 26, no. 1, pp. 39-55.

Bhasi, A. & Rajagopal, K. 2013, 'Numerical investigation of time dependent behavior of geosynthetic reinforced piled embankments', *International Journal of Geotechnical Engineering*, vol. 7, no. 3, pp. 232-240.

Bi, Z. Gong, Q. & Huang, J. 2020, 'Long-Term Stability of High-Speed Railway Geosynthetic Reinforced Pile-Supported Embankment Subjected to Traffic Loading Considering Arching Effect', *Transportation Research Record*, vol. 2674, no. 7, pp. 596-607.

Briançon, L. & Simon, B. 2012, 'Performance of pile-supported embankment over soft soil: full-scale experiment', *Journal of Geotechnical and Geoenvironmental Engineering*, vol. 138, no. 4, pp. 551-561.

Briançon, L. & Simon, B. 2017, 'Pile-supported embankment over soft soil for a high-speed line', *Geosynthetics International*, vol. 24, no. 3, pp. 293-305.

Brzeziński, K. & Michalowski, R.L. 2021, 'Diffused arching in embankments supported by non-compliant columns with capping beams', *Computers and Geotechnics*, vol. 132, pp. 104031.

BS8006, B.S. 1995, *Strengthened/reinforced soils and other fills. British Standard BS8006*, section 8, pp. 80-121.

BSI, 2010, 'BS 8006-1: 2010: Code of practice for strengthened/reinforced soils and other fills', *Design of embankments with reinforced soil foundations on poor ground*.

Cao, W.Z. Zheng, J.J. Zhang, J. & Zhang, R.J. 2016, 'Field test of a geogrid-reinforced and floating pile-supported embankment', *Geosynthetics International*, vol. 23, no. 5, pp. 348-361.

Chen, R.P. Chen, Y.M. Han, J. & Xu, Z.Z. 2008, 'A theoretical solution for pile-supported embankments on soft soils under one-dimensional compression', *Canadian Geotechnical Journal*, vol. 45, no. 5, pp. 611-623.

Chen, R.P. Wang, Y.W. Ye, X.W. Bian, X.C. & Dong, X.P. 2016, 'Tensile force of geogrids embedded in pile-supported reinforced embankment: A full-scale experimental study', *Geotextiles and Geomembranes*, vol. 44, no. 2, pp. 157-169.

Chen, R.P. Xu, Z.Z. Chen, Y.M. Ling, D.S. & Zhu, B. 2010, 'Field tests on pile-supported embankments over soft ground', *Journal of Geotechnical and Geoenvironmental Engineering*, vol. 136, no. 6, pp. 777-785.

CUR 226, 2016, *Design guideline basal reinforced piled embankments*. In: Design Guideline Basal Reinforced Piled Embankments, CRC press.

Das, B.M. 2021, *Principles of geotechnical engineering*. Cengage learning.

Da Silva Burke, T.S. & Elshafie, M.Z. 2021, 'Arching in granular soils: experimental observations of deformation mechanisms', *Géotechnique*, vol. 71, no. 10, pp. 866-878.

Daniell, J. E. & Love, D. 2010, 'The socio-economic impact of historic Australian earthquakes', *In Australian Earthquake Engineering Society 2010 Conference*, pp. 8.

Deng, L. Kutter, B. L. & Kunnath, S. K. 2014, 'Seismic design of rocking shallow foundations: displacement-based methodology', *Journal of Bridge Engineering*, vol. 19, no. 11, pp. 04014043.

Di Donna, A., Ferrari, A. & Laloui, L. 2016, 'Experimental investigations of the soil–concrete interface: physical mechanisms, cyclic mobilization, and behaviour at different temperatures', *Canadian Geotechnical Journal*, vol. 53, no. 4, 659-672.

Doyle, N.F. 1980, *Railway track design: a review of current practice*.

EBGEO, 2011, *Recommendations for design and analysis of earth structures wing geosynthetic reinforcements*, Digital in English, German geotechnical society.

Esmaeili, M. & Arbabi, B. 2015, 'Railway embankments stabilization by tied back-to-back system', *Computers and Geotechnics*, vol. 67, pp. 110-120.

Esveld, C. 2001, *Modern railway track*, vol. 385, Zaltbommel: MRT-productions.

Fagundes, D.D.F. Almeida, M.D.S.S.D. Girout, R. Blanc, M. & Thorel, L. 2015, 'Behaviour of piled embankment without reinforcement', *Proceedings of the Institution of Civil Engineers-Geotechnical Engineering*, vol. 168, no. 6, pp. 514-525.

Fagundes, D.F. Almeida, M.S. Thorel, L. & Blanc, M. 2017, 'Load transfer mechanism and deformation of reinforced piled embankments', *Geotextiles and Geomembranes*, vol. 45, no. 2, pp. 1-10.

Fattah, M.Y. Mohammed, H.A. & Hassan, H.A. 2016, 'Load transfer and arching analysis in reinforced embankment', *Proceedings of the Institution of Civil Engineers-Structures and Buildings*, vol. 169, no. 11, pp. 797-808.

Feld, J. 1948, 'Early history and bibliography of soil mechanics', *In Proceedings, Second International Conference on Soil Mechanics and Foundation Engineering*, Rotterdam, vol. 1, pp. 1-7.

Filz, G. Sloan, J. McGuire, M.P. Collin, J. & Smith, M. 2012, 'Column-supported embankments: settlement and load transfer', *In Proceedings of Geo-Congress 2012*, pp. 54-77.

Fonseca, E.C. & Palmeira, E.M. 2019, 'Evaluation of the accuracy of design methods for geosynthetic-reinforced piled embankments', *Canadian Geotechnical Journal*, vol. 56, no. 6, pp. 761-773.

Geoscience Australia. *Historic Earthquakes of Australia*. Available online: https://geoscience-au.maps.arcgis.com/apps/MapSeries/index.html?appid=72ad590cc9364e41b06907406bb7712e.

George, T.I. & Dasaka, S.M. 2021, 'Numerical Investigation of Soil Arching in Dense Sand', *International Journal of Geomechanics*, vol. 21, no. 5, pp. 04021051.

Guido, V.A. 1987, 'Plate loading tests on geogrid-reinforced earth slab', *In Geosynthetic'87 Conference*, pp. 216-225.

Han, G.X. Gong, Q.M. & Zhou, S.H. 2015, 'Soil arching in a piled embankment under dynamic load', *International Journal of Geomechanics*, vol. 15, no. 6, pp. 04014094.

Han, J. & Gabr, M.A. 2002, 'Numerical analysis of geosynthetic-reinforced and pile-supported earth platforms over soft soil', *Journal of Geotechnical and Geoenvironmental Engineering*, vol. 128, no. 1, pp. 44-53.

Han, J. Wang, F. Al-Naddaf, M. & Xu, C. 2017, 'Progressive development of two-dimensional soil arching with displacement', *International Journal of Geomechanics*, vol. 17, no. 12, pp. 04017112.

Heitz, C. Lüking, J. & Kempfert, H.G. 2008, 'Geosynthetic reinforced and pile supported embankments under static and cyclic loading', *Strain*, vol. 1, pp. 1-5.

Hewlett, W.J. & Randolph, M.F. 1988, 'Analysis of piled embankments', *In International Journal of Rock Mechanics and Mining Sciences and Geomechanics Abstracts*, vol. 25, no. 6, pp. 297-298.

Hong, W.P. Lee, J. & Hong, S. 2014, 'Full-scale tests on embankments founded on piled beams', *Journal of Geotechnical and Geoenvironmental Engineering*, vol. 140, no. 12, pp. 04014067.

Hosseinpour, I. Soriano, C. & Almeida, M.S. 2019, 'A comparative study for the performance of encased granular columns', *Journal of Rock Mechanics and Geotechnical Engineering*, vol. 11, no. 2, pp. 379-388.

Huang, J. & Han, J. 2009, '3D coupled mechanical and hydraulic modeling of a geosynthetic-reinforced deep mixed column-supported embankment', *Geotextiles and Geomembranes*, vol. 27, no. 4, pp. 272-280.

Huang, J. & Han, J. 2010, 'Two-dimensional parametric study of geosynthetic-reinforced column-supported embankments by coupled hydraulic and mechanical modelling', *Computers and Geotechnics*, vol. 37, no. 5, pp. 638-648.

Iglesia, G.R. Einstein, H.H. & Whitman, R.V. 1999, 'Determination of vertical loading on underground structures based on an arching evolution concept', *In Geo-engineering for underground facilities*, pp. 495-506, ASCE.

Iglesia, G.R. Einstein, H.H. & Whitman, R.V. 2014, 'Investigation of soil arching with centrifuge tests', *Journal of Geotechnical and Geoenvironmental engineering*, vol. 140, no. 2, pp. 04013005.

Indraratna, B. Nimbalkar, S. Christie, D. Rujikiatkamjorn, C. & Vinod, J. 2010, 'Field assessment of the performance of a ballasted rail track with and without geosynthetics', *Journal of Geotechnical and Geoenvironmental Engineering*, vol. 136, no. 7, pp. 907-917.

Jenck, O. Dias, D. & Kastner, R. 2009, 'Three-dimensional numerical modeling of a piled embankment', *International Journal of Geomechanics*, vol. 9, no. 3, pp. 102-112.

Kelesoglu, M. K. & Cinicioglu, S. F. 2010, 'Free-field measurements to disclose lateral reaction mechanism of piles subjected to soil movements', *Journal of geotechnical and geoenvironmental engineering*, vol. 136, no. 2, pp. 331-343.

Kempfert, H.G. Göbel, C. Alexiew, D. & Heitz, C. 2004, 'German recommendation for reinforced embankments on pile-similar elements', *In Proceedings 3rd European Geosynthetics Conference*, pp. 279-284.

Khansari, A. & Vollmert, L. 2020, 'Load transfer and deformation of geogrid-reinforced piled embankments: field measurement', *Geosynthetics International*, vol. 27, no. 3, pp. 332-341.

King, D.J. Bouazza, A. Gniel, J.R. Rowe, R.K. & Bui, H.H. 2017, 'Load-transfer platform behaviour in embankments supported on semi-rigid columns: implications of the ground reaction curve', *Canadian Geotechnical Journal*, vol. 54, no. 8, pp. 1158-1175.

King, L. Bouazza, A. Dubsky, S. Rowe, R.K. Gniel, J. & Bui, H.H. 2019, 'Kinematics of soil arching in piled embankments', *Géotechnique*, vol. 69, no. 11, pp. 941-958.

Kramer, S. L. 1996. *Geotechnical earthquake engineering*. Pearson Education India.

Krishnamoorthy, A. & Kamal, S. 2016, 'Stability of an embankment on soft consolidating soil with vertical drains', *Geotechnical and Geological Engineering*, vol. 34, no. 2, pp. 657-669.

Lai, H.J. Zheng, J.J. Zhang, J. Zhang, R.J. & Cui, L. 2014, 'DEM analysis of "soil"-arching within geogrid-reinforced and unreinforced pile-supported embankments', *Computers and Geotechnics*, vol. 61, pp. 13-23.

Lai, H.J. Zheng, J.J. Zhang, R.J. & Cui, M.J. 2018, 'Classification and characteristics of soil arching structures in pile-supported embankments', *Computers and Geotechnics*, vol. 98, pp. 153-171.

Lai, H.J. Zheng, J.J. & Cui, M.J. 2021, 'Improved Analytical Soil Arching Model for the Design of Piled Embankments', *International Journal of Geomechanics*, vol. 21, no. 3, pp. 04020261.

Lee, T. Van Eekelen, S.J. & Jung, Y.H. 2021, 'Numerical verification of the concentric arches model for geosynthetic-reinforced pile-supported embankments: Applicability and limitations', *Canadian Geotechnical Journal*, vol. 58, no. 3, pp. 441-454.

Le Hello, B. & Villard, P. 2009, 'Embankments reinforced by piles and geosynthetics-Numerical and experimental studies dealing with the transfer of load on the soil embankment', *Engineering Geology*, vol. 106, no. 1-2, pp. 78-91.

Lehn, J. Moormann, C. & Aschrafi, J. 2016, 'Numerical investigations on the load distribution over the geogrid of a basal reinforced piled embankment under cyclic loading', *Procedia Engineering*, vol. 143, pp. 435-444.

Liang, R. & Zeng, S. 2002, 'Numerical study of soil arching mechanism in drilled shafts for slope stabilization', *Soils and foundations*, vol. 42, no. 2, pp. 83-92.

Li, L. Nimbalkar, S. & Zhong, R. 2018, 'Finite element model of ballasted railway with infinite boundaries considering effects of moving train loads and Rayleigh waves', *Soil Dynamics and Earthquake Engineering*, vol. 114, pp. 147-153.

Li, X. Miao, Y. & Cheng, K. 2018, 'Soil arching effect analysis via a modified finite element model based on a field test', *Journal of Testing and Evaluation*, vol. 46, no. 5, pp. 2218-2226.

Liu, H.L. Ng, C.W. & Fei, K. 2007, 'Performance of a geogrid-reinforced and pile-supported highway embankment over soft clay: case study', *Journal of Geotechnical and Geoenvironmental Engineering*, vol. 133, no. 12, pp. 1483-1493.

Liu, K.W. & Rowe, R.K. 2015, 'Numerical modelling of prefabricated vertical drains and surcharge on reinforced floating column-supported embankment behaviour', *Geotextiles and Geomembranes*, vol. 43, no. 6, pp. 493-505.

Liu, S.Y. Du, Y.J. Yi, Y.L. & Puppala, A.J. 2012, 'Field investigations on performance of T-shaped deep mixed soil cement column-supported embankments over soft ground', *Journal of Geotechnical and Geoenvironmental Engineering*, vol. 138, no. 6, pp. 718-727.

Low, B.K. Tang, S.K. & Choa, V. 1994, 'Arching in piled embankments', *Journal of Geotechnical Engineering*, vol. 120, no. 11, pp. 1917-1938.

López-Acosta, N.P. Espinosa-Santiago, A.L. Pineda-Núñez, V.M. Ossa, A. Mendoza, M.J. Ovando-Shelley, E. & Botero, E. 2019, 'Performance of a test embankment on very soft clayey soil improved with drain-to-drain vacuum preloading technology', *Geotextiles and Geomembranes*, vol. 47, no. 5, pp. 618-631.

Lu, W. & Miao, L. 2015, 'A simplified 2-D evaluation method of the arching effect for geosynthetic-reinforced and pile-supported embankments', *Computers and Geotechnics*, vol. 65, pp. 97-103.

Lysmer, J. & Kuhlemeyer, R.L. 1969, 'Finite dynamic model for infinite media', *Journal of the Engineering Mechanics Division*, vol. 95, no. 4, pp. 859-877.

Ma, L. Shen, S.L. Luo, C.Y. & Xu, Y.S. 2011, 'Field evaluation on the strength increase of marine clay under staged construction of embankment', *Marine Georesources & Geotechnology*, vol. 29, no. 4, pp. 317-332.

Marston, A. 1930, 'The theory of external loads on closed conduits in the light of the latest experiments', *In Highway research board proceedings*, vol. 9.

McKelvey III, J.A. 1994, 'The anatomy of soil arching', *Geotextiles and Geomembranes*, vol. 13, no. 5, pp. 317-329.

Meena, N.K. & Nimbalkar, S. 2019, 'Effect of water drawdown and dynamic loads on piled raft: Two-dimensional finite element approach', *Infrastructures*, vol. 4, no. 4, pp.75.

Meena, N.K. Nimbalkar, S. Fatahi, B. & Yang, G. 2020, 'Effects of soil arching on behavior of pile-supported railway embankment: 2D FEM approach', *Computers and Geotechnics*, vol. 123, pp. 103601.

NGG (Nordic Geosynthetic Group), 2005, *Nordic guidelines for reinforced soils and fills*.

Nimbalkar, S. & Indraratna, B. 2016, 'Improved performance of ballasted rail track using geosynthetics and rubber shockmat', *Journal of Geotechnical and Geoenvironmental Engineering*, vol. 142, no. 8, pp. 04016031.

Niu, T. Liu, H. Ding, X. & Zheng, C. 2018, 'Model tests on XCC-piled embankment under dynamic train load of high-speed railways', *Earthquake Engineering and Engineering Vibration*, vol. 17, no. 3, pp. 581-594.

Nunez, M.A. Briançon, L. & Dias, D.C.F.S. 2013, 'Analyses of a pile-supported embankment over soft clay: Full-scale experiment, analytical and numerical approaches' *Engineering Geology*, vol. 153, pp. 53-67.

Pham, H.V. & Dias, D. 2019, '3D numerical modeling of a piled embankment under cyclic loading', *International Journal of Geomechanics*, vol. 19, no. 4, pp. 04019010.

Pham, T.A. 2020a, 'Analysis of geosynthetic-reinforced pile-supported embankment with soil-structure interaction models', *Computers and Geotechnics*, vol. 121, pp. 103438.

Pham, T.A. 2020b, 'Load-deformation of piled embankments considering geosynthetic membrane effect and interface friction', *Geosynthetics International*, vol. 27, no. 3, pp. 275-300.

Phutthananon, C. Jongpradist, P. Jongpradist, P. Dias, D. & Baroth, J. 2020, 'Parametric analysis and optimization of T-shaped and conventional deep cement mixing column-supported embankments', *Computers and Geotechnics*, vol. 122, pp. 103555.

Potts, V.J. & Zdravkovic, L. 2008, 'Finite element analysis of arching behaviour in soils', *In Proceedings of the 12th International Conference on Computer Methods and Advances in Geomechanics*, pp. 3642-3649.

Potyondy, J.G. 1961, 'Skin friction between various soils and construction materials', *Geotechnique*, vol. 11, no. 4, pp. 339-353.

Puppala, A.J. Ruttanaporamakul, P. & Congress, S.S.C. 2019, 'Design and construction of lightweight EPS geofoam embedded geomaterial embankment system for control of settlements', *Geotextiles and Geomembranes*, vol. 47, no. 3, pp. 295-305.

Reid, W.M. & Buchanan, N.W. 1984, 'Bridge approach support piling', *In Piling and ground treatment*, Thomas Telford Publishing, pp. 267-274.

Rowe, R.K. & Liu, K.W. 2015, 'Three-dimensional finite element modelling of a full-scale geosynthetic-reinforced, pile-supported embankment', *Canadian Geotechnical Journal*, vol. 52, no. 12, pp. 2041-2054.

Rui, R. Han, J. Van Eekelen, S.J.M. & Wan, Y. 2019, 'Experimental investigation of soil-arching development in unreinforced and geosynthetic-reinforced pile-supported embankments', *Journal of Geotechnical and Geoenvironmental Engineering*, vol. 145, no. 1, pp. 04018103.

Rui, R. Han, J. Zhang, L. Zhai, Y. Cheng, Z. & Chen, C. 2020, 'Simplified method for estimating vertical stress-settlement responses of piled embankments on soft soils', *Computers and Geotechnics*, vol. 119, pp. 103365.

Rui, R. van Tol, F. Xia, Y.Y. van Eekelen, S. & Hu, G. 2018, 'Evolution of soil arching: 2D analytical models', *International Journal of Geomechanics*, vol. 18, no. 6, pp. 04018056.

Russell, D. & Pierpoint, N. 1997, 'An assessment of design methods for piled embankments', *Ground Engineering*, vol. 30, no. 10.

Saride, S. Puppala, A.J. Williammee, R. & Sirigiripet, S.K. 2010, 'Use of lightweight ECS as a fill material to control approach embankment settlements', *Journal of Materials in Civil Engineering*, vol. 22, no. 6, pp. 607-617.

Scopus Database, https://www.scopus.com/search/form.uri?display=basic#basic (assessed on September 2021).

Shen, P. Xu, C. & Han, J. 2020, 'Centrifuge tests to investigate global performance of geosynthetic-reinforced pile-supported embankments with side slopes', *Geotextiles and Geomembranes*, vol. 48, no. 1, pp. 120-127.

Sun, Q.D. Indraratna, B. & Nimbalkar, S. 2014, 'Effect of cyclic loading frequency on the permanent deformation and degradation of railway ballast', *Géotechnique*, vol. 64, no. 9, pp. 746-751.

Tang, Y. Xiao, S. & Yang, Q. 2020, 'The behaviour of geosynthetic-reinforced pile foundation under long-term dynamic loads: model tests', *Acta Geotechnica*, vol. 15, no. 8, pp. 2205-2225.

Terzaghi, K. 1936, 'Stress distribution in dry and in saturated sand above a yielding trap-door', *In proceedings First International Conference on Soil Mechanics and Foundation Engineering*, pp. 307-311.

Terzaghi, K. 1943. *Theoretical soil mechanics*, John Wiley & Sons, New York, pp. 11-15.

Thai Son, Q. Hassen, G. & de Buhan, P. 2010, 'Seismic stability analysis of piled embankments: A multiphase approach', *International Journal for Numerical and Analytical Methods in Geomechanics*, vol. 34, no. 1, pp. 91-110.

Van Eekelen, S.J.M. Venmans, A.A.M. Bezuijen, A. & Van Tol, A.F. 2020, 'Long term measurements in the Woerden geosynthetic-reinforced pile-supported embankment', *Geosynthetics International*, vol. 27, no. 2, pp. 142-156.

Van Eekelen, S.J. Bezuijen, A. Lodder, H.J. & Van Tol, A.F. 2012, 'Model experiments on piled embankments. Part I', *Geotextiles and Geomembranes*, vol. 32, pp. 69-81.

Van Eekelen, S.J. Bezuijen, A. Lodder, H.J. & Van Tol, A.F. 2012, 'Model experiments on piled embankments. Part II', *Geotextiles and Geomembranes*, vol. 32, pp. 82-94.

Van Eekelen, S.J.M. Bezuijen, A. & Van Tol, A.F. 2013, 'An analytical model for arching in piled embankments', *Geotextiles and Geomembranes*, vol. 39, pp. 78-102.

Van Eekelen, S.J.M. Bezuijen, A. & Van Tol, A.F. 2015, 'Validation of analytical models for the design of basal reinforced piled embankments', *Geotextiles and Geomembranes*, vol. 43, no. 1, pp. 56-81.

Wang, D. Sánchez, M. & Briaud, J.L. 2019, 'Numerical study on the effect of rigid inclusions on existing railroads', *International Journal for Numerical and Analytical Methods in Geomechanics*, vol. 43, no. 18, pp. 2772-2796.

Wang, H.L. & Chen, R.P. 2019, 'Estimating static and dynamic stresses in geosynthetic-reinforced pile-supported track-bed under train moving loads', *Journal of Geotechnical and Geoenvironmental Engineering*, vol. 145, no. 7, pp. 04019029.

Wu, L. Jiang, G. & Ju, N. 2019, 'Behavior and numerical evaluation of cement-fly ash-gravel pile-supported embankments over completely decomposed granite soils', *International Journal of Geomechanics*, vol. 19, no. 6, pp. 04019048.

Xu, C. Song, S. & Han, J. 2015, 'Scaled model tests on influence factors of full geosynthetic-reinforced pile-supported embankments', *Geosynthetics International*, vol. 23, no. 2, pp. 140-153.

Yang, T. Lu, Z. Ni, J. & Wang, G. 2019, '3D finite-element modelling of soil arch shape in a piled embankment', *Proceedings of the Institution of Civil Engineers-Geotechnical Engineering*, vol. 172, no. 3, pp. 255-262.

Ye, G.B. Wang, M. Zhang, Z. Han, J. & Xu, C. 2020, 'Geosynthetic-reinforced pile-supported embankments with caps in a triangular pattern over soft clay', *Geotextiles and Geomembranes*, vol. 48, no. 1, pp. 52-61.

Yi, Y. Liu, S. Puppala, A.J. & Xi, P. 2017, 'Vertical bearing capacity behaviour of single T-shaped soil-cement column in soft ground: laboratory modelling, field test, and calculation', *Acta Geotechnica*, vol. 12, no. 5, pp. 1077-1088.

Yun-Min, C. Wei-Ping, C. & Ren-Peng, C. 2008, 'An experimental investigation of soil arching within basal reinforced and unreinforced piled embankments', *Geotextiles and Geomembranes*, vol. 26, no. 2, pp. 164-174.

Yu, Y. Bathurst, R.J. & Damians, I.P. 2016, 'Modified unit cell approach for modelling geosynthetic-reinforced column-supported embankments', *Geotextiles and Geomembranes*, vol. 44, no. 3, pp. 332-343.

Zaeske, D. 2001, *Zur Wirkungsweise von unbewehrten und bewehrten mineralischen Tragschichten über pfahlartigen Gründungselementen. Fachgebiet u. Versuchsanst. Geotechnik*, Univ. Gh Kassel, (in German).

Zhang, C. Jiang, G. Liu, X. & Buzzi, O. 2016, 'Arching in geogrid-reinforced pile-supported embankments over silty clay of medium compressibility: Field data and analytical solution', *Computers and Geotechnics*, vol. 77, pp. 11-25.

Zhang, S.P. Cui, C.Y. & Wang, Z.T. 2012, 'Dynamic Analysis of the Piled Embankment under Seismic Excitations', *In Applied Mechanics and Materials*, Trans Tech Publications Ltd, vol. 178, pp. 1422-1425.

Zhang, Z. Han, J. & Ye, G. 2014, 'Numerical investigation on factors for deep-seated slope stability of stone column-supported embankments over soft clay', *Engineering Geology*, vol. 168, pp. 104-113.

Zhang, Z. Tao, F.J. Han, J. Ye, G.B. Cheng, B.N. & Xu, C. 2021, 'Arching Development in Transparent Soil during Multiple Trapdoor Movement and Surface Footing Loading', *International Journal of Geomechanics*, vol. 21, no. 3, pp. 04020262.

Zhang, Z. Wang, M. Ye, G.B. & Han, J. 2019, 'A novel 2D-3D conversion method for calculating maximum strain of geosynthetic reinforcement in pile-supported embankments', *Geotextiles and Geomembranes*, vol. 47, no. 3, pp. 336-351.

Zhou, M. Liu, H. Chen, Y. & Hu, Y. 2016, 'First application of cast-in-place concrete large-diameter pipe (PCC) pile-reinforced railway foundation: a field study', *Canadian Geotechnical Journal*, vol. 53, no. 4, pp. 708-716.

Zhuang, Y. & Cui, X. 2016, 'Case studies of reinforced piled high-speed railway embankment over soft soils', *International Journal of Geomechanics*, vol. 16, no. 2, pp. 06015005.

Zhuang, Y. & Li, S. 2015, 'Three-dimensional finite element analysis of arching in a piled embankment under traffic loading', *Arabian Journal of Geosciences*, vol. 8, no. 10, pp. 7751-7762.

Zhuang, Y. & Wang, K. 2017, 'Analytical solution for reinforced piled embankments on elastoplastic consolidated soil', *International Journal of Geomechanics*, vol. 17, no. 9, pp. 06017010.

Zhuang, Y. & Wang, K.Y. 2018, 'Finite-element analysis of arching in highway piled embankments subjected to moving vehicle loads', *Géotechnique*, vol. 68, no. 10, pp. 857-868.

Zhuang, Y. & Wang, K.Y. 2015, 'Three-dimensional behavior of biaxial geogrid in a piled embankment: numerical investigation', *Canadian Geotechnical Journal*, vol. 52, no. 10, pp. 1629-1635.

Zhuang, Y. Ellis, E.A. & Yu, H.S. 2010, 'Plane strain FE analysis of arching in a piled embankment', *Proceedings of the Institution of Civil Engineers-Ground Improvement*, vol. 163, no. 4, pp. 207-215.

Zhuang, Y. Ellis, E. & Yu, H.S. 2012, 'Three-dimensional finite-element analysis of arching in a piled embankment', *Géotechnique*, vol 62, no. 12, pp. 1127-1131.

Zhuang, Y. Wang, K.Y. & Liu, H.L. 2014, 'A simplified model to analyze the reinforced piled embankments', *Geotextiles and Geomembranes*, vol. 42, no. 2, pp. 154-165.

APPENDIX A

Derivation of analytical approach to determine soil arching in the three-dimensional (3D) condition

A.1 Soil arching in the three-dimensional (3D) condition when the arching crown is critical

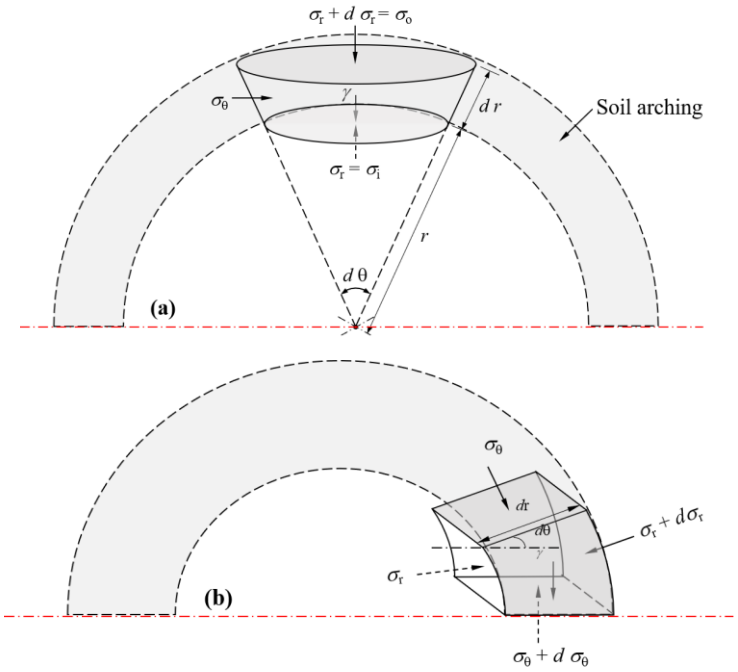

Figure A.1: Soil element at the (a) soil arching crown (b) pile head

From Figure A.1(a), areas and volume of the soil arcing top element are:

Area of the element which is located on the inner side,

$$dA_i = \frac{1}{4}\pi(r.d\theta)^2$$

Area of the element which is located on the top of the soil arching,

$$dA_o = \frac{1}{4}\pi(r+dr)^2$$

Area of side of the element (refer to Figure 5.1 (case a)), **(A-1)**

$$dA_s \approx \frac{1}{4}\pi.r.d\theta.dr$$

Volume of the element located on the soil arching top,

$$dV \approx \frac{1}{4}\pi . r^2 . d\theta^2 . dr$$

The radial equilibrium equation follows that:

$$-\sigma_r . dA_i + (\sigma_r + d\sigma_r) . dA_o - \sigma_\theta . \sin\left(\frac{d\theta}{2}\right) . dA_s + \gamma . dV = 0 \qquad \textbf{(A-2)}$$

Substituting Equations (A-1) into (A-2), and ignoring the terms with a product of more than one increment:

$$\frac{d\sigma_r}{dr} + \frac{2(\sigma_r - \sigma_\theta)}{r} + \gamma = 0 \qquad \textbf{(A-3)}$$

For limit state analysis, Equation A-3 becomes:

$$\frac{d\sigma_r}{dr} + \frac{2.\sigma_r(1-k_p)}{r} + \gamma = 0 \qquad \textbf{(A-4)}$$

Equation A-4 is represented the differential equation for the radial stress in the three-dimensional hemisphere as explained by Hewlett and Randolph (1988).

Equation A-4 can be written as:

$$\frac{d}{dr}\left(e^{\int P(r)dr} . \sigma_r\right) = e^{\int P(r)dr} . q(r) \qquad \textbf{(A-5)}$$

with, $P(r) = \frac{2(1-k_p)}{r}$; $q(r) = -\gamma$;

Solution of Equation A-5:

$$e^{(\int P(r)dr)} = e^{\int\left(\frac{2(1-k_p)}{r}\right)dr} = e^{(2(1-k_p).\ln r)} = r^{\left(2(1-k_p)\right)} \qquad \textbf{(A-6)}$$

Thus, Equation A-5 becomes:

$$\frac{d}{dr}\left(r^{\left(2(1-k_p)\right)} . \sigma_r\right) = -\gamma . r^{\left(2(1-k_p)\right)} \qquad \textbf{(A-7)}$$

$$r^{\left(2(1-k_p)\right)} . \sigma_r = -\frac{\gamma}{(2(1-k_p)+1)} . r^{\left(\left(2(1-k_p)\right)+1\right)} + C' \qquad \textbf{(A-8)}$$

$$\sigma_r = \gamma.\left(\frac{r}{2.k_p-3}\right) + C'.r^{2(k_p-1)} \quad \textbf{(A-9)}$$

Equation A-9 is the general solution of Equation A-4. From Figure A.1(a), it is clear that the outer radius of the hemisphere is $r = s/\sqrt{2}$, and stress become (σ_r) = $\gamma(h - s/\sqrt{2})$. Substituting these into Equation A-9:

$$C' = \gamma.\left(s/\sqrt{2}\right)^{2-2k_p}.\left[h - \left(s/\sqrt{2}\right).\left(\frac{2k_p-2}{2k_p-3}\right)\right] \quad \textbf{(A-10)}$$

In this thesis, a railway track and the equivalent dynamic load is considered on the embankment top. Thus, total vertical stress on the soil arching crown due to the self-weight of the rail track and the equivalent dynamic load (σ_{RT}) is calculated similar to Equation 4.4. Using the constant of integration (C') and the σ_{RT}, the radial stress at the soil arching crown is:

$$\sigma_r = \gamma.\left(\frac{r}{2k_p-3}\right) + \left(\frac{\sqrt{2}\,r}{s}\right)^{2.(k_p-1)}\left[\gamma h - \gamma\frac{s}{\sqrt{2}}\left(\frac{2k_p-2}{2k_p-3}\right) + \sigma_{RT}\right] \quad \textbf{(A-11)}$$

Equation of A-11 is the same as Equation 5.4.

From Figure 5.1(case a), the inner radius of soil arching ($r_i = (s - d)/\sqrt{2}$), and thus, the vertical stress on the inner boundary of the soil arching (σ_i) can be calculated by putting $r = (s - d)/\sqrt{2}$ into Equation A-11.

$$\sigma_i = \gamma\left(\frac{(s-d)}{\sqrt{2}\,(2k_p-3)}\right) + \left(\frac{s-d}{s}\right)^{2(k_p-1)}\left[\gamma h - \gamma\frac{s}{\sqrt{2}}\left(\frac{2k_p-2}{2k_p-3}\right) + \sigma_{RT}\right] \quad \textbf{(A-12)}$$

Equation of A-12 is the same as Equation 5.5.

The vertical stress (σ_s) acting at the base of embankment on geosynthetic layer is the

product of the (σ_i) and overburden stress below the inner boundary of soil arching:

$$\sigma_s = \sigma_i + \frac{\gamma(s-d)}{\sqrt{2}} \quad \textbf{(A-13)}$$

Substituting Equations (A-12) into (A-13),

$$\sigma_s = \gamma \frac{(s-d)}{\sqrt{2}}\left(\frac{2k_p-2}{2k_p-3}\right) + \left(\frac{s-d}{s}\right)^{2(k_p-1)}\left[\gamma h - \gamma \frac{s}{\sqrt{2}}\left(\frac{2k_p-2}{2k_p-3}\right) + \sigma_{\mathrm{RT}}\right] \quad \textbf{(A-14)}$$

Equation of A-14 is the same as Equation 5.7.

A.2 Soil arching in the three-dimensional (3D) condition when the pile head is critical

Total force acting on the pile head (P) which is arranged in a square pattern is arisen by four hemispherical shape of soil arching (refer to Figure A.2), and is obtained by integrating the tangential stress (σ_θ) = $k_p.\sigma_r = k_p.\sigma_{geo}$.

Thus,

$$P = 4.\int_{(s-d)/2}^{s/2} \sigma_\Theta \, . dA_{pile} \quad \textbf{(A-15)}$$

Equation of A-15 is the same as Equation 5.11.

Substituting Equations (A-11) into (A-15),

$$P = 2\,\sigma_{geo}.s.(s-d)\left(\frac{k_p}{k_p+1}\right)\left[\left(\frac{s}{s-d}\right)^{k_p} - 1 - k_p.\left(\frac{d}{s}\right)\right] \quad \textbf{(A-16)}$$

Equation of A-16 is the same as Equation 5.12.

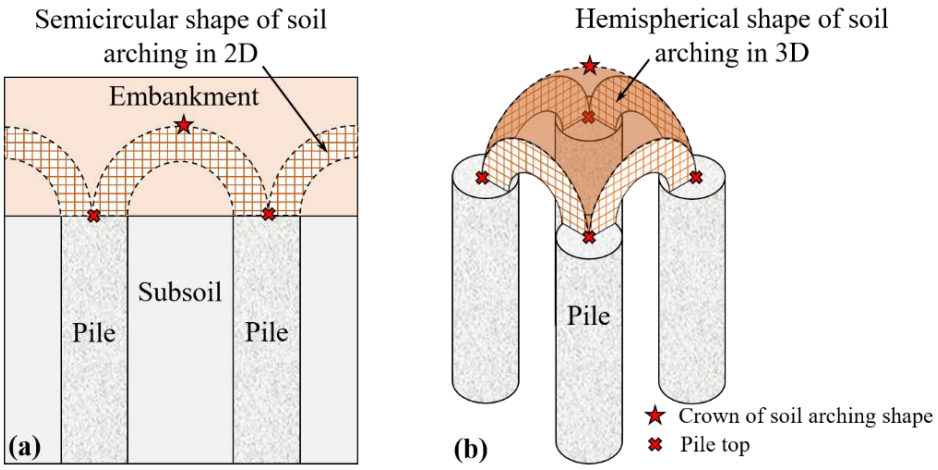

Figure A.2: Failure theory for (a) 2D plane strain and (b) 3D condition (modified from Hewlett and Randolph 1988).

Now for overall equilibrium condition;

$$(\gamma h + \sigma_{\mathrm{RT}}).s^2 = P + \sigma_s(s^2 - d^2) \qquad \textbf{(A-17)}$$

Substituting Equations (A-16) into (A-17),

$$\sigma_{geo} = (\gamma h + \sigma_{\mathrm{RT}}) / \left\{ \left(\frac{s^2-d^2}{s^2}\right) + \left(\frac{2k_p}{k_p+1}\right) \left[\left(\frac{s-d}{s}\right)^{(1-k_p)} - \left(\frac{s-d}{s}\right)\left(\frac{s+k_p.d}{s}\right) \right] \right\} \qquad \textbf{(A-18)}$$

Equation of A-18 is the same as Equation 5.15.